Dissertation
submitted to the
Combined Faculty of Mathematics, Engineering and Natural Sciences
of Heidelberg University, Germany
for the degree of
Doctor of Natural Sciences

Put forward by
Luzian Merlin Rhys Seeburger
born in: Vienna, Austria
Oral examination: July 22nd, 2025

Hunting for dormant Black Holes in the Milky Way

Luzian Merlin Rhys Seeburger

Supervisors

Prof. Dr. Hans-Walter Rix
Asst.-Prof. Kareem El-Badry, PhD

Examination committee

Prof. Dr. Hans-Walter Rix (referee)
Priv.-Doz. Dr. Anna Pasquali (referee)
Prof. Dr. Michela Mapelli
Prof. Dr. rer. nat. Werner Aeschbach

Summary

Stellar population models predict 10^7 stellar mass black holes (BHs) in the Milky Way, with an unknown fraction in mostly dormant binary systems. To date, less than a handful of dormant BH binaries have been identified, and post-interaction star-star systems masquerading as BH systems — so-called impostors — have greatly complicated this identification.

In this thesis, we develop a set of tools to identify and characterise these impostors using spectroscopy. We demonstrate the power of spectral disentangling using both simulated and real data. Applying the tools to multi-epoch spectra of a sample of impostor systems, we confirm their post-interaction nature and place constraints on their stellar parameters. Critically, we now ascertain their rotation rates and can make improved inferences on their mass transfer history.

We also develop single-epoch high-resolution spectra as a diagnostic tool for Galactic binaries identified by *Gaia* , showing the capabilities of such data to determine fundamental properties, in particular the flux ratio, of these systems. We have been able to add flux ratio measurements or constraints to 80,000 spectra of *Gaia* binaries, which are crucial for the interpretation of the *Gaia* data.

These toolsets will prove invaluable when analysing upcoming data releases, allowing us to constrain important processes in (binary) stellar evolution and BH formation.

Zusammenfassung

Sternpopulations-Modelle sagen etwa 10^7 stellare Schwarze Löcher (SL) in der Milchstraße vorher, wobei ein unbekannter Anteil in überwiegend ruhenden Doppelsternsystemen existiert. Bis heute wurde weniger als eine Handvoll solcher ruhenden SL-Doppelsterne identifiziert, und post-interaktive Stern-Stern-Systeme, die sich als SL-Systeme ausgeben – sogenannte Imitatoren – erschweren diese Identifikation erheblich.

In dieser Arbeit entwickeln wir eine Reihe von Werkzeugen, um diese Imitatoren mittels Spektroskopie zu identifizieren und zu charakterisieren. Wir demonstrieren die Leistungsfähigkeit des "Spectral Disentangling" anhand sowohl simulierter als auch realer Daten. Durch Anwendung dieser Werkzeuge auf Multi-Epochen-Spektren einer Stichprobe von Imitator-Systemen bestätigen wir deren post-interaktiven Charakter und schränken ihre stellaren Parameter ein. Insbesondere können wir nun ihre Rotationsraten bestimmen und verbesserte Rückschlüsse auf ihre Massetransfer-Historie ziehen.

Darüber hinaus entwickeln wir Einzel-Epochen-Hochauflösungsspektren als diagnostisches Werkzeug für galaktische Doppelsterne, die von *Gaia* identifiziert wurden, und zeigen, welche fundamentalen Eigenschaften – insbesondere das Flussverhältnis – sich aus solchen Daten ableiten lassen. Wir konnten Flussverhältnisse oder entsprechende Einschränkungen für 80,000 Spektren von *Gaia* -Doppelsternen hinzufügen, was für die Interpretation der *Gaia* -Daten von zentraler Bedeutung ist.

Diese Methoden werden bei der Analyse bevorstehender Datenveröffentlichungen von unschätzbarem Wert sein, da sie es ermöglichen, zentrale Prozesse der (binären) Sternentwicklung und der Entstehung stellarmassiver SL besser einzugrenzen.

List of abbreviations

BH Black hole

BLS Blue lurker star

BSS Blue straggler star

CCF Cross-correlation function

CE Common envelope

CMD Colour-magnitude diagram

CO Compact object

DR Data release

FOM Figure of merit

HRD Hertzsprung-Russell diagram

MS Main sequence

MT Mass transfer

NS Neutron star

PISN Pair-instability supernova

PMa Proper motion anomaly

RL Roche lobe

RUWE Renormalised unit weight error

RV Radial velocity

RVS Radial velocity spectrometer

S/N Signal-to-noise ratio

SB1 Single-lined spectroscopic binary

SB2 Double-lined spectroscopic binary

SED Spectral energy distribution

SN Supernova

SVD Singular value decomposition

List of physical constants

symbol	name	value in SI units
$M_\odot$	Solar mass	$1.988410 \times 10^{30}\,\mathrm{kg}$
$L_\odot$	Solar luminosity	$3.828 \times 10^{26}\,\mathrm{W}$
$R_\odot$	Solar radius	$6.957 \times 10^{8}\,\mathrm{m}$
σ	Stefan-Boltzmann constant	$5.6703744191844314 \times 10^{-8}\,\mathrm{W\,m^{-2}\,K^{-4}}$
c	Speed of light in vacuum	$2.99792458 \times 10^{8}\,\mathrm{m\,s^{-1}}$
G	Gravitational constant	$6.6743 \times 10^{-11}\,\mathrm{m^{3}\,kg^{-1}\,s^{-2}}$

Contents

"For that one fraction of a second, you were open to options you had never considered. That is the exploration that awaits you. Not mapping stars and studying nebulae, but charting the unknown possibilities of existence." - *All Good Things, Star Trek: The Next Generation*

Context and theoretical background

As early as the 17th century, astronomers have been recording observations of "double stars", two stars close to each other on the night sky (Riccioli, 1651). Herschel (1803) discovered that the parallaxes of many of these objects do not imply a chance alignment, but rather two stars physically close and orbiting each other. He writes in Herschel (1802):

> *If, on the contrary, two stars should really be situated very near each other, and at the same time so far insulated as not to be materially affected by the attractions of neighbouring stars, they will then compose a separate system, and remain united by the bond of their own mutual gravitation towards each other. This should be called a real double star; and any two stars that are thus mutually connected, form the binary sidereal system which we are now to consider.*

1.1. Binaries and their Role in Astrophysics

Much has happened in the last ~ 200 years in the field of binary astrophysics.

Perhaps most centrally, we are now aware that binary (and higher order) systems are in fact very common (e.g. Sana et al., 2012; Moe and Di Stefano, 2017; Offner et al., 2023) . In Figure 1.1 we see the multiplicity fraction (left panel, separated into general multiplicity and triple- or higher order systems) and companion frequency (right panel) as a function of primary mass. Generally, the primary is the more massive star of the binary and the secondary or companion the less massive component. We immediately notice a strong trend with primary mass; higher mass primaries are extremely likely to occur in binary, triple, or higher order systems, with almost all of them having at least one companion, while stars like our sun have a companion about 50% of the time. One reason for this is that massive stars require massive gas clouds to form. These massive clouds form large discs, where fragmentation occurs at larger separations compared to less massive discs. Surviving fragments migrate inwards by accreting from the disc, forming stars that are close enough to remain gravitationally bound in multiple systems (Tokovinin and Moe, 2020).

These systems affect multiple areas of astrophysics. Binary interactions affect the evolution of many stars (Offner et al., 2023); stellar nucleosynthesis; supernova (SN) progenitors

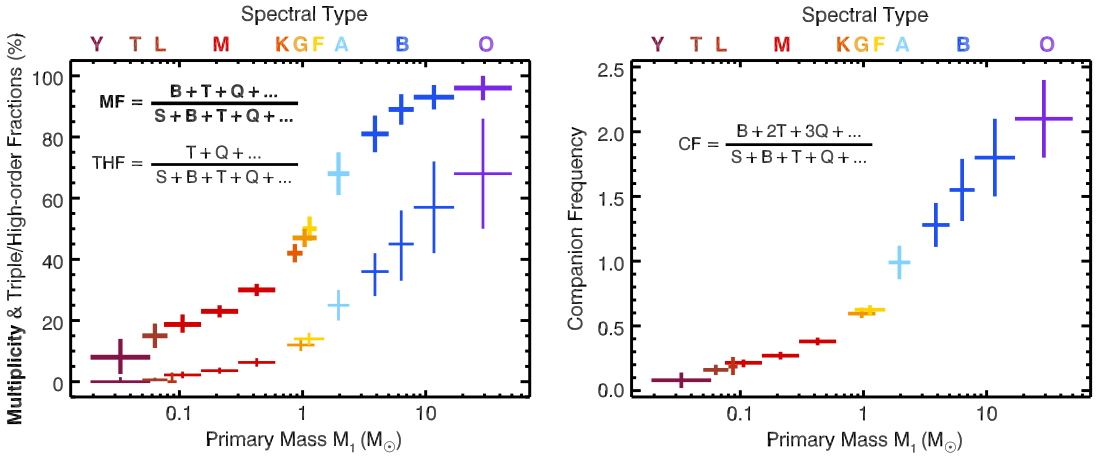

Figure 1.1: Left: Multiplicity (bold) and Triple/Higher order fraction as a function of primary mass. Among the most massive stars (O- & B-type), the multiplicity fraction is $\gtrsim 80\%$, while for solar-like stars, it is closer to 50%. Right: Companion frequency as a function of primary mass. Figure from Offner et al. (2023)

and thus the explosions themselves (Metzger, 2022); compact object (CO) formation, and hence gravitational wave sources (Tauris et al., 2017). It is clear that binaries form an important chapter of stellar physics, and a better understanding of these is crucial to many processes.

1.1.1. Binary Classification

Before diving into how binaries interact, it is useful to clarify some language commonly used when discussing these systems. Very importantly, the **Roche Lobe** (RL) is the region around a star in a binary system where material is bound to the star, bounded by the two stars' gravitational equipotential. This is illustrated in Figure 1.2. The RLs of two stars in a binary touch at the Lagrange point L1. We consider the RL filling factor to be the fraction of the star's radius over the radius of a sphere approximating the RL. Then, with illustrations found in Figure 1.3:

- In a **detached** binary, neither star fills its RL (panel a).
- A **semidetached** binary consists of one star filling its RL (generally due to its evolution), and one star which does not (panel b).
- In a **contact** binary, both stars have a RL filling factor of 1 (panel c).

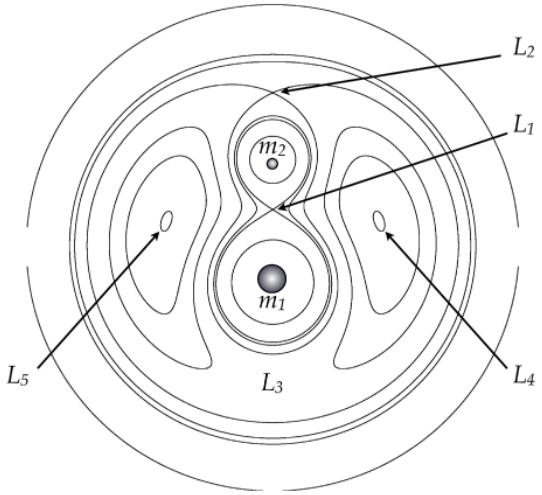

Figure 1.2: Cross section of the equipotential surfaces for two stars with mass ratio 0.4. The 5 Lagrange points are also clearly marked. Figure from Benacquista and Downing (2013)

- Finally, for **overcontact** binaries, both stars *overfill* their RLs, leading to a characteristic peanut shape (panel c).

In detached systems, the stars generally do not interact with each other, but an amount of mass transfer (MT) due to stellar wind may still occur (Shakura et al., 2015). In semidetached systems, mass is transferred from the RL filling star to its companion, while in contact systems, it can flow both ways. Overcontact binaries share the same outer layer of hot gas, which rotates with the system, unlike a **common envelope** (CE), where the two cores rotate within the envelope. Both overcontact and CE phases can be short-lived, but due to a higher degree of instability, CE is usually shorter. Whether a star fills its RL can be determined approximately by using Eggleton (1983)'s formulae for the size of a sphere with a volume approximating that of the RL as a function of the mass ratio $q = M_{\rm B}/M_{\rm A}$ and orbital separation a. For $R_{\rm star} < R_{\rm RL}$, the binary is detached; if $R_{\rm star} = R_{\rm RL}$ for one star, semi-detached, and for both stars, the system is a contact binary; if $R_{\rm star} > R_{\rm RL}$ for both stars, the system is an overcontact binary.

1.1.2. Importance of Binary Interactions in Stellar Evolution

For massive stars, life is rarely a peaceful coexistence within a small family. Instead, the vast majority interact with a companion throughout their relatively short lifetimes, impacting their evolution (Sana et al., 2012). Figure 1.4 shows the ways and frequencies in which O stars (the most massive stars) interact with their companion(s). For the shortest initial period systems, a stellar merger is the most likely outcome. At longer periods, other interactions become more and more relevant. These include stripping, where a star loses its envelope, accretion of that envelope material by the other star, which subsequently rotates faster, and CE evolution, where both stellar cores enter a shared envelope. Only the longest periods lead to effectively single evolution with no stellar interaction (Sana et al., 2012; Henneco et al., 2024).

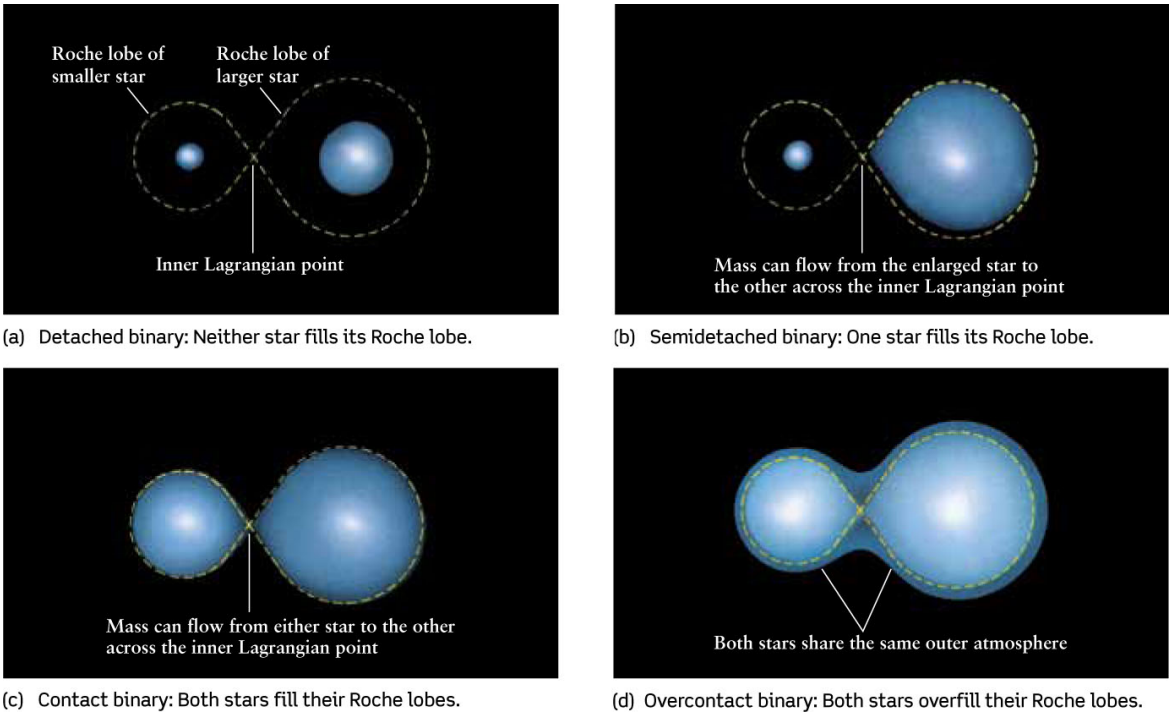

(a) Detached binary: Neither star fills its Roche lobe.
(b) Semidetached binary: One star fills its Roche lobe.
(c) Contact binary: Both stars fill their Roche lobes.
(d) Overcontact binary: Both stars overfill their Roche lobes.

Figure 1.3: Illustrations of the different types of binaries. Figure from Freedman et al. (2014)

1.1.2.1 Stellar mergers

Stellar mergers are likely one of the phenomena giving rise to *blue stragglers* (BSS) and *blue lurkers* (BLS). BSS are stars that do not fall neatly on the main sequence (MS) of their population, but lie beyond the blue end of the MS turn-off. They thus look "too young" for the rest of the population, but in reality are potentially the product of two lower-mass stars (which have longer expected lifetimes) merging to form a higher mass, "younger-looking" BSS (Schneider et al., 2015). BLS are similar in that they may be merger products, but are of low enough mass that they do not "fall off" the MS, but instead "lurk" amongst other intermediate mass star below the MS turn-off (Subramaniam et al., 2020). As the population continues to evolve, with single-born intermediate mass stars leaving the MS, BLS will become BSS.

1.1.2.2 Mass transfer

MT is, generally speaking, mass moving from one star (donor) onto the other (accretor). If neither star fills its RL, this can happen via stellar wind from the donor being accreted by the accretor (Bondi and Hoyle, 1944). If the donor fills its RL, then mass can overflow via L1 (and in extreme cases L2) onto the accretor (Kippenhahn and Weigert, 1967).

This has a multitude of effects on both stars. As the donor loses (part of) its envelope, it becomes a (partially) stripped star, generally rich in helium (Götberg et al., 2017), though it may retain or re-accrete a significant amount of hydrogen (Bodensteiner et al., 2020). The process can also expose the stellar core of the donor. If the core is very compact, hot and underluminous compared to an MS star, it may be called a hot subdwarf (Heber, 2009). As the core is of high temperature and low mass, hydrostatic equilibrium may not be maintained; radiation pressure can cause the core to expand and cool. The result is commonly referred to as a bloated or puffed-up stripped star, which is overluminous considering its low

mass. However, this phase is only short-lived, and eventually the donor shrinks and heats again (El-Badry and Quataert, 2021).

The accretor is also affected. Accretion of the donor's envelope increases its total mass and can deliver additional hydrogen, rejuvenating the star (Schneider et al., 2015). Further, the increase in mass leads to a higher temperature. As angular momentum of the system has to be conserved, mass moving from the donor onto the accretor causes the latter to spin up (de Mink et al., 2013), potentially to critical rotation, with only about $5 \sim 10\%$ of the mass of the accretor necessary to reach $v_{\rm crit}$ (Packet, 1981). Observationally, however, we frequently find stars where more than enough mass has been transferred but the accretor is not rotating at critical. A sample of such objects is discussed in chapter 3.

MT is commonly categorised into Case A, B or C (Kippenhahn and Weigert, 1967). Case A describes MT due to RL overflow from a MS donor, Case B from an evolved star during hydrogen shell burning, and Case C during core helium burning and after core helium depletion. If multiple episodes of MT occur, combination names may be used (e.g. Case AB to describe a system with both MS and evolved donor MT).

There are many uncertainties in much of the physics underlying stellar interactions. Observing binaries at various stages of interaction (before, during, and after MT) can help constrain these processes.

An important parameter is MT *conservativeness*. It describes how much of the mass lost by the donor is retained by the accretor, or alternatively lost from the system. There are three main channels through which mass can be lost: from the donor via stellar wind, from the accretor via isotropic re-emission, or by forming a circumbinary ring. The fraction of mass lost via each of these channels can be parameterised as α (stellar wind), β (isotropic re-emission) and δ (circumbinary ring) - then, equations from Soberman et al. (1997) relate the evolution of the orbital period to these parameters and the initial period. MT conservativeness is poorly constrained, but has profound effects on the evolution of both stars and the orbital parameters of the system. Very non-conservative MT can lead to orbital widening if the mass is lost from near the donor star (for example via stellar wind, the α channel), and shrinking if mass is lost from near the accretor or a circumbinary ring (β and δ channels) (Sepinsky et al., 2009). The geometry of the orbit can also be altered with eccentricity pumping mechanisms due to e.g. the presence of a circumbinary ring (Krynski et al., 2025). This has an effect on the predictions of phenomena critically dependent on orbital separation, such as merger and CE rates (Willcox et al., 2023). Mass ratio reversal is also less likely with strongly non-conservative MT (Pols, 2007), suppressing the formation of Algol-type systems where the more massive star appears less evolved due to MT. MT conservativeness can be constrained observationally if a reasonable guess at the initial period of a post MT system can be made (e.g. from stellar evolution models). Certain scenarios can be ruled out if they would cause the orbit to become unphysical, e.g. by shrinking too much.

As has been discussed, MT and the associated transfer of angular momentum in binaries is also a root cause of stellar spin-up in the accretor. The exact extent and mechanisms behind this are still debated, with simple models predicting spin-up to critical rotation with comparatively little MT (Packet, 1981), while alternative models of angular momentum transport paint a different picture. Popham and Narayan (1991) and Paczynski (1991) describe interactions between the accretor and its acccretion disc that may slow down the rotation or prevent the star from spinning up to critical. In their models, mass may flow inward onto the star as angular momentum is transported outwards. Generally, stellar spin-down,

a decrease in the star's rotational velocity, plays a vital role in binary and stellar evolution. This spin-down may occur due to a number of possible mechanisms. In cool stars, magnetic braking may play a major role (Kraft, 1967), while in binaries tidal forces can come into action (Zahn, 2008). Numerous efforts have been made over the years to analyse and constrain these mechanisms across different mass regimes (e.g. Leiner et al., 2018; Vanbeveren et al., 2018; Dervişoğlu et al., 2010). Frequently, however, these processes are not sufficient to explain observed rotational velocities (see e.g. Section 3.4), and extensions to simple physical models must be considered.

1.1.2.3 Common envelope evolution

CE evolution is among the most poorly understood binary stellar interactions, partially due to simulations being very expensive (Röpke and De Marco, 2023). It occurs when the donor begins overflowing its RL. This can cause a redistribution of the mass and an increase of the mass ratio q, and/or may transfer angular momentum from the orbit to the envelope. Consequently, the orbit and thus the donor RL shrink, increasing the MT rate and leading to runaway MT and a CE event. Here, both stars (or rather, the primary's core and the secondary) share a CE. Drag forces inside the CE cause the orbit of the binary to shrink and circularise. This can lead to a merger inside the CE (in-spiral, thought to be an important formation channel for merging COs (Tauris et al., 2017)), or sufficient heating and subsequent ejection of the envelope.

There are also efforts to model these processes using 3D simulations (e.g. Röpke and De Marco, 2023). The outputs of these can be compared to observations, providing insight into likely, unlikely and even unphysical scenarios.

1.1.3. Binary systems as laboratories for compact object studies

Most stars are projected to end their lives as a CO, its type determined mostly be the star's mass prior to its demise. Stars up to around 10 $M_\odot$ leave behind a white dwarf, stars between 10 and 25 $M_\odot$ a neutron star (NS) and more massive stars a black hole (BH) (for more details, see section 1.3.1 and references therein). These stellar remnants have the potential to provide answers to many of the questions raised in this chapter. Especially our understanding of massive stellar evolution has many gaps that massive COs may help to fill. However, BHs are famously dark and do not radiate any light of their own, making their detection quite literally the search for a needle in a haystack (except the haystack is in a completely dark room and the needle is black). Binary systems can help remedy this problem somewhat. A BH and star in a bound system will result in orbital motion of the objects around their shared centre of mass. This movement of the star can be detected in a variety of ways, depending principally on the orbital configuration and masses of both objects. Thus, binaries present a unique opportunity to find COs and, at the same time, obtain information on how the system evolved up to this point.

1.2. Diagnostic tools for Binaries

Binary systems can be identified as such and further studied using a variety of observational techniques. The possible mode of observation is dictated by the properties of the observed system, most importantly, the distance from the observer and the orbital period of the system.

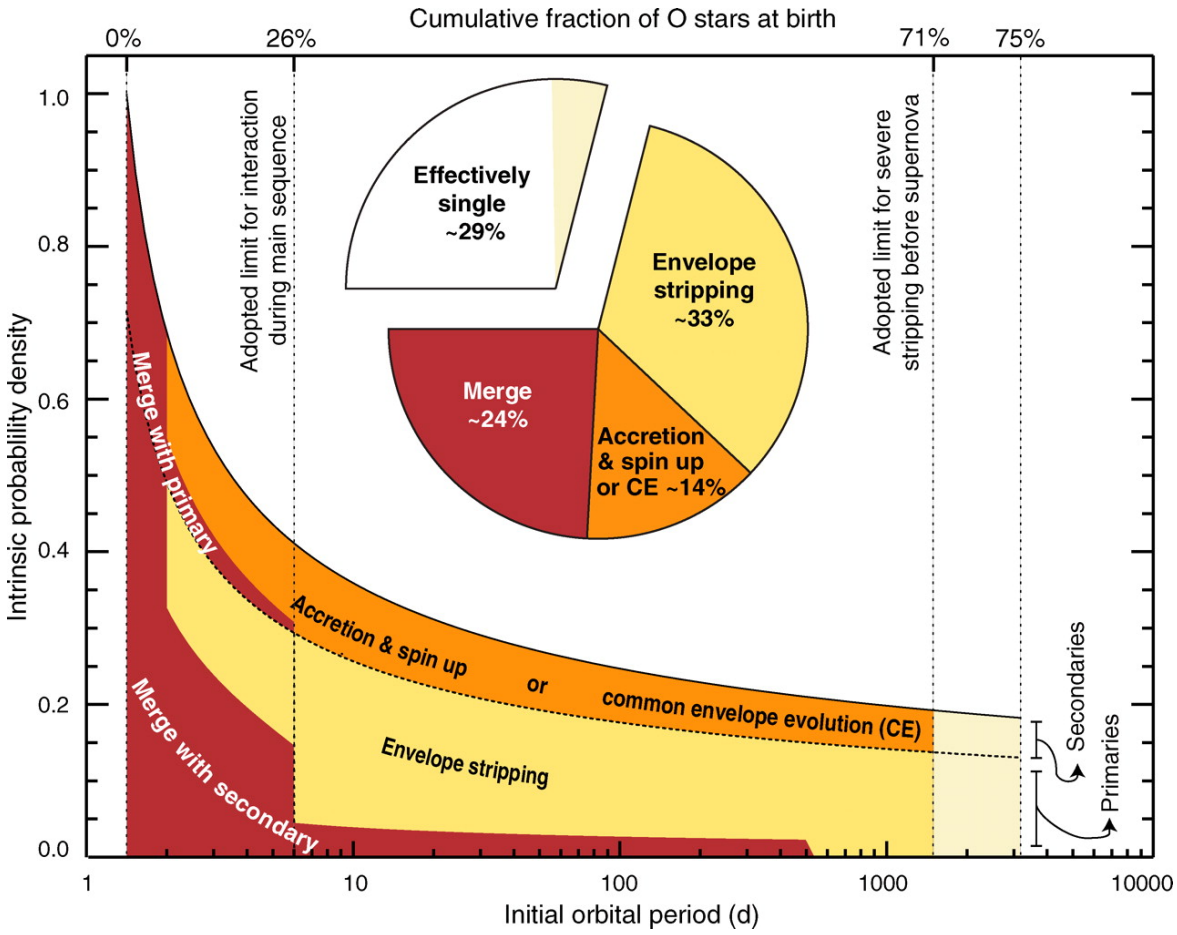

Figure 1.4: Probability of different stellar interactions in O stars as a function of initial orbital period. Figure from Sana et al. (2012)

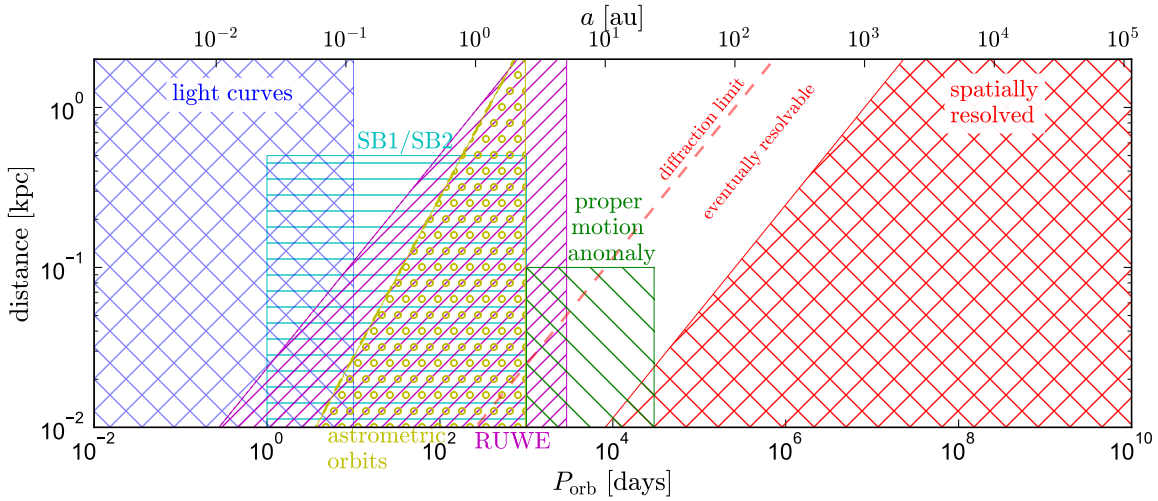

Figure 1.5: Summary of the binary parameter space as probed by *Gaia*. Figure from El-Badry (2024)

Further, the inclination of the orbital plane, the relative brightness of the two components and the mass ratio, among others, play an important role in the observability of the binary with a given technique. Figure 1.5 shows a schematic of observational techniques for binaries with the *Gaia* satellite and the regimes they are most effectively applied in.

Additionally, different observational techniques yield different kinds of information about the parameters of the system and/or the two components. As such, it can often be advantageous to combine multiple types of observations for a well-characterised system.

Most trivially, if the binary is close enough/its orbit large enough, the two components, if bright, can be spatially resolved. This then allows individual targeting of each component in turn, effectively treating them as single stars, which massively simplifies the analysis. However, in the vast majority of cases the observed system is too far away to use this technique on anything but wide binaries, which are generally not expected to interact and essentially evolve as single stars (El-Badry, 2024). While interesting, this lack of interaction makes wide binaries less crucial for understanding specifically binary effects on stellar evolution and CO formation; close, potentially interacting (or post-interaction) binaries provide more insight into these processes. For close systems, more involved techniques are necessary to gain insight into the physical properties, as they generally cannot be spatially resolved.

In the following, the different techniques and the stellar and orbital parameters obtainable with each method will be discussed. Furthermore, we point out how these techniques can be applied specifically in the context of looking for a binary containing a massive, unseen companion. This work primarily uses spectroscopic data to infer information about the systems studied, but occasionally employs other tools.

1.2.1. Spectroscopy

Spectroscopy is the technique of analysing spectra, i.e. the flux from an object over different wavelengths. The smaller the smallest resolvable wavelength, $\Delta\lambda$, the higher a spectrum's resolution ($R = \frac{\lambda}{\Delta\lambda}$, where λ is the wavelength) allowing for detailed study of emission and absorption features. In this work, we commonly refer to $R \lesssim 2,000$ as low-resolution, $R \gtrsim 10,000$ as high-resolution, and everything in between as moderate resolution. We point

out that there is, however, no agreed-upon standard.

1.2.1.1 Radial Velocity Monitoring

The Technique Radial velocity (RV) monitoring exploits the fact that the components of a binary move around each other in a predictable fashion, orbiting their shared centre of mass. For any non-face-on orbit, this means that the components will have some time-varying velocity along the observers line of sight. By observing the system at various orbital phases, these RVs can be determined as a function of time (or phase, if the period is known) and used to construct a spectroscopic orbit.

The RV for a component from a spectrum can be determined in a number of ways; most commonly, template cross-correlation is used. Here, a synthetic spectrum which approximates the real, rest-frame spectrum of the star in question is cross-correlated with the observed spectrum. The peak of the cross-correlation function (CCF) will be offset from zero by the shift of the spectrum, which directly translates to its RV via the Doppler formula. In the log-wavelength regime, the shift is linear with the RV, making calculations simple:

$$\Delta \log \lambda = \log\left(1 + \frac{v}{c}\right). \tag{1.1}$$

Here, $\Delta \log \lambda$ is the shift of the spectrum from its rest-frame in the logarithm of the wavelength, v the component's RV, and c the speed of light.

In the case of an SB1 (single-lined binary), where only one component shows up in the spectrum, single-template cross-correlation can be used to constrain the orbit. For a double-lined (SB2) system, the single-template CCF is likely to have a (potentially blended) double peak (as similar spectral lines can show up across a range of temperatures), indicating the velocities of both components. Here, a two-dimensional algorithm such as TODCOR (Zucker and Mazeh, 1994) is preferred as it allows for the use of different templates for the two components. An illustration of the shifting spectral lines in SB1 and SB2 systems can be seen in figure 1.6

Finding Compact Objects The search for COs using RV monitoring is a search for signatures implying the existence of a compact companion, rather than a direct detection.

Most simply, a clear detection of two sets of RVs evolving in a fashion predicted by a simple binary orbit rules out a dark secondary, since we would expect such a companion to show no lines. However, finding only one set of RVs does not necessarily imply a CO companion; the secondary may simply be too dim, or its spectral lines too broad to create a clear signal in the CCF. An incorrect choice of template spectra can also lead to a null detection when there actually is a luminous (enough) secondary present. Thus, caution is important.

However, candidates can still be identified by looking for signatures strongly indicative of a massive, dark companion. Concretely, this means looking for SB1s with large binary mass functions. The binary mass function is:

$$f = \frac{M_\mathrm{B}^3 \sin^3 i}{(M_\mathrm{A} + M_\mathrm{B})^2} = \frac{P_\mathrm{orb} K^3}{2\pi G}. \tag{1.2}$$

Here, M_A and M_B are the masses of the primary and secondary respectively, i is the orbital inclination of the system, P_orb the orbital period, K the semi-amplitude of the primary's

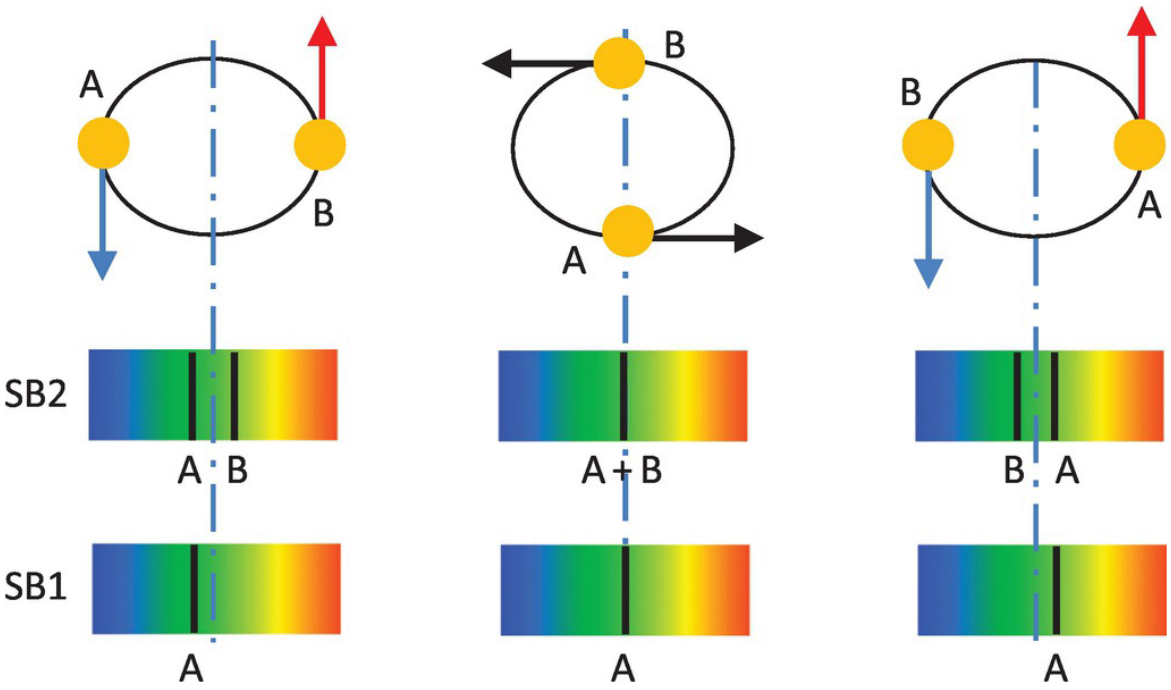

Figure 1.6: Illustration of the shifting of spectral lines for SB2 and SB1 systems. Figure from Walker (2017)

RVs, and G Newton's constant. We see that we can determine the value of f solely from observables ($P_{\rm orb}$ and K), which, in turn, allows us to constrain the unseen companion mass $M_{\rm B}$, subject to the inclination and an estimate for $M_{\rm A}$. Without information on the inclination, we can only place a lower limit on $M_{\rm B}$. For an edge-on orbit ($i = 90°$), this lower limit is the mass of the secondary, while for other configurations, it must be larger.

To surmise, systems containing a luminous primary and a dark, compact secondary are likely to exhibit large mass functions (fast primary RVs), especially if the luminous star is not massive, implying high secondary masses.

Information about the system As detailed above, in the case of an SB1, the technique can be used to constrain the secondary mass. Further, the template used to obtain the primary RVs provides information (most centrally, $T_{\rm eff}$, $\log g$ and $v \sin i$) about the star in question. In the case of an SB2, the same information can also be inferred for the secondary via template cross-correlation.

For both SB1s and SB2s, provided enough observations, the orbit of the system can also be constrained. The velocity of an object in a binary orbit is given by:

$$\mathrm{RV}(t) = v_{\rm COM} + K\left[\cos\left(\nu(t) + \omega\right) + e\cos\omega\right], \tag{1.3}$$

where $v_{\rm COM}$ is the centre-of-mass velocity, K the semi-amplitude, ω the longitude of periastron, e the eccentricity, and ν the true anomaly as a function of time, given by:

$$\tan\left(\frac{\nu}{2}\right) = \sqrt{\frac{1+e}{1-e}}\tan\left(\frac{E_0}{2}\right) \tag{1.4}$$

with E_0, the eccentric anomaly, related to the mean anomaly M_0 as:

$$M_0 = E_0 - e\sin(E_0) = \frac{2\pi}{P}(t - T_0). \tag{1.5}$$

Here, T_0 is the time of passage at periastron and P the period. Thus, solving for the orbit provides the period, centre-of-mass velocity, semi-amplitude (of the primary and/or secondary), eccentricity, longitude of periastron and time of passage at periastron. Figure 1.7 shows the result of such an orbital fitting procedure. Importantly, it is not possible to constrain the system's inclination with spectroscopic data alone, hence why the companion mass can only be inferred down to a minimum mass. If this degeneracy can be broken (i.e. by using astrometry, or photometry, given favourable inclination for eclipses to occur), the secondary mass can be determined. In an SB2, minimum masses for both components and the mass ratio of the system can be found (or mass estimates if astrometry is available).

Even with only a few observations (minimally two), some orbital parameters can be found, as the RVs of the primary and secondary are related:

$$v_\mathrm{B} = v_\mathrm{COM} + \frac{v_\mathrm{COM} - v_\mathrm{A}}{q} \tag{1.6}$$

Here, v_A and v_B are the velocities of the primary and secondary respectively, q the mass ratio and v_COM the centre-of-mass or systemic velocity. This technique can also be used to constrain the latter two parameters of the system.

Regime & Limitations This technique works best when RV variations are large. In practise, this means that extremely long orbital periods are unsuitable, as the component RVs would be too small. For very small orbits, the rapid rotation of the component stars arising from tidal synchronisation would drastically smear out any spectral lines, making RV determination difficult. Further, spectroscopy in general requires high flux compared to e.g. photometric studies, as the light is split up into the various wavelength bins. Thus, distance limits on spectroscopic observations are generally more stringent.

While RV monitoring of a binary's orbit provides a wealth of information, it is also expensive in terms of observation time, necessitating multiple observations to constrain the orbit, with generally lengthy integration times compared to photometry. The technique also has a tendency to produce spurious results when one (or both) of the components show "exotic" spectra, e.g. containing emission lines, rapid rotation, or strong depletion/enhancement in various elements. This can lead to erroneous RVs being determined as incorrect lines are matched with each other. Further, incorrect stellar parameters may be found, e.g. cool stars with significant rotation may be matched with a hotter, non-rotating template if rotation is absent in the templates, as both can cause line-broadening. If the set of templates used to determine the RV for each component does not contain a close enough analogue to the actual star, success is thus unlikely. Further, the CCF is sensitive to cosmic rays, telluric or interstellar lines, saturated pixels, and other data issues, so great care has to be taken to remove these.

1.2.1.2 Spectral disentangling

The Technique As this technique is described in great detail in section 2.2, only a brief summary will be given here.

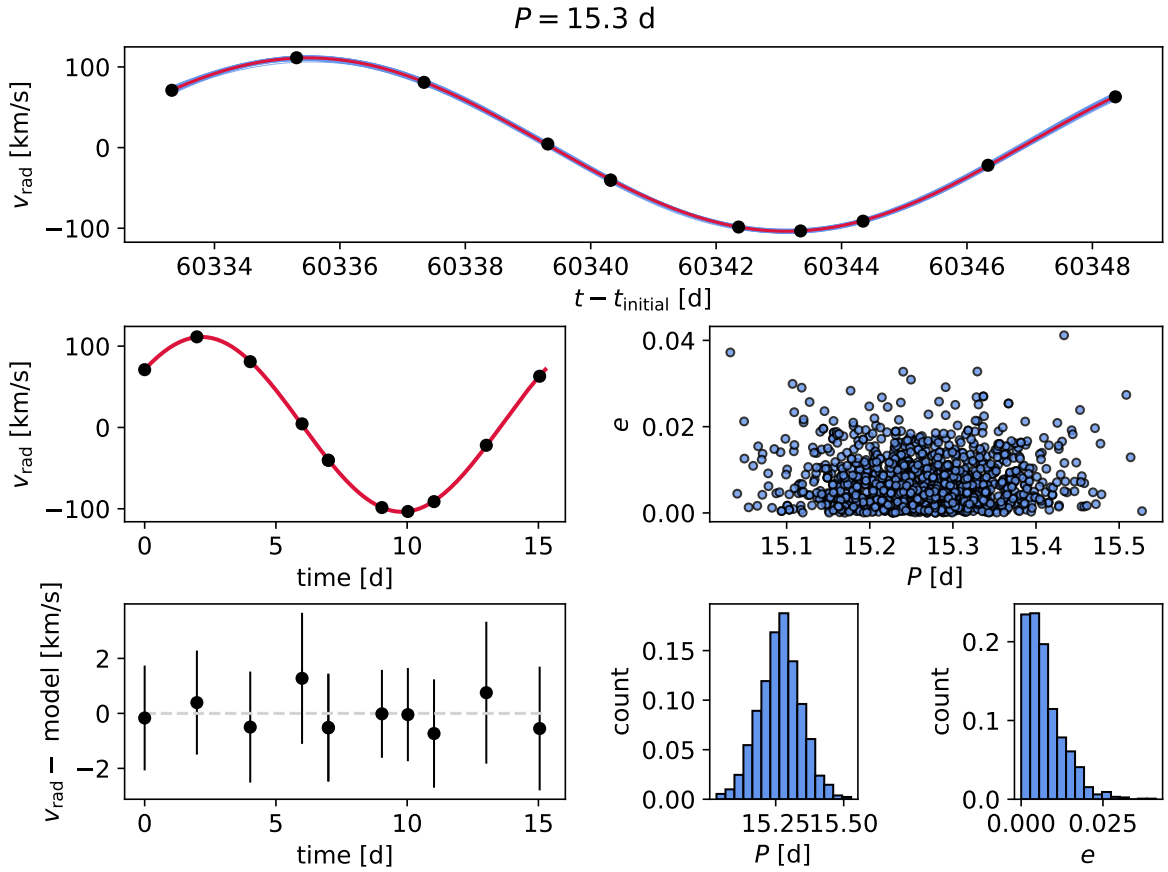

Figure 1.7: The results of orbital fitting performed following the procedure described in Müller-Horn et al. (2024). Top panel shows the evolution of the RV of one component as a function of time. Middle-left shows the same but phase-folded over the period (here, the observations are all within one period, so it looks the same as the top panel). Middle-right shows the samples of the optimiser in the eccentricity-period plane. Bottom-right shows the marginalised distributions over period and eccentricity. Bottom-left displays the residuals for the fit velocities - a strong trend away from 0 or large residuals relative to the errors would indicate a bad fit. Figure by Johanna Müller-Horn.

Spectral disentangling exploits the fact that an observed spectrum of multiple components is simply a linear addition of each components. Then, we assume that the individual spectra are time-independent in their shape and only change by being red- or blue-shifted at each epoch. Presupposing this, one can ask the question "What two vectors do we have to use to shift and co-add at each epoch to recover the observations?". With multi-epoch data, this is a purely mathematical problem, returning both the two best-fit spectra, as well as their velocities at each epoch.

Finding Compact Objects Spectral disentangling is particularly powerful at detecting "exotic" secondary spectra in the data, where traditional template-based method might miss these. If there is a second component that is moving in a manner predicted by the mass ratio, given sufficient signal-to-noise, spectral disentangling will uncover it. If no such component is found, strict upper limits can be placed on the possible brightness of the unseen component. From the analysis of the primary spectrum and using the binary mass function, a lower limit on the secondary mass can be placed. If this brightness and mass limit are incompatible with a stellar companion, a CO is required to explain the observations.

Information about the system As spectral disentangling uncovers the mathematical best-fit spectrum for each bright component, it presents a data-driven approach to determining its nature. Once disentangled, each spectrum can be analysed as a single star, opening up possibilities to determining stellar parameters ($T_{\rm eff}$, $\log g$, $v \sin i$). Additionally, for an SB2 the mass ratio, centre-of-mass velocity and (primary) epoch-RVs are also recovered. By splitting the disentangled spectra into chunks and comparing each to templates, an approximate wavelength-dependent light ratio of the two components can also be determined, placing further constraints on the natures of the two stars.

Regime & Limitations Disentangling works best with large RV shifts (compared to the spectral resolution), as lines that are (almost) stationary provide no new information for the algorithm. Thus, systems that have a large signal-to-noise ratio (S/N), with high RVs and small periods are most suitable. We have found that for $R \sim 2000$ and $S/N \sim 30$, 6 epochs can be sufficient to achieve satisfactory disentangling, but higher S/N and/or more epochs are generally desirable. Compared to RV monitoring, rapid stellar rotation is less of an issue, as no templates are necessary to determine the two component spectra; it does, however, broaden the lines, leading to a less accurate RV determination.

Similarly to RV monitoring, spectral disentangling requires multiple (mathematically at least 3) high-quality observations of the composite spectrum, making it comparatively expensive. Additionally, a sufficiently high resolution relative to the velocity separation of the two components and good S/N are necessary to enable disentangling. We desire the RVs to be significantly larger than the minimum RV precision. In cross-correlation studies, the achievable RV precision is generally:

$$\sigma_{RV} \approx \frac{\mathrm{FWHM}}{S/N}, \tag{1.7}$$

Where FWHM is the full-width half maximum of the line being studied, and S/N is the per-bin signal to noise ratio. If the FWHM is dominated by the spectral resolution, then FWHM $\approx$ $\mathrm{FWHM_{spec}}$ $\approx$ c/R, with c the speed of light and R the resolution. This generally holds for stars with sharp, narrow lines; cool stars without significant rotation.

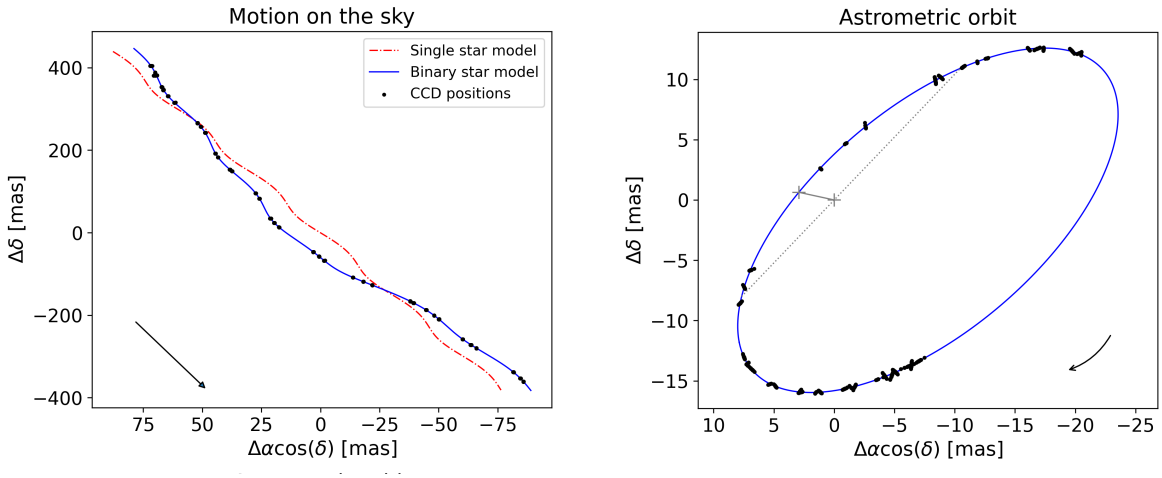

Figure 1.8: Left: The observed position of the bright component of *Gaia* BH3 (black dots) on the sky, as well as single (red) and binary (blue) model fits to the motion. We see that a single star model cannot adequately explain the observed positions of the target, while a binary model can. Right: Astrometric orbit from the observations, i.e. the remaining motion of the target after parallax and proper motion have been removed. Figure from Gaia Collaboration et al. (2024)

If the star's lines are broad, then FWHM $\approx \sqrt{\text{FWHM}^2_{\text{star}} + \text{FWHM}^2_{\text{spec}}}$. $\text{FWHM}_{\text{star}}$ is the intrinsic full-width half maximum of the spectral lines. If their width is rotation dominated, then $\text{FWHM}_{\text{star}} \approx v \sin i/c$, with $v \sin i$ the projected rotational velocity. We see that it is not straight-forward to place a definitive limit on the required resolution and S/N, as they are strongly dependent on the stars' rotation, RVs, and spectral types.

1.2.2. Astrometry

Astrometry is the study of the locations and movements of astronomical objects on the night sky. It is one of the oldest observational techniques, and has evolved tremendously throughout human history. Today, missions like *Gaia* provide astrometric data for billions of objects.

1.2.2.1 Astrometric Orbits

The Technique By observing a target's precise position on the sky over a period of time, its motion can be reconstructed. For single stars, this motion is made up of a proper motion component (due to the targets motion in the galaxy) and a parallax component (due to the earth's motion around the sun). In the case of a binary, the orbital motion of the components around each other also affects the observed motion of the photocentre (the unresolved light source from the binary) across the sky. An example of this can be seen in the left panel of Figure 1.8. Here, a model for single star motion is shown in red, and a binary model in blue. The observed positions on the sky of the target are plotted in black, and align much better with the binary than the single star model.

With sufficient coverage, the orbit can be reconstructed from a series of astrometric positional observations (Figure 1.8, right panel). This orbit follows the motion of the photocentre, which is not necessarily aligned with the motion of either of the components of the binary.

This is illustrated further in the cartoon in Figure 1.9. In the top panel, we see a schematic of a binary with a lower mass (magenta) and higher mass (cyan) star, in orbit around their shared centre of mass. Orbits are plotted in ellipses, with colours corresponding to their respective star. However, as most objects are too far away/the orbits are too small to resolve individual components, we usually only observe the photocentre motion, shown here in the middle panel as a yellow star. For two bright components, the motion of this photcentre is generally small compared to the orbital motion of the lighter component.

Finding Compact Objects This method can also be employed to look for binaries with only one bright component, and a dark, massive secondary. In this case, the photocentre is not affected by the light of the dark component (since there is none), and essentially traces the motion of the sole bright component, leading to unusually large photocentre motion (see Figure 1.9, bottom panel).

Let us consider Kepler's third law,

$$P^2 = \frac{4\pi^2 a_0^3}{G(M_\mathrm{A} + M_\mathrm{B})}, \tag{1.8}$$

where P is the orbital period, a_0 is the semi-major axis, G is Newton's gravitational constant, and M_A and M_B are the masses of the primary and secondary, respectively. We see that for fixed component masses, we expect the period to increase as the semi-major axis increases. Thus, if we observe large photocentre motion (implying a large semi-major axis and/or a binary containing only one bright component) and an unexpectedly short period (implying large masses), we have encountered a potential CO candidate.

Information about the system By solving for the full astrometric orbit, we constrain the six Keplerian orbital parameters, which fully define the orbital geometry. *Gaia* astrometric orbital solutions are parameterised by the period P, eccentricity e, epoch of periastron passage T_0, the semi-major axis (in this case, of the photocentre) a_0, the inclination of the orbit i, the position angle of the ascending node Ω, and the periastron longitude ω. Unconstrained by astrometry is the flux ratio of the components (and their respective semi-major axes).

In the context of binary evolution, the orbital period, eccentricity and semi-major axis are of particular interest. The period and semi-major axis are related via Kepler's third law (Equation 1.8), and together provide information about the total mass of the system. By making assumptions about the components of the binary (e.g. their relative brightness or evolutionary stage), further conclusions about the nature of the two components can be drawn. Especially in the context of close binary systems, the eccentricity is an important parameter, as interactions in close systems are predicted to circularise orbits. The dominant mechanisms for this are tidal interactions (Zahn, 1975, 1977; Burkart et al., 2014). Thus, high eccentricities in close orbits suggest a pre-interaction stage.

Regime & Limitations We frequently parameterise the observational space of binaries in terms of period and distance from the observer (see Figure 1.5). When considering astrometric orbital solutions, the lower limit in terms of the period at a given distance is set by the minimum resolvable motion of the photocentre. Generally, the shorter the period, the smaller the orbit, and below a certain threshold this motion cannot be resolved, thus the orbit

not calculated. With increasing distance, this lower limit increases, as the same angular size on the sky corresponds to a larger orbital size when viewing systems which are further away.

The upper period limit for astrometric orbits depends on the observational baseline. The observations have to cover a significant fraction of the orbit (preferably also with favourable sampling), to be able to constrain the orbital parameters. In practise, this means that e.g. *Gaia* DR3 is most sensitive to astrometric orbits with periods between ~ 100 and ~ 1000 days. Orbits much longer than this are simply not sampled well enough to constrain their elements, leading to a distance-independent upper limit on the period.

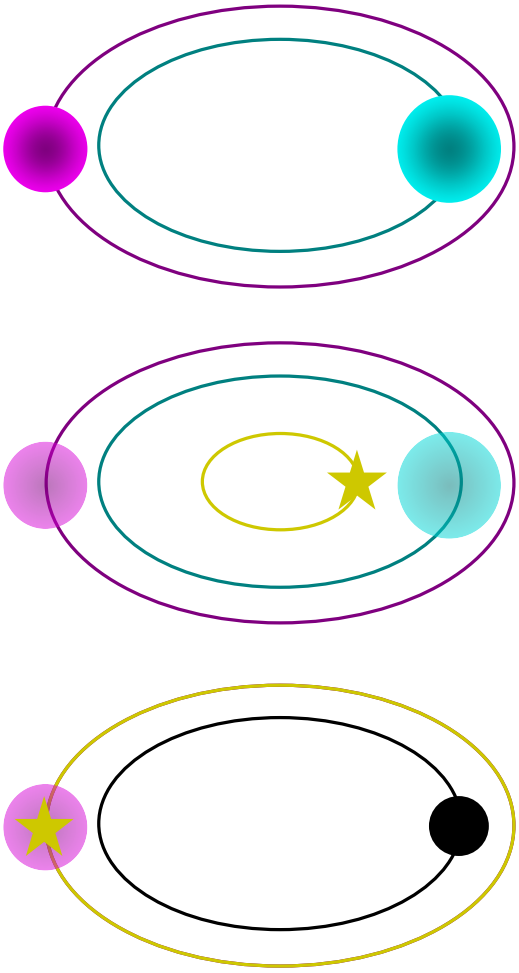

Figure 1.9: Cartoon illustrating the observed astrometric orbit for different binaries. Top: In a spatially resolved star-star binary, the orbit of each component (magenta and cyan) can be determined separately. Middle: Most binaries cannot be spatially resolved, and thus we generally observe the photocentre motion (yellow). Bottom: in a star-BH binary (BH in black), the photocentre traces the motion of the luminous component, drawing large orbits compared to star-star binaries

1.2.2.2 Other astrometric Techniques

While determination of astrometric orbits provides a plethora of valuable information about the system at hand, there are other methods for determining whether a system is likely a binary. Within the *Gaia* dataset, the renormalized unit weight error (RUWE) provides a metric of the goodness-of-fit of the single-star astrometric solution. While only a comparatively small number of full astrometric binary orbits were published in *Gaia* DR3, the RUWE metric is available for many more sources, and can provide a robust measure of "normal, single starness". High RUWE values suggest a relatively large disagreement between the basic single star astrometric solution and the actual observed positions of the target on the sky. This points towards a potential binary system. However, caution has to be taken; a low RUWE value does not automatically rule out a system as a binary - rather, RUWE is mostly sensitive to binaries with large photocentre motion (i.e. large orbits) but periods within the *Gaia* observing baseline. Very tight binaries or those with very long periods, as well as systems that are too faint or too far away, will likely present with a low, "inconspicuous" RUWE value, while still not being a single system.

Finally, the proper motion anomaly (PMa) is another potential metric for identifying binaries using astrometric data. PMa measures changes in the proper motion due to orbital

acceleration. Thus, a long baseline between proper motion computations is useful for detecting long-term changes, for example by comparing *Hipparcos* data with proper motions from *Gaia* DR2 and DR3 (El-Badry, 2024).

1.2.3. Photometry

Photometry describes the measurement of the intensity of light from an object. In astronomy, this often includes the evolution of light over time, or the relative brightness in different bandpass filters.

1.2.3.1 Lightcurves

The Technique When observing certain binaries' brightness over time, one might discover that the system appears to brighten and dim in a periodic fashion. By plotting the evolution of the magnitude against the phase of the system, the *lightcurve* can be analysed, providing unique insight into the binary.

The variations in the brightness stem from a number of possible sources:

- **Ellipsoidal variation** When two bodies are close enough to each other, their gravitational attraction not only binds them into an orbit, but can also distort their shape. In very close binaries, rather than spherical, the stars are deformed into a more ellipsoidal shape, with the long axis pointing towards the other object in the binary. Then, as the two bodies orbit around each other (assuming edge-on orbit), we alternatingly see the "short side" and the "long side" of each star. When the long side is facing the observer, the star and thus the system appear brighter. This causes variations with a periodicity of half an orbital period: twice per orbit there is a peak in brightness due to the long side of each star facing towards the observer, with brightness maxima occurring at phases of $\pi/2$ and $3\pi/2$.

- **Doppler Beaming** As the two bodies in the system orbit around each other, they are alternatingly approaching and receding from the observer. While approaching, the observed brightness of an object increases due to relativistic Doppler beaming. In the case of stars, this effect is generally small but can be observable if orbital velocities are high enough; it is much more pronounced in e.g. the relativistic jets of Quasars. Beaming is most pronounced in a binary with a large light ratio, as the receding body will appear dimmer as the approaching body appears brighter - large differences in relative flux contribution between the two leads to a stronger effect.

- **Reflection** The two bodies may partially reflect each other's light (as the moon reflects light from the sun and is thus visible). This causes variations in the observed system brightness, with maxima occurring at phase 0 and π, assuming the orbit is fairly but not entirely edge-on, or that the objects are of different angular size.

- **Eclipses** If a star passes between its companion and the observer, an eclipse occurs. This causes a sharp decrease in brightness and thus a dip in the lightcurve. These systems are referred to as Eclipsing Binaries (EB), but are comparatively rare objects. There are stringent requirements for an eclipse to be observable. The two bodies must be close enough, and the inclination near enough edge-on to enable one star to obscure the other when viewed by an observer. Due to size differences, only one eclipse may

occur; if each star can eclipse the other, the lightcurve shows two dips. If the stars are also of different sizes, one dip is larger than the other, referred to as primary and secondary eclipse, respectively.

These effects add together in varying strengths depending on the nature of the two bodies (e.g. a less gravitationally bound star such as a giant is more prone to deformation than an MS star), the shape, size and inclination of the orbit (face-on orbits do not show strong lightcurve variations due to binary effects) and the relative mass, angular size and brightness of the two components.

Finding Compact Objects In a binary containing one luminous and one compact, dark component, ellipsoidal variations and Doppler beaming as described are present, while reflection does not play a role. Due to the comparatively high mass of a CO, the distortion of the stellar component is often very pronounced, leading to large variations in the lightcurve. As all the light of the system now comes from one component, Doppler beaming becomes more simple to model, as no second bright component needs to be taken into account. Doppler beaming depends on the RV of the bright component, which, in turn, depends on the orbital configuration.

A schematic of this can be seen in figure 1.10. The top part shows a simple cartoon of a binary containing a star and BH on a near edge-on obit at different phases. The bottom plot displays a (not to scale) example lightcurve the system above may exhibit. We clearly see the two maxima from ellipsoidal variations of the stellar component, as well as the contribution of Doppler beaming of the same component, leading to two maxima of different brightness per orbit. The smaller maximum occurs when we see the "long side" of the star but it is receding, while the larger maximum occurs half an orbit later, again with the "long side" of the star facing the observer, but this time while it is approaching.

Information about the system Analysis of the lightcurve of a binary yields a plethora of information. Most straightforward, the best-fit period can be determined, e.g. by creating a periodogram. The orbit's eccentricity and inclination can also be constrained. Further, the relative radii of the bodies can be determined from ellipsoidal variations or the duration of the eclipse compared to the orbital period. If reflection is present, potential relative stellar temperatures can be found.

For eclipsing binaries, the shape and depth of the primary and secondary eclipses provide insight into the relative radii and temperatures of the stars, as well as suggesting a nearly edge-on orbit.

Long-term variations in the light curve can also hint at other ongoing processes, such as MT (causing a change in relative temperatures, radii, and/or masses), or a hierachical triple the binary is part of. Short-term, irregular variations can also hint at ongoing MT or the presence of an accretion disc. Periodic signals not on an orbital timescale might be indicative of stellar pulsations or sunspots.

Regime & Limitations While astrometric orbit fitting is best suited to binaries with comparatively long periods, the analysis of light curves lends itself to the other end of the spectrum; binaries with periods on the order of hours or days. If the orbit is too large, the tidal effects from the components are simply not strong enough to cause significant distortion,

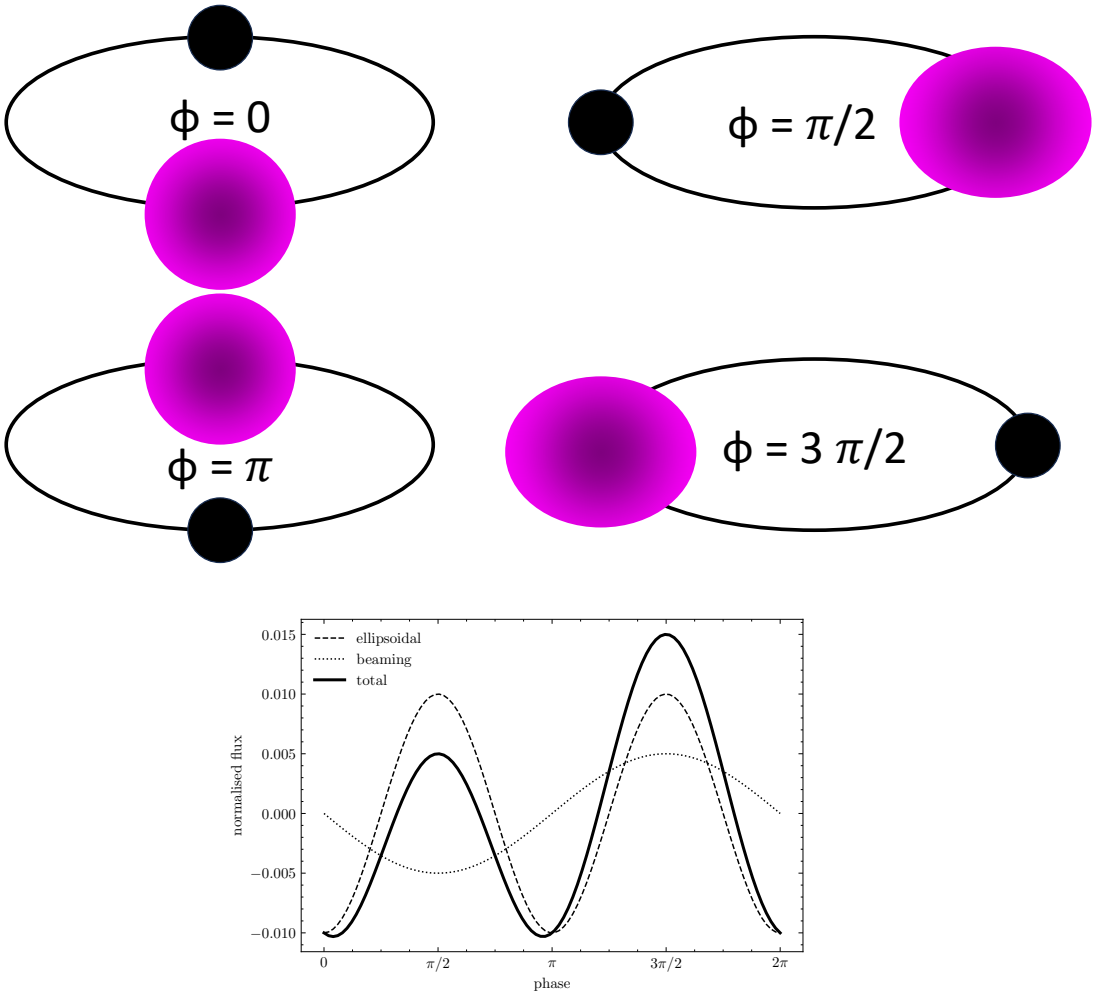

Figure 1.10: Top: A cartoon illustrating the variations in brightness of a close binary containing a BH and a tidally distorted star. At phase 0, the star shows its "short side" and has no velocity along the line of sight - the ellipsoidal variations are at a minimum, while Doppler beaming is at 0. The same is true for phase π. For phases $\pi/2$ and $3\pi/2$, the "long side" of the star is visible, and thus the system appears brighter. However, at phase $\pi/2$ the star is receding from the observer, while it is approaching at phase $3\pi/2$, leading to an overall brighter appearing system at phase $3\pi/2$. Bottom: Qualitative summary of the ellipsoidal (dashed) and beaming (dotted) effects on the overall perceived flux of the star (solid line). Ellipsoidal variations occur with a period of half the orbital period, while Doppler beaming effects have a period the same as the orbital period. This leads to a distinct shape of the overall flux changes, which can be used to constrain orbital and stellar parameters.

eliminating ellipsiodal effects. Similarly, as binaries with large orbital periods tend to orbit more slowly, radial velocities are unlikely to be large enough to cause significant Doppler beaming. Further, reflection depends on the irradiation of one body by the other, which requires them to be close to each other to contribute meaningfully to the lightcurve.

For eclipsing binaries in particular, a too-large separation of the components makes an already fairly unlikely alignment of the orbital plane with the observer's line of sight even less likely, as well as leading to smaller dips in the lightcurve due to the eclipses.

1.2.3.2 Spectral Energy Distribution

The Technique While lightcurve analysis requires multiple observations of the target over time to chart the evolution of its brightness, analysis of the spectral energy distribution (SED) of a system can be done with much less time-intensive observations. By observing the same target in a number of photometric filters and comparing to models, the constituents of the SED can be determined (see e.g. El-Badry and Rix (2022)). The shape of a star's SED is mostly determined by its radius and effective temperature, and then modulated by the extinction and distance from the observer. Using a distance prior (e.g. from *Gaia*) along with an extinction map (such as e.g. Edenhofer et al. (2024), contained in `dustmaps` (Green, 2018)), the stellar radius and temperature can be fit for each component, along with the distance to the system.

Finding Compact Objects This technique is mostly useful as a potential means of determining false positive SB1s. Photometric observations are readily available for a large volume of objects, owing to their cost efficiency compared to e.g. multi-epoch spectroscopic observations. If a potential candidate SB1 system with a high mass function has been identified, this technique can be used to test if the observed photometry can indeed be fit by a single stellar SED, or if two or more components are necessary to explain the observations. This is particularly useful in post MT systems. These often contain an overluminous/undermassive bloated, cooler donor star and a rapidly rotating hotter accretor. Due to their different temperatures and radii, their SEDs are very distinct from each other, and neither single-temperature SED can usually approximate the observations consistently. An example of this can be seen in Figure 1.11. We see that the observations (limegreen dots) cannot be fully explained by a cool star (magenta line), as there is too much flux in the blue/UV, nor a hot one (cyan line), as this does not match the observations in the red/IR. Only a composite model (black line) consisting of a cooler and a hotter component aligns with the observed photometry, revealing this system to indeed consist of two bright components.

Information about the system While this technique reveals little about the dynamics and orbit of the system, it can provide useful insight into the nature of the components. The SED fitting process seeks to determine the radii and effective temperatures of each component, as well as the distance to the system (though, due to degeneracies of the radii with the distance, a prior has to be placed on this). Using the temperature and radius, the bolometric luminosity of each star can be estimated, allowing placement on a Hertzsprung-Russel Diagram (HRD). Unusual pairings of stars can also hint at potential system histories, such as in the case of post MT systems.

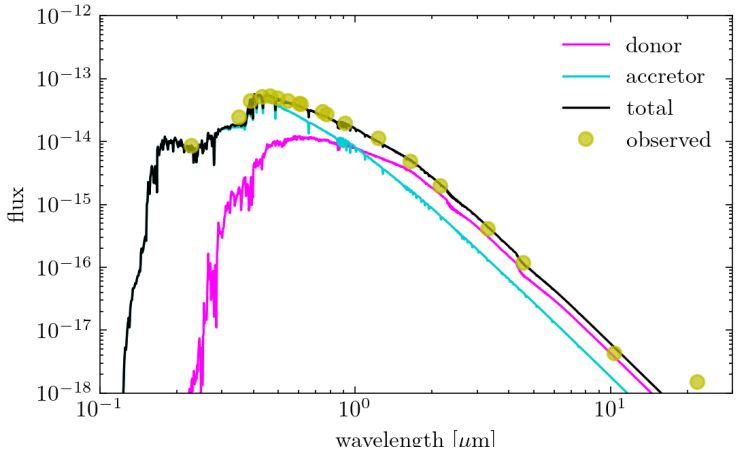

Figure 1.11: Photometry for *Gaia* DR3 5536105058044762240 (limegreen dots), as well as a best-fit two-component model to the data. The system consists of a cool, puffed up donor star (magenta line), and a hotter accretor (cyan line), which, taken together (black line), can explain the observations, while neither individual component can do so.

Regime & Limitations While analysing the SED can be a powerful tool to determine the nature of the constituents of an SB2, it does have its shortcomings. Systems with very similar components in terms of temperature and radius are hard to differentiate from single-component or single-lined systems. As the composite SED is simply the sum of the component SEDs, sufficiently different individual SEDs are a prerequesite for this method. This method is thus not well suited to determining the individual SEDs of twin ($q = 1$) systems. However, extreme mass ratios ($q << 1$) are also unfavourable, as the composite SED is likely to be dominated by the bright component, which vastly outshines the secondary across wavelengths.

Further, due to the aformentioned degeneracy of the stellar radius with the distance from the observer, a prior on the distance is required if one wishes to meaningfully constrain the radius.

1.3. Stellar-Mass Black Holes in Binaries & their Impostors

When particularly massive stars reach the end of their life, they explode in a spectacular SN, leaving behind an extremely compact, dark remnant: a BH. These stars were generally $\gtrsim 25 M_\odot$ before the SN (Heger et al., 2023), though lower mass stars may also form BHs (Laplace et al., 2025). According to population models, we expect around 10^7 such objects in the Milky Way (Breivik et al., 2017). Since massive stars are frequently born in multiple systems (Sana et al., 2012), and BHs require high mass progenitors, many BHs are likely formed in multiple systems (but may not necessarily remain bound, for example due to SN kicks). Systems consisting of a BH with a luminous companion are of great astrophysical interest, as they are progenitors to binary BH mergers, common sources of gravitational waves (Abbott et al., 2016). Population models (such as those employed by Breivik et al. (2017); Yamaguchi et al. (2018); Janssens et al. (2023)) make many assumptions about the underlying physics of SN kicks, CE evolution, stellar winds and other important mechanisms. Thus, understanding the true underlying population of star+BH binaries, their orbits

and parameters, can help constrain fundamental physical processes that underpin much of binary and single stellar evolution.

X-ray binaries were first discovered in the 1960s (Giacconi et al., 1962). These are systems where the star and CO are close enough for mass from the star to be accreted by the companion, in the process forming a hot accretion disc which radiates in the X-ray. However, we expect only a small fraction of all star-CO binaries to be in this phase, as it requires the system to be in a comparatively short-lived evolutionary stage (with one star having already become a remnant while the other is still luminous) and precise orbital configuration (close enough for accretion, not so close as to merge). A much larger fraction of star-BH systems are expected to be in a *dormant* phase, where no or only very little accretion onto the remnant occurs (Langer et al., 2020). These dormant BHs are difficult to identify compared to their X-ray loud accreting cousins, as they can only be detected via their gravitational effect on their luminous companion, as described in Section 1.2. BHs that have become unbound from their companion or underwent single stellar evolution are even harder to find, as they can only be detected via microlensing (Lam et al., 2022).

1.3.1. Formation of Stellar-Mass Black Holes

The canonical path for stellar mass BH formation is from a core collapse event involving a very massive star. To quickly recap massive stellar evolution, a massive star forms from the collapse of a massive molecular gas cloud, burning hydrogen via the CNO cycle on the MS for a short time compared to lower mass stars, while losing a substantial amount of mass due to strong stellar winds. Once hydrogen in its core is depleted, it starts to expand and become a red, yellow, blue supergiant, classified according to temperature (red supergiant $T_{\rm eff} \lesssim 4800$ K, yellow supergiant 4800 K $\lesssim T_{\rm eff} \lesssim 7500$ K and blue supergiant $T_{\rm eff} \gtrsim 7500$ K (Drout et al., 2012)). The supergiant successively burns helium and then heavier elements (C, Ne, Si, O, ...) until eventually the core begins to contract and heat up, allowing for heavy-element fusion up to Fe. This leads to a shell-like structure of the star, with an iron core and successive shells burning different elements, as illustrated in figure 1.12. As the stellar core can generate no more energy from fusing elements heavier than iron, once it reaches the Chandrasekhar limit (~1.4 $M_\odot$), it collapses as electron degeneracy pressure is no longer sufficient to support the core (Lieb and Yau, 1987).

For massive stars between around 8 and 130 $M_\odot$, this core collapse generally leads to the formation of a CO, with the type of object and SN process dependent on the mass and chemical makeup of the star and particularly its core (Sukhbold et al., 2016, 2018; Laplace et al., 2021)

For the lower-mass end (8 - 30 $M_\odot$), neutron degeneracy pressure may abruptly halt the collapse of the core, leading to a shock. If the shock is strong enough (generally for progenitor masses below 25 $M_\odot$), this leads to a SN, with the shockwave driving out the stellar material and leaving behind a NS. If the shock is too weak, it will stall, and material will fall back onto the core, increasing the mass past the Tolman-Oppenheimer-Volkoff limit ($2.01 \leq M_{\rm TOV}/M_\odot \lesssim 2.16$), after which neutron degeneracy pressure can no longer support the core and it collapses into a BH (Rezzolla et al., 2018). Observationally, no BHs in the 2-5 $M_\odot$ mass range have been found; this is commonly called the lower BH mass gap (Özel et al., 2010).

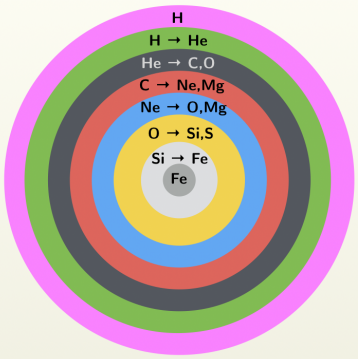

Process	Bi-product	Duration (roughly)
H → He	^{18}N	10 million years
He → C,O	^{18}O,^{22}N	1 million years
C → Ne,Mg	Na	1000 years
Ne → O,Mg	Al,P	3 years
O → Si,S	Cl,Ar,K,Ca	9 months
Si → Fe	Ti,V,Cr,Mn,Co,Ni	1 week
Core collapse		¼ second

Figure 1.12: Cartoon of the structure of a massive star shortly before core collapse. Successive burning of different elements has created a shell-like structure in the star. Credit: anisotropela/data from Stan Woosley.

For more massive progenitors (30 - 130 $M_\odot$), the infall rate is generally very high, and the shock from the core reaching nuclear densities is insufficient to halt the collapse. There may still be a weak SN, with some of the outer layers of the star being ejected, or, as in the case of NGC 6946-BH1, the SN fails and the star appears to "vanish", collapsing directly into a BH (Murphy et al., 2018). Direct collapse is further favoured by stars at low metallicity because they lose less mass to wind during their lifetime.

For extremely massive progenitors (M_* between 130 and 250 $M_\odot$), theories predict a *pair-instability SN* (PISN). Here, the extremely energetic photons in the core can spontaneously produce electron-positron pairs, which lowers the radiation pressure in the core, causing it to contract. The contracting core heats up, leading to more pair formation. This causes a runaway thermonuclear explosion with such energy that the star is completely blown apart, and no remnant survives (Fraley, 1968). Between the Tolman-Oppenheimer-Volkoff limit at the lower end, and the occurrence of PISN at the higher end, there is a range of masses at which BHs can theoretically form from stars.

Alternatively to this, very massive gas clouds may also directly collapse into COs without forming a star (Loeb and Rasio, 1994); however, these BHs are expected to be of much higher masses than stellar remnant BHs, and thus not the focus of this thesis.

1.3.2. Dormant Stellar-Mass Black Holes in Binaries

As stellar BH form from massive stellar evolution, and the vast majority of massive stars is born in binaries, the assumption that most stellar BH are found in binaries seems an obvious one. However, there are many mechanisms that can lead to a binary becoming unbound or otherwise destroyed, before, during, or after BH formation. Conversely, BHs may also enter bound systems that they were not originally born in.

One mechanism that may result in a massive star not even turning into a BH at the end of its life in the first place is mass loss due to stellar winds. These winds are particularly strong in massive stars, famously instrumental in the formation of Wolf-Rayet stars, where the star's own winds have stripped away most of its envelope, exposing the hot core rich in non-hydrogen elements (Conti, 1975). If the star loses too much mass throughout its evolution, the mass of the core prior to SN may not be enough to collapse into a BH, and may instead

form, for example, a NS (Heger et al., 2003, 2023). Additionally, high metallicities can also drive stronger stellar winds, due to the higher cross-section stemming from larger opacities of metals compared to hydrogen and helium (Vink et al., 2001). Stronger winds lead to more mass loss and thus a lower progenitor mass more likely to result in a NS remnant over a BH.

Some stars may retain enough mass, but the binary configuration is destroyed during the stellar evolution process. There are many possible pathways for a massive binary, depending on the initial configuration (masses of the components, orbital parameters, metallicities of the components). The formation of a CE as the BH progenitor evolves may lead to disruption of the secondary or a stellar merger, especially if the secondary cannot eject the CE due to being too low mass. Depending on how long the secondary survives inside the CE, strong drag forces will likely cause it to spiral in towards the more massive BH progenitor and merge with the core. Further, mass loss from the progenitor, even if moderate enough to retain sufficient mass for BH formation, may drive the companion further away (as $a \cdot (M_{\rm A} + M_{\rm B})$ is conserved) and even disrupt the orbit.

Another possible cause of the destruction of the binary is the SN "birth-kick" the system may receive upon the BH progenitor's explosion. This kick may arise from recoil due to the sudden change of the centre-of-mass of the system as mass is rapidly ejected (Blaauw, 1961); it may also be due to anisotropy in the energy carried away by neutrinos due to magnetic fields (Chugai, 1984); and, as the stellar envelope prior to SN may not be uniform, neither is the resulting explosion, meaning energy is released in an asymmetric fashion, imparting a "kick" on the system (Janka, 2017). Depending on the strength and direction of this kick, it may shrink, widen, or even break the orbit. Generally, the kick is likely to impart eccentricity; if this exceeds 1, the orbit is broken.

Even if the star-BH system survives the formation of the BH, as the companion evolves, a second CE phase may occur. If the envelope cannot be ejected, again, the companion's core may inspiral towards the BH, leading to a single surviving BH without a companion (see left panel of Figure 1.13). These are, of course, not the only formation pathways towards star+BH and BH+BH binaries. Other possible channels include stable MT (Picco et al., 2024), chemically homogenous evolution (Mandel and de Mink, 2016), overcontact binaries (Marchant et al., 2016); for a review see Mapelli (2021).

Dynamical Formation of Black Hole Binaries

Beyond formation in "isolated binary" systems, there is another formation channel for dormant BHs in binaries: dynamical formation. This channel produces BH binaries through gravitational interactions in dense stellar environments such as globular clusters and nuclear star clusters (Sigurdsson and Phinney, 1993; Portegies Zwart, 2000). An illustration is shown in the right panel of Figure 1.13. The process involves three-body encounters where energy exchange allows formation of bound systems (Heggie, 1975):

$$\frac{dE_{bin}}{dt} \propto \frac{G^2 m_1 m_2 m_3 \rho}{v\sigma^2}, \tag{1.9}$$

where ρ is the stellar number density and σ is the velocity dispersion. This is particularly important in the dense environment of stellar clusters where ρ is large and interactions between systems are frequent compared to e.g. the Milky Way field (where ρ is small). Especially massive objects are more likely to be able to acquire a companion via this process (Hills and Fullerton, 1980) - and as BHs tend to be massive compared to most stars, they are likely

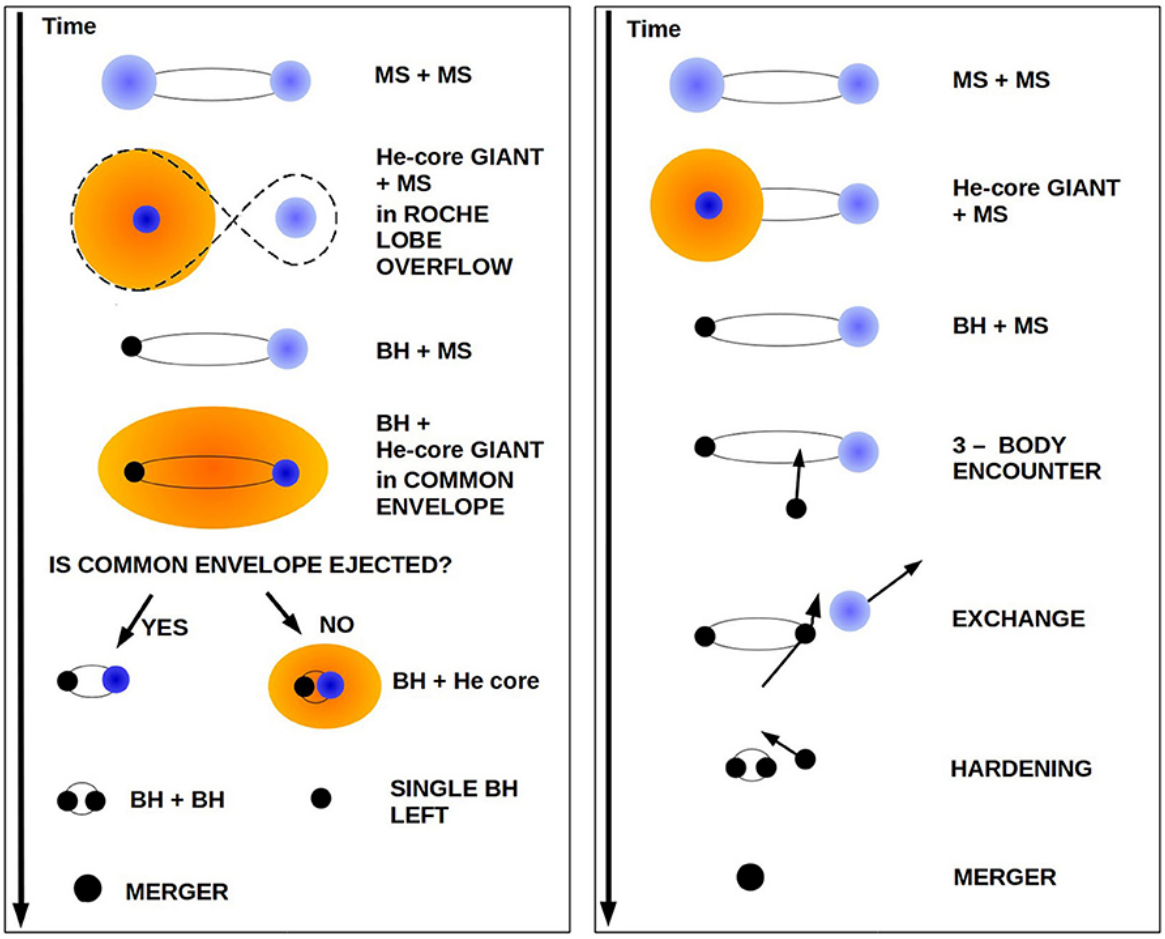

Figure 1.13: Illustration for two possible pathways towards a binary BH merger from a star-star binary. Left: Evolution through CE scenario. Right: Dynamical formation in stellar clusters. Figure from Mapelli (2020)

efficient at picking up companions in the dense cluster environment (Ziosi et al., 2014), naturally forming BH-BH binaries (Rodriguez et al., 2016).

Recent LIGO/Virgo detections hint at evidence for the efficacy of dynamical assembly, particularly systems with high masses, significant eccentricities, or misaligned spins (Antonini and Rasio, 2016; Rodriguez and Loeb, 2018). Di Carlo et al. (2020) argued that up to 70% of LIGO sources may originate through this channel. Also, the three recently discovered dormant BH binaries from the *Gaia* mission lie in a period range where dynamical formation is most plausible (Nagarajan et al., 2025).

Compared to isolated binary evolution, the dynamical channel produces distinct mass distributions and spin alignments (Abbott et al., 2021), enabling observational discrimination between formation pathways for gravitational wave sources. For dormant BHs the period distribution, along with a well-understood selection function, may tell us eventually about the relative importance of these two mechanisms.

1.3.3. Observational Evidence for Dormant Black Holes in Binaries

The discovery of dormant stellar-mass BHs in binaries has been a challenging endeavor, primarily because these objects do not exhibit the characteristic X-ray emission associated with accretion. Instead, their presence must be inferred dynamically through their gravitational influence on a luminous companion (see section 1.2 for a summary). In recent years, several such systems have been identified, significantly advancing our understanding of non-interacting BH binaries. Confirmed targets and strong potential candidates are summarised in table 1.1.

1.3.3.1 Astrometrically discovered BHs

Recent advancements in astrometric surveys, particularly with the *Gaia* mission, have led to the discovery of several dormant BHs through their influence on companion stars. These discoveries provide crucial insights into the population and distribution of non-interacting BHs in the Milky Way.

- ***Gaia* BH1** (El-Badry et al., 2023b): Located in the Milky Way's thin disk at a distance of ~ 1,560 light-years from Earth, *Gaia* BH1 is the closest known dormant BH. It has a mass of approximately 10 solar masses and is orbited by a Sun-like G-type MS star.
- ***Gaia* BH2** (El-Badry et al., 2023a): Found in the Milky Way's thin disk at a distance of ~ 3,800 light-years, this system hosts a BH with an estimated mass of ~ 9 solar masses. Its companion is a red giant, indicating that the system has undergone significant stellar evolution.
- ***Gaia* BH3** (Gaia Collaboration et al., 2024): The most recently identified astrometric BH, *Gaia* BH3, is located at a distance of ~ 2,000 light-years. Its companion star is a metal-poor giant of spectral type G whose orbital motion reveals the presence of a CO with a mass of about 33 solar masses, the heaviest known stellar BH in the Milky Way.

For all of these systems, astrometric orbits were constructed using *Gaia* data (DR3 for BH1 and BH2, pre-release DR4 for BH3), revealing a large binary mass function and thus

implying a massive secondary. Spectroscopic follow-up was conducted for all targets (BH1: GMOS (Hook et al., 2004), HIRES (Vogt et al., 1994), FEROS (Kaufer et al., 1999), MagE (Marshall et al., 2008) and ESI (Sheinis et al., 2002), as well as using archival data from LAMOST (Cui et al., 2012); BH2: FEROS and UVES (Dekker et al., 2000); BH3: *Gaia* RVS (Cropper et al., 2018). Spectroscopic RV data can be used in conjunction with astrometric data to create a joint fit, generally increasing the precision of the constraints.

1.3.3.2 Spectroscopically discovered BHs

- **VFTS 243** (Shenar et al., 2022a): This system resides in the Large Magellanic Cloud and consists of an O-type MS star orbiting a $\sim$ 10 solar mass BH. The lack of X-ray emission suggests the BH is truly dormant, making it one of the best dynamically confirmed BHs.
- **NGC 3201 12560** (Giesers et al., 2018): A dormant BH in the globular cluster NGC 3201, this system features a low-mass ($\sim$ 0.8 $M_\odot$) MS star near the turn-off orbiting an unseen companion with a minimum mass of $\sim$ 4 solar masses. Given its location in a dense stellar environment, this system provides valuable insights into BH formation in clusters.
- **HD 130298** (Mahy et al., 2022): A highly eccentric SB1 system in the Milky Way. It features a nitrogen-rich O-type companion, and its RV variations suggest the presence of a massive ($\gtrsim$ 8 $M_\odot$) unseen companion, likely a quiescent BH, though a stripped star cannot be strictly ruled out. No X-Ray emission was detected.

For the spectroscopically discovered systems, candidates were identified initially via analysis of their RV variations, which can be very large ($\gtrsim$ 100 km/s for NGC 3201 12560). In the case of VFTS 243 and HD 130298, spectral disentangling was also performed, but revealed no bright secondary. If such a luminous companion existed, mass constraints imply it should be visible; thus, the lack of a secondary signature strongly points towards a dark companion, while the minimum mass implied by the orbital solution suggests it is likely above the Chandrasekhar and Tolman–Oppenheimer–Volkoff limits.

1.3.3.3 Candidate BHs

For some candidate systems, the present evidence is inconclusive as to whether the companion in question is a BH or not. As BHs are rare compared to most types of stellar binary interaction products, it is particularly important to thoroughly rule out a more common "impostor" masquerading as a BH.

- **NGC 1850 BH1** (Saracino et al., 2022; El-Badry and Burdge, 2022; Saracino et al., 2023): This system was originally proposed to consist of an MS turn-off star ($M \approx$ 5 $M_\odot$) with a $\sim$ 11 $M_\odot$ BH companion by Saracino et al. (2022). Subsequently, El-Badry and Burdge (2022) proposed an alternative scenario involving a (lower mass, $M \approx$ 1.5 $M_\odot$), stripped envelope star, lowering the implied companion mass to be consistent with a 2.5$\sim$5 $M_\odot$ MS star. Saracino et al. (2023) revised the RVs, doubling the implied binary mass function, and placed luminosity constraints on the secondary using spectral disentangling. This revised model implies that if a luminous companion of the requisite mass is present, it would have to be hidden behind an optically thick disk.

- ***Gaia* DR3 3425577610762832384** (Wang et al., 2024): A wide system with a period of 880 days and circular orbit determined from LAMOST (Cui et al., 2012) radial velocities combined with *Gaia* DR2 and DR3 astrometric data. The orbit and mass of the giant companion imply a BH mass of 3.6 $M_\odot$, suggesting this may be a mass-gap BH. However, *Gaia* does not propose a binary astrometric orbit, but rather a single-star solution. Combining DR2 and DR3 allows an attempt at determining the astrometric orbit, but this is an under-constrained problem. As the luminous component is on the red giant branch, its mass and exact stellar evolution stage is uncertain. The authors propose an edge-on orbit and mass-gap BH companion, however alternative explanations, including a further away system with a larger giant and luminous massive companion (impostor), or a more face-on orbit with a more massive BH, cannot be ruled out at this time.

ID	RA deg	DEC deg	$P_{\rm orb}$ day	Mag	$M_{\rm BH}$ $M_\odot$	Discovery	Status	Reference
Gaia BH1	262.17120816	-0.58109202	185.59±0.05	13.77 (G)	9.62±0.18	Astrometric	Confirmed	El-Badry et al. (2023b)
Gaia BH2	207.56971624	-59.2390050	1276.7±0.6	12.28 (G)	8.94±0.34	Astrometric	Confirmed	El-Badry et al. (2023a)
Gaia BH3	294.8278502301	14.9309190869	4253.1±98.5	11.23 (G)	32.7±0.82	Astrometric	Confirmed	Gaia Collaboration et al. (2024)
Gaia DR3 3425577610762832384	94.27876	23.73022	879±3	12.24 (G)	3.6±0.82	RV	Candidate	Wang et al. (2024)
HD130298	222.3906878085	-56.42735406085	14.6296±0.0009	9.12 (G)	>7.70	Spectroscopic	Confirmed	Mahy et al. (2022)
NGC 1850 BH1	77.19458	-68.76544	5.0402±0.0004	16.136 (V)	>4.71	Spectroscopic	Candidate	Saracino et al. (2022, 2023)
NGC 3201_12560	154.40454	-46.41537	167.01±0.09	17.52 (G)	>3.9	Spectroscopic	Confirmed	Giesers et al. (2018)
VFTS 243	84.53503	-69.15527	10.4031±0.0004	15.236 (G)	10.1±2.0	Spectroscopic	Confirmed	Shenar et al. (2022a)

Table 1.1: BH Candidates

ID	RA deg	DEC deg	$P_{\rm orb}$ days	Mag	Type	Original Reference	"Debunking" Reference
V723 Mon	97.2693750	-5.5722861	59.9	7.97 (G)	stripped + G2	Jayasinghe et al. (2021)	El-Badry et al. (2022b)
2M04123153+6738486	63.1314167	67.6468306	81.2	13.49 (G)	stripped + K1	Jayasinghe et al. (2022)	El-Badry et al. (2022b)
HR 6819	274.2813750	-56.0233500	40.3 ± 0.3	5.26 (G)	stripped + B2-3 Ve	Rivinius et al. (2020)	Bodensteiner et al. (2020); El-Badry and Quataert (2021); Frost et al. (2022)
LB-1	92.9545000	22.8257472	78.7999 ± 0.0097	11.5 (V)	stripped + B3	Liu et al. (2019)	Shenar et al. (2020)
NGC 2004#115	82.7693333	-67.3097111	2.9	15.48 (G)	stripped + B + BE tertiary	Lennon et al. (2022)	El-Badry and Burdge (2022)

Table 1.2: BH Impostors

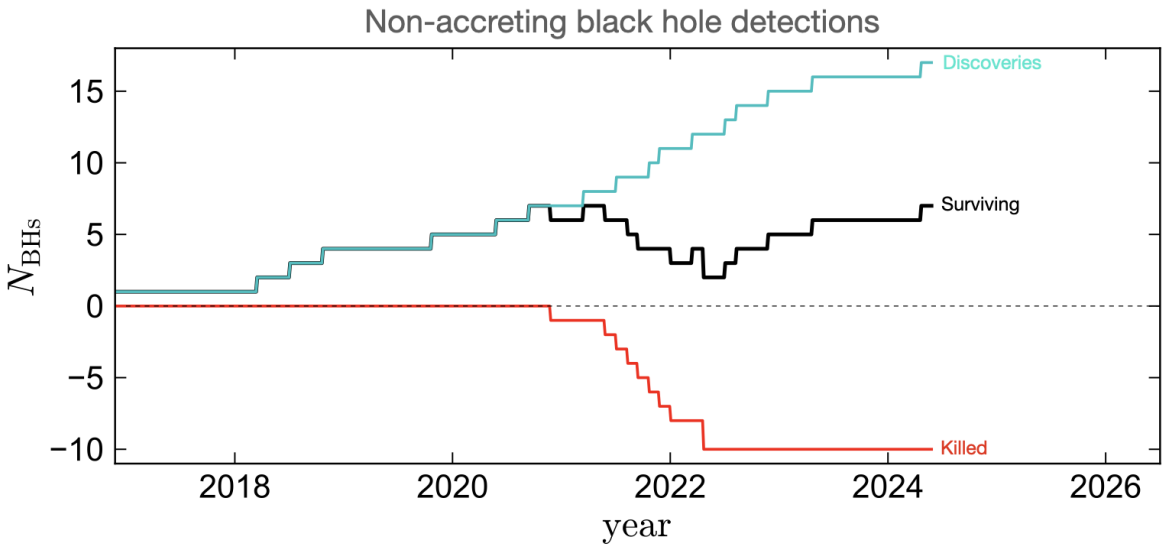

Figure 1.14: Number of proposed BHs (cyan), debunked systems (red), and remaining candidates (black) as a function of time. Figure by Kareem El-Badry.

1.3.4. Impostors and Alternative Explanations

The search for dormant BHs has been marked with the discovery of many so-called "impostor" systems. These are systems containing two bright companions, which, by various means, masquerade as dormant BH candidates in the observations. A number of these impostors are summarised in table 1.2; we explore them in more detail in this section. In figure 1.14, we see the evolution of the number of dormant BHs found, as well as the systems revealed to be impostors; their difference is the number of still "surviving" BHs, as discussed in section 1.3.3.

- **V723 Mon** (Jayasinghe et al., 2021), disproven in El-Badry et al. (2022b): colloquially also referred as the "Unicorn" due to its location in the constellation Monoceros. Originally identified as a triple system by Strassmeier et al. (2012), Jayasinghe et al. (2021) later argued that the triple configuration would be unstable, and instead proposed a solution consisting of a giant with a dark companion, with the giants lines "veiled" by another light source with no notable stellar spectral features. Spectral disentangling of the system in El-Badry et al. (2022b) revealed a luminous, rapidly rotating companion with wide, shallow absorption features.

- **2M04123153+6738486** (Jayasinghe et al., 2022), disproven in El-Badry et al. (2022b): the "Giraffe" found in Camelopardis. Similarly to the Unicorn, it contains a red giant primary, with the binary mass function at face-value implying a massive compact secondary, as an MS star of the implied mass would be violate observed brightness limits in the UV; instead, the authors proposed an accretion disc around the suggested BH to explain the observed spectral features in antiphase with the primary. Again, spectral disentangling revealed a luminous stellar secondary, however with much lower $v \sin i$.

- **HR 6819** (Rivinius et al., 2020), disproven in Bodensteiner et al. (2020), El-Badry and Quataert (2021), Frost et al. (2022): originally identified as a triple system containing a B-type star in an orbit with a stellar BH, with a Be (a B star with strong emission

lines due to a disc formed from rapid rotation) star in wide orbit. As the system is only about 1100 ly from Earth, it would have been the closest BH discovered (and is even closer than *Gaia* BH1 at $\sim$ 1500 ly), with the stellar component visible to the naked eye. An alternative scenario was proposed, consisting of a stripped B star with a Be companion. High-angular resolution follow-up eventually confirmed the two-star scenario with no unseen dark component.

- **LB-1** (Liu et al., 2019), disproven in Shenar et al. (2020): drew attention from the wider community in 2019 after being proposed as a potential binary system of a B-star with a ~ 70 $M_\odot$ BH companion. This would imply the BH to be the most massive stellar BH discovered, falling into the pair-instability gap. A pair-instability SN is predicted to occur for extremely massive stars as a result of gravitational collapse following electron-positron pair formation, and resultant runaway thermonuclear explosion, leaving behind *no remnant*. Due to the puzzling nature of the system, it was studied further, with spectral disentangling revealing two luminous component, a stripped helium star with a rapidly rotating B-type companion.

- **NGC 2004#115** (Lennon et al., 2022), disproven in El-Badry et al. (2022a): identified as a B-type + BH inner binary in a tight orbit ($P \sim 3$ days) at low inclination with a Be star tertiary, located in the Large Magellanic cloud. However, lightcurve analysis revealed strong variation incompatible with the low inclination necessary for a massive companion, as well as reflection effects consistent with a normal MS secondary of lower mass (~ 2.5 $M_\odot$).

Considering these objects as a population, a number of common, but not universal, trends can be identified. First, the majority of these systems contain a stripped star of lower mass than initially assumed, highlighting the importance of stellar interactions when analysing multiple systems. These stars, in many cases, formed through MT, affecting the fundamental properties of the system components (temperatures, surface gravities, abundances, rotation rates) and orbital parameters. Second, hierarchical dynamics and triple system orbital motion has a major effect on implied masses of the components.

1.4. Scope of the Thesis

1.4.1. Motivation

Binary stars form a cornerstone of modern stellar astrophysics - their interactions have profound effects on the evolution of both components (via envelope stripping (Götberg et al., 2023), MT (Henneco et al., 2024), CE evolution, etc). The most massive stars commonly occur in binaries (Sana et al., 2012) and contribute to the ionisation of the medium around them (Bresolin et al., 2008). Binaries also affect the dynamics of dense stellar environments, such as clusters, via dynamical exchange (Heggie, 1975) and other processes. Additionally, star-star binaries are the precursors to double-compact merger events giving rise to gravitational waves (Abbott et al., 2016). However, much of the process of how a star becomes a CO is poorly understood, let alone for two stars in a bound system.

The intermediate steps between a simple MS-MS binary and a CO merger can help shed light onto many aspects of (binary) stellar evolution, but observations of these systems

are rare and their analysis requires specific tools. Simple assumptions about stellar spectra do not necessarily hold when the stars have exchanged mass, lost part of their envelope (Götberg et al., 2018), spun up via accretion (Packet, 1981) or down due to tidal synchronisation (Zahn, 1975). Thus, more data-driven approaches that relax some of the presumptions can paint a more complete picture of the system at hand.

This thesis presents the (continued) development, expansion and implementation of such a toolset: spectral disentangling. Applications are presented on both simulated and real spectra of varying types of binaries, spanning different temperature ranges, mass ratios, and evolutionary stages. The lessons learned are also applied to a more extreme case of high resolution single-epoch spectroscopic data, where disentangling is not possible. Regardless, we ask what we can learn from this data.

While this thesis did not yield new dormant BH candidates, tools developed here will prove useful in analysing current and upcoming large surveys (*Gaia* (Gaia Collaboration et al., 2016) DR4, 4MOST (de Jong et al., 2019), SDSS-V (Kollmeier et al., 2017), WEAVE (Dalton et al., 2012), ...). By focussing on lower-mass stars, we have access to datasets that are simply not (yet) available for massive stars, both in terms of the number of objects and of parameters such as astrometric solutions or stellar properties. This has allowed us to thoroughly test this suite of tools on high-quality, extensive data; once the same kind of data exists for the higher-mass regime, the tools will be fully applicable to this range.

We expect multi-epoch spectra for $\sim 380,000$ OBA stars with SDSS-V, at similar resolution ($R \sim 2000$) as the simulated spectra in chapter 2 (Kollmeier et al., 2017). Additionally, *Gaia* DR4 will expand the catalogue of astrometric data, probing greater volumes and thus increasing the number of solutions available for comparatively rare massive stars. It is also expected to release $\sim 10^8$ RVS spectra: these $R \sim 11,500$ multi-epoch spectra will present an unprecedented opportunity to explore binary systems across mass regimes, and call for computationally efficient methods that make minimal prior assumptions about the systems. There are also efforts among individual researchers and groups to use existing facilities to identify and follow up on candidate systems. These include, but are not limited to:

- *A search for detached black holes and neutron stars in binaries* (0106.A-9008(A), 0107.A-9002(A), 0108.A-9001(A), 0109.A-9001(A); PI: H.-W. Rix)
- *Surveying the brightest luminous and hot stars in the Milky Way* (0110.A-9014(A), 0111.A-9014(A), 0112.A-6007(A); PI: E. Zari)
- *A search for solar-type orbiting black holes and neutron stars* (0111.A-9003(A); PI: K. El-Badry
- *Characterising a sunlike star orbiting a black hole* (2109.D-5047(A); PI: K. El-Badry)
- *Characterising a red giant orbiting a black hole* (2110.D-5024(A); PI: K. El-Badry)
- *Precision RVs of a sunlike star orbiting a black hole* (0111.D-2120(A); PI: K. El-Badry)
- *FEROS observations of compact objects in astrometric binaries* (0112.A-6010(A), 0113.A-3014(A), 0113.A-3014(B); PI: K. El-Badry

- *Hunting for stellar-mass black holes in low-metallicity binaries* (0114.D-6011(A), 0114.D-6011(B), 0115.A-4011(A); PI: K. El-Badry)
- *Constraining mass transfer in massive stars with Algol binaries* (0113.A-3012(A), 0114.D-6014(A); PI: J. Villaseñor),
- *Hunting for BH candidates among SDSS-V massive OB stars* (0115.A-4010(A); PI: J. Villaseñor)
- *Stellar-mass black hole binaries in the Milky Way* (0113.A-3010(A), PI: M. Green)
- *Novel Gaia candidates for dormant BH or NS binaries* (0114.D-6010(A), 0115.A-4009(A); PI: J. Müller-Horn)

All these data require careful analysis, accounting for the often strange nature of binary stars. The tools developed and explored in this thesis translate well into the higher mass ranges, allowing us to identify the progenitors of gravitational wave sources and other BH systems. Even if no new dormant BHs can be identified, the methods provide an excellent toolset for analysing star-star binaries, in particular post interaction systems.

1.4.2. Thesis Outline

Chapter 1 presents an overview of the current state-of-the art of research into binary stars and stellar BHs. We summarise the basics of binary interaction and evolution, and highlight their importance in the wider field of (stellar) astrophysics and their role in explaining a number of interesting observed phenomena. We also discuss some of the methods commonly employed to analyse binaries, their strengths and shortcomings, and how they can be applied to finding dormant BHs, which are the focus of the last part of the introduction. Their significance and formation channels are briefly laid out, with particular attention paid to the effect of binaries. We describe the known dormant BH candidates, as well as previously identified impostor systems.

In Chapter 2 we present the development of a spectral disentangling pipeline based on Simon and Sturm (1994) and apply it to a set of simulated spectra to explore its efficacy in different temperature and mass ratio regimes. We also re-analyse the "Giraffe" and the "Unicorn", previously disentangled with an earlier iteration of the algorithm in El-Badry et al. (2022b) (not included in this thesis).

Chapter 3 discusses the detailed analysis of a set of post MT binaries all previously identified as single-lined binaries in *Gaia* DR3. We apply the pipeline developed in Chapter 2 and determine stellar and orbital parameters of the systems to make inferences about their evolutionary history and MT conservativeness.

In Chapter 4 we explore the case of single-epoch high-resolution spectra for a large volume of stars. We refine the *Gaia* DR3 binary solution where possible, constrain the light ratios of the systems (placing upper limits in the case of single-lined systems), and reassess their SB1 or SB2 status based on APOGEE data. Thus, we demonstrate the value of even just one additional high-resolution epoch when analysing binary systems.

Chapter 5 presents a summary of the main findings of the thesis, and also looks to the future, both in terms of possible further applications of the methods developed on current and future survey data, and the implications of potential findings (or lack thereof).

2

Autonomous Disentangling for Spectroscopic Surveys

Authors Rhys Seeburger, Hans-Walter Rix, Kareem El-Badry, Maosheng Xiang, Morgan Fouesneau

Chapter info This chapter is a reproduction of Seeburger et al. (2024), the first paper I published as part of my doctoral work. It outlines the development, testing and first application of the disentangling pipeline also used in subsequent work. As the main author of the paper, I performed all the relevant programming work (creating the package, setting up the simulated spectra for testing, applying to data for the "Giraffe" and "Unicorn"), as well as interpreting the result. Kareem El-Badry and Hans-Walter Rix were my advisors for this project, and provided ideas shaping the pipeline and its features, as well as suggesting targets and providing data. Maosheng Xiang provided the spectral templates used to create the simulated data. Morgan Fouesneau was instrumental in making the code efficient and bug-free, as well as supplying helpful feedback for best programming practises. All co-Authors gave helpful feedback and comments on the text and figures.

The first application of the pipeline developed here is shown in El-Badry et al. (2022b). I supplied my code with instructions to Kareem El-Badry, the publication's lead author, while he performed most of the analysis and wrote the manuscript.

Abstract A suite of spectroscopic surveys is producing vast sets of stellar spectra with the goal of advancing stellar physics and Galactic evolution by determining their basic physical properties. A substantial fraction of these stars are in binary systems, but almost all large-survey modeling pipelines treat them as single stars. For sets of multi-epoch spectra, spectral disentangling is a powerful technique to recover or constrain the individual components' spectra of a multiple system. So far, this approach has focused on small samples or individual objects, usually with high resolution ($R \gtrsim 10.000$) spectra and many epochs ($\gtrsim 8$). Here, we present a disentangling implementation that accounts for several aspects of few-epoch spectra from large surveys: that vast sample sizes require automatic determination of starting guesses; that some of the most extensive spectroscopic surveys have a resolution of only $\approx 2,000$; that few epochs preclude unique orbit fitting; that one needs

effective regularisation of the disentangled solution to ensure resulting spectra are smooth. We describe the implementation of this code and show with simulated spectra how well spectral recovery can work for hot and cool stars at $R \approx 2000$. Moreover, we verify the code on two established binary systems, the "Unicorn" and "Giraffe". This code can serve to explore new regimes in survey disentangling in search of massive stars with massive dark companions, e.g. the $\gtrsim 200,000$ hot stars of the SDSS-V survey.

2.1. Introduction

The fact that a significant fraction of all stars or stellar remnants is in multiple stellar systems with a period of less than a few years (e.g. Sana et al., 2012; Moe and Di Stefano, 2017) fundamentally affects many aspects of astrophysics. It affects the stellar evolution of both components, in some cases already during their MS phases, and more often in the evolved phases that will result in COs (such as white dwarfs, NS, and BHs); it affects nucleosynthesis, the formation channels of supernovae (SN), and the interpretation of photometric, astrometric, or spectroscopic sky surveys. And massive binaries – or their descendants – are the most prominent and frequent source of gravitational waves so far (e.g. Abbott et al., 2023).

Most of these systems cannot be spatially resolved, with projected separations that often are $\lesssim 1$ mas. However, their orbital velocities make it possible to separate the constituents of such multiple stellar systems in velocity space, especially if spectra at different orbital phases exist. We commonly categorize spectroscopic binaries into SB1 and SB2. Here, SB1 denotes a single-lined spectroscopic binary, where only one of the component spectra is apparent in the observations, and SB2 describes a double-lined spectroscopic binary, where two sets of lines are visible in the observed spectra. The approach of using multi-epoch observations of spectroscopic binaries to determine the components is called *spectral disentangling* (e.g. Bagnuolo and Gies, 1991; Simon and Sturm, 1994; Hadrava, 1995).

In broad terms, spectral disentangling assumes that spectra of a presumed multiple stellar system – when observed at different epochs – can be described as the sum of two (or more) spectra that are invariant in their rest-frame, but whose radial velocities (RVs) change as a function time, reflecting orbital motion. The mathematical foundation of spectral disentangling has been established for 30 years (e.g. Bagnuolo and Gies, 1991; Simon and Sturm, 1994; Hadrava, 1995). End-to-end disentangling requires the simultaneous, or iterative, solution to two problems, (a) reconstructing the rest-frame spectra of each component and (b) determining the components' radial velocities at each epoch or, alternatively, the orbital solution of the overall system. If the velocities at all epochs are known, the reconstruction of the disentangled spectra reduces to a linear χ^2-optimisation problem, aiming to match the combined spectra at all the different epochs.

However, the application of spectral disentangling to large data sets has some serious practical limitations. First, some literature work has assumed that (a very good guess for) various system parameters can be obtained independently (e.g. Ilijic (2004)'s code CRES requires input of both the primary's and the secondary's velocities, shift-and-add as described in Shenar et al. (2020) and Shenar et al. (2022b) requires input of a few orbital parameters, see table 2.1). If the data are of limited resolution, or if the components contribute comparably to the total spectrum's absorption lines, this may not be possible. Second, there are several inherent degeneracies, foremost the fact that any featureless continuum portion of

the spectrum can be assigned to either spectral component without consequences in the data match. Third, the approach works manifestly best in the regime of many epochs with data at high spectral resolution (compared to the orbital velocity changes) and at very high signal-to-noise, so that the dimmer component causes distinct changes in the combined spectrum. Finally, solving the full non-linear problem, i.e. optimising the model-data match over all possible primary velocities, mass ratios, and disentangled spectra is very time-consuming.

Over the last decade and for the next decade, vast spectral surveys are driving an exponential growth in the number of high-quality stellar spectra. Current or upcoming surveys include SDSS (York et al., 2000; Kollmeier et al., 2019), LAMOST (Cui et al., 2012), DESI (DESI Collaboration et al., 2016), WEAVE (Dalton et al., 2012) and 4MOST (de Jong et al., 2019). Further, the *Gaia* Data Release 4 will provide a vest set of spectra. Many of these surveys, in particular *Gaia* (Gaia Collaboration et al., 2023) and SDSS-V (Kollmeier et al., 2019) have multi-epoch observations scheduled across the entire sky.

These surveys offer vast potential to map the stellar binary population via spectral disentangling. Some surveys, such as SDSS-V have explicit programs to systematically survey stars searching for massive dark companions; there spectral disentangling is crucial to identify "contaminants" with two luminous components (e.g. Shenar et al., 2022b,a; Mahy et al., 2022).

In this context of vast spectral surveys, new requirements – or *desiderata* – arise for practical approaches to spectral disentangling. The approach must be

- fast, so that multi-epoch data for 10^4 to 10^6 systems can be analyzed.
- autonomous, in the sense that initial parameter guesses that permit sensible solutions must be found algorithmically and reliably.
- astrophysically flexible; many close binary systems will contain non-standard (stripped, accreting, rapidly rotating) stars.
- robust, given that large surveys typically have fewer epochs, a lower signal-to-noise ratio (S/N) and lower resolution than single-object studies
- user-friendly, as a wide community should be in a position to consistenly analyze different data sets, or reanalyze a given data sets with different constraints on acceptable solutions.

In this paper, we propose a new implementation of spectral disentangling, designed to address these issues. It wraps the process of finding starting guesses, solving for the disentangled spectra, and optimising the flux- and mass ratio parameters into one continuous pipeline written in Python. The approach is also fast enough that it can be applied to surveys of many thousands of objects. We include features such as regularisation to ensure desired properties in the spectra, as well as other adaptations on the original method to optimise the code for survey disentangling.

Due to Python's rise to popularity, we have elected to write this implementation of the method in this language. While at the surface level, speed might be a concern, many of Python's modules are partially written in compiled languages (such as C) and merely provide an interface familiar to the average Python user. Thus, this issue remains manageable. Python does have the advantage of being widely known in the scientific community, making an eventual release of the code as a package accessible to many.

Comparison of prominent existing disentangling codes

Code	KOREL	fd3	Spectangular	CRES	shift&add
Author	Hadrava (2004)	Ilijić (2017)	Sablowski and Weber (2017)	Ilijic (2004)	Shenar et al. (2022b)
Language	Fortran	C	C++	C	Python
WL or Fourier	Fourier	Fourier	WL	WL	WL (iterative)
Solves	Spectra + Orbit	Spectra + Orbit	Spectra + Orbit/RVs	Spectra	Spectra + K1, K2
Third component?	Y	Y	Y	N	Y
Required Input	Orbit	Orbit	Orbit/RVs	RVs	P, T_0, ω, e

Table 2.1: This table summarises a number of properties of some prominent disentangling codes, which include the author(s) who wrote the codes, the programming language they are written in, whether disentangling takes place in wavelength (WL) or fourier space, whether they solve only for the spectra or also attempt to find the RVs and/or Orbital solutions, whether the code is equipped to handle a third component, and which input or guesses are required.

2.2. Spectral Disentangling Methodology

We first briefly review the existing method and codes in spectral disentangling in 2.2.1, then contrast disentangling as an approach with other methods in the literature in 2.2.2. We lay out the desired characteristics of a code for survey disentangling in 2.2.3. In subsection 2.2.4 we describe the prepocessing of the data. We explain the two-step process of optimising for the velocities and mass ratio in 2.2.5, and how we obtain the systemic velocity and light ratio in 2.2.6.

2.2.1. Established Disentangling Codes

There are a number of existing codes, based on and building further upon the concepts introduced in Bagnuolo and Gies (1991), Simon and Sturm (1994) and Hadrava (1995). Some prominent examples of these include KOREL (Hadrava, 2004), CRES (Ilijic, 2004), fd3 (Ilijić, 2017), Spectangular (Sablowski and Weber, 2017) and shift&add (Shenar et al., 2022b). A brief summary of these codes can be found in table 2.1.

These codes employ one of two major methods for solving the linear disentanging problem, either in fourier space (KOREL, fd3) or in wavelength space (CRES, Spectangular). More discussion on this can be found in e.g. Ilijic et al. (2004), but in summary, both methods come with their own advantages and disadvantages. The Fourier method, most notably, outperforms the wavelength-based alogorithm in terms of speed and thus allows for the implementation of further generalisations (Hadrava, 2009). However, this comes at the cost of requiring all spectra to be sampled on the same grid, as well as giving each point the same weight, and implicitly assuming the resulting spectrum to be a periodic function of the wavelength (Sablowski and Weber, 2017). Performing the disentangling in wavelength space allows the user to extend the wavelength range on which the component spectra are computed based on the RV shifts of the individual epochs, as well as being less vulnerable to edge effects arising from the Fourier method.

2.2.2. Disentangling vs Spectral Model Fitting

Spectral disentangling entails the "non-parametric" reconstruction of the individual components' rest-frame spectra. Alternatively, one can view the whole problem as a forward-

modelling problem, drawing on a set of stellar templates. This has been explored and implemented by several groups (e.g. Traven et al., 2020). An important downside of these methods is the fact that spectra in close binaries often do not look like simple, single-star spectra: they may be "exotic" objects such as stripped stars, they may show exceptionally fast rotation or may show emission lines from decretion disks. It can thus be easy to miss the signatures of "strange" companions (e.g. Jayasinghe et al., 2021, 2022; Shenar et al., 2020; El-Badry et al., 2022b; Bodensteiner et al., 2020; Frost et al., 2022) when only considering a limited set of stellar templates.

This highlights the strength of template-independent methods, such as direct subtraction (Ferluga et al., 1997) iterative subtraction, also known as shift & add (González and Levato, 2006, implemented in Shenar et al. (2020, 2022b)), or, as described here, disentangling (Simon and Sturm, 1994). By not having to pre-select a template, we remain flexible to a range of potential outcomes of the procedure.

2.2.3. A Disentangling Approach for Large Spectral Surveys

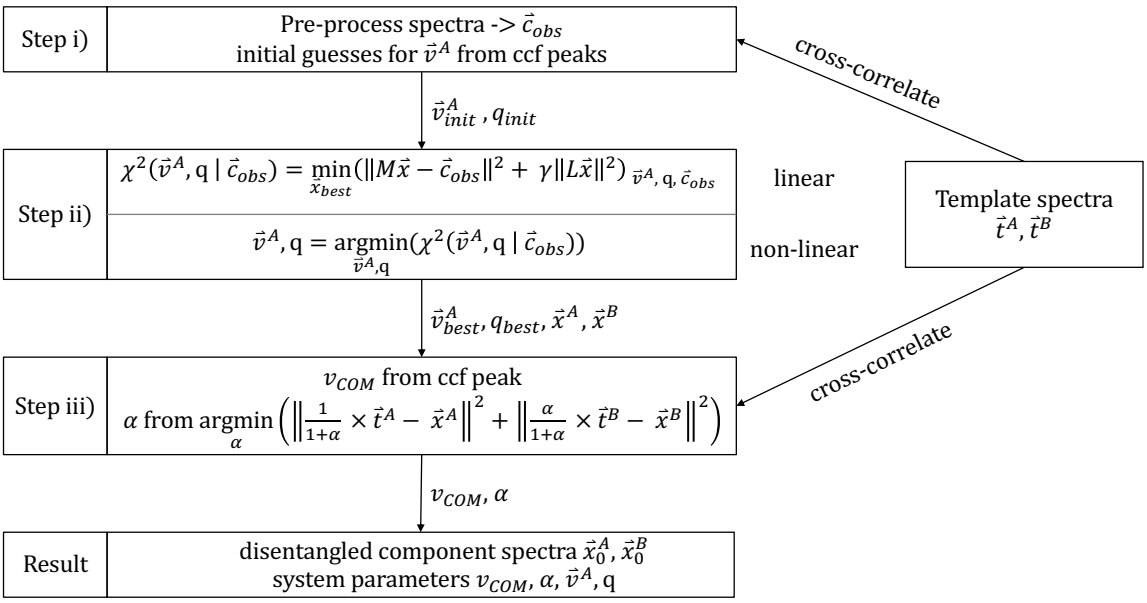

Figure 2.1: A flowchart showing the disentangling process as implemented in this work.

As mentioned in the Introduction, practical approaches to disentangling for vast spectral surveys call for a code that is fast, autonomous with respect to the initial parameter guesses, astrophysically flexible to accommodate the unusual spectra of close binaries, and robust with respect to suboptimal numbers of epochs, S/N and spectral resolution.

Here we set out to devise, test and verify such an approach. The end-to-end approach can be divided into several steps, which are conceptually illustrated in Figure 2.1, which serves as a guide and schematic representation of the process.

We want to start with multi-epoch spectra for any given object, and at the end have both an estimate of the (usually two) disentangled spectra of the primary component's velocities at each epoch, the systemic velocity, the component mass ratio, and the mean component flux ratio. To achieve this for any one object, there are essentially three stages:

1. The spectra at all epochs for any one object have to be consistently pre-processed (normalisation, wevelength rebinning); and initial guesses for the velocities of the primary spectral component (defined as the component with the most prominent spectral lines) need to be derived algorithmically.

2. The optimisation of the main parameters consists of two parts. A non-linear part – trying to find the best primary velocities at all epochs, $\vec{v}^A$ and the mass ratio q. And, a linear part, determining the two disentangled component spectra, $\vec{x}^A$ and $\vec{x}^B$ that best match the multi-epoch spectra $\vec{c}_{obs}$ for each assumed $(\vec{v}^A, q)$.

3. The resulting spectra $\vec{x}^A$ and $\vec{x}^B$ have two remaining problems: they are pure mathematical constructs and know nothing about the rest-frame wavelengths of features. And any (modestly small) constant can be subtracted from $\vec{x}^A$ and added to $\vec{x}^B$, leaving the data match to the $\vec{c}_{obs}$. The last step then uses template spectra to a) fix the rest-frame of the disentangled spectra (or the systemic velocity of the system) and fix the luminosity ratio of the two components, by requiring physically sensible absorption line equivalent widths.

We now describe these three stages in turn.

2.2.4. Preprocessing of the Spectra

Before disentangling, it proves convenient and useful to pre-process the observed multi-epoch spectra to simplify the subsequent math, labelled as step *(i)* above. This first entails masking, or interpolating over, bad pixels. Then resampling the spectra to a wavelength grid that is uniformly sampled in $\ln\lambda$ (hereafter abbreviated as Λ), which linearises velocity shifts. Finally, we normalise the spectra by dividing them by a running median filter, where the filter must be chosen to be much wider than individual spectral features. The point of this is not necessarily to remove the "continuum" of the stellar spectrum, which is often conceptually and practically poorly defined, especially in cool stars with many spectral lines. We are much more concerned with removing the low-frequency variations in the observed spectra, as they may be dominated by instrumental effects. For our disentangling it is most important that we do this consistently across all observed epochs. We also apply the same median filtering to all the templates, i.e. we remove the low-frequency variations in the model spectra fully consistently. Other methods, such as polynomial fitting and clipping were considered, but ultimately median filtering was selected as the method of choice due to its speed, ease of use, and consistency across spectral types.

From this normalised spectrum, we then subtract 1 at all pixels, as this further simplifies the subsequent analysis. The different epochs are then concatenated into one long vector of length $N_{ep} \cdot N_{px}$ (number of epochs times number of pixels). We call this vector $\vec{c}_{obs}$.

As the next part of pre-processing, we must find initial guesses for the primary component's radial velocities for each epoch j , $\vec{v}^A$), to aid the convergence of the non-linear parameter optimisation of step *(ii)*. We have implemented two ways to obtain these initial guesses, either using template cross-correlation, or using the TIRAVEL algorithm (Zucker and Mazeh, 2006, described in the appendix).

For the cross-correlation, we first construct a grid of (rest-frame) template spectra from Kurucz (1979). These templates cover a suitable range of effective temperatures ($\sim$ 20, 2.7

kK to 25 kK), surface gravities (~ 5, -0.35 to 5.4), and two different rotation velocities $v \sin i$ (10 and 100 km/s) and are matched in resolution and wavelength sampling to the observed spectra. For any given epoch we perform a CCF between the observed spectrum and all templates, and take the best template to be the one that yields the highest CCF peak, when averaged over all epochs. The position of the CCF peak for the best template yields our starting guess for the primary velocity at that epoch, yielding the initial $\vec{v}^A$. As starting guesses for the mass ratio, we adopt $\frac{M_B}{M_A} \equiv q \equiv 1$.

In the system's center of mass frame, the primary and secondary velocities are related via $\vec{v}^B \equiv -q \times \vec{v}^A$. But the $\vec{v}^A$ we derive for each epoch are in the barycentric frame and we do not know the actual systemic velocity, v_{COM}. However, we can for the subsequent steps simply *assume* that $v_{COM} \equiv 0$. This will then yield disentangled spectra of the correct shape, just in an ill-defined velocity reference frame. However, this can be remedied by correlation with template spectra in a subsequent step, as we show below.

2.2.5. Parameter optimisation and initial disentangling

We can now proceed to step *(ii)*, indicated in the second box (from the top) of the graphical representation in Figure 2.1. As mentioned, this step consists of two aspects. The linear part estimates the disentangled spectra that best match the observations at all epochs for given $\vec{v}^A$ and q. Each execution of this linear disentangling step yields $\chi^2(\vec{v}^A, q)$. This step is wrapped in a nonlinear parameter optimiser (we settled on the Nelder and Mead (1965) method) that then finds most likely parameter estimates $\vec{v}^A_{best}, q_{best}$ as

$$\vec{v}^A_{best}, q_{best} \equiv \arg\min_{\vec{v}^A, q} \left(\chi^2(\vec{v}^A, q)\right). \tag{2.1}$$

2.2.5.1 The linear disentangling step

It is more sensible to describe the linear disentangling step first. We restrict ourselves to the *binary* (rather than triplet, etc.) case, where we seek the initially disentangled components $\vec{x}^A$ and $\vec{x}^B$, specified on a logarithmic wavelength grid with the same $\Delta\Lambda$ as the observed spectra: $\vec{x}^{A/B} \equiv \{x^{A/B}(\Lambda_i)\}$ with $i = [0, N_{px}]$.

In this context, non-relativistic velocity changes correspond to constant shifts in $\ln \lambda$ and can be specified as

$$\Delta\Lambda = \ln\left(1 + \frac{v}{c}\right). \tag{2.2}$$

In this first step we will retrieve 'initial' disentangled spectra in an ill-determined velocity frame rather than in the physical *rest-frame*. We will remedy this in a subsequent step (Section 2.2.6). For now, we can assume formally that the systemic velocity is not only constant but also zero; then the two component's velocity shifts at epoch j are related via $\Delta\Lambda^B_j = -\Delta\Lambda^A_j / q$. In this case we only need to know the velocities for one component (say, A) and the system's mass ratio to determine all relevant velocities.

The shifted spectra of the components for each epoch j can be written as:

$$\vec{x}^A_j = \{x^A(\Lambda_i - \Delta\Lambda^A_j)\} \tag{2.3}$$

$$\vec{x}^B_j = \{x^B(\Lambda_i - \Delta\Lambda^B_j)\}. \tag{2.4}$$

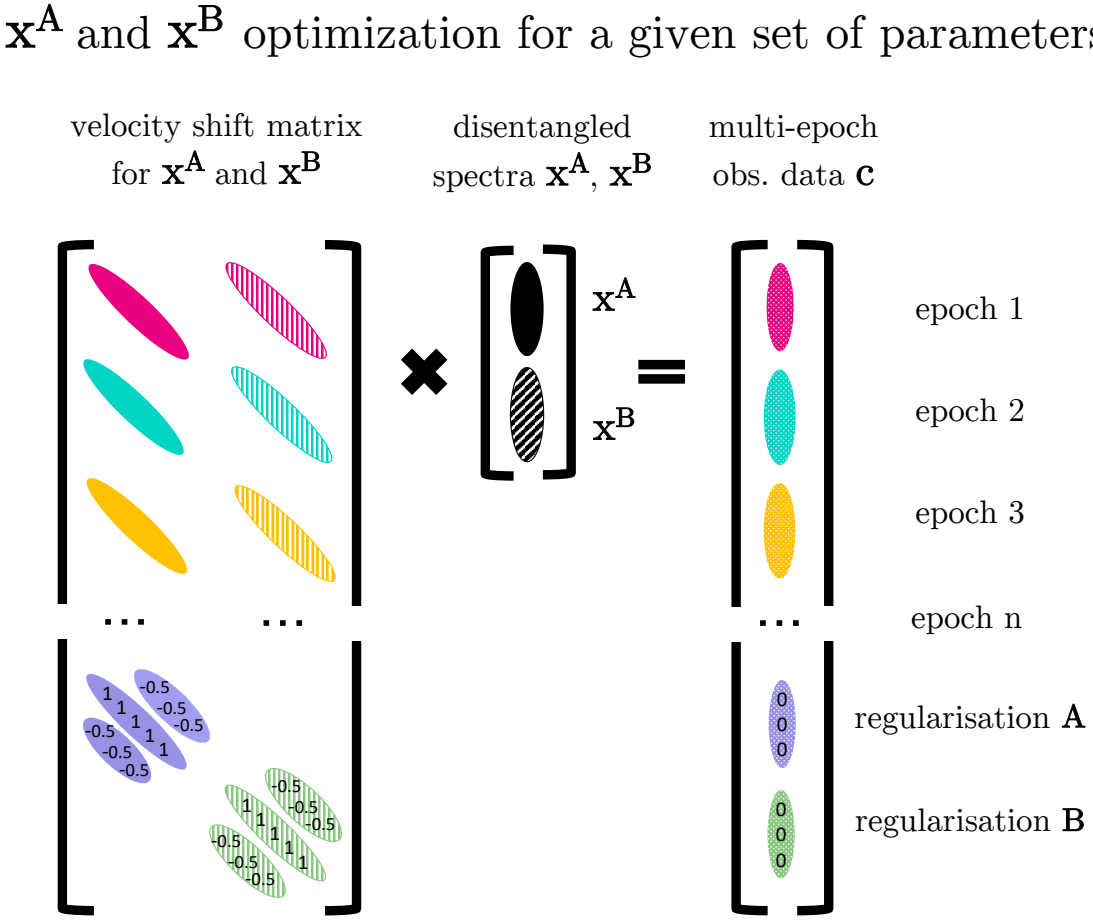

Figure 2.2: A cartoon of the setup of the linear algebra portion of the disentangling scheme. The top portion of matrix M on the left-hand side consists of (off-) diagonals whose position relates to the per-epoch velocity shifts. The vector in the center is simply the component spectra stacked on top of each other and the desired output of the linear algebra procedure. The vector on the right is the individual epoch composite spectra, stacked as well. The regularisation scheme detailed at the bottom of the cartoon is described in more detail in section 2.2.5.2

The predicted composite spectrum $\vec{c}_{j,pred}$ at epoch j is then given by:

$$\vec{c}_{j,pred} = \{x^A(\Lambda_i - \Delta\Lambda_j^A) + x^B(\Lambda_i - \Delta\Lambda_j^B)\}. \tag{2.5}$$

The predictions for the composite spectra at all epochs j can be cast more elegantly into a matrix of form:

$$\mathbf{M} \cdot \vec{x} = \vec{c}_{pred}, \tag{2.6}$$

where the column vector $\vec{x}$ is the concatenation of $\vec{x}^A$ and $\vec{x}^B$, and $\vec{c}_{pred}$ the concatenation of all $\vec{c}_{j,pred}$ at all different epochs N_{ep}. Thus, $\vec{x}$ is a column vector of length $2N_{px}$, and $\vec{c}_{pred}$ a column vector of length $N_{px} \cdot N_{ep}$. The matrix $\mathbf{M}$ is then a matrix of dimensions $(N_{px} \cdot N_{ep}) \times 2N_{px}$ made of $2 \times N_{ep}$ blocks (one for each component and each epoch) of dimensions $(N_{px} \times N_{px})$. $\mathbf{M}$ is a sparse matrix, with the only nonzero elements being (off-)diagonals, whose position and value are governed by the per-epoch shifts of both components, $\Delta\Lambda_j^{A/B}$. Figure 2.2 shows a simplified schematic of Equation 2.6, and a more detailed description of the matrix structure can be found in Appendix A.1.3.

For a given set of $\Delta\Lambda_j^A$ and q, we then wish to find the $\vec{x}_{best}$ for which $\vec{c}_{pred}$ best matches – in the L2-norm or chi^2 sense – the concatenated set of multi-epoch observations $\vec{c}_{obs}$:

$$\vec{x}_{best} = \arg\min_{\vec{x}} ||\mathbf{M} \cdot \vec{x} - \vec{c}_{obs}||^2. \tag{2.7}$$

As the matrix $\mathbf{M}$ is sparse and frequently very large, it makes sense to look for efficient methods for the use case. Simon and Sturm (1994) propose the use of Singular Value Decomposition (SVD) (e.g. Forsythe et al., 1977) to solve for $\vec{x}$. However, we found that the LSMR algorithm by Fong and Saunders (2011) provided a more efficient iterative algorithm that exploits the sparsity of the matrix to arrive at a solution quickly. The resulting $\vec{x}_{best}$ can then be separated into $\vec{x}^A_{best}$ and $\vec{x}^B_{best}$.

Figure 2.3 shows an example of the disentangling result for a MS binary consisting of a 1.1 $M_\odot$ primary with a 0.95 $M_\odot$ secondary, i.e. a mass ratio of $q = 0.86$. The velocity semi-amplitude of the primary is 200 km/s, we have assumed a circular, edge-on orbit and sampled the velocities regularly for 6 epochs at a resolution of $R = 2000$ and with a signal-to-noise ratio of 30. The systemic velocity is 100 km/s. Disentangling has been performed assuming $\Delta\Lambda_j^A$ and q are known. Both the composite spectra (black and grey lines) and the individual disentangled component spectra are in excellent agreement with the observations (top) and input spectra (two panels below).

2.2.5.2 Regularisation

While the method described so far can yield acceptable results, the two disentangled spectra are often not smooth. This is due to the nonuniqueness of the solutions: especially for sections of the continuum with no/few lines, it is ill-defined how much each component spectrum is specifically contributing to the composite.

Tikhonov regularisation (Tikhonov, 1963; Phillips, 1962) introduces an additional term in the least-squares minimisation (Equation 2.7), which can be used to penalise certain undesired features in the solution, and encourage desired properties. So, instead of minimising the expression in Equation 2.7, we seek to minimise:

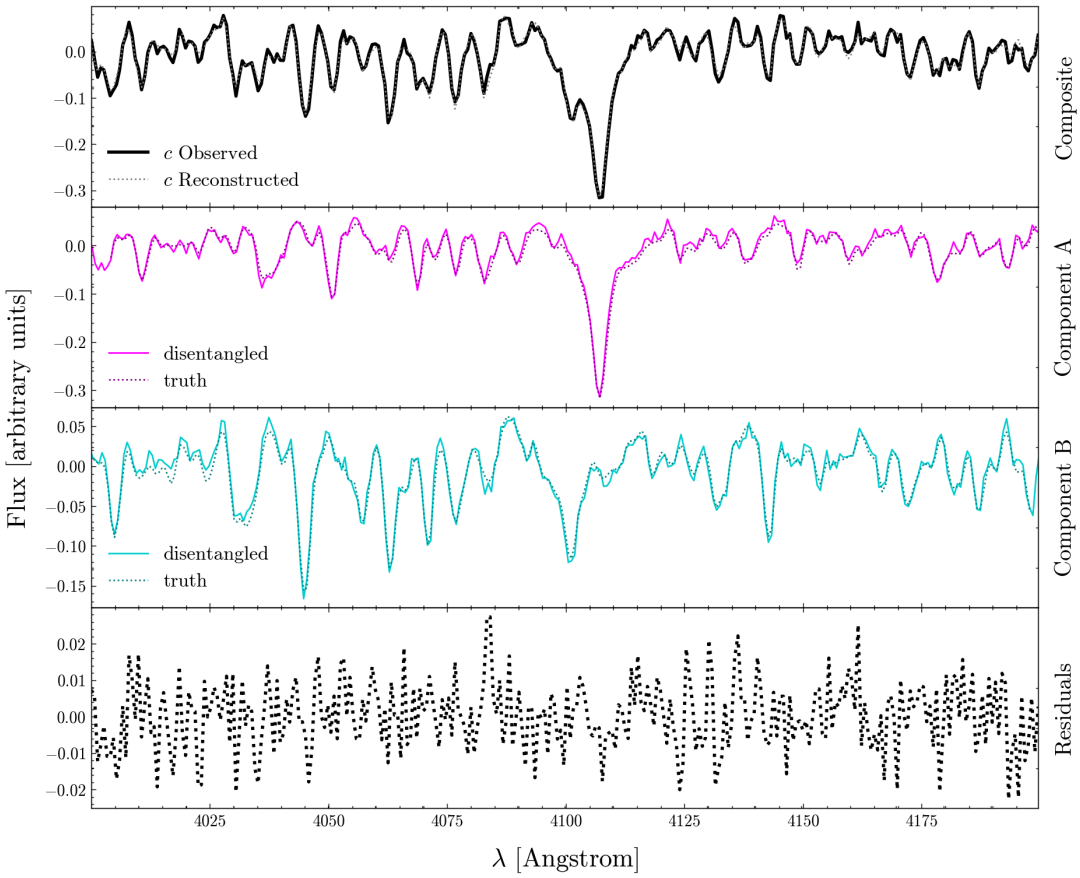

Figure 2.3: An example of a disentangled spectrum, displaying one epoch. The top panel shows the observed spectrum at that epoch in black, and the sum of the two disentangled and velocity-shifted component spectra in grey. The second and third panel show the rest-frame spectra for the disentangled components, with the true spectra shown as dotted lines. The bottom panel displays the difference between the observed and the reconstructed spectrum (shown separately in the top panel).

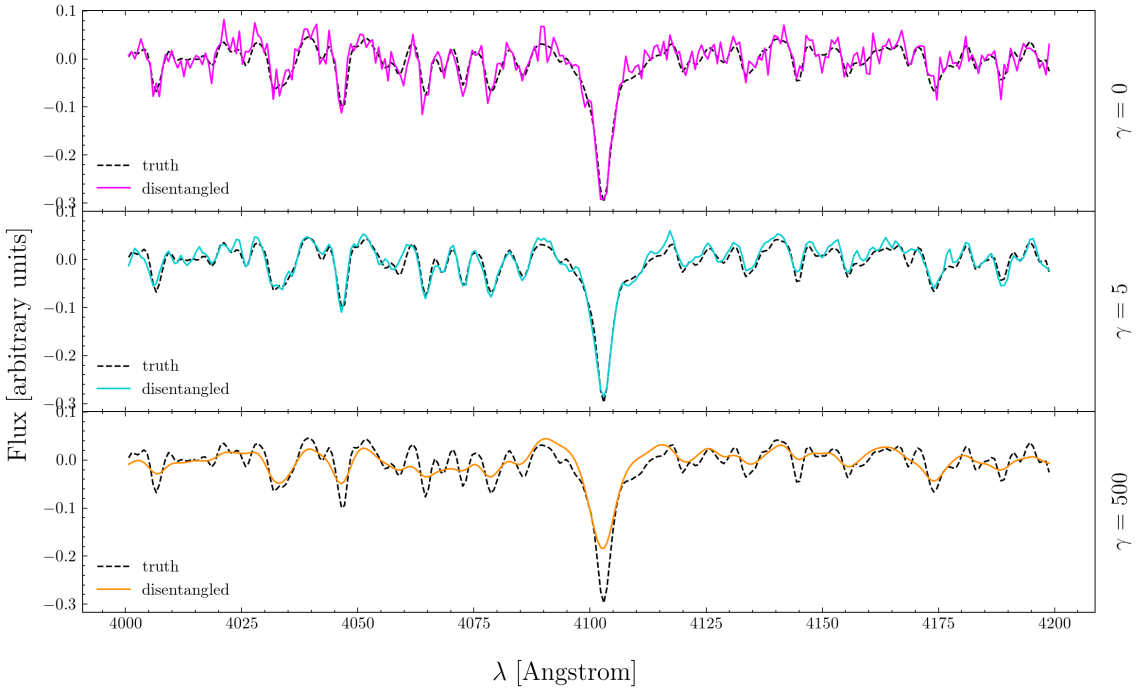

Figure 2.4: The spectrum of the primary as obtained from disentangling with varying degrees of regularisation. The first panel shows the result without regularisation, the second panel with $\gamma = 5$ and the last with $\gamma = 500$. In each panel, the true spectrum is shown with a black dashed line.

$$||\mathbf{M} \cdot \vec{x} - \vec{c}_{obs}||^2 - \gamma||\mathbf{L} \cdot \vec{x}||^2, \tag{2.8}$$

where $\mathbf{M}$, $\vec{x}$ and $\vec{c}_{obs}$ are as previously described. $\mathbf{L}$ is a matrix by which we regularise the solution for $\vec{x}$ and γ expresses the weight of this regularisation compared to the disentangling problem. There is a trade-off: very small γ will lead to very little regularisation (and $\gamma = 0$ reduces to the original problem posed), while very large γ will over-regularise the solution, leading to a loss of the original features.

This can be recast into a form very similar to Eq.2.7:

$$\vec{x}_{best} = \arg\min_{\vec{x}} \left|\left|\left| \begin{bmatrix} \mathbf{M} \\ \sqrt{\gamma}\mathbf{L} \end{bmatrix} \vec{x} - \begin{bmatrix} \vec{c}_{obs} \\ \vec{0} \end{bmatrix} \right|\right|\right|^2 . \tag{2.9}$$

Here, $\mathbf{L}$ is of shape $(2N_{px} \times 2N_{px})$, and $\vec{0}$ is of length $2N_{px}$. Thus, this extension to the original problem allows regularisation of $\vec{x}$ by simply appending to the matrix $\mathbf{M}$ and the vector $\vec{c}_{obs}$.

We want matrix to $\mathbf{L}$ push for smooth $\vec{x}$ solutions but without enforcing a specific shape onto the spectra. We do this by minimising the second derivative or curvature among adjacent elements of $\vec{x}_{best}$. In practice, the matrix $\mathbf{L}$ has 1's along the diagonal , and -1/2 along the two first off-diagonals above and below the main, as illustrated in the scheme shown in Figure 2.2. This matrix leads to a norm that is simply the sum of the second derivatives among all sets of adjacent 3 pixels (expressed as a finite difference). Therefore, it penalizes strong local curvature of the result, and thus "jaggedness" of the disentangled spectra.

In Figure 2.4 we compare the result of different regularisation strengths, ranging from none (top) to a good amount (middle) to too much (bottom). We see that when no regu-

larisation is applied, the disentangled spectrum is jagged due to the degeneracies. With an appropriate amount of regularisation, this can be remedied. If too much regularisation is applied, features and details will start to be "washed out" - it is thus important to choose the regularisation parameter correctly, e.g. by requiring it not increase the least-squares or χ^2 significantly. In practice, we seek a regularised solution that fits the data to within $\Delta\chi^2 \sim 3$ as well as the unregularised solution. We have found a suitable γ for each (simulated) dataset by trial and error; automatisation of this is an endeavour for future work.

2.2.5.3 The non-linear optimisation step

So far, we have shown how to robustly solve the disentangling problem if the RVs $\vec{v}^A$ for all epochs j and the mass ratio q are known.

We now need to implement a robust way to find the optimum parameters $\vec{v}^A$ and q such that the two constructed component spectra $\vec{x}^A$ and $\vec{x}^B$, shifted by their respective epoch velocities, optimally reconstruct the observed composite spectrum $\vec{c}_{obs}$ for all epochs. To this end, we define the residual between the observed and reconstructed spectra as:

$$\vec{R} = \vec{c}_{j,obs} - \vec{c}_{j,pred} \tag{2.10}$$

or, more explicitly,

$$\vec{R} = \vec{c}_{j,obs} - \left(\vec{x}^A(\Lambda_i - \Delta\Lambda_j^A) + \vec{x}^B(\Lambda_i - \Delta\Lambda_j^B)\right). \tag{2.11}$$

Equation 2.11 explicitly recognises that the residuals are a function of $\Delta\Lambda_j^{A/B}$. As the next step, we have to find the best values for these $\Delta\Lambda_j^{A/B}$ by minimising the value of χ^2 as a function of q and $\vec{v}^A$, defined as:

$$\chi^2(\vec{v}^A, q \mid \vec{c}_{obs}) = \vec{R}^T \cdot \mathrm{cov} \cdot \vec{R}, \tag{2.12}$$

where cov is the covariance matrix of the observed spectra.

We do this minimisation via the Downhill Simplex Optimisation by Nelder and Mead (1965), specifically the `scipy.optimise` implementation.

Robust optimisation requires a sensible initial starting guess. We initialise it with $\vec{v}^A$ and q as described in 2.2.4. Then the optimiser solves at each step the linear problem (Equation 2.9) for the current values of $\vec{v}^A$ and q. This returns the component spectra $\vec{x}^A$ and $\vec{x}^B$ and from them $\vec{c}_{pred}$, which yields χ^2 from Equation 2.12 from the comparison with the data $\vec{c}_{obs}$. Eventually, we expect the optimiser to return the best values for the RVs and mass ratio, those that allowed for the most accurate reconstruction of the observed spectra.

2.2.6. Determining the systemic velocity and light ratio

Mathematically, spectrum disentangling is possible while only knowing the relative per-epoch RVs of the primary and the mass ratio, as has been demonstrated. However, this yields two disentangled spectra that are in an unspecified velocity frame that is neither the center-of-mass frame nor the rest-frame; and the velocity frames for the two components

will generally not be the same. But in practice, we are interested in the systemic velocity v_{COM} and the light ratio of the two components α.

We now describe how we find these parameters and move the disentangled spectra to a well-defined rest-frame, as outlined in step *(iii)* of Figure 2.1. In doing so, we basically draw on external astrophysical information: the rest-frame wavelengths and (approximate) equivalent widths of prominent stellar absorption lines in the disentangled spectra must resemble – at least roughly – those in a comprehensive set of template spectra.

We start by using such template spectra to find the systemic velocity. We do this by computing the cross-correlation function (CCF) of the initial solution vectors $\vec{x}^{A/B}_{best}$ with spectra in the template set and identifing the best template. We denote the velocity of that CCF peak as $\epsilon^{A/B}$, which describes the offset of the velocity found by the optimiser from the true observed velocity of the primary. In this notation we have

$$\tilde{v}^A = v^A + \epsilon^A = w^A + v_{COM} + \epsilon^A \tag{2.13}$$

where $\tilde{v}^A$ are the velocities in the initial ill-defined frame, v^A the true velocities in the observer frame, and w^A are the center-of-mass-frame velocities. With starting guesses via template cross-correlation, we expect ϵ^A to be close to zero. This is because the templates are in the rest frame, so initial velocities found using them should also be in the rest frame, meaning the offset ϵ^A should be small. TIRAVEL (Zucker and Mazeh, 2006) determines initial guesses by cross-correlating the different epochs with each other and solving for the most probable vector of RVs. Then, ϵ^A could be large, as we have no prior information about absolute RVs, only relative (to other epochs). By contruction from the disentangling, the primary and secondary velocities in our ill-defined frame are related by $\tilde{v}^B = -\tilde{v}^A/q$ holds. And, we have the relations

$$v^B = w^B + v_{COM} = -\frac{w^A}{q} + v_{COM}, \tag{2.14}$$

with nomenclature analogous to Equation 2.13; Eq. 2.14 simply states that the true observed velocity is the secondary's center-of-mass frame velocity plus the systemic velocity, which in turn is related to the true velocity of the primary via the mass ratio q. We can now use these offsets $\epsilon^{A/B}$ and Equations 2.13 and all 2.14 to determine the systemic velocity of the system:

$$\epsilon^B = \tilde{v}^B - v^B \;\; = \;\; -\frac{\tilde{v}^A}{q} + \frac{w^A}{q} - v_{COM} \tag{2.15}$$

$$v_{COM} = -\frac{\epsilon^B + \epsilon^A/q}{1 + 1/q} \tag{2.16}$$

Note that even when ϵ^A is small, ϵ^B might be large, especially when the originally assumed systemic velocity is far from the truth.

This puts us in a position to solve for the component spectra in the rest-frame using these results and Equation 2.13. This process also gives us templates $\vec{t}^A$ and $\vec{t}^B$, the templates that had the highest CCF peak with the respective disentangled component spectra.

We can now turn to determining the light ratio α, using the best-fitting templates. In the end we attribute different portions of the "featureless continuum" to the two disentan-

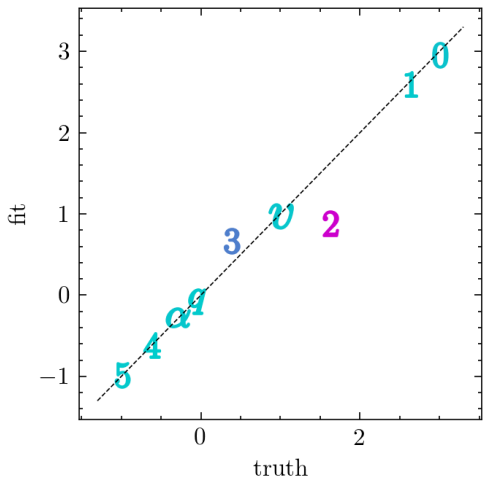

Figure 2.5: An example of the results for the different parameters obtained by the optimiser. The correct value is plotted along the x-axis, with the value recovered by the optimiser along the y-axis. The dashed line indicates agreement between the two, and the further away from this line a value falls, the less accurately it was determined. The colour of each symbol also indicates how well the parameter was fit, with pink indicating a bad, and cyan a good agreement of the fit value with the truth relative to the other parameters. The symbol used for each point represents the parameter, with numbers 0-5 indicating the per-epoch RVs for each epoch (divided by 100), q the log_{10} of the mass ratio, v the systemic velocity (divided by 100) and α the log_{10} of the light ratio. We selected these scaling of the different parameters for better visualisation. We see good recovery for all parameters, except two of the RVs. This is, however, not further surprising, as these RVs are fairly close to the systemic velocity, meaning there is only a small doppler shift of the two spectra relative to each other, making determination of the accurate velocities difficult at these low resolutions.

gled components so that their equivalent widths are physically plausible. We obtain α by minimising

$$\arg\min_{\alpha} \| \frac{1}{1+\alpha} \vec{t}^{A} - \vec{x}^{A} + \frac{\alpha}{1+\alpha} \vec{t}^{B} - \vec{x}^{B} \|^2, \tag{2.17}$$

which scales the templates for both components, $\vec{t}^{A}$ and $\vec{t}^{B}$, such that the scaled templates most resemble the disentangled spectra.

An example of the results of this 3-step (preprocessing, optimising $\vec{v}^{A}$ and q, finding v_{COM} and α) process can be seen in Figure 2.5, where the accuracy of each parameter as found in the optimisation or subsequent step, is explored. The system has the same parameters as the one discussed in section 2.2.5.1 whose disentangled spectrum can be seen in Figure 2.3.

2.3. Algorithm Validation

We now proceed to validate this autonomous multistep approach to spectral disentangling that we have laid out. In particular, we want to explore under which circumstances it yields sensibly disentangled spectra and reasonable physical parameters. This will depend on both the physical properties of the binary system (velocity semi-amplitude K, mass and light ratios, effective temperatures) and on the observational set-up (S/N, spectral resolution, number of epochs).

In exploring this, we will particularly focus on the observational parameter regime pertinent to large spectroscopic surveys: modest resolution and S/N along with relatively few epochs. We do this by simulating composite spectra of binaries with both hot and cool primaries, and then running the algorithm 'blindly', or autonomously, on them. These simulations allow us to assess both the *robust* and the *problematic* disentangling regimes. After these simulations, we illustrate the approach using a well-established binary system.

2.3.1. Simulated Data

We perform an initial test of the method on simulated data, given that it allows us to precisely control the system parameters and check how well the algorithm recovers them. To simulate co-evolving binary components, we use a 1 Gyr and 250 Myr isochrone from Bressan et al. (2012) for the cool- and hot-star primary simulations, respectively, selecting a 1.1 $M_\odot$ and 3 $M_\odot$ star as the primary.

For resolutions of $R \approx 2,000$ and $R \approx 20,000$, we then explore a grid of different RV semi-amplitudes K, linearly spaced from 50 km/s to 250 km/s, and light ratios α. For α, we consider logarithmically spaced values from 0.01 to 1 to explore the more "extreme" regimes of very faint secondaries, as well as a linearly spaced grid from 0.1 to 0.9. With the primary's parameters (mass, age, $T_{\rm eff}$ and $\log g$) and α, we can use the isochrones to get analogous parameters for the secondary; the two components' masses then also yield q. We then select spectral templates, using Kurucz (1979) spectra for the two components. Then, we set the orbital parameters of the system (assuming a circular, edge-on orbit), sample the RVs of both components at 6 different epochs uniformly in phase-space over half an orbit, and create composite spectra, adding noise. Here, we assumed a signal-to-noise ratio of 30.

We feed these simulated spectra to the disentangling and optimisation algorithm, assessing how well it is able to obtain the correct system parameters, reconstruct the observed composite spectra $\vec{c}_{obs}$ and solve disentangled rest-frame spectra $\vec{x}_0^{\mathcal{A}}$ and $\vec{x}_0^{\mathcal{B}}$.

We assess the quality of the parameter through this figure of merit:

$$\mathrm{FOM} = 1 - \frac{1}{\mathrm{n}} \sum_{\mathrm{i}=1}^{\mathrm{n}} \mathrm{w_i} \cdot \frac{|\theta_{\mathrm{i,pred}} - \theta_{\mathrm{i,true}}|}{|\theta_{\mathrm{i,pred}}| + |\theta_{\mathrm{i,true}}|}, \tag{2.18}$$

which is bound between 0 and 1, where $\theta_{i,\mathrm{pred}}$ are the estimates returned by our algorithm, $\theta_{i,\mathrm{true}}$ the true (simulation input) values, and w_i are the normalised weights assigned to each parameter. We have assigned weights of 0.25 to q, v_{COM} and α, and a weight of $\frac{0.25}{N_{ep}}$ to each of the primary RVs. The weighting avoids the FOM being dominated by the accuracy of the recovered primary RVs (especially in the case of many epochs), which are comparatively easy to find, and places greater importance in correctly determining the parameters associated with the secondary. It is pertinent to note, at this point, that a "good" FOM means that the system parameters have been recovered accurately, not necessarily that the disentangled spectra are equivalent to the "ground truth". It is simply a metric to assess the performance of the optimiser.

The results of this validation are shown in Figure 2.6 for cool (left panel) and hot primaries (right panel). The different subpanels show a grid in velocity semi-amplitude K and light ration α. The background color of each subpanel indicates the FOM, with lighter colors indicating better parameter retrieval. For high velocity semi-amplitudes (compared to

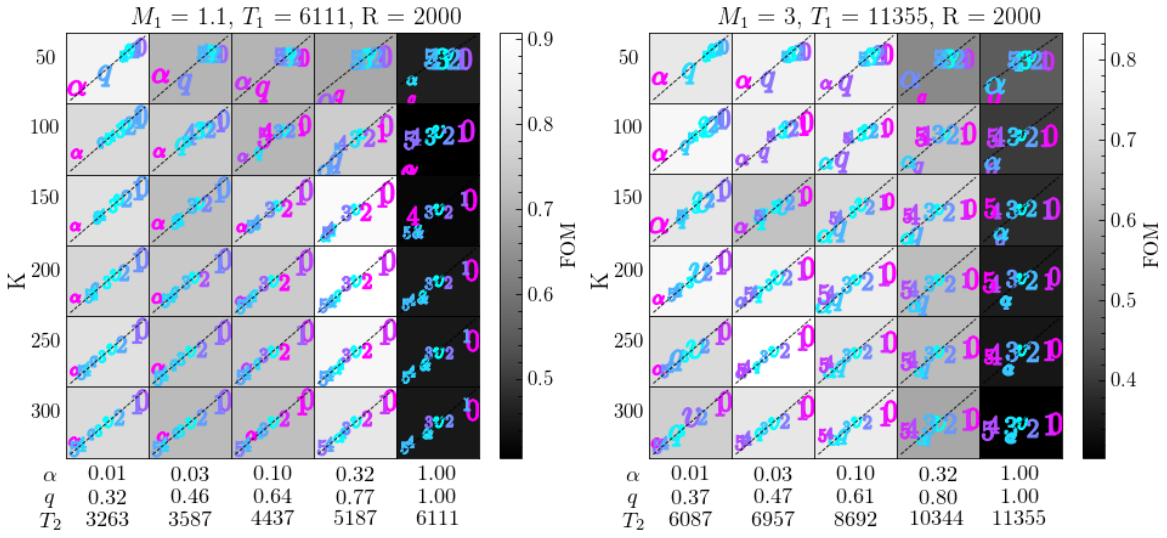

Figure 2.6: A grid of the results of the autonomous disentangler on a range of different systems. The left panel shows the case of a low mass primary (1.1 $M_\odot$), while the right panel displays the case of a higher mass primary (3 $M_\odot$). Each panel consists of multiple cells, varying in the semi-amplitude of the radial velocities, K, along the y-axis, and in light ratio α, and consequently, the mass ratio q and effective temperature of the secondary, $T_{\mathrm{eff},2}$, along the x-axis. The colour of each cell indicates the figure-of-merit value the disentangler achieved for the recovery of the parameters, with white indicating a higher, and thus better, figure-of-merit, and black indicating a lower, worse FOM. Each cell also contains the accuracy and precision achieved for each individual parameter, analogous to Figure 2.5. The x-axis here displays the true value of the parameter, and the y-axis the one recovered by the optimiser. If the optimiser determined the correct parameter, we expect it to lie along the dashed grey diagonal line. The colour of each parameter indicates how well it was recovered within its specific system, with pink indicating a comparatively large distance between truth and fitted parameter, and cyan indicating a small distance, and thus good agreement. Lastly, the size of each symbol is related to its variance in the bootstrapping process, with a large symbol indicating a large variance (and thus a low precision) and a small symbol indicating a small variance and higher precision.

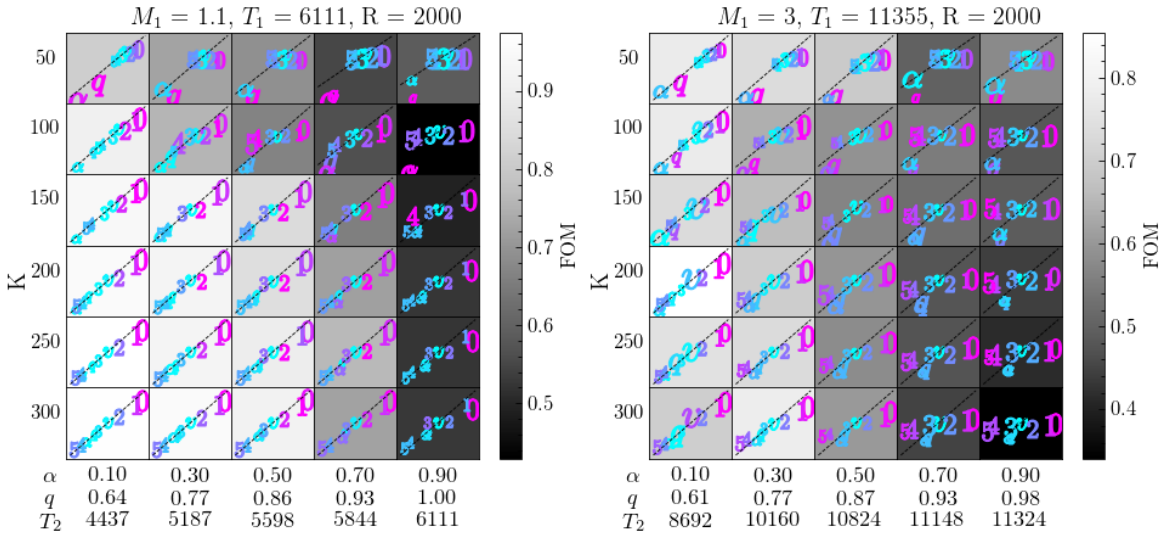

Figure 2.7: Analogous to Figure 2.6, with the light ratio now varying between 0.1 and 0.9 in steps of 0.2.

the spectral resolution) and distinctly different component temperatures (whenever $\alpha \ll 1$) the parameter retrieval is robust and quite precise; this is particularly true if the primary star is already cool. But the Figure also shows that there are two regimes where our algorithm struggles: first, for a mass ratio of unity (twin star spectra) there is a degeneracy between the two components' velocities. Consequently, the optimiser cannot determine the other parameters correctly. For the very faint secondary regime ($\alpha = 0.01$), the optimiser finds the correct primary velocities, but has some difficulties with the mass and light ratio, as well as q. This is not particularly surprising, as in this regime the signal of the secondary is on the level of the noise, and thus finding parameters that pertain not just to the primary (as the RVs do, in this case) is problematic.

Second, Fig. 2.6 also shows that lower velocity semi-amplitudes (below the spectral resolution) lead to a worse determination of the individual component's velocities, and consequently of the other parameters. For the higher-mass and hotter primary, the broader spectral lines and comparatively similar spectra between the primary and secondary also lead to an underestimation of the RVs, as the CFF peak is substantially affected by the secondary.

Figure 2.7 is analogous to Figure 2.6, with α varying from 0.1 to 0.9 in steps of 0.2. Again we see that for both the cool and the hotter primary, our disentangler has difficulties correctly recovering the velocities for the lowest RV semi-amplitudes. As we are now excluding the more extreme cases of twin stars and extreme light ratios, where the secondary contribution is on the level of the noise, we observe generally higher (and thus better) figure-of-merit values. With the linear grid in α we can see a more gradual trend in the robustness of our disentangling approach, with accuracies getting worse as we get "too close" to an equal mass binary, especially for the 3 $M_\odot$ primary, as the spectra of the primary and secondary show rather similar features.

Figure 2.8 shows individual disentangled spectra for different simulated systems. We show a smaller wavelength range for the cooler primary, as there are more and narrower lines, whereas for the hotter primary, the lines are wider and fewer. We see that the disentangler successfully recovers the primary component in all cases, using both the "true" parameters as well as the ones found by the optimiser. For the smallest light ratio of 0.01, both in the hot- and the cool-star case, the disentangler struggles to recover the secondary, due to its small contribution to the spectrum. There are still some issues with the secondary spectrum recovery for the hotter primary even at a more moderate light ratio of 0.1. We believe this to be due to the very similar lines between the primary and secondary - for moderate velocity shifts, two similar spectra being shifted against each other look like the lines are "widening" and "narrowing", rather than fully seperating, which causes some issues in the disentangling process.

2.3.1.1 Disentangling SB1 Systems with Dark Companions

Part of the motivation for this work is to find systems where the secondary is dark, i.e. does not show up in the disentangling. To explore how our code responds to such systems, we have simulated a binary consisting of a 1.1 $M_\odot$ primary with a dark companion (a so-called SB1 system). Like before, we set a velocity semi-amplitude of 200 km/s for the bright component and assume a circular, edge-on orbit. RVs are sampled uniformly in time at a spectral resolution of $R = 2000$ and a signal-to-noise ratio of 30.

We then applied our optimiser and disentangling procedure to this system in the same way as the previous simulations, presuming we have no prior knowledge of its SB1 nature.

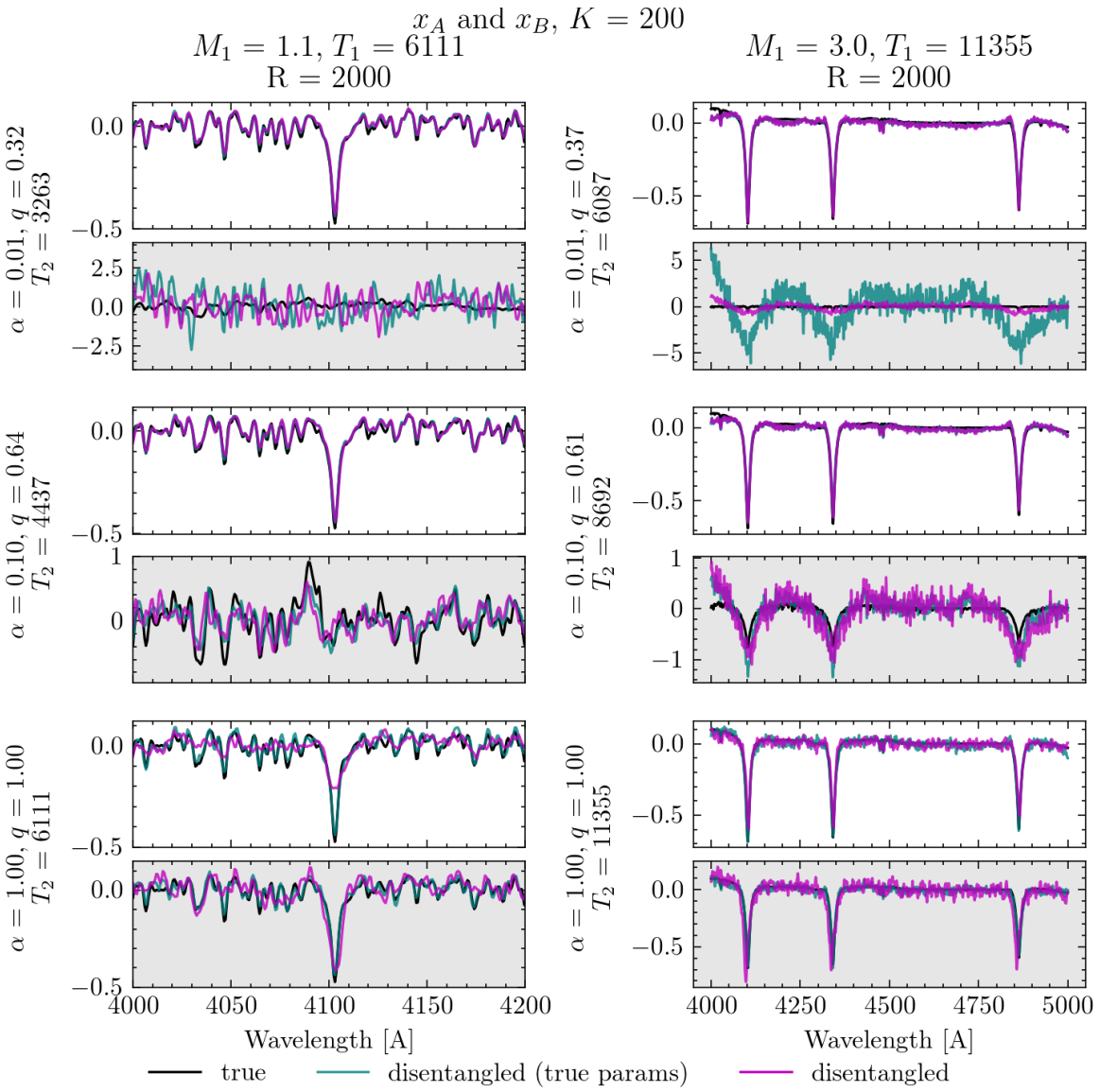

Figure 2.8: A selection of individual results of the autonomous disentangler, here for a RV semi-amplitude of 200 km/s. The left column shows the low-mass primary case, and the right the higher-mass primary. The different rows show different light ratios α and thus mass ratios q and effective temperature of the secondary, $T_{\mathrm{eff},2}$. The top panel (white background) in each row shows the result of the disentangling for the primary, and the bottom (grey background) for the secondary. For each panel, the truth is plotted in black, with the disentangling result achieved by using the "correct" input parameters in green, and the actual result cyan the autonomous disentangler in magenta. The disentangler solutions are scaled by the light ratio (true value for cyan, value recovered by the optimiser for magenta) to match them to the true input. Thus, a "correctly shaped" spectrum that is scaled incorrectly indicates an incorrect light ratio, while a spectrum that is offset relative to the truth indicates that the systemic velocity was not found correctly. For the most extreme light ratios (top row), even with "correct" input parameters, the disentangler struggles to recover the correct spectrum of the secondary. The optimiser also has difficulties recovering the correct spectrum in the higher-mass case, owing to the wide lines found in hot stars.

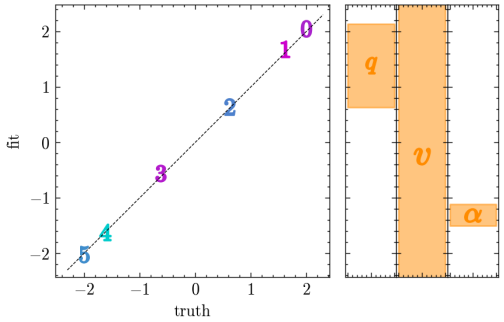

Figure 2.9: Formal disentangling results for a simulated SB1 system (dark companion), analogous to figure 2.5. The single-epoch velocities of the luminous component are well-determined. The parameters v_{COM} and q are ill-determined (because there is no second spectrum); the 1 σ range for one noise-realization is shown by the orange bands in the right panels. The value for α in such cases (implicitly an upper limit) is always found to be small.

Inevitably, the optimiser will find some v_{COM} and q, which must be spurious. And then it determines an α from the disentangled spectra that were computed using these v_{COM} and q. We would expect the secondary spectrum to be essentially noise, and the resulting α to be small, presumably an upper limit.

Figure 2.9 shows the results of the optimiser in one realization of this scenario. We see that the primary velocities are found near perfectly. In the right panels, we show the formal results for the three problematic parameters. As expected, the best-fit v_{COM} and q vary greatly among different noise-realizations of the mock data, after being initialized as before.

However, α is always found to be small. This can be traced back to the fact that the disentangled spectrum of the (non-existing) "secondary" is close to noise, as illustrated in Figure 2.10, which shows the disentangling results using the parameters as determined by the optimiser. The primary spectrum is of course recovered well. The computed secondary spectrum essentially appears to be noise, which then leads to the small recovered α.

This shows that our approach degenerates gracefully for an SB1 system towards an ill-defined v_{COM} and q, with high variance or uncertainty, and towards a small estimate of α. Further, inspection of the actual disentangled component spectra reveals a lack of features in the secondary, in line with the input of a zero secondary.

The physically most sensible upper limit on α in this scenario depends on the template and its spectral features, effectively $\alpha^{max}(T_{\rm eff}, v \sin i)$. If one has external priors e.g. on the temperature, this can be easily incorporated into the α^{max} estimate.

2.3.2. Sample Application: the "Unicorn" & "Giraffe"

The two systems, V723 Mon ("The Unicorn") & 2M04123153+6738486 ("The Giraffe"), present excellent examples of the power of disentangling compared to cross-correlation and other template-based methods. In an initial study, Jayasinghe et al. (2021) and Jayasinghe et al. (2022) had reported to have found SB1 binaries with a primary mass and orbital parameters requiring the secondary to be a dormant BH. Further study by El-Badry et al. (2022b) (hereafter E22) found that the authors of the first study had been led to incorrect inferences about the nature and mass of the primary, which then led to an incorrectly inferred

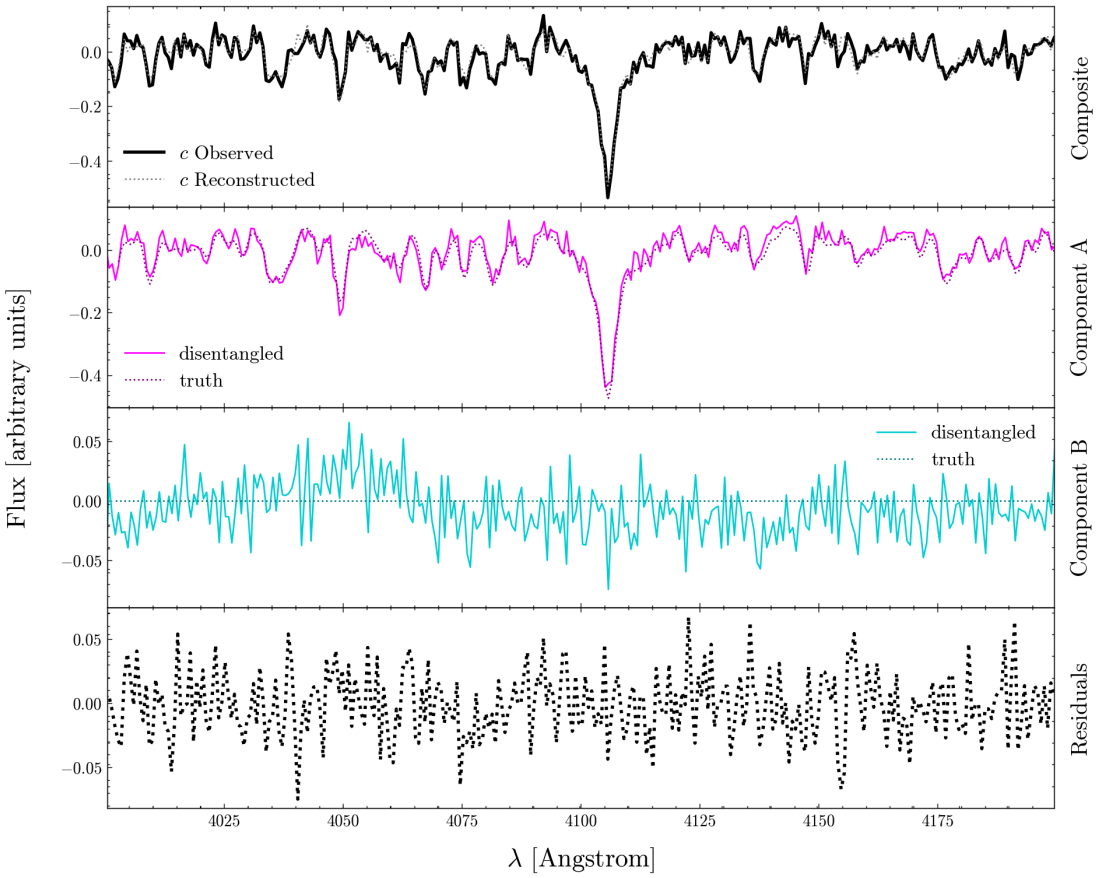

Figure 2.10: Formal disentangling result shown for one epoch for a simulated SB1 system, computed using the best-fit parameters found by the optimiser, analogous to figure 2.3. The spectrum of the primary is recovered, as it is the only luminous component in the system. The code also constructs of course a second component, which is close to just noise, as it should be for a dark secondary.

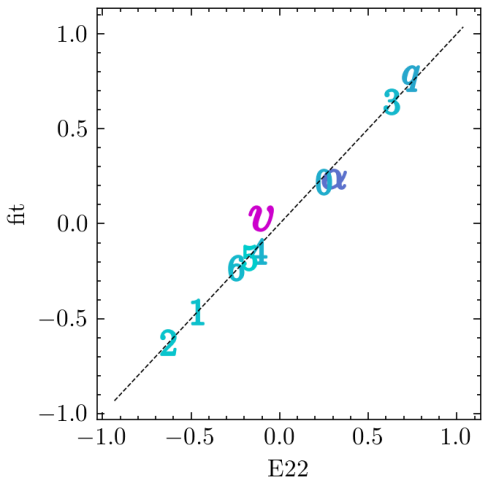

Figure 2.11: The parameters of the Unicorn as recovered by the optimiser (y-axis) compared to the ones found by E22 (x-axis). In the case of agreement, we expect the points for each parameter to lie on the grey, dashed, diagonal line.

a mass limit for the secondary. In E22, spectral disentangling revealed a non-degenerate stellar secondary in both cases. Both systems were products of previously occurring mass transfer (MT), leading to a stripped, luminous, but very low-mass primary "masquerading" as a much higher mass star, and a higher mass secondary. In the case of the Unicorn, the secondary had also been significantly spun up, smearing out its spectral lines.

Disentangling was able to reconstruct the component spectra and help identify the stars, but took significant attention to detail in the analysis, as well as prior knowledge of the velocities of the primary, and solid guesses about further system parameters.

In this work, we present "blind" disentangling of the Unicorn (with the Giraffe included in the Appendix), assuming no prior knowledge of the systems other than the assumption that they are binaries, and thus disentangling is expected to yield sensible results. We also explore the performance of the disentangler assuming the spectra had been more "large survey style", i.e. at lower resolution. We apply our method to the Unicorn here, as it is the more "complicated" of the two systems to identify, due to the very rapid rotation of the secondary.

Both in E22 and in this work, we use data from the Keck/HIRES spectrograph (Vogt et al., 1994) to identify the components of the systems. Natively, the data have resolution of $R \approx 60,000$, with 7 epochs for the Unicorn, and 8 for the Giraffe. The data cover a wavelength range from 3900 to 8000 Å, and have a typical S/N of 20 per pixel at 5000 Å. More details can be found in Jayasinghe et al. (2021) and Jayasinghe et al. (2022) for the Unicorn and Giraffe data, respectively.

Figure 2.11 shows how well the optimiser was able to recover the parameters of the Unicorn system at the native resolution of the data, $R \approx 60,000$. This was performed on the wavelength range from 5275 to 5370 Å, as this section contains enough lines to successfully disentangle while still being narrow enough for the assumption of a constant light ratio not to break down. We see the optimiser seems to recover the individual velocities of the primary very well, owing to the clear and dominant lines in the composite spectrum. It struggles slightly more with the systemic velocity, and light ratio, likely because of the very

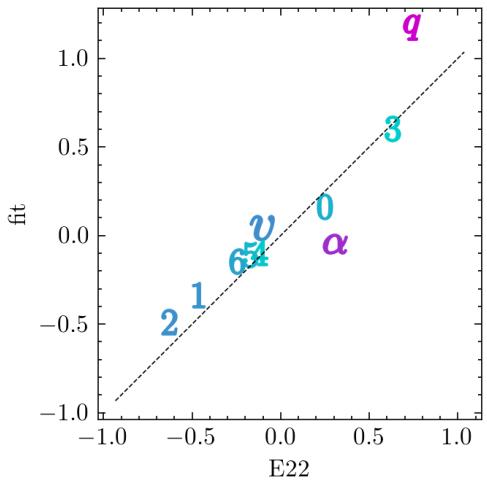

Figure 2.12: Analogous to Figure 2.11, with an artificially reduced resolution of $R \approx 2,000$.

rapid rotation and thus broadened lines of the secondary. Despite this, the light ratio is still found to an acceptable accuracy. This is likely due to a combination of the light ratio finder using both the primary and secondary spectra, and the set of templates used in the process containing non-rotating and rapidly rotating ($v \sin i = 100$ km/s) templates.

In contrast to this, we see Figure 2.12, which shows the performance of the optimiser for the same data, now artificially resampled to a lower resolution of $R \approx 2,000$. A larger wavelength window of 5200 to 5450 Åwas chosen here for disentangling to account for the more broadened and thus fewer lines. We see here that the RVs tend to be underestimated, with the disentangler finding generally smaller velocities than E22. This is unsurprising, as the lower resolution leads to broader CCF peaks, where eventually the peaks of the primary and secondary velocities are so broad that the secondary peak "drags" the primary down. Because of this underestimation in velocities and the broadened lines of the secondary, the optimiser also cannot correctly assess the mass ratio.

However, we do see that the optimiser has pushed q away from its initial starting guess of $\log(q) = 0$ towards higher values, meaning the data do tell us that the secondary is heavier than the primary, but struggles to perfectly determine how much heavier. As a consequence of this, the disentangled spectra are less accurate, also making it difficult to find the correct light ratio.

In Figure 2.13, we see the disentangled Unicorn spectra for the native resolution of $R \approx 60,000$, as well as the models from E22. Here, we see generally good agreement between the two, with one of the more apparent differences stemming from the slightly different light ratios between their work and this one. For example, we see that the E22 model for the secondary generally shows slightly "stronger" lines, i.e. a bigger difference between maxima and minima. There does not seem to be a significant offset along the wavelength axis, suggesting that the systemic velocity was recovered (mostly) accurately, at least to within the resolution limit.

Figure 2.14 shows the disentangling result for the $R \approx 2,000$ case, zoomed out more to cover a larger wavelength range than Figure 2.13. We elected to do this due to the "smearing out" at lower resolutions that removes many of the finer features and broadens the dominant lines. To still show a good number of features, a wider wavelength window is necessary.

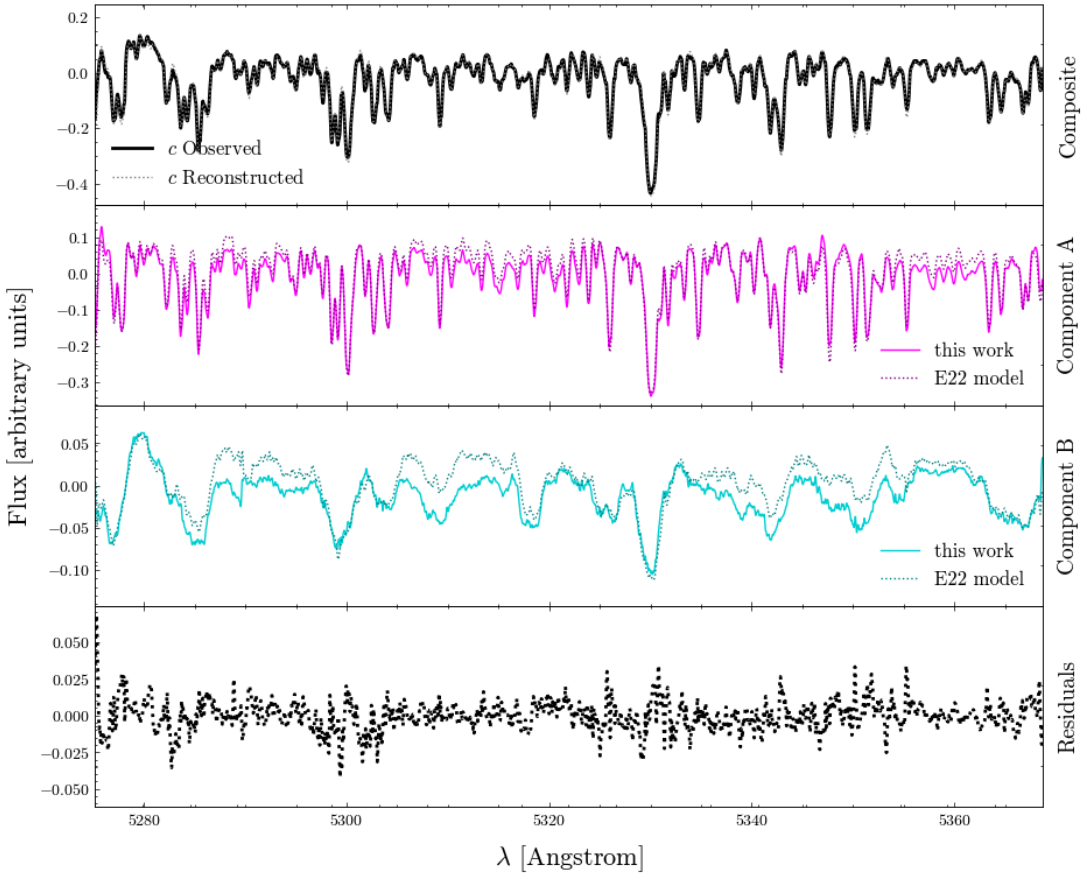

Figure 2.13: The results of the autonomous disentangling applied to the Unicorn for one epoch. The top panel shows the observed spectrum (black, solid line) as well as the reconstruction from the velocity shifted disentangled component spectra (grey, dashed line). The other two panels display the disentangled rest-frame solutions for the primary and secondary, respectively, in magenta and cyan. The dashed, darker lines in these two panels indicate the model spectrum found by E22 to most closely fit the disentangled solutions found there. The bottom panel shows the residual between the reconstructed and observed composite spectra. We see generally good agreement between the solutions from this work and E22 models.

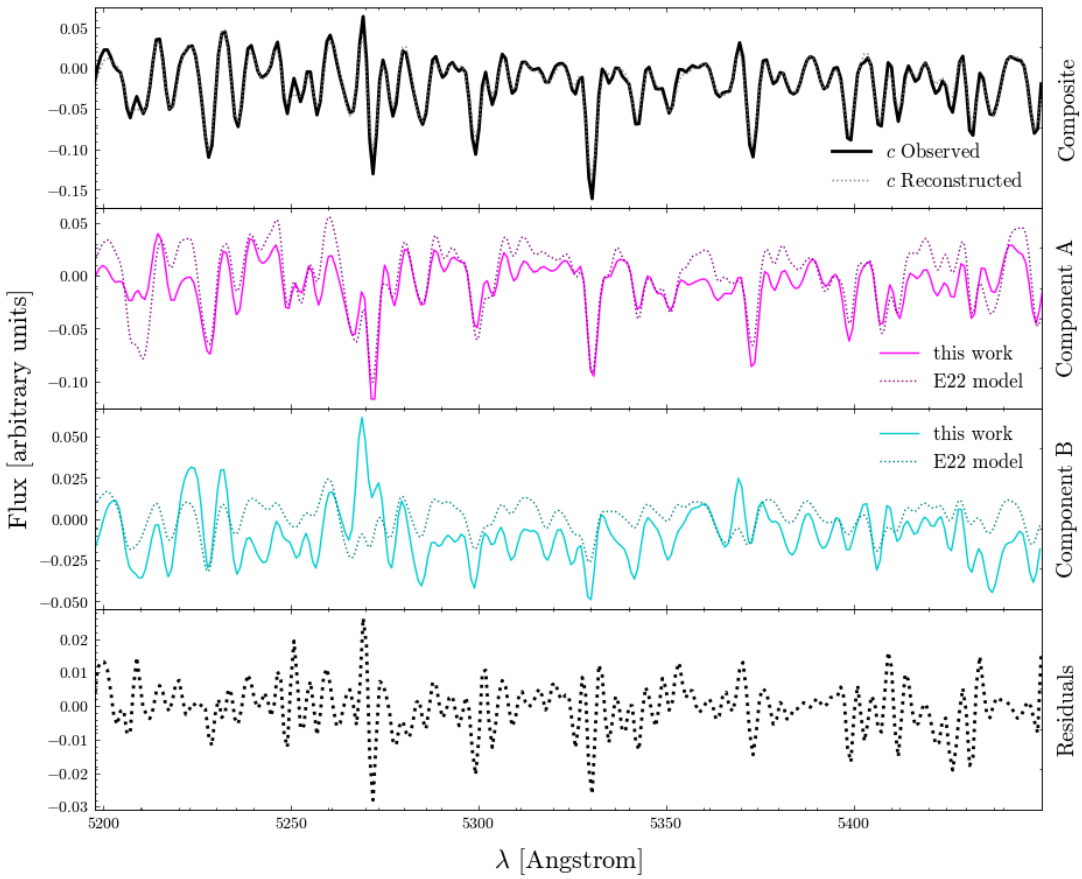

Figure 2.14: Analogous to Figure 2.13, with an artificially reduced resolution of $R \approx 2,000$.

Despite the underestimations of the velocities and mass ratio, the disentangled component spectra still resemble the (downsampled) models from E22. Many of the visible features are recovered, even though the underestimated velocities likely lead to some of the features of the primary being more "washed out". Similarly, these in conjunction with the incorrect q have an analogous effect on the recovered spectrum of the secondary. The issues with the light ratio then arise naturally as a consequence of the recovered spectra being more "smeared out" than the templates we are comparing to. Additionally, for larger wavelength window, the assumption of a constant light ratio across the spectrum holds less true, which is likely a contributing factor here.

2.4. Discussion and Summary

In this work, we have set out to implement spectral disentangling as described by Simon and Sturm (1994) and Hadrava (1995), among others, in an algorithm tailored for million-stars surveys. This meant adapting the process to be suitable for the regime of few epochs, modest S/N, and moderate resolution ($R \approx 2,000$). At the same time, we required the code to be robust in a range of scenarios (e.g. both hot and cool stars with a range of companions), as well as able to autonomously find the parameters necessary for the disentangling procedure precisely and accurately. Given the goal of applying it to large volumes of data, the code also needed to be fast.

Our approach has been to combine a number of known aspects and strategies to create an end-to-end autonomous pipeline that fulfills all of the above criteria, while consisting of a number of internal steps. We have implemented wavelength-space disentangling based on Simon and Sturm (1994); Tikhonov regularisation (Tikhonov, 1963; Phillips, 1962) to ensure smoothness of the disentangled spectra; downhill-simplex optimisation (Nelder and Mead, 1965) to optimise parameters; template cross-correlation and TIRAVEL (Zucker and Mazeh, 2006) to get initial velocity guesses; as well as template-based methods to find the systemic velocity and light ratio of the system, all in one. We have explored the efficacy of this process using a variety of synthetic SB2 spectra that emulate those provided by the large surveys we developed this pipeline for.

We have found overall satisfactory performance on our simulated systems, as well as a real-life example (the Unicorn), which had previously been misidentified (Jayasinghe et al., 2021), and required great care to analyse correctly (E22). We have shown that in the target regime of few epochs, modest S/N and moderate resolution, the algorithm can still recover the relevant system parameters and the component spectra for many of the systems explored. However, there are still areas of the parameterspace where our method fails or encounters issues:

- Extreme light ratio, relative to S/N. For light ratios below $\alpha \sim 0.1$, while the algorithm generally still recovers the primary and associated velocities correctly, the spectrum of the secondary is overwhelmed by the noise, and thus both the spectrum of the secondary and the mass ratio q cannot be determined correctly. In this case, the disentangler reacts similarly as if the system were an SB1, meaning we can set a light ratio "cut-off", below which we can no longer separate an SB1 from an SB2.

- Low velocity semi-amplitude, relative to resolution. If the velocity semi-amplitude (especially of the primary) falls close to or below the minimum resolvable velocity, the

first step of the optimisation, finding starting guesses for the velocities of the primary, fails, and subsequent steps cannot rectify the issue. Here, the majority of parameters are determined incorrectly, and thus the disentangled spectra are also spurious.

- Equal-mass binaries. For systems where the primary and secondary are of equal mass, or close to it, the associated spectra look too similar, introducing an ambiguity as to which set of lines belongs to which object at which epoch. In this case, the velocities for the primary and secondary are degenerate for any one epoch (as the method cannot tell "which is which"), causing further issues with the disentangler. One method to rectify this might be to invoke orbital fitting, however this would only be possible in the regime of sufficient epochs. Careful, individual treatment of these systems might provide another path to a successful solution, but goes against the spirit of this work, and autonomy of the process. However, despite the issues with finding the correct parameters, the disentangled spectra often still resemble the truth quite well. This is because a simple switch of the velocities in the matrix solver step simply means that the spectra are swapped for the affected epoch. If the spectra are the same or very similar, this has only a minor effect on the disentangling result.

- Hot stars. Due to the relatively few and broad lines of hot stars compared to cooler stars, the disentangler encounters more issues for these objects. The broader lines lead to a less precise determination of radial velocities, which creates problems when trying to find the mass ratio, spectra, and other parameters. In many cases, the disentangler does still arrive at a satisfactory solution, but less consistently than for a similar system in terms of light ratio and velocity semi-amplitude but with a cooler primary.

One of the novelties of this work is the inclusion of Tikhonov regularisation (Tikhonov, 1963; Phillips, 1962) to ensure that spectra are smooth. This process allows us to remove much of the high-frequency noise from the solution, much like a truncated SVD would, but it is independent of the solver method employed and allows us to use fast, iterative algorithms to solve for the spectra while retaining desired characteristics. It also does not enforce physical constraints on the solutions, allowing a great deal of "freedom" when determining the component spectra.

An important aspect of survey disentangling is the sheer volume of data to be processed, which requires short optimisation times for any one object and consistent optimisation. We have parallelised the code using Python's `multiprocessing` library. On 72 CPUs, the computation of the parameters and spectra of 120 simulated systems (2 masses, 2 resolution regimes, 5 different light ratios, and 6 different velocity semi-amplitudes, see section 2.3.1 for details) took about 3 minutes. This includes running each system through the optimiser 6 times (once for each epoch that is removed from the data) for bootstrapping. As the systems are all independent of each other, the process scales without much difficulty to larger clusters with more cores. This bodes well for the application to even a million stellar systems.

The examples provided in this work have demonstrated that even in the regime of few epochs, moderate resolution, and signal-to-noise ratio, disentangling poses a very viable option for analyzing spectroscopic binaries. This, as well as the fast runtime of the algorithm, allows disentangling to be performed on large surveys, such as LAMOST (Cui et al., 2012) and SDSS-V (York et al., 2000). The SDSS-V catalog will contain multi-epoch spectra of $\sim 380,000$ OBA stars, which are predicted (Sana et al., 2012; Moe and Di Stefano, 2017) to have a high multiple fraction, making them great candidates for disentangling. Thus, the

method developed here will allow us to weed out contaminants in our continued search for dark companions, and select ideal targets for higher-resolution, better-S/N and more-epoch follow up investigation.

Acknowledgements RS and HWR acknowledge the European Research Council for support from the ERC Advanced Grant ERC-2021-ADG101054731.

We thank Tsevi Mazeh, Silvia Almada Monter, Johanna Müller-Horn and Jaime Villaseñor for stimulating and helpful discussion.

We also thank Tomer Shenar for insightful and constructive comments on the manuscript.

This publication made extensive use of the online authoring Overleaf platform (`https://www.overleaf.com/`).

The data processing and analysis made use of `matplotlib` (Hunter, 2007), `NumPy` (Harris et al., 2020), the `IPython` package (Perez and Granger, 2007), `SciPy` (Virtanen et al., 2020), `AstroPy` (The Astropy Collaboration et al., 2013, 2018, 2022) `SpectRes` (Carnall, 2017) and `SpectResC` (Lam, 2023)

3

The Physical Properties of Post Mass Transfer Binaries

Authors Rhys Seeburger, Hans-Walter Rix, Kareem El-Badry, Johanna Müller-Horn, Alexander Dimoff, Jan Henneco, Jaime Villaseñor

Chapter info This chapter is a reproduction of a paper currently under review at *Astronomy and Astrophysics*. It details the analysis of a set of (post) interaction binaries using multi-epoch spectroscopic data gathered with the FEROS instrument at the MPG 2.2 m telescope in La Silla. I am the lead author of the paper and produced the majority of the text and figures and also wrote the original observing proposal which led to the data being gathered. The disentangling algorithm used in the paper was developed by me and is described in Chapter 2. I performed the analysis of the data and interpretation of the results. Kareem El-Badry and Hans-Walter Rix were my advisors for this project. Kareem El-Badry was also the original lead author of El-Badry and Rix (2022), and suggested these targets for closer study based on his findings. Both gave crucial input on the interpretation of the findings and suggested potential avenues to explore with the data. Johanna Müller-Horn performed the orbital fitting based on the radial velocities and wrote the relevant section detailing the process. Alexander Dimoff provided input on best practices when performing spectral classification. Jan Henneco helped with interpretation of the MT process, as well as MESA model execution and interpretation, much of which was removed from the final manuscript. Jaime Villaseñor helped with analysis of the spectra. All co-Authors provided helpful comments and suggestions on the manuscript.

Note: In the context of this chapter, we refer to the flux ratio (named α in chapter 2) as a. This is to avoid confusion with the α mass-loss channel from Soberman et al. (1997).

Abstract We present and analyze the detailed physical properties of six binary stellar systems, originally proposed as possible star – BH binaries on the basis of Gaia DR3 radial velocities, but soon recognized as likely post MT binary systems with stripped companions.

We used multi-epoch high-resolution FEROS spectra and spectral disentangling to derive $T_{\rm eff}$, R_*, $v \sin i$ for both components in all systems, along with the mass ratio q and the components' flux ratio as a function of wavelength.

From this analysis we confirm our previous conclusion, that all systems have two luminous stars that have experienced MT, with a hotter A-type ($\sim$ 9000 K) rapidly rotating accretor and a cooler ($\sim$ 5000 K), $\sim 5\times$ less massive, but luminous donor. Five of the systems show no trace of any emission lines implying that there is no current MT, consistent with our inferred $R_* < R_{\rm RL}$. The systems may have reached their current state plausibly through MT, unless it was highly non-conservative. While the accretor components rotate rapidly, they rotate well below $v_{\rm crit}$, even though there must have been enough MT to spin them up to $v_{\rm crit}$, according to conventional models. As neither magnetic braking nor tidal synchronisation should have been effective in spinning down the stars, our results point to one of the postulated regimes, where mass accretion does not increase the accretors' angular momentum to their critical values.

3.1. Introduction

Most massive stars and an appreciable fraction of lower-mass stars are born in binaries (Moe and Di Stefano, 2017). The initially more massive star evolves first and expands, potentially leading to MT towards its companion. Such MT can fundamentally alter both components and the whole configuration of the system: the donor loses most of its envelope and becomes a low-mass stripped star, while the accretor gains mass and is spun up by the angular momentum of the accreted material (Packet, 1981). The outcome of this interaction depends critically on the initial orbital period, component masses, and the efficiency with which mass and angular momentum are accreted by the mass gainer (Packet, 1981; Soberman et al., 1997).

For a brief period, the low-mass stripped star can become very luminous, outshining its far more massive (accretor) companion star in the binary. During this phase, the high orbital velocities of this luminous star and the lack of obvious evidence of a secondary star due to rotationally broadened spectral lines, can make these systems appear as black-hole binary "impostor" systems (Shenar et al., 2020; Bodensteiner et al., 2020; El-Badry et al., 2022a; El-Badry and Burdge, 2022; El-Badry et al., 2022b). Immediately after the *Gaia* DR3 data release (Gaia Collaboration et al., 2021), El-Badry and Rix (2022) (henceforth EB+22) analysed a sample of *Gaia* DR3 binaries initially flagged as possible BH hosts based on their high mass functions. By modelling their SEDs and light curves, they showed that these systems were actually systems containing a stripped donor star and a MS accretor.

These systems, containing a relatively hot ($\sim$ 9000 K) accretor and a cooler ($\sim$ 5000 K), less massive but luminous donor, represent an important stage in binary stellar evolution. When seen edge-on, they may appear as Algol-type variables, where, initially paradoxically, the less massive component is the more luminous of the two (Kopal, 1955). This is due to previous MT in the system, which reversed the mass ratio (Kippenhahn and Weigert, 1967). While the basic physical picture of how such systems form through MT is understood, many aspects remain poorly constrained empirically. In particular, the conservativeness of MT (how much mass is retained in the binary versus lost to the interstellar medium), the mechanisms governing stellar spin during and after MT, and the detailed physical properties of stripped donor stars constitute some of the biggest uncertainties in binary evolution while tremendously affecting the outcome of binary evolution models. The donor stars in these systems are particularly interesting as they represent a rarely observed intermediate stage between normal giants and low-mass white dwarfs (Götberg et al., 2018).

Here, we present a detailed spectroscopic follow-up study of six systems from the sample of 14 objects identified by EB+22. Using multi-epoch high-resolution FEROS spectra and spectral disentangling, we derive fundamental parameters (effective temperature $T_{\rm eff}$, stellar radius R_*, and projected rotational velocity $v \sin i$) for both components, along with mass ratios, q and wavelength-dependent component flux ratios.

This allows us to constrain the current physical state of these systems and probe their MT history. Compared to the work of El-Badry and Rix (2022), our analysis provides not only spectroscoppic stellar parameters but also clarifies whether determining MT is still ongoing, how conservative the MT must have been, and how much rotation the accretor exhibits.

3.2. Observations and Data Modelling

3.2.1. FEROS observations

We acquired multi-epoch spectroscopic data using the FEROS (Fiber-fed Extended Range Optical Spectrograph) instrument at the 2.2m telescope at La Silla, ESO (Kaufer et al., 1999). During our observation period (ESO period P114), six of the 14 targets presented in EB+22 were visible, listed in Table 3.1. For brevity, we will henceforth refer to them in the text by their first 4 numbers only (i.e. *Gaia* 2933630927108779776 is G-2933) . We observed each target ∼10 times with a nightly cadence. As all targets have orbital periods of ∼10 to 20 days, this cadence provides good coverage of the RV dynamical range. While fewer epochs can suffice (with a theoretical minimum of 3 for disentangling (Simon and Sturm, 1994)), more epochs lead to better constraints on the disentangled spectra and are therefore desirable. We used exposure times of 20-30 min to reach a signal-to-noise ratio (S/N) of about 50 near the Hβ line, depending on the G-band magnitude as reported by *Gaia* (see Table B.1 in the Appendix).

FEROS is well suited to this kind of analysis, as it provides a resolution of R ∼48,000 over a wavelength range from ∼3500 Åto ∼9200 Å, which includes the most important Balmer lines, relevant for our analysis of the hotter accretor, as well as many metal lines. Although a lower resolution would not be a limiting factor for disentangling (see Seeburger et al. (2024)), higher resolution allows for a more precise determination of the RVs and thus better constraints on the binary orbit.

3.2.2. Spectral Disentangling

In this work we make extensive use of the spectral disentangling pipeline described in Seeburger et al. (2024), based on Simon and Sturm (1994). Spectral disentangling is a data-driven method that seeks to decompose multi-epoch observational spectra of a multiple system into the individual component spectra. By assuming that the component spectra are time invariant in their shape and only change by being red- and blue-shifted, one can construct a matrix that, when multiplied by the two component spectra, will reconstruct the observations at each epoch. The values of the matrix elements are determined by the RVs of each component at each epoch. This can be simplified by first determining the primary velocities and the mass ratio of the system, and then computing the secondary velocities from these (see section 2.5 in Seeburger et al. (2024) for details).

Seeburger et al. (2024) combine this linear algebra problem with a nonlinear optimization step. At each step of the optimizer, a vector of primary RVs and a mass ratio is proposed, the spectra are disentangled, and the residuals between the multi-epoch observations and reconstruction are computed. This residual is taken to be a metric of fit, and sought to be minimised by the optimizer, in theory returning the parameter set for which the algorithm could most accurately decompose the spectra, as well as the best-fit component spectra.

The strength of disentangling compared to template-based methods lies in its flexibility. No physical information enters into the matrix-solving stage, meaning the disentangled spectra are essentially just vectors which best reconstruct the observations, with no constraints on, for example, which spectral lines exist or how they should present themselves. Thus, it is an ideal method for systems with non-standard spectra (rapid rotation, stripped stars, etc), such as the ones presented in this work.

3.2.3. Orbital fitting

Once the RVs have been recovered by the disentangling algorithm, they can be used to determine the orbital parameters of the system.

Similar to Müller-Horn et al. (2024), we used a nested sampling framework and the UltraNest package (Buchner, 2021) to estimate posterior probability distributions for the orbital parameters. The RV curve is described by six parameters: $(K, P, M_0, e, \omega, v_{\rm COM})$. K represents the RV semi-amplitude of the visible star, P is the orbital period, and $M_0 = \frac{2\pi t_0}{P}$ defines the mean anomaly at a reference time t_0. The parameters e and ω correspond to the orbital eccentricity and argument of pericenter, while $v_{\rm COM}$ denotes the system's barycentric velocity. Uniform, non-informative prior distributions were adopted for all parameters, with prior ranges set as follows: $K \in [0, 500]$ km/s, $P \in [1, 100]$ d, $M_0, \omega \in [0, 2\pi]$ $e \in [0.0, 0.9]$, and $v_{\rm COM} \in [-100, 100]$ km/s.

With the period from the orbital fit (c.f. with EB+22 and *Gaia* in Table B.1, and the mass ratio from the disentangling, we can then estimate the MT history of the system. We use equations from Soberman et al. (1997), which relate the period and mass ratio in an MT system subject to the MT parameters α, β and δ. Here, the parameters describe the fraction of the transferred mass lost via various channels: $\alpha = \frac{\partial m_{\rm wind}}{\partial m_{\rm don}}$ is the fraction lost via a wind from the donor, $\beta = \frac{\partial m_{\rm iso-r}}{\partial m_{\rm don}}$ is the fraction ejected from the accretor, and δ is the fraction retained in a circumbinary ring. Here, $\partial m_{\rm wind}$ is the mass of stellar wind from the donor, and $\partial m_{\rm iso-r}$ the mass of stellar wind from the accretor (isotropic re-emission). $\partial m_{\rm don}$ is the mass lost from the donor. If all these parameters are set to 0, MT is fully conservative, i.e. no mass is lost and 100% of the mass donated by the donor is accreted by the accretor. If these parameters add up to 1, then MT is fully non-conservative, meaning all mass ejected by the donor is lost to the surrounding medium; the accretor does not successfully accrete any of it. Functionally, the relative values of α, β, and δ determine the amount of angular momentum carried away by the matter lost from the system, and thus the extent to which the orbit widens or tightens.

For simplicity, we assume $\alpha = \delta = 0$, meaning no mass is lost to the interstellar medium from the donor or a circumbinary ring. This scenario is commonly referred to as isotropic re-emission. By varying β, we can explore a number of MT conservativeness scenarios, particularly the evolution of the period with the changing mass ratio. Further, we can set a minimum period P_{min}, which is where the donor will overflow its Roche Lobe (RL) on the

MS Eggleton (1983). The argument here is that we assume the binary was detached at some point in its evolution. If the MT was too non-conservative (i.e. too much mass loss), the past orbit would have been too tight, and the donor would not have fit. For an in-depth analysis of binary contact tracing, see Henneco et al. (2024).

3.2.4. Determining stellar parameters from spectra

Applying the Seeburger et al. (2024) pipeline requires a number of consecutive steps.

3.2.4.0.1 Data preparation First, we acquire and reduce the data for each system and each epoch using the `ceres` pipeline (Brahm et al., 2017), and subsequently normalise the observed spectra with a running median filter. Additionally, we create a set of template spectra by normalising and resampling Coelho (2014) model spectra in the relevant temperature, metallicity and log$g$ ranges onto the same wavelength grid as the FEROS data. The spectra are computed assuming local thermal equilibrium and spaced in intervals of 250 K ($T_{\rm eff}$), and 0.5 (log$g$). Here, we consider temperatures from 4000 K to 11000 K, and surface gravities from 2 to 4. We assume solar metallicity and apply rotational broadening with the `RotBroadInt` package by Carvalho and Johns-Krull (2023) from 0 km/s to 300 km/s.

3.2.4.0.2 Determining RVs We compute initial guesses for the primary RVs by cross-correlating the observed spectra with our templates. Then, we iteratively optimise the primary velocities and mass ratio by proposing a set of candidate parameters, disentangling and computing the residual for that set, seeking to minimize the residual. We have found the region around Hβ to be optimal for this, as both spectra contribute similarly to the flux ratio, and there are sufficient features in both components to perform the disentangling. This is particularly important for the accretor, which is hot and has only a few lines.

3.2.4.0.3 Finding best-fit templates Next, we fix the velocities and mass ratio to their best-fit values, and perform the disentangling around the red end of the spectrum, where the cooler donor dominates the flux, allowing us to fit a template to the disentangled donor spectrum. We do so by considering the template spectra described above, at all available effective temperatures and surface gravities, but only a selection of rotational velocities, as these are determined in a subsequent step. We scale each template by a set of different light ratios between 0.01 and 100, and perform a least squares fit with the distentangled donor spectrum. We repeat the same procedure in the blue for the hotter accretor. This provides the effective temperatures and surface gravities of each component from the corresponding best-fit template. Additionally, by disentangling around the Mg II line at 4481 Å, we can determine the rotational velocity of the accretor, crucial to understanding the spin-up and/or spin-down that has occurred during MT. We achieve this by selecting the best-fit template in terms of $T_{\rm eff}$ and log$g$ from the previous step (where we considered only a handful of potential rotational velocities), and consider all rotationally broadened instances thereof, subsequently determining the best-fit rotational velocity via a least-squares fit of the disentangled spectra and broadened templates. We prefer Mg II over one of the (deeper) Balmer lines, as the shape of the Balmer lines is predominantly set by the stellar temperature and surface gravity, and rotation only has a comparatively small effect.

3.2.4.0.4 Applying TODCOR for an independent mass ratio estimation Using the best-fit templates for each component, we use the TODCOR algorithm (Zucker and Mazeh, 1994), a two-dimensional cross-correlation method, to determine the velocities of the two components for each epoch. The primary and secondary velocity at each epoch are chosen such that they maximise the value of the 2D cross-correlation of the light ratio scaled templates with the observed spectrum at that epoch. The primary and secondary velocity are related by $v_B = v_{\rm COM} + \frac{v_{\rm COM} - v_A}{q}$, where $v_{\rm COM}$ is the centre-of-mass velocity. We see that they should lie along a straight line in the $v_B - v_A$ plane, with slope $-\frac{1}{q}$ and intercept $v_{\rm COM} + \frac{v_{\rm COM}}{q}$. We fit this straight line using scipy's `curve_fit` and derive the desired quantities. `curve_fit` also returns the covariance matrix, which allows us to determine the error on the parameters. Thus, TODCOR provides an independent measurement of the mass ratio and centre-of-mass velocity from the individual epoch velocities.

3.2.4.0.5 Finding the light ratio as a function of wavelength Finally, we apply the disentangling method to the whole spectral range, subsequently splitting up the disentangled components into 20 wavelength windows. For each window, we scale the donor and accretor templates by a factor $\frac{1}{1+a}$ and $\frac{a}{1+a}$ respectively, computing the best fit via least-squares minimisation between the disentangled spectra and the respective scaled templates. This allows us to determine the optimal light ratio $a = \frac{f_{\rm accretor}}{f_{\rm donor}}$, and, trivially, the relative light contribution of the donor $l_d = \frac{f_{\rm donor}}{f_{\rm total}}$ for the window in question. Using this method, we get a piecewise approximation of the light ratio as a function of wavelength, which subsequently will provide an additional constraint in our SED fits.

3.2.5. SED fitting

SED fits were initially used by EB+22 to identify the systems studied here as potential SB2s, without priors on the stellar parameters from spectroscopy. We follow a similar method as the original authors. We acquire photometry for each target from WISE, SkyMapper, APASS, GALEX and 2MASS, covering a wide wavelength range. We simulate synthetic spectra with `pystellib` and create mock photometry using `pyphot` (Fouesneau, 2024). We perform dust attenuation using the `dustmaps` package (Green, 2018) with the 3D dustmap from Edenhofer et al. (2024). Then, using `emcee` (Foreman-Mackey et al., 2013), we determine the best set of parameters for each component of the SED to reconstruct the observed photometry. Here, we hold the effective temperatures fixed to the values acquired from the spectroscopy and set the surface gravities to the values inferred by EB+22. We place a Gaussian prior on the parallax based on the *Gaia* DR3 parallax and its error, and a flat prior on the radii for both components. Thus, we perform a three-parameter fit: the parallax, radius of the donor and radius of the accretor. As an additional constraint, we compute the flux ratio of the two simulated components and introduce an additional term to the likelihood function based on the agreement between our spectroscopic flux ratio determined in a previous step, and the flux ratio of the model spectra in the wavelength range covered by the FEROS observations. As this is a noisy estimate we down-weigh this constraint relative to the photometry. Our full likelihood function is then:

$$\mathcal{L} = -0.5 \cdot \left(\frac{f_{\rm model} - f_{\rm data}}{f_{\rm error}} \right)^2 - 0.5 \cdot w \cdot \log_{10} \left(\frac{\mathrm{l}_{\rm d,model} - \mathrm{l}_{\rm d,data}}{\ln(10)} \right)^2$$

.

Here, $f_{\rm model}$ is the mock photometry, while $f_{\rm data}$ the observations in the various passbands, and $f_{\rm error}$ their associated errors. $l_{d,\rm model}$ is the ratio $\frac{f_{\rm donor}}{f_{\rm total}}$ in the simulated model fluxes, and $l_{d,\rm data}$ the relative light contribution of the donor as a function of wavelength determined in section 3.2.4. The weight w is chosen to ensure the flux ratio term does not dominate the likelihood function.

3.3. Results

We present the face-value observational results for our sample in this section, with a discussion of their implication for the physical state and history of these systems in the subsequent Section 3.4.

The basic result of our analysis are the disentangled spectra for all six systems, following the approach described above. These disentangled spectra are shown in Figure 3.1, for the Mg II wavelength region, where, in all six systems, both components show prominent features. For each of the six panels, the top displays the total spectrum at one epoch, the next two the two disentangled components, and the bottom panel shows the residuals. Figure 3.1 demonstrates that all systems yield well-defined and physically plausible disentangled solutions that leave only small systematic residuals. This immediately confirms that all these systems are indeed SB2 binary systems with two luminous components, as surmised by EB+22.

All panels of Figure 3.1 show that one disentangled component exhibits an abundance of narrow metal absorption lines, characteristic of cool stars. The other spectrum shows far fewer and much broader lines, indicative of a hotter and rapidly rotating star. Qualitatively, this is very much in line with the picture where the cool star is a low log$g$ donor, while the hotter star is the spun-up accretor. The nature of the hotter disentangled component is illustrated further in Figure 3.2 for one of the objects (G-2966): the Figure zooms in on four Balmer line sub-regions (α to δ), in addition to the Mg II region shown already in Figure 3.1: the Balmer lines are the dominant spectral features of the hotter component, indicative of A-type stars with $T_{\rm eff} \approx 10,000$ K. This Figure also illustrates that our sample stars have no Hβ emission (with the exception of G-2933, which shows emission in both Hβ and Hα) affirming expectations for systems currently not undergoing MT. Analogous figures for the other 5 targets are shown in Figure 3.2 in the Appendix.

Our disentangling also provides us with an estimate of the wavelength-dependent flux ratio of the two components. The donor spectrum's contribution to the total flux, $l_d(\lambda) = f_{\rm donor}/f_{\rm total}$ is shown for all objects in the bottom sub-panels of Figure 3.3 (red line). This Figure shows that in all cases the donor flux contribution increases strongly towards longer wavelengths, as expected from the much cooler temperature of the donor. This also explains why the disentangled donor spectra at short wavelengths in Figure 3.2 appear so noisy: the total spectrum at the bluest wavelengths is dominated by the accretor.

Our best fit templates in the disentangling provide an estimate of the component's effective temperature and projected rotation velocity. The strong wavelength dependence of the components' flux ratios suggests that we should determine the best donor template from the red end of the spectrum where it dominates, and the accretor template from the blue end of the spectrum where it dominates. Table 3.1 lists the best template temperatures and rotation velocities for both components. All donors show significant but moderate rotational velocities consistent with tidal synchronisation. The accretors rotate more rapidly, but in all cases

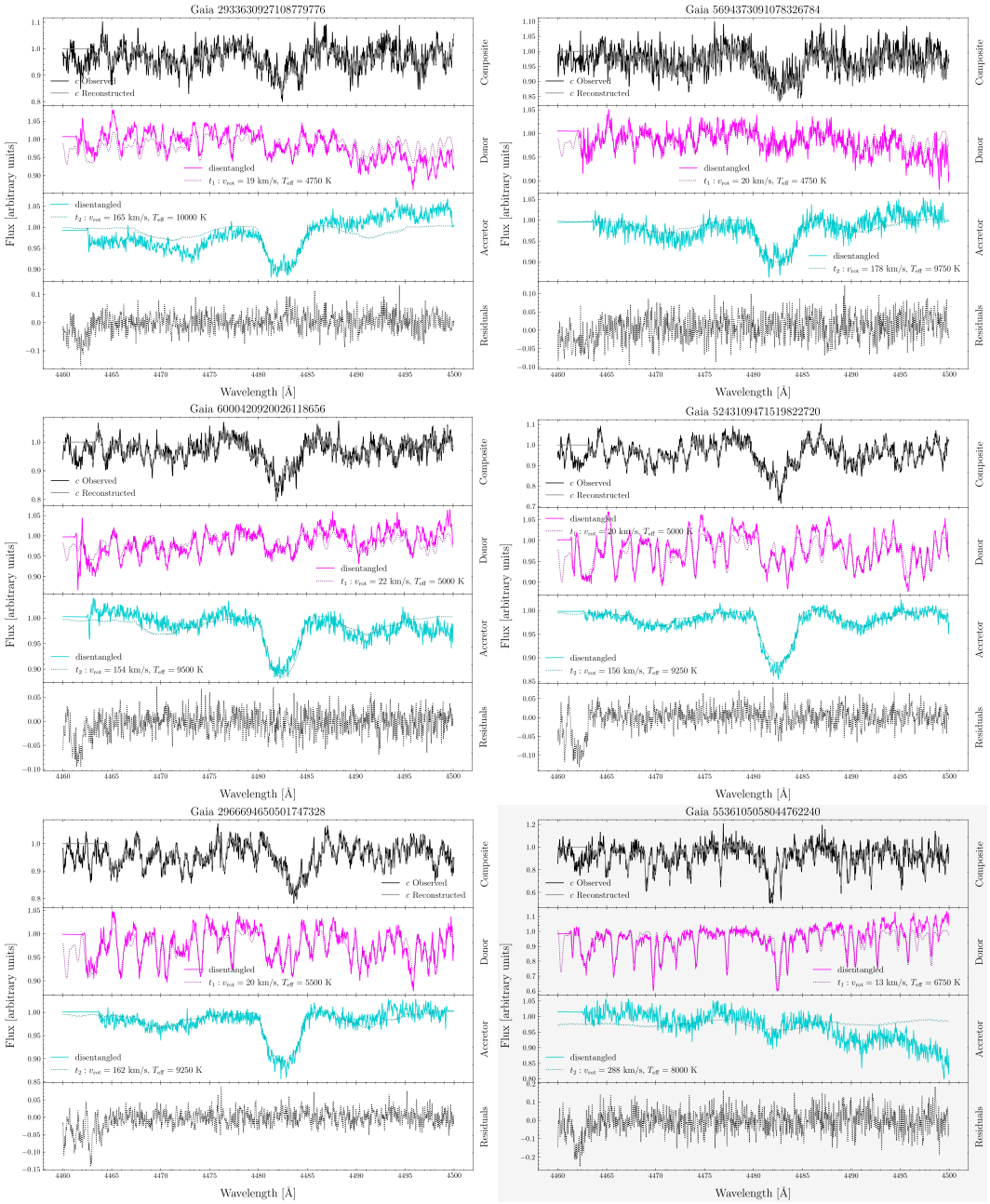

Figure 3.1: The observed spectra for one epoch (black, top row), the two disentangled components (cyan and magenta, middle row, shown in the rest frame), their sum (grey, top row, computed by shifting and co-adding), and the residual (bottom row) for the six targets of this study. We also show the best-fit template spectra for each disentangled component in the middle rows (dotted lines)

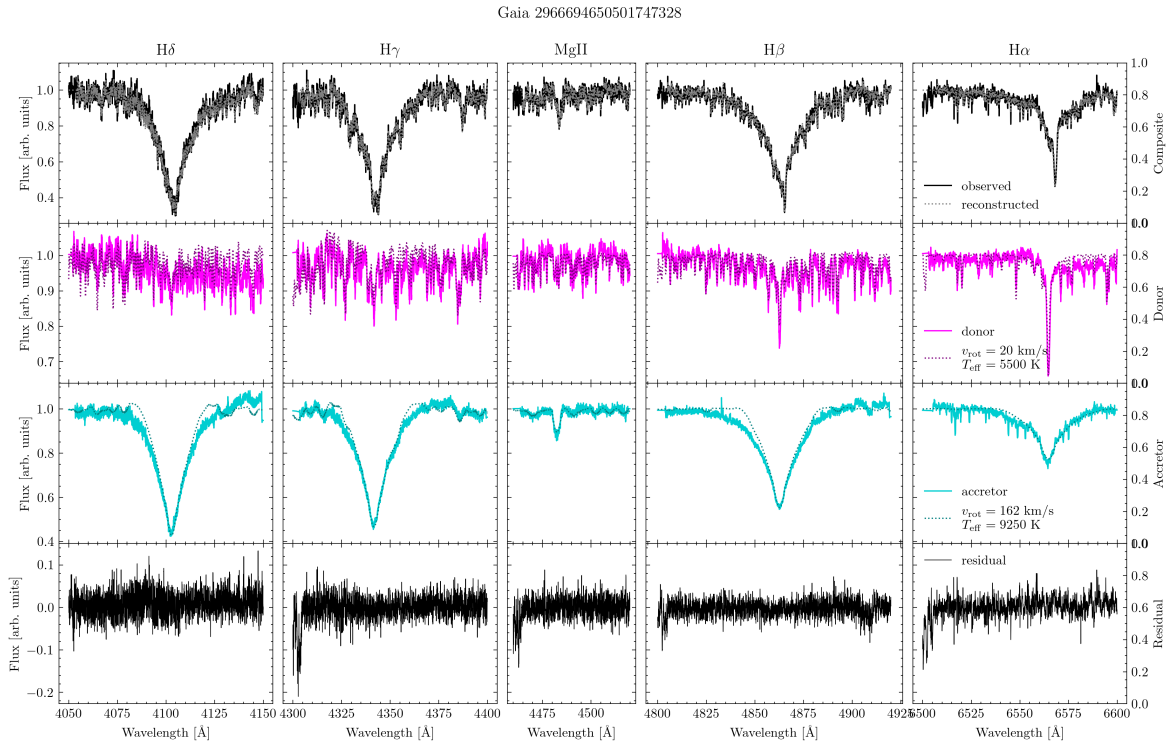

Figure 3.2: The observed spectra for one epoch (black, top row), the two disentangled components (cyan and magenta, middle row), their sum (grey, top row), and the residual (bottom row) for a number of different wavelength ranges. We also show the best-fit template spectra for each disentangled component in the middle rows (dotted lines). The windows here show the Balmer series and Mg II in the accretor, which is hot and has few lines. The apparently narrow lines visible in the accretor spectrum around Hα are tellurics, but show up here because of the small RVs of the accretor. For larger inter-epoch red- and blueshifts, these lines would get smeared/averaged out. Here, we only show the spectra for one object (G-2966), the rest can be found in Figure 3.2 in the Appendix.

well below critical rotation $v_{\rm crit} = \sqrt{\frac{G \cdot M_*}{R_*}}$, see section 3.4. We then use these best templates for the wavelength-dependent flux ratio, and for the velocity determinations (see below).

Gaia Source ID	$T_{\rm eff,\,don}$ [kK] EB+22	$T_{\rm eff,\,acc}$ [kK] EB+22	q EB+22	$T_{\rm eff,\,don}$ [kK] S+25	$T_{\rm eff,\,acc}$ [kK] S+25	$q_{\rm TODCOR}$ S+25	$v \sin i_{\rm don}$ [km/s] S+25	$v \sin i_{\rm acc}$ [km/s] S+25
Gaia 2933630927108779776	4.4 ± 0.2	9.7 ± 0.3	8.1 ± 1.4	4.75 ± 0.25	10.00 ± 0.25	5.7 ± 0.8	19 ± 1	165 ± 1
Gaia 5694373091078326784	4.6 ± 0.2	9.9 ± 0.3	8.8 ± 1.7	4.75 ± 0.25	9.75 ± 0.25	7.1 ± 1.1	20 ± 1	178 ± 1
Gaia 6000420920026118656	4.5 ± 0.2	9.5 ± 0.3	11.6 ± 2.1	5.00 ± 0.25	9.50 ± 0.25	5.4 ± 0.7	22 ± 1	154 ± 1
Gaia 5243109471519822720	4.6 ± 0.2	9.4 ± 0.3	7.1 ± 1.2	5.00 ± 0.25	9.25 ± 0.25	6.5 ± 1.1	20 ± 1	156 ± 1
Gaia 2966694650501747328	4.7 ± 0.1	9.4 ± 0.2	8.7 ± 1.2	5.50 ± 0.25	9.25 ± 0.25	6.7 ± 1.4	20 ± 1	162 ± 1
Gaia 5536105058044762240	4.9 ± 0.2	8.4 ± 0.3	8.3 ± 1.7	6.75 ± 0.25	8.00 ± 0.25	2.0 ± 0.5	13 ± 1	288 ± 1

Table 3.1: Table summarising the results of the spectral analysis for the donor (don) and accretor (acc) for each system from EB+22 and this work (S+25)

As part of the analysis we constrained the two components' velocities at all epochs using the TODCOR algorithm (see Section 3.2.4). We illustrate this for one of the objects (G-2966) in Figure 3.4, which shows the component velocities, estimated from a range of different wavelength windows. The velocity estimates for the cool, narrow-lined donor component (along the X-axis of Fig. 3.4) are consistent across wavelength windows with very small uncertainties. For the accretor, however, the velocity estimates vary substantially and are inconsistent across the different wavelength windows, even though their formal uncertainties are considerably larger than those of the donor velocities. Indeed, these (presumably also systematic) uncertainties make determination of the mass ratio – from the slope of the best-fit line – difficult for all objects. We discuss further in Section 3.4. Our best estimates of the dynamical mass ratios, q, are listed in Table 3.1.

In Figure 3.6 (top panels) we summarise information from the spectral fits (effective temperatures) and SEDs (stellar radii) in a Hertzsprung-Russel diagram (HRD). The positions of the components are also shown in the log$g$-$T_{\rm eff}$ and log(R)-$T_{\rm eff}$ planes (bottom panels). Here, log$g$ was determined not from our disentangled spectra, but by combining the masses from EB+22 with the radii from our SED fits.

3.4. Discussion

Taken together, our spectroscopic analysis shows and confirms that all these systems have all expected signatures of post MT binaries. Spectral disentangling reveals a cool, synchronously rotating donor and a hot, rapidly rotating accretor. The systems show no emission lines (except for object G-2933), indicating that there is no significant MT at present.

More quantitatively, our analysis provides four new pieces of information on each system: an independent measure of the temperatures $T_{\rm eff}$ from those computed by EB+22 from the two best-fitting templates, the wavelength-dependent flux ratio of both components, their projected rotation velocities $v \sin i$; and the kinematically determined mass ratio q.

We illustrate the first two aspects in Figure 3.3, where we overplot the observed photometry (lime dots) with the SEDs corresponding to our spectroscopic temperatures and radius estimates, both for the whole binary system (black) and for the individual components (magenta, cyan). The bottom sub-panel for each object shows the spectroscopically determined donor flux contribution (red), compared that implied by the two components' SED.

The SEDs with the parameters inferred by EB+22 are shown as dotted lines in the top sub-panels for each object. Comparing these spectroscopic constraints with the SED constraints from EB+22, shows broad consistency. For all objects we find spectroscopic donor temperatures that are slightly higher than those in EB+22. Similarly, four of the six accretors also show higher temperatures than those found by EB+22. It must be noted, however, the accretor temperatures lie in the regime of $T_{\rm eff} \approx 10000$ K where spectral LTE modelling (Coelho, 2014; Xiang et al., 2022), including ours, has difficulty matching the spectra, especially the very strong Balmer lines. The net effect of the smaller temperature difference among the components is a more gradual change in the component flux ratio with wavelength in our results, compared to EB+22.

Figure 3.3 shows that the SEDs *predicted* by our spectroscopic temperatures match the observed photometry almost as well as the SED *fits* in EB+22, after finding the best fitting

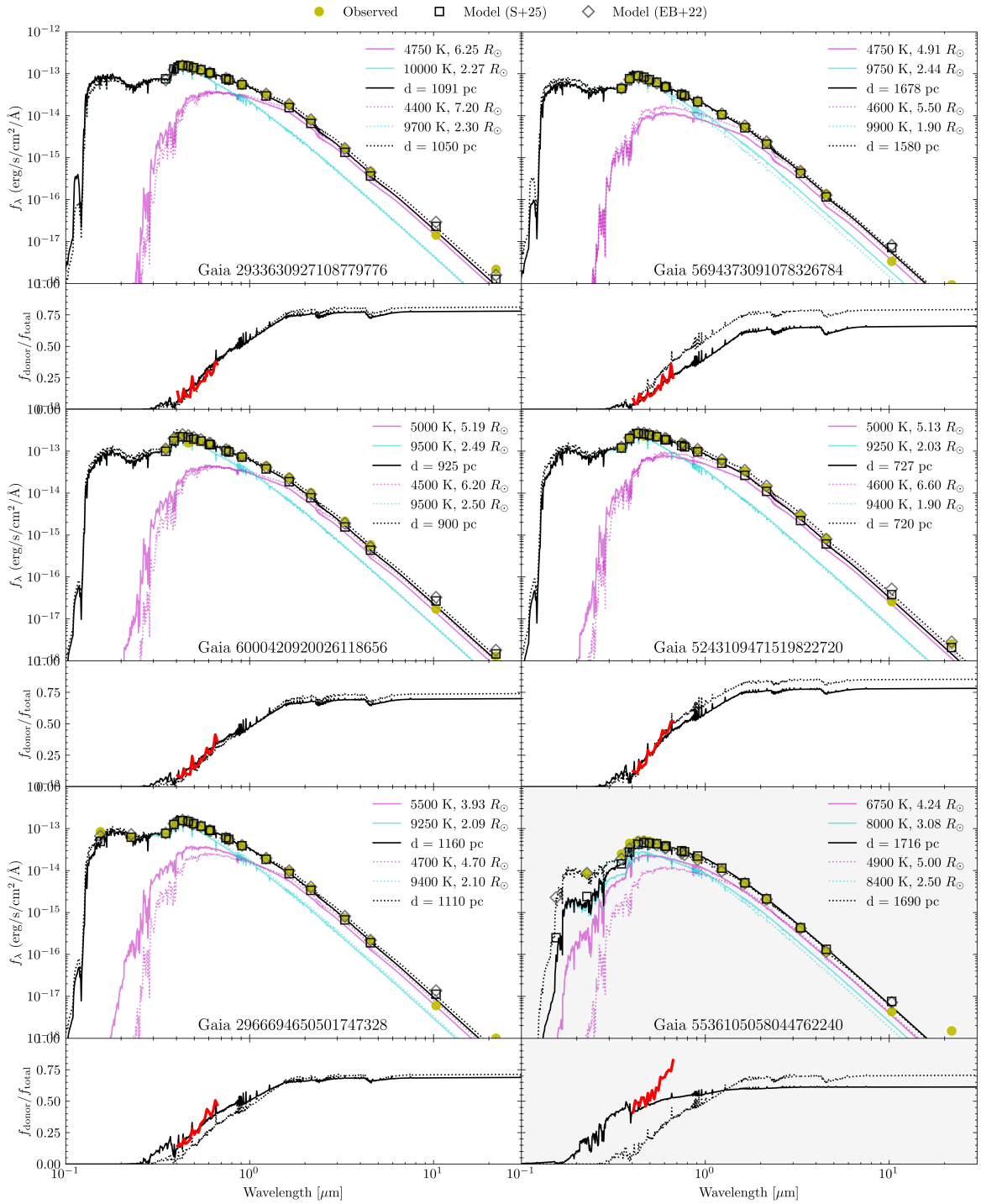

Figure 3.3: The SED fits and light ratio as a function of wavelength for each target. In the top plot of each set, we see the donor's (magenta) and accretor's (cyan) model SED, as well as their sum (black). Solid lines use stellar parameters from this work, and dotted lines the parameters derived in EB+22. We also overplot the observed photometry (lime dots), as well as the mock photometry from this work (black squares) and EB+22 (grey diamonds). The bottom panel shows the contribution of the donor to the total flux as a function of wavelength. Again, solid indicates this work, dotted EB+22. The red line shows the spectroscopic light ratio derived in this work, providing an additional constraint in the SED fitting process.

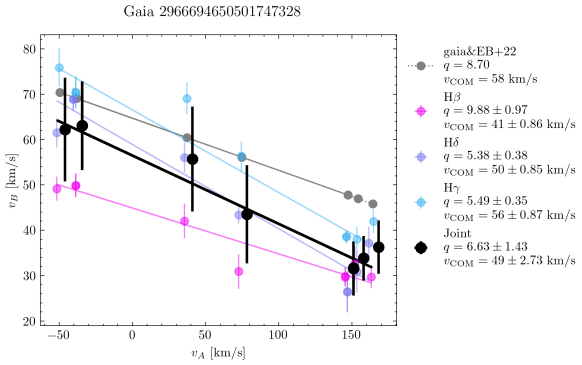

Figure 3.4: The results of the TODCOR algorithm applied to one object. RV of the donor and accretor are shown on the x- and y-axes respectively. Markers show the RVs of both components determined for each epoch with different methods and in various wavelength windows, with each marker displaying a different epoch. The lines indicate the linear best-fit to the RVs, as the relationship between donor and accretor RVs is linear. Grey shows the results using the donor RVs from `ceres` (Brahm et al., 2017), mass ratio from EB+22 and centre-of-mass velocity from *Gaia* . Coloured markers and lines show the results from TODCOR for a number of wavelength windows centered on different lines. Black shows the mean for each epoch velocity over the different wavelength windows. From the slope and intercept of the best fit line, the mass ratio and centre-of-mass velocity can be computed.

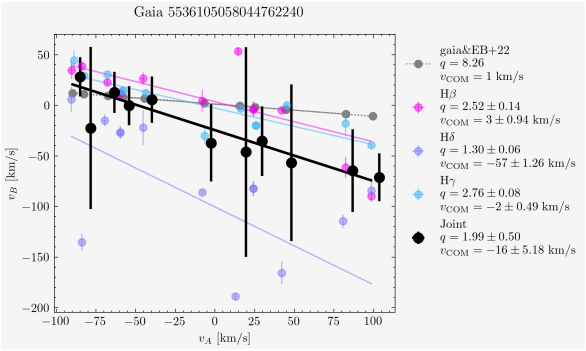

Figure 3.5: The results of the TODCOR algorithm applied to object G-5536. Colours and lines are the same as in figure 3.4. We see that while there is a big discrepancy between the mass ratio from TODCOR and the one found by EB+22, the quality of the linear fit with TODCOR is not good, calling this result into question.

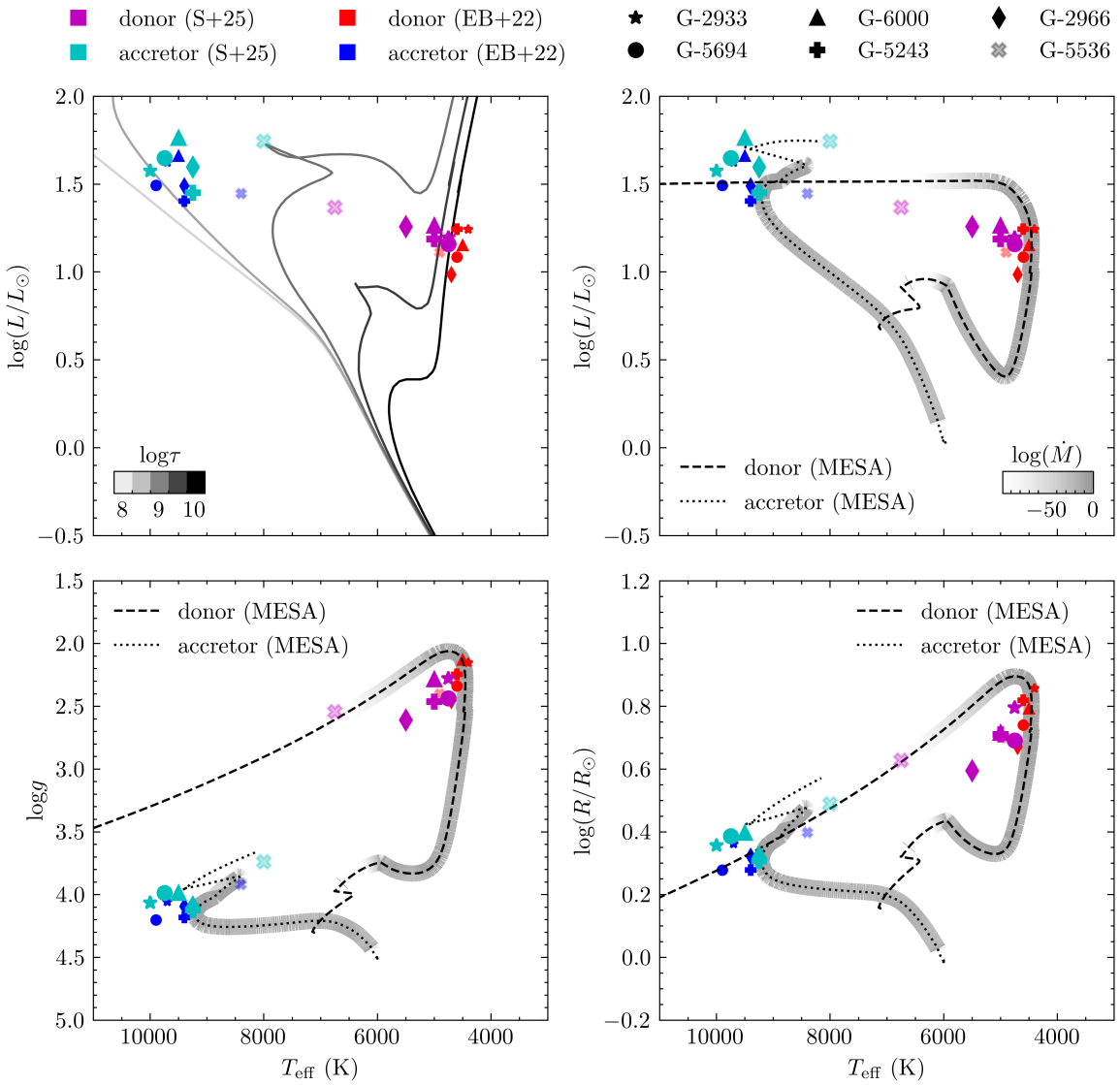

Figure 3.6: The parameters of both components of each system as determined in this work (S+25) and EB+22. Findings from S+25 are shown in magenta (donor) and cyan (accretor), while those from EB+22 are in red (donor) and blue (accretor). Different symbols have been chosen to represent the 6 different systems, with the problematic system (G-5536) shown as more transparent than the rest. The top left panel shows a HRD, including PARSEC isochrones spanning a range of ages (Bressan et al., 2012). The top right panel shows the same parameter space, but now possible MESA (Paxton et al., 2011, 2013, 2015, 2018, 2019; Jermyn et al., 2023) evolutionary paths for the donor (dashed line) and accretor (dotted line), computed by EB+22, have been included. The bottom two panels show log$g$ vs. $T_{\rm eff}$ and $log(R)$ vs, $T_{\rm eff}$ respectively, as well as including the aforementioned MESA tracks. The grey shading behind each line indicates the amount of MT in the MESA model at that evolutionary stage.

stellar radii. This presumably reflects the uncertainties and covariances inherent in multi-parameter photometry fits, which can be mitigated with our spectroscopic temperatures and component flux ratio estimates.

The HRD in Figure 3.6 (top panels) illustrates the nature of the systems, as well as the similarities and differences among them. We show our results (magenta and cyan symbols for the donor and accretor, respectively), and compare them to those from EB+22 (red and blue symbols for the donor and accretor, respectively). For context, we show single-star PARSEC isochrones (Bressan et al., 2012) of various ages in the top left panel and pertinent MESA (Paxton et al., 2011, 2013, 2015, 2018, 2019; Jermyn et al., 2023) stellar evolution tracks for the donor and accretor computed by EB+22 in the top right. Here, the MESA tracks assumed a binary with MS (before MT started) masses of 1.5 $M_\odot$ and 1.1 $M_\odot$ for the donor and accretor respectively. The initial period was assumed to be 1.3 days. Further details are described in EB+22. Analogously, we show the positions of all components in the log$g$-$T_{\rm eff}$ and $log(R)$-$T_{\rm eff}$ planes (bottom panels), along with the aforementioned MESA tracks.

Overall, we see qualitatively good agreement between the two works, with the exception of object G-5536. We also note that the accretors are consistent with much younger (single-star) isochrones than the donors, an expected outcome of MT onto the accretor and the resulting rejuvenation. Both sets of results are also roughly consistent with the fiducial MESA tracks, which we did not try to optimize for all the individual systems.

Note that our sample contains one system where all these analysis steps do not work as well (G-5536), starting with a poor spectral disentangling result (see Figure 3.3, which we attribute – at least in part – to the observations' lower signal-to-noise ratio. This is also encapsulated in the less-good fit of the model flux ratio (bottom panel, black line) to the observed spectroscopic flux ratio (red line).

We originally anticipated that our high-resolution multi-epoch spectra should enable tight constraints on the systems' mass ratio q. But using TODCOR (Zucker and Mazeh, 1994) with our best-fitting templates still faced serious difficulties, manifested for example as inconsistent velocity estimates when using different wavelength windows to derive them. We attribute this to several compounding factors: First, the accretors are rapidly rotating – which severely broadens their lines – and have few strong lines beyond the inherently broad Balmer series. Second, the spectra in some of our systems (especially object G-2933, showing an emission signature) are unusual. This may lead to rather imperfect template match, and in turn may cause systematic problems in TODCOR. This is exacerbated by the fact that the 5 – 10× more massive accretor has both far smaller velocity variations, and no sharp spectral lines. As the accretor contributes more at the shortest wavelengths, we deem the q-estimates based on Hγ and Hδ more reliable, compared to Hβ and certainly Hα. We also explored whether the Mg I and Mg II lines present in the accretor spectrum worked better, but found this not to be the case.

For most objects, our kinematic mass ratios are somewhat smaller than those in EB+22, consistent with our smaller temperature difference between the donor and accretor components.

For object G-5536, the mass ratio found here is close to 1 (depending on the wavelength range used). However, as can be seen in figure 3.5, the quality of the individual straight-line fits (which give mass ratio q and systemic velocity $v_{\rm COM}$), is not very good. This can be

explained by reconsidering the disentangled spectra (figure 3.1): the disentangled components for object G-5536 are noisy, making selecting the correct template difficult. This is due to the fact that object G-5536 is fainter than the rest of the sample, but was observed for a similar number of epochs, leading to a lower S/N overall. Additionally, object G-5536 is likely further evolved, since the independent template fits suggest a higher effective temperature for the donor than found in EB+22. The puffed-up stripped star has likely started contracting and heating up again. This can also be seen in Figure 3.6: Specifically, we note that the G-5536 components lie further along their respective MESA evolution tracks in all three panels which include them.

This further evolution of object G-5536 results in more similar temperatures of the donor and accretor, and thus a more similar spectral signature: especially in the Balmer series, the higher donor temperature leads to wider and deeper lines, more similar to those of the accretor. This causes difficulties in the disentangling and subsequent TODCOR analysis

3.4.1. Mass loss conservativeness

We now turn to the constraints on any mass loss (or "non-conservativeness") during the preceding MT evolution that arises from the constraint that the systems must have been *detached* (see Section 3.2.3). With the system's present day period from orbit fitting and mass ratio from TODCOR, we can back-calculcate the period as a function of the evolving mass ratio, $P(q)$, for any set of mass-loss coefficients α, β and δ from Soberman et al. (1997). Following Bodensteiner et al. (2020); El-Badry et al. (2022b), we assume that α and δ are zero, implying no mass loss from the donor or a circumbinary ring, and vary the mass loss form the accretor β (isotropic re-emission). Figure 3.7 then shows the past evolution of the period as the system underwent MT, for different β values. At $q = 1$, the mass ratio is flipped, and the (initially) more massive donor is now the less massive star of the binary. The colored lines show how the past period depends on the assumed β. Some, but not all, of these lines dip below the minimum period (grey gradient, with darker colours corresponding to higher, and lighter colours to lower MS masses). Below this minimum period, the radius of the donor's progenitor on the MS would have exceeded its RL, calculated using Eggleton (1983). Those reflect values of β excluded by the data.

In Figure 3.7, the solid lines reflect the possible $P(q)$ for our determination of the present day q and period, while the dashed lines reflect the $P(q)$ implied by EB+22. This illustrates the importance of the q determination, as it immediately translates into constraints on the MT "physics", β. Analogous plots for the other systems are found in Figure B.3 in the Appendix.

Taken at face value the plots imply that MT cannot have more than $\beta \sim 0.5$ in such systems, as for larger β (i.e. more mass loss), the period would be too short at some point during the binary's evolution. This affirms the conclusions of Bodensteiner et al. (2020); El-Badry and Rix (2022) that MT has to be quite conservative.

3.4.2. Stellar rotation

As a final point of discussion, we now turn to the level of rotation in the accretors that we could determine from our disentangled spectra: we see projected rotational velocities between 150 $\sim$ 200 km/s (see Table 3.1). While this is clearly rapid rotation, as expected

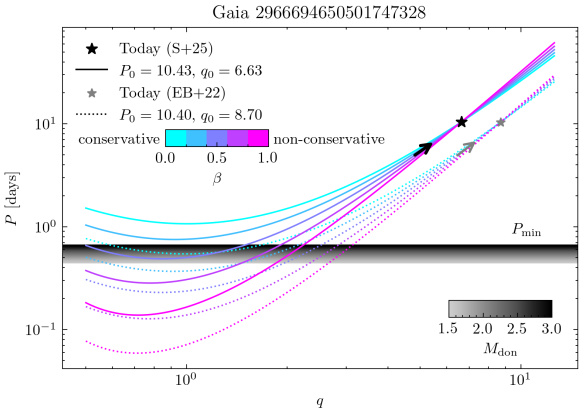

Figure 3.7: Period vs mass ratio for one of the targets (G-2966), showing the evolution of the period as mass is transferred from the donor to the accretor. Solid lines use present-day parameters found in this work (S+25), while dotted lines use the results from EB+22. The present-day locations of the systems in the P-q plane are marked with black (this work) and grey (EB+22) stars. Arrows indicate the direction of evolution as mass is transferred from the donor onto the accretor. The minimum Period is shown as a grey horizontal stripe, with colours indicating the donor mass on the MS. We see that the higher mass ratio from EB+22 places a much tighter constraint on the conservativeness of MT than the lower estimates found in this work. For this object in particular, the present-day mass ratio and Period from EB+22 require almost fully conservative MT to avoid a merger.

for an accretor, these velocities are well below the critical velocities that are expected to be $\gtrsim$ 350 km/s (from $v_{crit} = \frac{G \cdot M_*}{R_*}$) for these systems, assuming masses and radii from EB+22. Following Packet (1981), we expect a star to have to accrete only $\sim 5 - 10\%$ of its initial mass to spin up to critical rotation. As our analysis suggests the accretors approximately doubled their mass through MT, they should have easily achieved critical rotation.

This discrepancy between expected and observed rotational velocities is unlikely due to mere projection effects; EB+22 found the inclinations of the systems to lie mostly around 65°, which would reduce the velocities only by about 10%. Significantly larger inclinations are ruled out as they would produce eclipses, while significantly smaller inclinations are inconsistent with observed accretor parameters. Part of this disagreement may stem from equatorial gravity darkening: due to the reduced gravity at the equator and the Von Zeipel effect (von Zeipel, 1924), there is less flux coming from the equator, and the star appears to rotate less rapidly (Townsend et al., 2004). However, as the observed discrepancy between observed and expected rotational velocity is large (of order factor 2), it is likely that some mechanism has slowed the accretor's rotation. MT likely ended only recently, as the donors are still in the short-lived "puffed-up" stage. This implies that the spin-down mechanism must have been fairly efficient. Tides are likely in effect, as demonstrated by the donor rotating at tidally synchronous velocities and suggested by the short periods. However, the tidal synchronisation timescale $t_{\rm sync}$ following Zahn (2008) is significantly less efficient than required to reproduce the observed rotational velocities. Assuming parameters of a star representative of the accretors in our sample, we expect $t_{\rm sync} \approx 10^{10}$ years. As we know MT only ceased recently, as evidenced by the donors still being in the short-lived bloated stage, it is unlikely that tidal forces alone were sufficient to slow down the rotation of the accretor. Further, the accretors are too hot for magnetic braking (Kraft, 1967). If star-accretion disk interactions such as described by Popham and Narayan (1991) and Paczynski (1991) are in effect, it is possible that these are, or were, slowing down the accretor. The mechanism

allows for outward angular momentum transport at the same time as inward mass flow onto the star. These interactions may pose an alternative spin-up mechanism, as the conventional picture suggesting spin up to critical and then cessation of accretion leads to relatively low MT efficiencies.

3.5. Conclusions

In this work we have obtained and analyzed multi-epoch spectra of six targets, identified by EB+22 as likely post MT binaries with a puffed-up donor and hot, rapidly rotating accretor.

Our data and analysis yield component temperatures and sizes and mass ratios for all systems, confirming this initial assessment. Only for one of the systems (G-2933) we found clear Hβ and Hα emission, suggesting that MT is still ongoing.

To better understand the physical state of the systems' components, we used the spectral disentangling approach by Seeburger et al. (2024) to determine the effective temperatures and rotational velocities from the spectral features of each component. We found slightly higher temperatures (see Table 3.1) for the donors than EB+22 found from SED fits. SED fits with the spectroscopic temperatures are still consistent with the observed photometry.

We determined the dynamical mass ratios (Table 3.1) of the targets using TODCOR (Zucker and Mazeh, 1994), finding somewhat lower mass ratios than EB+22. This is consistent with our finding of warmer donors, as warmer donors are likely more massive, reducing q.

Combining the current orbital periods and mass ratios, we assessed the stability of MT following Soberman et al. (1997) and found that the MT had to have been fairly conservative ($\beta \lesssim 0.5$) to produce the observed systems.

Finally, we determined that all accretors are rotating rapidly, but – importantly – considerably more slowly than the critical rotation velocity. This implies some mechanism must have slowed down rotation efficiently after MT halted. Magnetic breaking is unlikely to have been effective to slow down rotation, given that the $T_{\rm eff} \sim 9000$ K of the accretors is well above the "Kraft-break" (Kraft, 1967). Given that we know the radii, masses and the orbit of the stars, the tidal spin-down prescriptions developed by Zahn (2008), imply slow-down timescales far in excess of the system ages.

One target (G-5536) was consistently difficult to analyse, due to comparatively lower signal-to-noise data and higher similarity of the donor and accretor spectra and subsequently more degeneracies in the disentangling. For this target, additional epochs at higher signal-to-noise ratios might help shed more light on its nature.

Acknowledgements RS, HWR, JMH and JV acknowledge support from the European Research Council through ERC Advanced Grant No. 101054731.

We thank Tomer Shenar for insightful discussion and helpful input on this work.

This publication made extensive use of the online authoring Overleaf platform (`https://www.overleaf.com/`).

The data processing and analysis made use of `pystellib` (Fouesneau), `matplotlib` (Hunter, 2007), `NumPy` (Harris et al., 2020), the `IPython` package (Perez and Granger, 2007), `SciPy` (Virtanen et al., 2020), `AstroPy` (The Astropy Collaboration et al., 2013, 2018, 2022) `SpectRes` (Carnall, 2017) and `SpectResC` (Lam, 2024)

4

Exploring *Gaia* binaries with APOGEE

Authors Rhys Seeburger, Andrew K. Saydjari, Hans-Walter Rix, Kareem El-Badry, Johanna Müller-Horn, Jaime Villaseñor, Jiadong Li, Ben Pennell

Chapter info This chapter is a reproduction of a manuscript currently in preparation, to be submitted to a peer-reviewed journal later this year (2025) as part of the SDSS collaboration. It describes the analysis of a set of APOGEE spectra of targets identified as binary stars in *Gaia* DR3. As the lead author, I performed the analysis and interpretation of the data and results, as well as producing the text and figures. Kareem El-Badry and Hans-Walter Rix were my doctoral advisors during this project, and suggested this dataset for analysis. Andrew Saydjari helped with data access and processing, as well as shaping the analysis process and providing input and code for the generation of the synthetic spectra used. Johanna Müller-Horn, Jaime Villaseñor, Jiadong Li and Ben Pennell all provided comments on the results. All co-Authors gave suggestions and feedback on the text and figures.

Note: In the context of this chapter, we refer to the flux ratio (named α in chapter 2 and a in chapter 3) as f_H or f_G depending on the relevant wavelength band. This is both to clarify the band and to avoid confusion with the alpha-process element fraction, commonly denoted as α and the semimajor axis, frequently labelled a.

Abstract *Gaia* DR3 has provided a truly unprecedented set of orbit solutions for (spatially) unresolved binaries, via spectroscopy (SB1 and SB2), astrometry ("orbit solutions") or photometry (eclipsing binaries). To be fully interpretable, all these solutions need an understanding of the luminosity ratio between the primary and secondary component.

The APOGEE instrument as part of SDSS-V's Milky Way Mapper survey has obtained over 80,000 spectra of targets identified as binaries in *Gaia* DR3. This provides an excellent complimentary dataset to *Gaia*: APOGEE's higher resolution, high signal-to-noise ratio (S/N), and infrared wavelength coverage can aid in validating and improving binarity measurements from *Gaia* by identifying smaller RVs, redder secondaries, and measuring flux ratios.

In this work, we perform an initial exploration of the APOGEE dataset and its suitability for follow-up to refine *Gaia* binary classifications. We use photometry from *Gaia* and 2MASS to place priors on the single/binary theoretical spectra we use to model the

APOGEE spectra. Using the 2D cross-correlation algorithm TODCOR, we confirm 70% of *Gaia* SB2s are detected as SB2s in APOGEE and place constraints on their H-band flux ratios. We also identify 5% of *Gaia* astrometrically-identified binaries as SB2s; future work will combine APOGEE spectroscopic flux ratios and *Gaia* orbital solutions to fully solve the component orbits.

4.1. Introduction

Most binary systems in the Milky Way Galaxy consist of two luminous, stellar components. Here, the flux ratio is a fundamental parameter that affects many observables and contains information about the mass- and temperature ratios of the system. Spatially unresolved binaries, which make up the vast majority of binaries due to their distance from Earth and small orbits compared to the galactic scale, can frequently be identified as such astrometrically, photometrically or spectroscopically. With astrometry, for favourable configurations we can observe the motion of the photocentre. For photometry, we use the SED to look for colours and magnitudes inconsistent with single star models. Similarly, in spectra we can search for signatures of two components, or those of one component orbiting about some companion. Both of these methods, however, are imperfect, suffering from false negative and false positive detections.

The 3rd *Gaia* Data Release Gaia Collaboration et al. (2023) contains non single star (NSS) solutions for over 440,000 objects. This sample is a treasure trove of binary (and higher order multiple) systems. As *Gaia* has astrometric, spectroscopic (using the *Gaia* radial velocity spectrometer (RVS)), and photometric capabilities, it can detect a wide variety of binaries. If a target in *Gaia* DR3 shows a non-constant signal in one of the three channels, various binary orbit models are tested to sort the target into one of several possible categories. These can be summarised as follows: Eclipsing (photometric), SB1 (single-lined spectroscopic), SB2 (double-lined spectroscopic), Orbital (astrometric) and AstroSpectroSB1 (combined astrometric and single-lined spectroscopic).

Despite this wealth of data, there are limitations to conducting population studies. One caveat is that, despite the strong focus on purity in *Gaia* NSS, there is a chance that a target has been misclassified as SB1 while being SB2, and vice versa. Additionally, the astrometry only solutions suffer from a degeneracy, as without a flux ratio in the relevant band it is only possible to constrain the orbit of the light centroid, and not of the two components. Thus, the flux ratio is a crucial component in impreterability of the *Gaia* astrometric solutions.

SDSS-V has amassed over 80,000 APOGEE spectra (Majewski et al., 2017), of binaries in the *Gaia* NSS catalogue across two identical instruments: Apache Point Observatory (APO) in the north and Las Campanas Observatory (LCO) in the south. These spectra are observed in the H-band at a resolution of $R \sim 22,500$, about twice that of *Gaia* RVS ($R \sim 11,500$). This dataset presents an excellent supplement to *Gaia*, as the flux ratio of MS stars is expected to be mostly constant across the H-band, and the additional resolving power lends itself to easier recognition of SB2 systems, even at smaller velocity separations, relative to RVS. This allows us to use APOGEE to measure the purity and revisit some of the *Gaia* NSS spectroscopic classifications. The data can also be used to ascertain the flux ratio in the H-band and convert this to a G-band flux ratio in order to constrain the astrometric orbital solution.

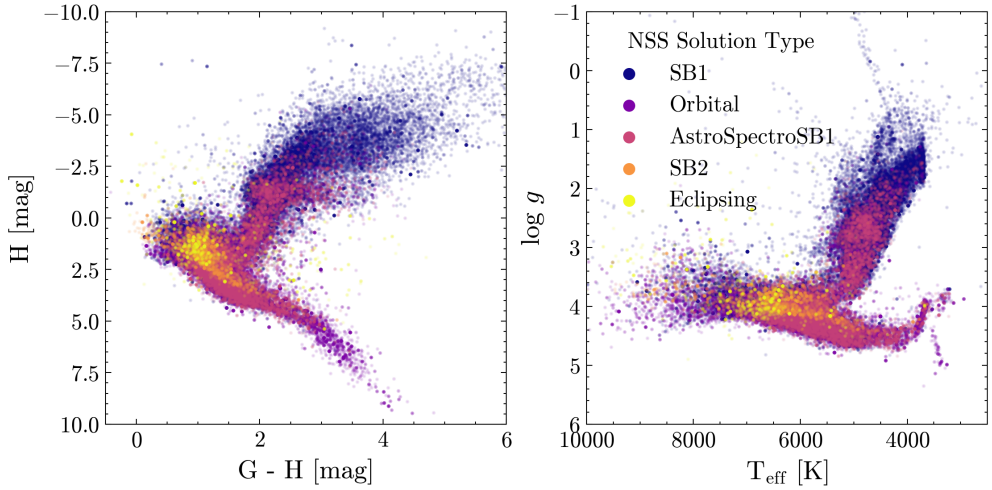

Figure 4.1: CMD and Kiel diagram of the sample considered in this work. Photometry is from *Gaia* and 2MASS, effective temperatures and surface gravities based on *Gaia* XP spectra from Zhang and Green (2024). Dots are coloured by their NSS solution type from *Gaia* and sorted from most to least common.

In this work, we employ a version of the TODCOR algorithm (Zucker and Mazeh, 1994), which uses 2-dimensional cross correlation with spectral templates to identify binaries by looking for multiple peaks as a function of RV. We also take into account photometric information from *Gaia* and 2MASS (Skrutskie et al., 2006), to explore this sample of *Gaia* NSS and provide some initial statistics. We confirm, revise or propose the targets' classification as SB1 or SB2. Further, we constrain the flux ratio (placing an upper limit in the case of SB1s), which will allow us us to refine the *Gaia* astrometric orbit further.

4.2. Method

To analyse APOGEE binaries, we have to undertake a number of steps.

4.2.1. Target Selection

We select all spectra in the APOGEE catalogue, for which a *Gaia* NSS solution is available by crossmatching the catalogues on the *Gaia* source-id. We do this regardless of the type of NSS solution provided in *Gaia* (Astrometric, SB1, SB2, Eclipsing). Further, we crossmatch with a catalog from Zhang and Green (2024) to get initial guesses of the effective temperature and surface gravity of the single star model from *Gaia* XP spectra, as well as the relevant extinction. We remove the extinction (as given by Zhang and Green (2024)) in the 2MASS H-band and *Gaia* G-band, allowing us to place the targets on a de-reddened colour-magnitude diagram (CMD) in H-magnitude and G-H colour. This diagram can be seen in figure 4.1.

Treating each visit to the same target separately, we find 86,673 APOGEE spectra. They are classified as SB1, SB2, Orbital (astrometric solution), Eclipsing (eclipsing binaries) and AstroSpectroSB1 (combined astrometric and SB1 spectroscopic solution), with numbers in each category shown in the first row in table 4.1.

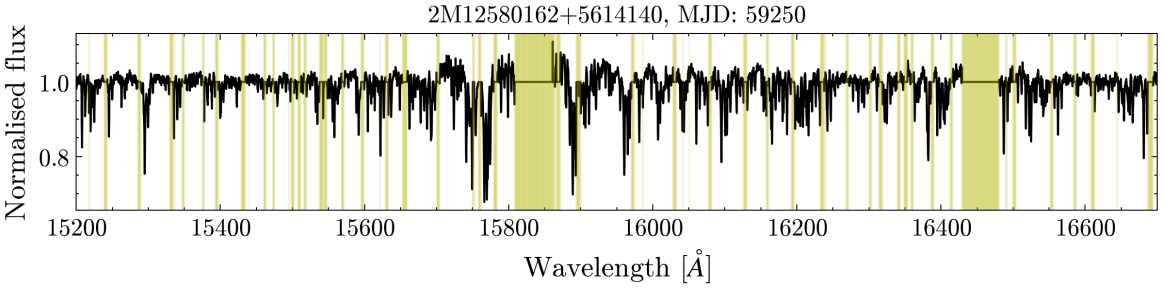

Figure 4.2: An example APOGEE spectrum, limited to the wavelength range considered in this analysis. Areas contaminated by skylines and the gaps between chips are masked out (i.e. flux set to the continuum), see yellow shaded areas.

	AstroSpectroSB1	Eclipsing	Orbital	SB1	SB2
Pre-Cut	17244 (19.9%)	1303 (1.5%)	19803 (22.8%)	45733 (52.8%)	2590 (3.0%)
Post-Cut	15886 (18.3%)	728 (0.8%)	14039 (16.2%)	41901 (48.3%)	2275 (2.6%)

Table 4.1: The number of spectra considered in this work and their associated *Gaia* NSS categories. Each cell also contains the percentage of the total sample that each category represents.

The spectra are delivered by SDSS on a standard wavelength grid (with a 6e-6 log spacing), and we normalise with a running median filter. The spectra are already pseudo normalised, but we perform this step to improve the comparison with the template spectra, which we also process this way. We consider the wavelength range from 15200 - 16700 Å, and mask out areas of the spectrum with significant sky lines, bad pixels (as indicated by the DRP), other issues, and the gaps between the three chips. We identify the sky lines by averaging the modelled sky spectrum from SDSS for each visit spectrum and excluding 5% of pixels with the most signal. An example spectrum is shown in figure 4.2.

We remove targets with S/N below 30, or effective temperatures below 2800 K or above 8000 K as found by Zhang and Green (2024). We perform these cuts as our spectral synthesis pipeline is limited by the MARCS atmosphere cutoffs and thus unable to synthesise spectra outside this temperature range. After applying these cuts, removing obvious data problems (such as all-nan fluxes), and photometries that lie outside the region covered by our isochrones, we are left with a total of 74,829 visits, distributed among the different categories by *Gaia* as shown in the second row in table 4.1.

4.2.2. Generating Synthetic Spectra

At its core, TODCOR requires a pair of templates and associated flux ratio to perform the 2D CCF with and ascertain the best-fit velocity shifts for each component. We would like for these pairs of templates and their flux ratios to be physically informed. Thus, we sample from theoretical isochrones to allow us to use photometry as a prior on the magnitudes and colours of composite systems, acquiring their light ratios and spectral parameters for template generation from the isochrones.

We use PARSEC (Bressan et al., 2012) isochrones for a range of stellar ages ($8 \leq \log\tau \leq 10$) at solar metallicity. We randomly draw 1000 samples from these isochrones in $T_{\rm eff}$ and $\log g$ without replacement and use the `Korg.jl` package (Wheeler et al., 2023, 2024) to synthesise spectra for these samples assuming no rotation and solar metallicity. The

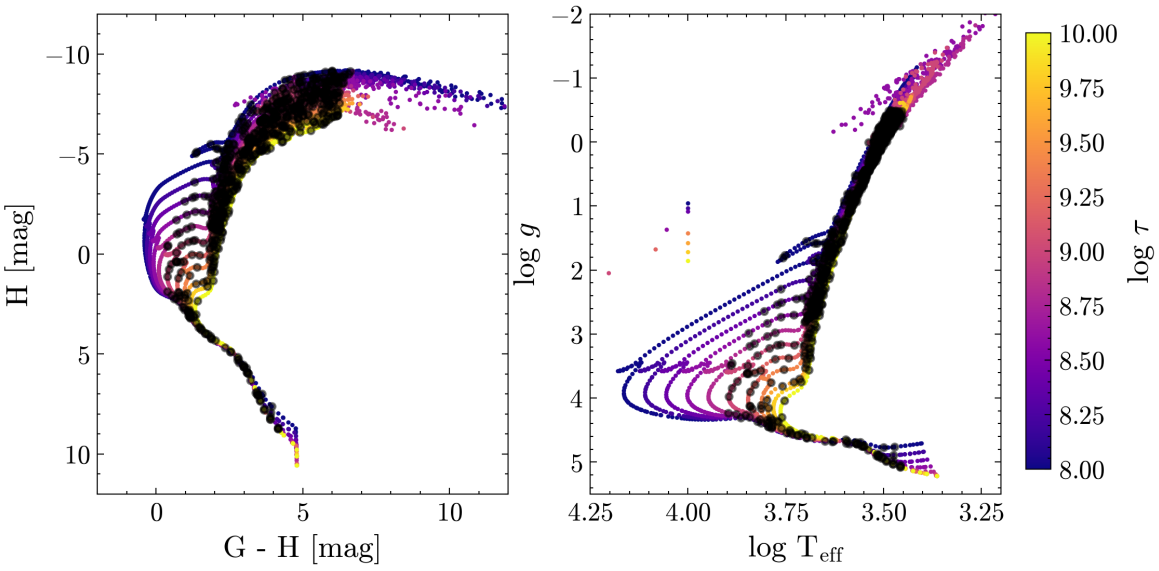

Figure 4.3: CMD and Kiel diagram of the isochrones used to determine draw samples from to generate synthetic spectra. Isochrones are coloured by log age, and black dots show where samples were randomly drawn from. We note a high density of samples on the MS and the red giant branch, explained by the fact that stars spend comparatively long times in these stages of their evolution.

isochrones, coloured by age, are shown in both a CMD and Kiel diagram in Figure 4.3. We also show the locations of the samples drawn for spectral generation with `Korg.jl`.

We use the stellar continuum from `Korg.jl` to normalise the spectra, and additionally apply a running median filter to ensure coherence between the data and synthetic spectra. We convolve with a Gaussian LSF kernel to interpolate the spectra onto the same wavelength grid used by APOGEE at a resolution of 22,500. We also create a flat, featureless dummy spectrum for each isochrone to act as an artificial, unseen secondary, and assign it $T_{\rm eff}$ = 0 K, $\log g = 10$ and a G- and H-magnitude of infinity.

4.2.3. TODCOR

We place a flat prior on the H-magnitude and G-H colour based on the values reported for the targets in the *Gaia* and 2MASS catalogues. We allow for a range of ±0.2 magnitudes both in H-magnitude and G-H colour to account for errors in the photometry and extinction. We then explore pairs of stellar models on the same isochrone whose combined photometry fits within the prior limits established by the 2MASS and *Gaia* photometric measurements. As we also made a dummy datapoint with infinite magnitude, this allows for photometry with no visible secondary contribution as well.

For each pair of models, we select the two spectra closest in the normalized $T_{\rm eff}$-$\log g$ plane to each model, as well as computing their flux ratio in the H-band, f_H based on each component's H-band magnitude. Then, for each pair, we use the TODCOR algorithm (Zucker and Mazeh, 1994) to compute the 2-dimensional CCF value for a range of radial velocities for each component, using the synthetic `Korg.jl` spectra and their flux ratio as suggested by the isochrones. We select the pair of models whose spectra and flux ratio achieve the highest peak CCF in TODCOR. We compute the significance of each peak by subtracting the mean CCF along each dimension and dividing by the variance. We only consider the

most significant peak and any other peaks that reach at least 50% significance along the same dimension, discarding all other peaks, which are likely caused by random fluctuations in the data.

The maxima in the v_A/v_B plane provide information on the velocities of each component. We select the component velocity/velocities according to which kind of binary the data suggests:

- SB1: Either one clear peak in each direction at the same velocity (if an equal-mass binary was selected from the isochrone but both templates match the same velocity), or a clear peak in one direction and no features in the other (if a luminous primary and an invisible secondary were selected). As in the first case, $v_A = v_B$ as suggested by TODCOR, the velocity of the visible component is simply v_A.
- SB2: Two peaks, frequently of different significance, in each direction. The relative significance of the peaks depends on the spectral information contained in each component spectrum (many narrow lines contain more information, and thus cooler spectra tend to be more rich in information), as well as the flux ratio of the components. There are four maxima, corresponding to coordinates (v_A, v_A), (v_A, v_B), (v_B, v_A) and (v_B, v_B). We take the component velocities corresponding to the highest peak, while requiring that $v_A \neq v_B$. It is possible to have only one CCF peak in each direction for an SB2 if the two components' spectra are sufficiently different from each other. This is unlikely as a large temperature difference would imply a mass ratio far from 1, which, in turn, would imply an extreme flux ratio and would likely make a fainter secondary undetectable. However, even so, different to the SB1 case, these peaks will lie at different velocities, meaning we can simply take v_A and v_B corresponding to the highest peak. In the unlikely case that the system was observed at phase 0, $v_A = v_B$, and the system will be incorrectly identified as an SB1.
- Other: For any other number or configuration peaks, more careful analysis of the system is necessary, and our standardised approach is insufficient. This scenario may arise due to a number of reasons. The spectrum may be very noisy, hence the removal of low S/N spectra in a previous step. Additionally, issues in the data reduction pipeline can lead to artifacts which hinder the algorithm from finding the correct maxima. Finally, stars outside the synthesised parameter space, such as very hot stars, Be stars, rapid rotators, or atypical abundances will lead to a poor spectral template fit, and thus cause TODCOR to fail. We have attempted to reduce these by removing the hottest stars, but cannot account for every failure scenario a priori. Thus, we flag these stars rather than attempting to get radial velocities.

Thus, by combining spectral analysis with TODCOR and 2MASS and *Gaia* photometry, we get information about the effective temperature, surface gravity and radial velocity of one or both components, depending if the system is an SB1 or SB2 and the flux ratio of the system. For SB1 systems, we can only put an upper limit on the flux ratio due to limited sensitivity.

4.2.4. Refining *Gaia* Solutions

Our analysis has given us two additional pieces of information: for all cases where we only see SB1 we have an upper limit on the difference between the primary orbit and the light

centroid orbit. For the cases where we see an SB2, we a) get the flux ratio directly, and b) via isochrones get the mass ratio which allows us to solve the system fully.

Following Shahaf et al. (2019), the semimajor axis of the photocentre of an unresolved binary is given by:

$$a_{\rm phot} = a_A \left(1 - \frac{f(1+q)}{q(1+f)}\right), \tag{4.1}$$

where a_A is the semimajor axis of the primary, $f = F_B/F_A$ is the flux ratio in the given band, and $q = M_B/M_A$ the mass ratio of the system. This can trivially be rearranged to give the semimajor axis of the primary as a function of $a_{\rm phot}$, f and q. a_B is then simply a_A/q.

For its astrometric orbital solutions, *Gaia* reports the Thiele-Innes elements A, B, F, and G. These are related to $a_{\rm phot}$, the inclination i, the position angle of the ascending node Ω and the periastron longitude measured from the ascending node ω by:

$$A = a_{\rm phot}\,(\cos\omega\cos\Omega - \sin\omega\sin\Omega\cos i) \tag{4.2}$$
$$B = a_{\rm phot}\,(\cos\omega\sin\Omega + \sin\omega\cos\Omega\cos i) \tag{4.3}$$
$$F = -a_{\rm phot}\,(\sin\omega\cos\Omega + \cos\omega\sin\Omega\cos i) \tag{4.4}$$
$$G = -a_{\rm phot}\,(\sin\omega\sin\Omega - \cos\omega\cos\Omega\cos i) \tag{4.5}$$

and can be used to recover $a_{\rm phot}$. Thus, with $a_{\rm phot}$ from the *Gaia* NSS catalogue, and mass- and flux ratios from isochrones, we can compute a_A and a_B for TODCOR SB2s with an associated *Gaia* orbital solution.

For the SB1 solutions, an MS primary with an unseen companion in the H-band generally implies a flux ratio in the G-band equal or below the upper limit inferred in the H-band. This is because on the MS, there is a relation between the temperature and luminosity of a star. More massive stars burn hotter and produce more energy, leading to larger luminosities. Thus, for a companion to be invisible in the H-band but visible in the G-band, it would need to be both smaller and hotter than the primary. This can only be the case if the primary is a red giant (and thus large and cool), or if the companion is a white dwarf. A star can be identified as a red giant by its position on the CMD, and we proceed with caution when making inferences on the G-band flux ratio from the H-band in these cases. A white dwarf companion can be identified at much bluer wavelengths, e.g. the GALEX UV band. Thus, if an SB1 is identified in the H-band, the primary is on the MS and no UV excess is found, one can proceed with the assumption that in the G-band, the photocentre traces the primary to within the upper limit derived in the H-band. Cross-matching with GALEX to ascertain which MS SB1 systems do not contain a white dwarf secondary will be the subject of future work.

4.3. Results & Discussion

By applying the procedure as described in section 4.2, we gain insight into a number of important system and stellar parameters of the targets in the sample, enabling us to compare them to the information obtained by the *Gaia* NSS pipeline and Zhang and Green (2024).

4.3.1. Individual Targets

As displaying every single target would exceed the scope of this paper, we have selected several interesting and/or representative examples in this section to discuss the different kinds of solutions found by the pipeline.

2D Cross-Correlations Figure 4.4 shows the 2D CCF plane for the best template combination for each spectrum for 6 selected targets. Overall, the panels show good agreement between the selected components and data, with peak heights close to 1 in most cases. As the CCF is normalised, a peak height of 1 would suggest perfect agreement between the templates and observations; this, of course, is unachievable in real data that has been affected by noise.

Targets in panels 4.4a, 4.4c and 4.4e show clear evidence of SB2-ness, with two peaks at different velocities in each dimension. Note again that this behaviour is expected when the two component spectra are sufficiently similar to each other, as each template will obtain a CCF peak when "matched" with any of the two component velocities. If the spectra are very different, this effect is not observed. We also note a difference in the height of the respective CCF peaks with the flux ratio. For a flux ratio near 1 (panel 4.4a), the two peaks are of similar height, while for significantly smaller flux ratios (panels 4.4c and 4.4e), their heights differ. This leads to a degeneracy in twin systems with similar fluxes (and masses): a single-epoch RV analysis cannot identify which velocity belongs to which star. Thus, care has to be taken when analysing further epochs to break this degeneracy. This can be achieved, for example, by fitting an orbit by successively swapping the two component velocities at each epoch until the fit is optimised.

As the velocity difference between the two components is sufficient (relative to the resolution) in these examples, line blending does not cause problems, as evidenced by the two clearly separated peaks. For lower separations in velocity space, it is sometimes not possible to discern the two velocities clearly, and more careful analysis is required. Interestingly, 2M12580162+5614140 was identified as an SB1 in the *Gaia* NSS catalogue, while here we clearly see evidence of a secondary peak in the CCF.

Panels 4.4b and 4.4d show two possible scenarios for the algorithm to identify an SB1 system. In panel 4.4b, the continuum-only dummy template was selected for the secondary, meaning it does not contribute to the CCF. This is evidenced by the lack of horizontal stripe in the plot. For panel 4.4d, the best fit templates selected were found to exhibit the same velocity shift, indicating that this, too, is an SB1 system. Finally, the peculiar pattern in panel 4.4f is likely due to a triple system, as indicated by the clearly separated three peaks in each dimension. TODCOR does not have a provision for dealing with these systems, hence they are classed as "other".

Observed and Component Spectra In Figure 4.5, we show the corresponding spectra for each of the targets in figure 4.4, zoomed in to 15220 – 15340 Å. The top panels for each plot show the observed and reconstructed spectra (black and grey, respectively), and the masked out areas (yellow). Middle panels show the component spectra, and bottom the residual. In all cases, the shifted and co-added component spectra achieve a decent reconstruction of the observed spectrum, with no major lines missed or spurious signatures. This is also evidenced by the generally small and mostly feature-less residuals and the comparatively large CCF

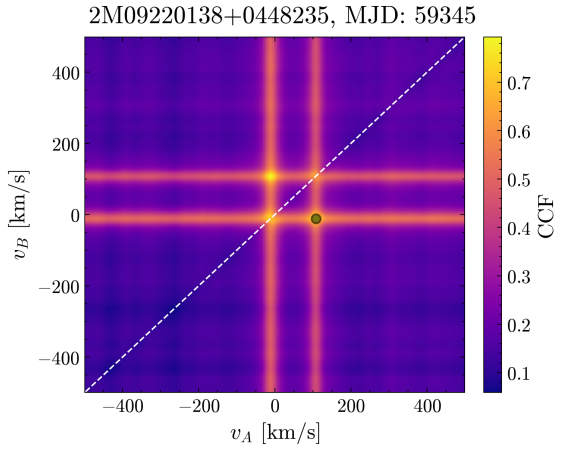

(a) An SB2 with a flux ratio near 1.

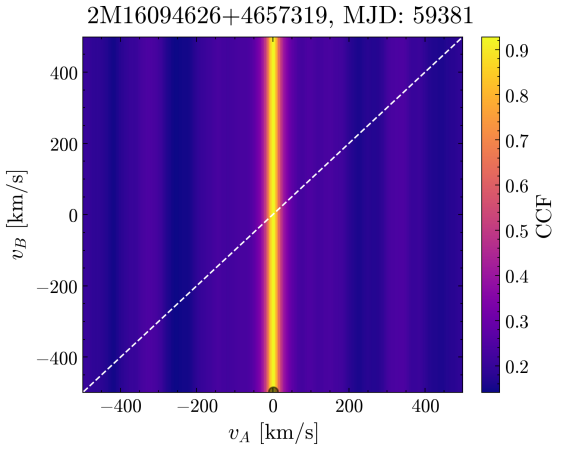

(b) An SB1 with a flux ratio of 0. Note the absence of a horizontal stripe.

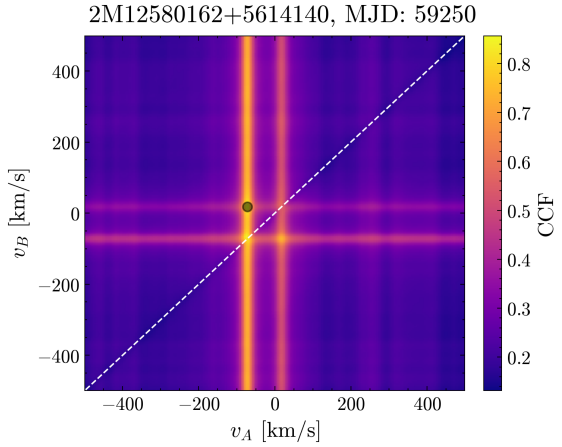

(c) An SB2 with a flux ratio around 0.35. Note the different heights of the CCF peaks.

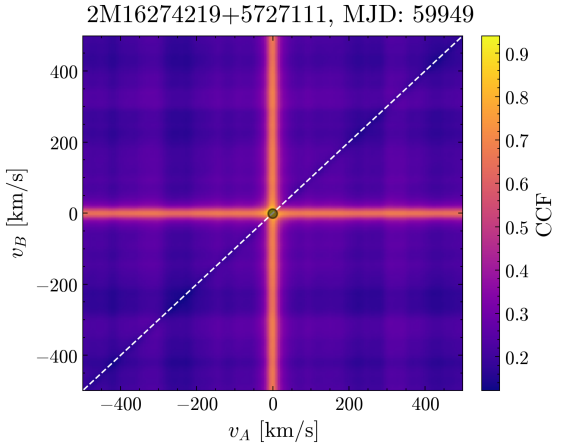

(d) An SB1 with two components shifted to the same velocity.

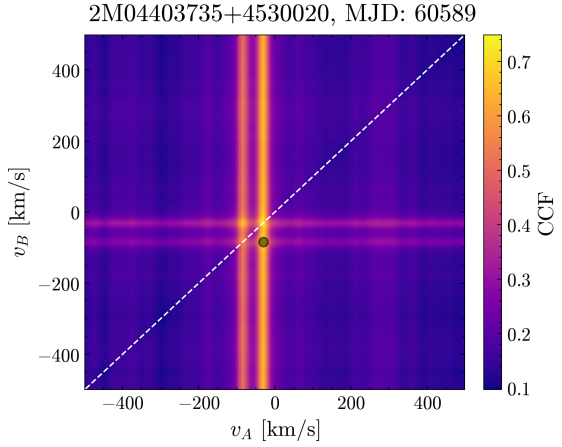

(e) An SB2 with a flux ratio around 0.35. Note the different heights of the CCF peaks.

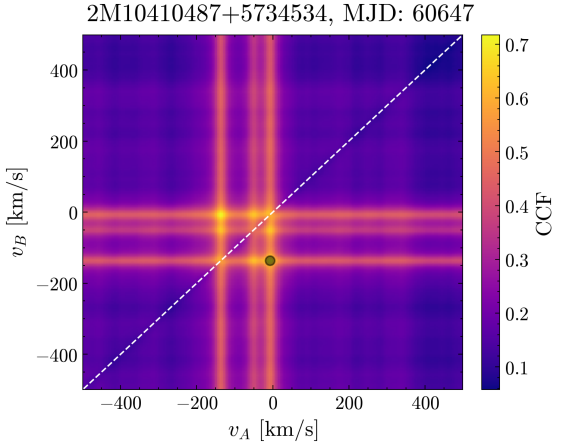

(f) A potential triple. Note the three distinct peaks in each dimension.

Figure 4.4: The 2D CCF for a selection of different targets. The x-axis shows the epoch RV of the primary, and the y-axis that of the secondary. A white diagonal is included to show where $v_A = v_B$, and a black circle indicates the selected best-fit velocities. The left column shows SB2 targets, and the right a mixture of SB1 and "other" targets.

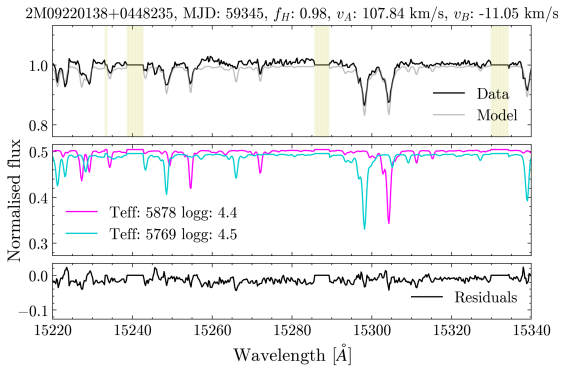

(a) An SB2 with a flux ratio near 1. We note that the effective temperatures and surface gravities of the templates are very similar but their RVs differ by over 100 km/s, identifying this system as a likely twin SB2.

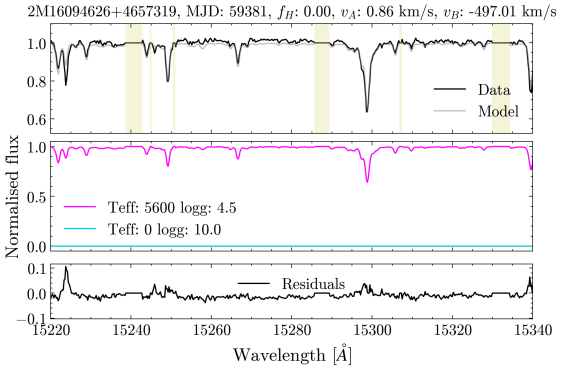

(b) An SB1. We note the flux ratio of 0 and the featureless companion spectrum, indicating no detectable flux from the secondary.

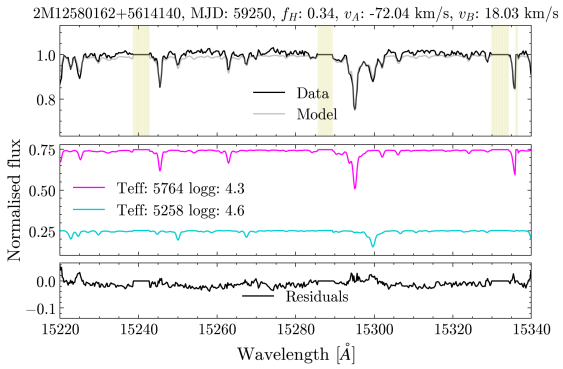

(c) An SB2 with a flux ratio around 0.35. Temperatures and surface gravities imply both components lie on the MS.

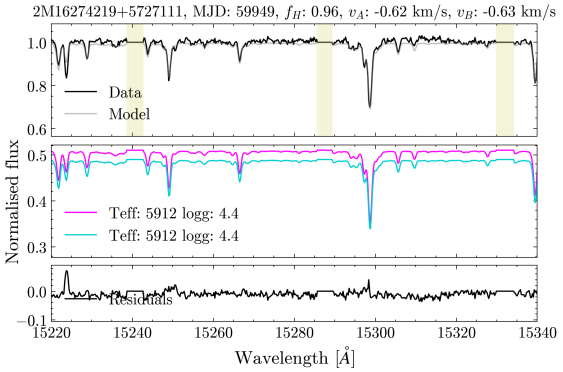

(d) An SB1 with two identical templates shifted to the same velocity.

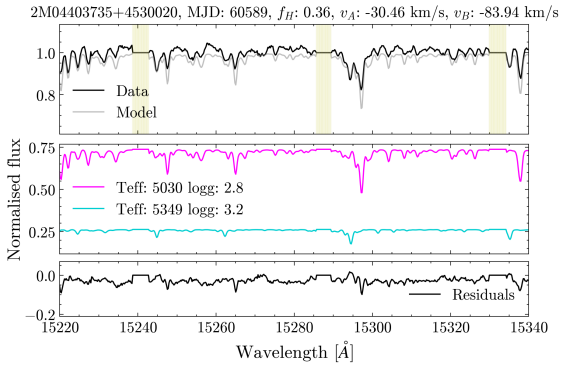

(e) An SB2 with a flux ratio around 0.35. Note the low surface gravity of the cooler star, indicating it likely has ascended the red giant branch.

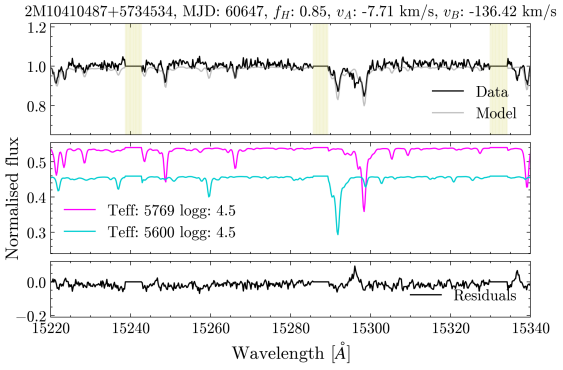

(f) A potential triple. While by eye, the residual does not seem to contain a strong spectral signature, it is revealed in the CCF in panel 4.4f.

Figure 4.5: The spectra for each of the 6 selected targets, zoomed into the region of 15220 – 15340 Å. Top panels show the normalised, observed spectrum in black, with the reconstructed spectrum in grey. This reconstruction is computed by shifting and co-adding the best-fit component spectra. Yellow areas are masked out. Middle panels show the two best-fit component spectra, scaled by their respective flux ratio. In the bottom panel, we see the residual, the difference between the observed and reconstructed spectrum.

value in the panels in figure 4.4. We see that some disagreement arises from the normalisation between the data and templates; a running median filter can cause "wings" on either side of wide and deep lines, and overall has a tendency to underestimate the continuum, leading to a slight offset between the continuum-normalised & median-filtered templates and the pseudo-normalised & median filtered observations.

The left column displays spectra for SB2 systems, while on the right panels 4.5b and 4.5d show SB1 spectra, and 4.5f a potential triple. The SB2s are all very clearly separated in velocity space, with RV differences between the two components in excess of 50 km/s in all cases, and even of 100 km/s in 4.5a and 4.5c. While one epoch is not enough to make any strong constraining statements on the orbital parameters, we point out that the lowest RV difference in this sample was observed for the system for which the templates and photometry suggest a likely red giant primary, which places constraints on the minimum period and thus maximum achievable RVs.

The velocities observed for the SB1 systems are also interesting. In panel 4.5b, the featureless secondary has been given a velocity of ~ -500 km/s, near the edge of the velocity space explored with TODCOR. While the vertical stripe in panel 4.4b shows no strong variation with v_B, small variations due to rounding errors may still lead to the algorithm picking a specific v_B. This is, however, inconsequential, as the target has been identified as an SB1, and thus the secondary velocity is unimportant. Panel 4.5d displays the alternative SB1 case of two identical or near-identical templates shifted to the same velocity. As the flux ratios of both components add up to 1 by construction, if the templates have the same spectral parameters and shifts, the flux ratio does not affect the height of the CCF peak. At times, the algorithm picks slightly different templates or recovers slightly different velocities for the components. This does not necessarily imply the system is not an SB1, though a twin SB2 system with small separation in velocity space may also be present. The latter is, however, statistically less likely, and there is a host of possible explanations for an SB1 presenting this way.

The algorithm may pick (slightly) different templates at (slightly) different shifts to represent an SB1 due to the fact that the templates 1) do not 100% sample the observed $T_{\rm eff}$-$\log g$ plane, 2) neglect the effects of metallicity and rotation, among others, and 3) assume local thermal equilibrium, which is an appropriate assumption for cooler stars, but starts breaking down at hotter temperatures. Thus, a slight mismatch between template and actual primary spectrum may be mitigated by e.g. shifting the secondary template relative to the primary to emulate stellar rotation. A more comprehensive sampling of $T_{\rm eff}$-$\log g$ space to generate templates, as well as considering metallicity and rotation, may help remedy these effects, but comes at a computational cost. Given the volume of targets considered here, we elected to value computational efficiency at some cost to accuracy.

CMDs and Kiel Diagrams While 2D cross-correlation can determine the best combination of spectral templates to reconstruct an observed spectrum, it does not discern whether those two components would reasonably occur in a binary, or whether the spectroscopic $T_{\rm eff}$ and $\log g$ make sense when considering other observations. Therefore, we included photometric information from 2MASS and *Gaia* as a prior on which sets of templates, at which flux ratios, would be considered by TODCOR. This vastly decreases the number of possible template combinations, also aiding in speeding up computation while ensuring the pairs considered make physical sense.

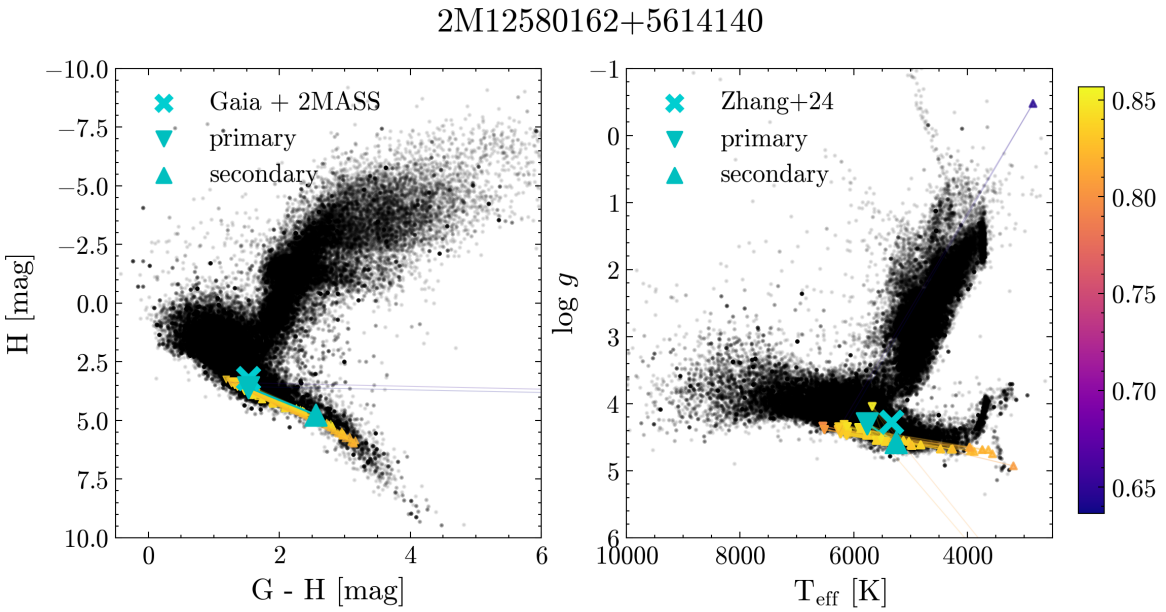

(a) An SB2 likely consisting of two MS stars of different temperatures.

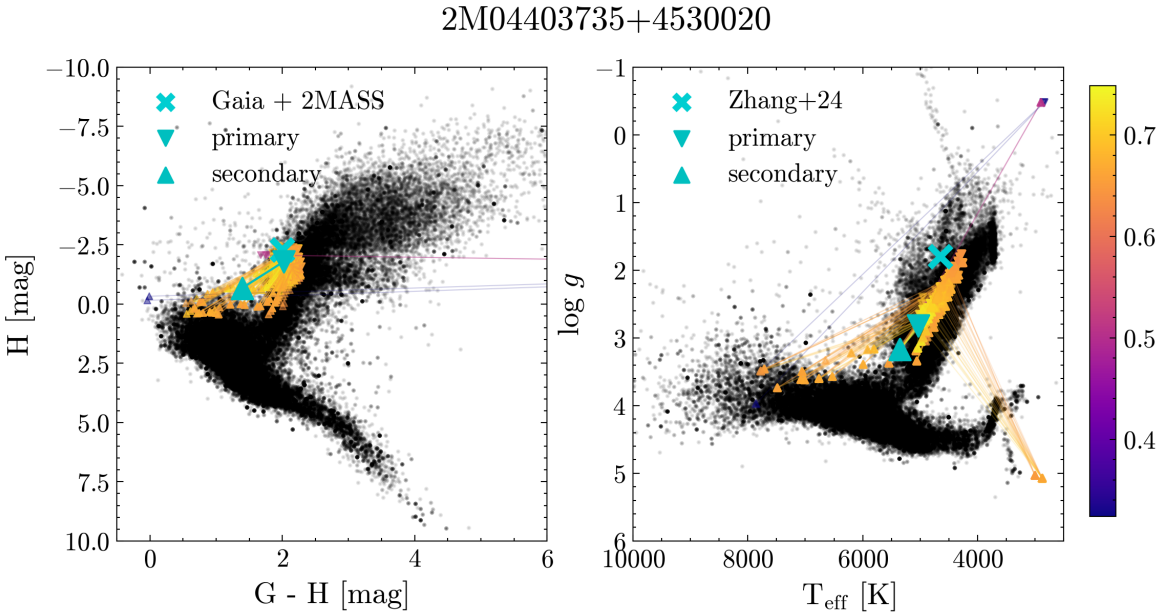

(b) An SB2 likely consisting of a red giant and a MS turnoff star. Note these stars likely started as a similar mass binary, with the more massive star evolving more quickly and ascending the red giant branch before its companion.

Figure 4.6: CMD (left) and Kiel diagram (right) of some of the selected SB2 targets. Small black dots are the overall *Gaia* + APOGEE sample. Cyan crosses show the location of the target in question on the CMD (using data from *Gaia* and 2MASS) and Kiel (using Zhang and Green (2024)) diagrams, assuming a single star. Downwards and upwards pointing triangles show locations of pairs of stars consistent with the photometry connected by a line, with the colours indicating the height of the CCF peak. Large cyan triangles show the best fitting models to the spectra.

In Figure 4.6 we plot the CMDs and Kiel diagrams for the underlying sample, as well as considered combinations for each target and the spectroscopically best-fit pair for the two presented SB2 systems. While both systems considered here show similar flux ratios, they are photometrically very different.

Panel 4.6a shows that for most viable considered combinations, both the primary and secondary lie on the MS, with the primary hotter and more luminous. The temperatures and surface gravities of both components are roughly in line with the single-star temperature derived from XP spectra by Zhang and Green (2024).

In panel 4.6b, we see an SB2 with a similar flux ratio but very different components. Here, pairs generally have at least one component on the red giant branch, with the companion either still on the MS or already ascending the branch as well. The positions on the CMD and Kiel diagram suggest the components are likely of similar initial mass (as vastly different masses would mean that the faster-evolving component would no longer be on the red giant branch by the time the secondary starts ascending). Here, while the spectroscopic temperatures are approximately in agreement with Zhang and Green (2024), the surface gravities differ significantly, with both stars more compact than suggested by the single-star fits to XP spectra.

Figure 4.7 is analogous to figure 4.6, but this time showing the location of the SB1 targets. We note that in the case where TODCOR selected a featureless secondary template and 0 flux ratio (panel 4.7a, the H-band magnitude of the primary alone is the same as the system H-band magnitude from 2MASS - as expected. In the other case, with two identical templates used by TODCOR (panel 4.7b, we see that each of their individual magnitudes is fainter than the observed 2MASS magnitude, though their combined magnitude, by construction, must lie within 0.2 mag of 2MASS. Further, each component's colour is seen to be slightly bluer than the *Gaia* + 2MASS colour for the system. While other pairs, including those with a dummy secondary, were considered by TODCOR, this combination achieved the best CCF peak (though the difference may be small). It is unclear what causes TODCOR to prefer a star+dummy fit or a identical pair to reconstruct an SB1, but a likely factor is the degree of agreement between the available individual templates and the observed primary spectrum. A two-component fit with a slight velocity offset may e.g. be preferable when reconstructing an observed spectrum with appreciable stellar rotation.

4.3.2. Population Study

Spectroscopic Classification Based on the labels found in this work (SB1, SB2 or Other) and those in *Gaia* NSS (summarised into AstroSpectroSB1, Eclipsing, Orbital, SB1 and SB2), we can explore the efficacy of single-epoch APOGEE spectra at discovering SB2 systems compared to multi-epoch *Gaia* RVS data. Figure 4.8 demonstrates how the NSS targets were labelled in this work, with labels on each bin indicating the total number of systems in it, and each bin coloured according to the fraction of *Gaia* NSS targets that were identified as one of the categories in our work.

We see, unsurprisingly, that most targets classified as SB1 in *Gaia* NSS are also classified as SB1 in this work; this includes both *Gaia*'s AstroSpectroSB1 (97%) and SB1 (95%). Similarly, the majority of *Gaia* SB2 targets are recovered as SB2 with single-epoch APOGEE data, though the relative fraction is lower (70%). Inspection of some of the CCF of *Gaia* NSS SB2s being identified as SB1 (22%) reveals two main trends. First, systems which

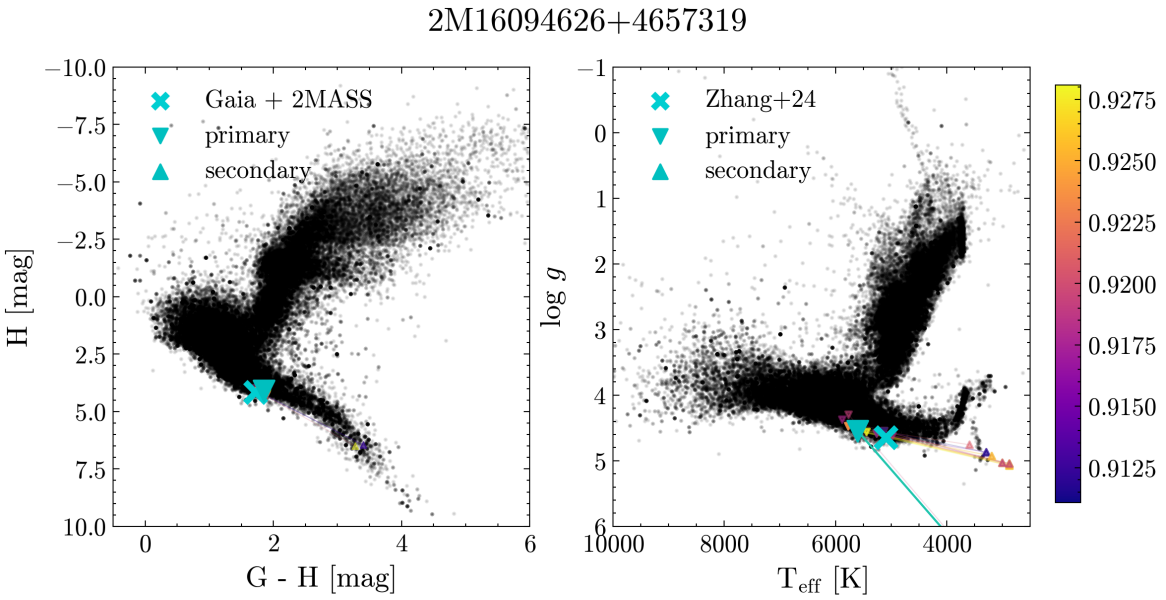

(a) An SB1 with an MS primary and unseen secondary.

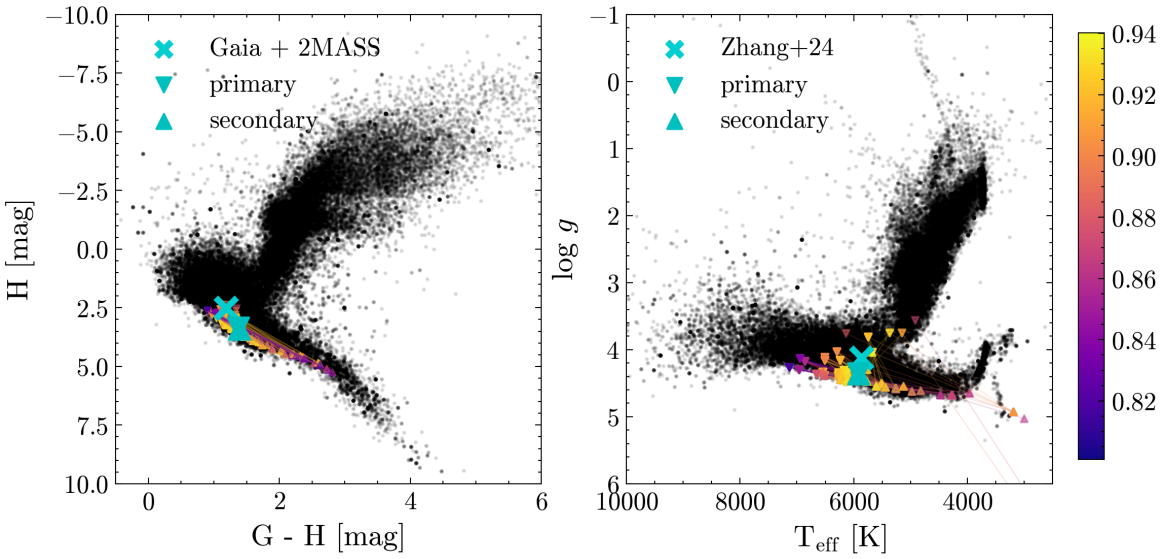

(b) An SB1 where the algorithm selected two identical templates at the same epoch RV.

Figure 4.7: As Figure 4.6, for some SB1 targets

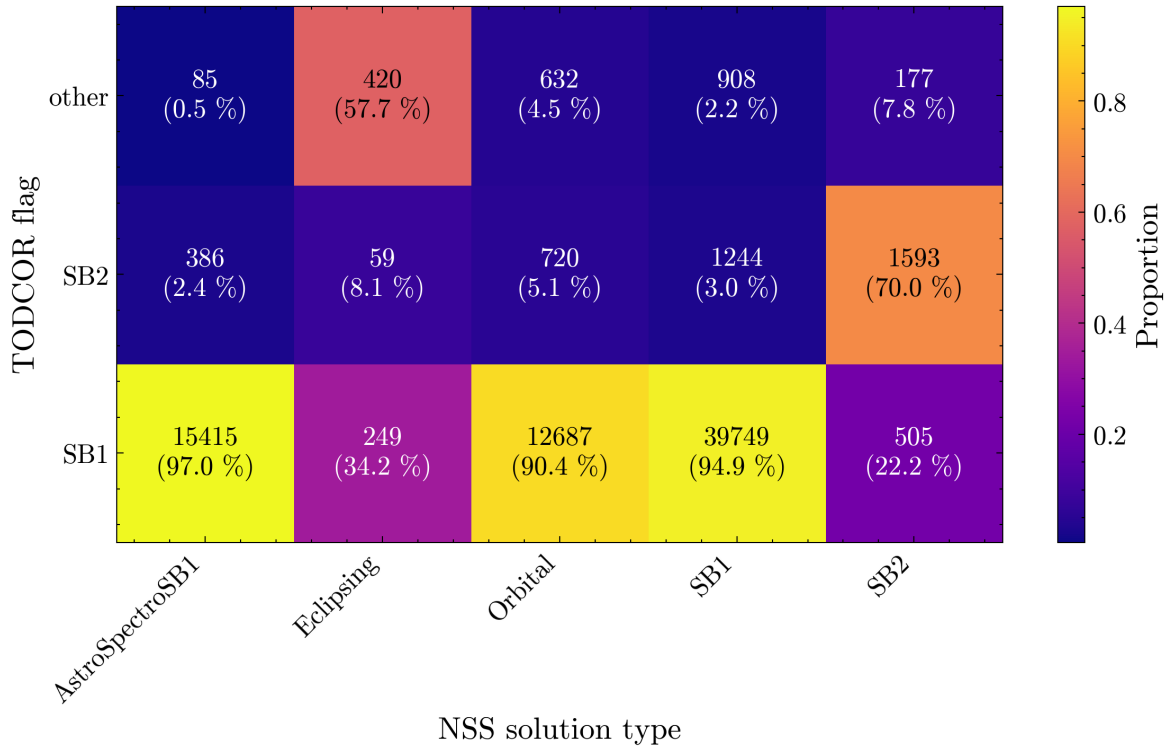

Figure 4.8: Matrix of labels assigned to the systems by the *Gaia* NSS pipeline against our labels derived from spectral analysis with TODCOR. SB1, SB2 and other flags are assigned as explained in section 4.2. We show the total number of targets in each bin as well as the column-normalised percentages.

show two peaks but the secondary peak is much less significant than the primary. It is expected that the selection of the minimum secondary peak significance (we chose 50% of the primary) will have an effect on purity vs. completeness. An adaptable peak threshold that scales e.g. with S/N could help mitigate this issue. Secondly, there are systems where the CCF shows only one peak. This may be due to line blending, if the velocity seperation of the components is very low at the observed epoch. This is unlikely to be the case for a majority of targets, but without access to the *Gaia* RVS spectra, it is difficult to diagnose sources of error. *Gaia* NSS SB2s identified here as "other" (8%) generally appear to suffer from poor spectral template match, due to high temperatures and stellar rotation. A more extensive set of spectra used that takes rotation into account and extends to higher temperatures may help remedy this.

To gain a better understanding of systems we identified as SB2, we can explore their occurrence in different *Gaia* NSS categories in greater detail, using figure 4.9. We plot CMDs for the ratio of the number of targets identified as SB2 by TODCOR over the number of targets identified as the respective class in *Gaia* NSS, given by the panel's title.

For astrometric (Orbital), combined astrometric and SB1 solutions, and SB1s, we note a number of things. First, we clearly see the binary MS along the top end of the MS, resulting from the higher H-band luminosity of a two component system relative to a one component system. We also see a dearth of SB2 systems in the red giant branch. This is also to be expected: red giant primaries vastly outshine any non-giant companions, making them hard to identify as SB2s. Additionally, the red giant branch lifetime of stars is generally much shorter than their MS lifetime - thus, for both stars of a binary to be giants at the same time, they would likely need to be very close in initial mass.

For the Orbital targets we see an excess of SB2 classifications towards the top end of the MS. This may be due to massive stars generally favouring equal-mass companions (Moe and Di Stefano, 2017) which are more likely to show up in the spectrum, but could also be caused by selection effects. Some of these SB2 identifications may also be spurious due to the broad spectral lines of hot stars and associated difficulty with determining components accurately.

Overall, we identified about 3% of visits with associated *Gaia* SB1 solutions, and 2.4% with SB1+Orbital solutions as SB2. Closer inspection of the CCF and spectra will reveal potential spurious identifications in our sample, and/or reasons why *Gaia* did not determine them as SB2. Possible reasons for a failure on our side could be poor spectral fit due to rapid rotation or strongly non-solar metallicity, as well as issues with the SDSS data reduction. Data errors may also cause misidentification in *Gaia*, as may low RV semi-amplitude (as the RVS resolution is lower than that of APOGEE).

Most consistently puzzling to TODCOR are the eclipsing binaries. One reason for this is that they tend to occupy the hotter parts of the CMD. Further, eclipsing binaries tend to mostly be found with small orbital separation, as this makes them more easily detectable at a wider range of inclinations. These short-period systems are prone to orbital synchronisation due to tidal forces (Lurie et al., 2017), leading to rapid rotation of the components, which dramatically smears out the spectral lines. Both of these mechanisms give rise to broad spectral lines, and thus a broad CCF peak, making analysis difficult. Further, as `Korg.jl` assumes LTE, stars towards the hotter end of the sample are more likely to suffer from poor approximation by the templates.

So far, we have been assuming that while *Gaia* may misidentify the type of spectroscopic

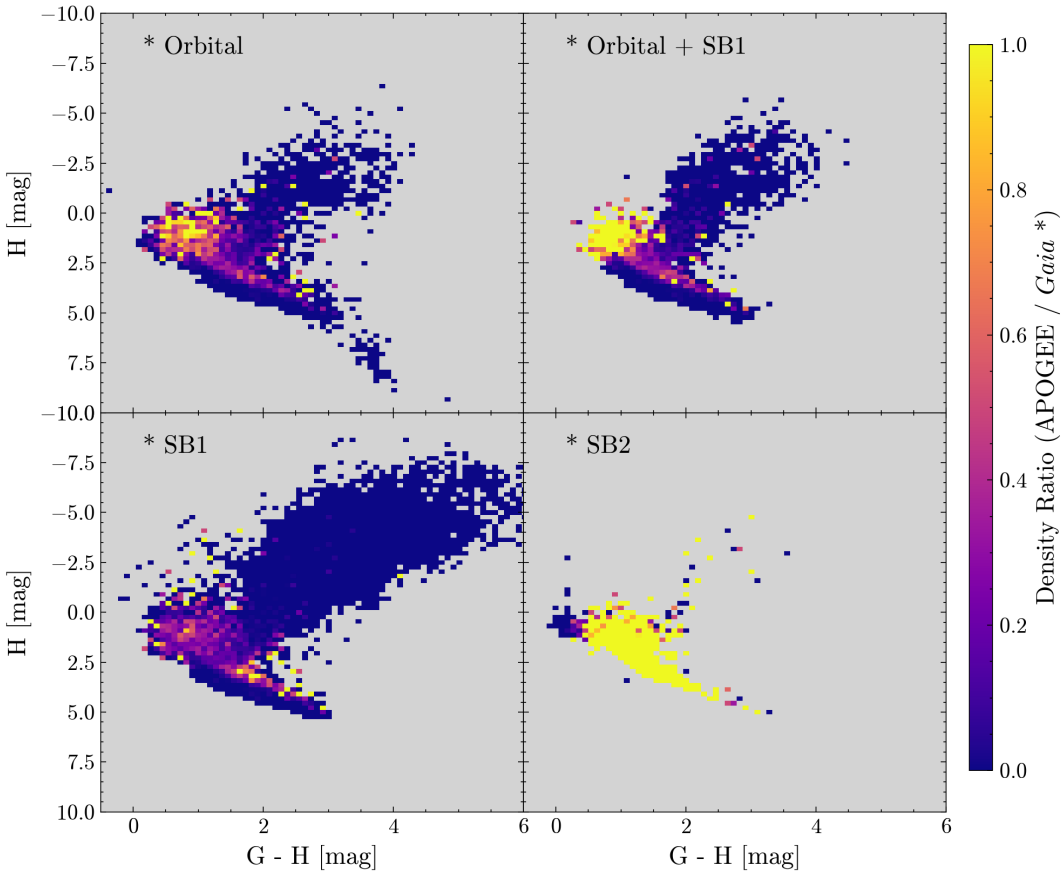

Figure 4.9: CMD of the density ratio of targets identified as SB2 in this work using APOGEE data over targets identified as astrometric, astrometric + SB1, SB1 or SB2 solution types by *Gaia* NSS.

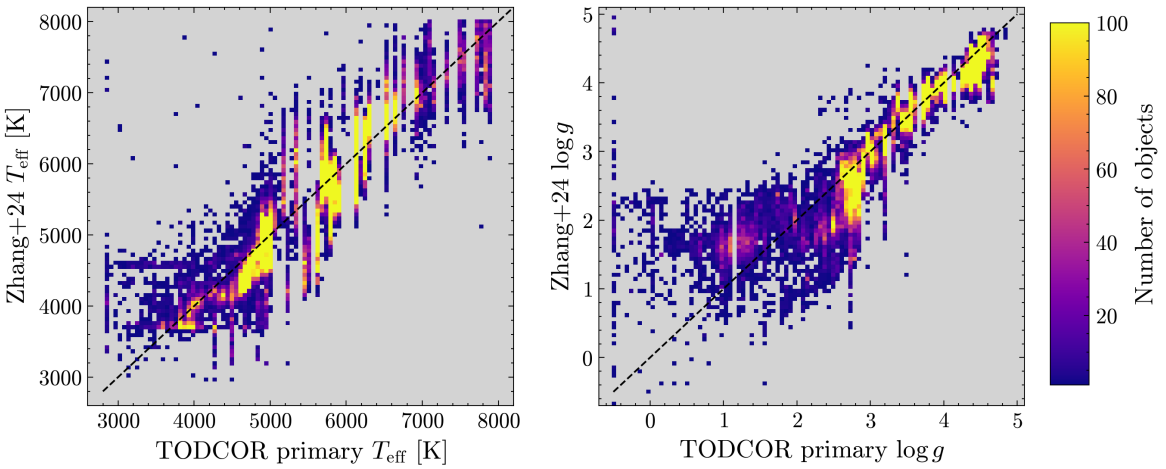

Figure 4.10: 2D histograms of spectral parameters of the primary determined in this work compared to Zhang and Green (2024). Left panel shows the effective temperature and right panel the surface gravity. The model used by Zhang and Green (2024) assumes a single star, thus we do not expect full agreement.

binary, its identification of a target as *any* kind of binary is generally correct. However, we have to consider the case that a target was spuriously identified as a binary, with the variability detected by *Gaia* that triggered the binary identification process being intrinsic or due to noise and not fit-able by an orbital solution. For *Gaia* spectroscopic binaries, multiple APOGEE spectra with no detectable RV variations, or variations small enough to fall within the expected noise, are a potential hint pointing towards this case. As APOGEE has higher spectral resolution than *Gaia* RVS, we expect RVs to be better resolved (given good S/N), unless the APOGEE observations suffer from very unlucky timing near phase 0 or π, where component velocities are very small. The more APOGEE visits of a target there are, however, the more unlikely it is that they were all taken during low RV phases.

Spectral Parameters In Figure 4.10, we compare the spectral parameters we recover for the primary to those determined by Zhang and Green (2024) from XP spectra assuming a single-star model. Due to this difference (binary vs single), we do not expect the parameters to be exactly the same; however, a strong deviation is concerning and points either at an issue with the assumption of a single star or with our fitting procedure. Generally, agreement seems to be good, with scatter around temperatures roughly constant with $T_{\rm eff}$, though there seem to be issues around 4500 K; there are both a range of systems that Zhang and Green (2024) assigned significantly different temperatures where the TODCOR fit suggests a $\sim$ 4500 K template, and vice versa. This is puzzling, and should be investigated further.

Considering surface gravities, we see that disagreements are larger for small $\log g$ than larger ones. This may be due to spectra being generally more sensitive to changes in temperature than in surface gravity. Due to the photometric constraints placed, MS stars are generally more constrained than giants, and precision when determining lower values of $\log g$ suffers as a consequence.

To more closely examine trends among spectral fits, we can explore the effect of the determined flux ratio. In figure 4.11, we show the agreement of parameters from Zhang and Green (2024) with our results from TODCOR for the SB2 targets, with the bins coloured

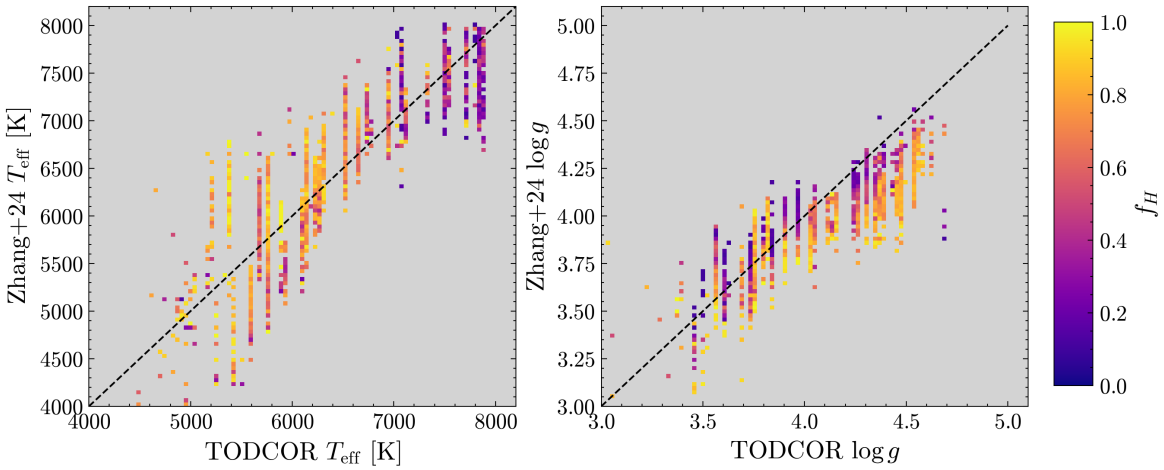

Figure 4.11: 2D histograms analogous to figure 4.10. Here, we only show TODCOR SB2 targets and have coloured each bin according to the average f_H found for targets in that bin.

according to the average H-band flux ratio of targets in that bin. For the effective temperatures, we see that the lowest flux ratios were determined for the highest temperatures; these targets are also generally associated with a poorer spectral fit due to issues with hot star spectra which have been discussed. Future work with an expanded template grid may reveal different trends.

In the right panel, we present the surface gravities, zoomed in on larger values of $\log g$ indicative of the MS, where most SB2 systems reside. Here, we note an interesting trend where systems with small flux ratios tend to lie along the diagonal, suggesting strong agreement between Zhang and Green (2024) and our parameters. This makes sense, as we expect binaries with little contribution from a secondary to be better approximated by single star models (such as those used by Zhang and Green (2024)) than those with significant light from the secondary. There is a slight tendency for Zhang and Green (2024) to report lower values of $\log g$ than TODCOR with larger flux ratios. This may be due to $\log g$ being mostly determined by the photometry (*Gaia* XP) and observed luminosity; a single-star solution must assume a larger stellar radius at the same temperature and luminosity than a binary fit. Consequently, Zhang and Green (2024) may infer a star that is further up the red giant branch and thus has a lower $\log g$.

4.3.3. Combining APOGEE with *Gaia* solutions

To refine astrometric solutions made using *Gaia* G-band data, we need to determine the flux ratio in this band (SB2), or place an upper limit (SB1).

About 5% of *Gaia* astrometric binaries showed evidence of SB2-ness in our analysis. We acquire the flux ratio in the G-band from the isochrones, which also provide masses for both components. Then, considering the *Gaia* astrometric solution as well as flux- and mass ratios, we can determine the semimajor axes of both components. As proof-of-concept, we select a number of targets with good SB2 spectral solutions (CCF peak > 0.7, all MS primaries), and associated *Gaia* NSS orbital solutions, and perform this computation. The left panel of figure 4.12 shows histograms of the photocentre, primary and secondary semimajor axes for our selected targets. We note that component semimajor axes are generally larger than photocentre semimajor axes; this is expected except when $f_H = 0$ (SB1), when the

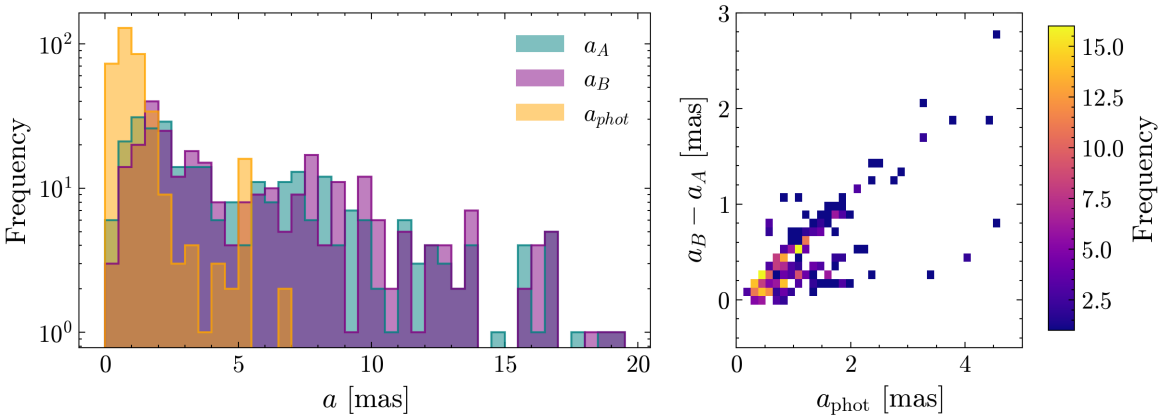

Figure 4.12: Left: Histogram of photocentre and component semimajor axes for a selection of TODCOR SB2 systems with an associated *Gaia* NSS astrometric solution. Primary, secondary and photocentre semimajor axes are shown in teal, purple and orange respectively. Right: 2D histogram of the difference in secondary and primary semimajor axes against that of the photocentre.

photocentre traces the primary. There is also a slight trend for larger secondary semimajor axes compared to the primary - this is unsurprising for $q < 1$, as is generally the case for non-interacting MS-MS SB2. This trend can also be observed in the right panel of the same figure, where we show a 2D histogram of the difference between the secondary and primary semimajor axes vs that of the photocentre. We may be seeing a double tail, with a population of (almost) twins where $a_A \approx a_B$ and one with smaller mass ratios where $a_B - a_A$ increases with $a_{\rm phot}$. However, more data is required to make any more definitive statements. To expand this procedure to the rest of the catalogue, we would first like to achieve a higher degree of confidence in our flux- and mass ratios; ideally via better spectral fits using a more comprehensive set of templates.

For SB1, we need to place an upper limit on the G-band flux ratio. Using APOGEE data and PARSEC isochrones, we can constrain the flux ratios of SB2 targets in the H-band. Figure 4.13 shows a histogram of the H-band flux ratios found for our SB2 targets in purple. By requiring that the maximum CCF peak be larger than 0.7, we can exclude solutions that have a poor spectral fit (due to e.g. rotation). We re-plot the histogram with only the "good" solutions in teal. Inspecting the plot, we see a dearth of solutions with $f_H < 0.2$ for the "good" solutions, suggesting SB2 solutions with smaller flux ratio achieve only a poor fit. We thus take $f_H = 0.2$ as the upper limit for the flux ratio of SB1 solutions. Of course, this limit depends strongly on the S/N and spectral type of the stars, but for an initial exploration of the sample, a flat limit is sufficient. As stated, for MS primaries the flux ratio is unlikely to be larger in the G-band than the H-band unless the secondary is a white dwarf.

Finally, we can use the RVs determined in this work to confirm or refine an existing *Gaia* orbital solution. In figure 4.14, we compare the epoch velocities of both components acquired for different observations of a single target, to the phase-shifted *Gaia* spectroscopic orbital solutions. This presents a test case of the procedure. We also differentiate between epochs where TODCOR identified the system as SB1 vs SB2. As *Gaia* identified this target as SB1, we compute the orbit for the secondary by taking $K_B = -K_A/q$, with K_A and K_B the primary (from *Gaia*) and secondary velocity semi-amplitude, respectively, and q the average mass ratio computed over all epochs where the system was identified as SB2.

We see good agreement between the model and our data for the primary, increasing our

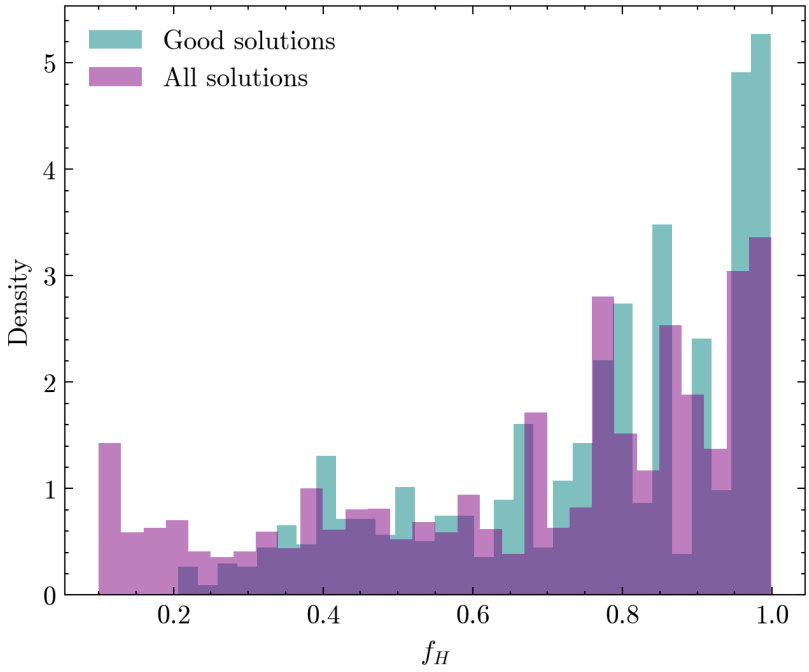

Figure 4.13: Histograms of the flux ratio in the H-band for our SB2 targets. We show the overall sample (purple) as well as a subsample with poor spectral fit (CCF peak < 0.7) removed (teal). We see that the low-f_H tail present in the overall sample disappears when removing bad solutions, leading us to adopt a limit of $f_H = 0.2$.

confidence both in the *Gaia* model and our velocities. We find that our observations suggest a larger secondary semi-amplitude than acquired by taking $K_B = -K_A/q$. This discrepancy may be due to an underestimation of q, which is only constrained by the isochrones. Furthermore, we note that the epochs where we fail to discern the target as SB2 are those where the primary and secondary RV are very close to each other, likely leading to line-blending and prohibiting TODCOR from determining two CCF peaks. The data imply that we can usually resolve RV separations down to $\approx$ 10 km/s. A future multi-epoch approach that computes a joint fit for all observations of the same target may help in producing more self-consistent results (such as employed in Seeburger et al. (2024)).

4.4. Conclusions and Future Work

In this work, we set out to demonstrate the capability of single-epoch APOGEE spectra to determine spectral parameters for a wide variety of binaries using the TODCOR algorithm. We explored over 80,000 spectra, treating them individually, and using PARSEC isochrones and *Gaia* and 2MASS photometry to place physically informed priors on the analysis. We found generally good agreement between the binary categories determined in this work compared with *Gaia* NSS. There were a number of systems identified as SB2 by *Gaia* which we did not classify as such; in several cases, the best-fit CCF did show two peaks, but the secondary peak fell below the threshold adopted by us. However, in a number of cases there was no clear secondary peak, suggesting either an unlucky timing of the observation near a low-RV phase, or perhaps an issue in the *Gaia* identification. On the flipside, we clearly identify a number of *Gaia* SB1s as SB2s, demonstrating the power of even single-epoch

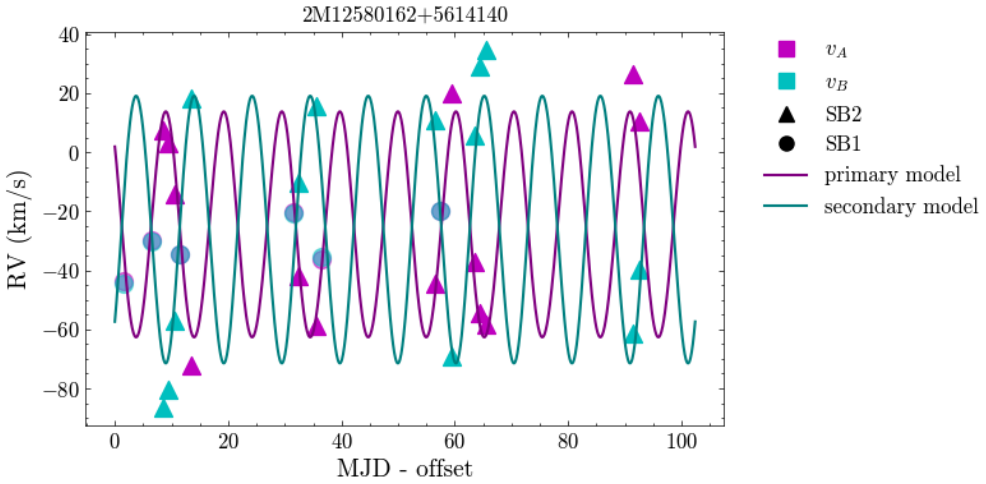

Figure 4.14: RVs of the primary (magenta) and secondary (cyan) for the MS-MS SB2 target, as well as the *Gaia* spectroscopic orbital solution (purple and teal lines for the primary and secondary respectively), shifted in phase to match the observations. Epochs where TODCOR identified the system as SB1 are shown with circles, SB2 with triangles.

high resolution observations in potentially classifying spectroscopic binaries.

There are a number of obvious extensions to this initial, exploratory work:

- Expand the catalogue of model spectra by considering metallicity, rotation, and higher temperatures. This will allow us to achieve better spectral fits, particularly for stars that are currently poorly approximated by the set of templates; either because their rotation is significant, their metallicity is non-solar, or their temperatures are in excess of those covered by `Korg.jl`. These stars are likely interesting targets for further study. Objects with good S/N where the algorithm performs poorly even with an expanded template set warrant closer examination. They might exhibit exotic features such as emission lines or be subject to data issues that are important to address.

- Determine the coherence of parameters obtained for different observations of the same system. In principle, barring variable stars, the spectral parameters for each component should remain the same across observations, as should the flux ratio of the system. Large discrepancies between the acquired parameters for different epochs may point towards a high sensitivity to noise or systems outside of the explored parameter space, allowing us to better quantify our certainty in the results. Further, obtaining multiple RVs for the same system, we can attempt to fit an orbit. This can serve two purposes. First, to constrain orbital parameters and compare e.g. the dynamical mass ratio to that implied by the photometry + spectral fit. Second, to contrast with the *Gaia* orbital solution, if it exists, and, if in concordance, use the additional data to tighten constraints on the parameters.

- Select MS SB1 systems with *Gaia* astrometric solutions and cross-match with GALEX UV photometry to rule out potential white dwarf secondaries. For systems without UV excess, take the G-band flux ratio to have an upper limit equal to the upper limit determined here in the H-band, and use this information to fully solve the astrometric orbit. For systems with UV excess, attempt to constrain the radius and temperature

of the white dwarf companion to derive a flux ratio in the G-band and proceed with refining the astrometric solution.

- For all SB2 systems with *Gaia* astrometric solutions, use the G-band flux ratio determined from the H-band flux ratio and spectral models, as well as the mass ratio from isochrones, to fully solve the orbit.
- Utilise the *Gaia* selection function and orbital solutions to query if the distributions of SB1, SB2 and other systems determined in this work is consistent with our understanding of the population of stellar multiplicity distribution functions. Further, test if distributions of orbital parameters among SB1 and SB2 is consistent with values reported in the literature.

Acknowledegments RS, HWR, JMH, JV, JL and BP acknowledge support from the European Research Council through ERC Advanced Grant No. 101054731.

This publication made extensive use of the online authoring Overleaf platform (`https://www.overleaf.com/`).
The data processing and analysis made use of `matplotlib` (Hunter, 2007), `NumPy` (Harris et al., 2020), the `IPython` package (Perez and Granger, 2007), `SciPy` (Virtanen et al., 2020) and `AstroPy` (The Astropy Collaboration et al., 2013, 2018, 2022)

5

Conclusions and Outlook

5.1. Summary

In this thesis, we set out to develop and thoroughly test methods to analyse the spectra of binary stars, with a focus on systems containing a dormant BH.

In Chapter 1 we laid out the current state-of-the-art in binary stellar research, as well as (dormant) stellar BHs. We explored the important mechanisms affecting binaries that differentiate their evolution from single stars (mergers, MT, CE, ...) as well as pointing towards open questions in the field. We discussed common observational techniques used to obtain information about binary systems (spectroscopic, astrometric and photometric), their strenghts, shortcomings, what kind of information they yield and how this applies to the search for dormant BHs.

Chapter 2 outlined the development of the main tool employed in this thesis, the spectral disentangling pipeline. We described the underlying algorithm, and its implementation, as well as taking note of the adaptations made to tailor the code to large survey applications. The pipeline was then rigorously tested on synthetic binary spectra set up to resemble BOSS spectra to explore its efficacy at 1) determining the two components contributing to the composite spectrum and 2) discerning important system parameters such as the mass ratio and RVs of the components. We also applied the same pipeline to real high-resolution data of confirmed impostor (star-star) systems ("Giraffe" (Jayasinghe et al., 2022) and "Unicorn" (Jayasinghe et al., 2021)) to demonstrate its capabilities in differentiating them from genuine dormant BH candidates. Additionally, we explored the same data artificially reduced to $R \sim 2000$, to illustrate that even in this lower resolution regime, some conclusions could still be drawn about the system, and a secondary spectrum could be recovered, though spectral parameter determination was, unsurprisingly, more difficult.

Chapter 3 zoomed in on an application of the spectral disentangling pipeline to a set of post MT "impostor" systems previously identified as SB1 systems by the *Gaia* NSS pipeline (El-Badry and Rix, 2022). We gathered and analysed multi-epoch spectra for 6 of these targets, using the spectral disentangling pipeline developed in chapter 2. This revealed their true SB2 nature, with all systems consisting of a cooler, bloated donor of exceptionally low mass ($<0.5\ M_\odot$ in all cases) which had previously transferred some of its envelope to the hotter, now rapidly rotating accretor, inverting the mass ratio. This led to the mass

of the overluminous donor being misidentified, thus implying a much higher mass for the accretor than is actually the case. Further, due to its rapid rotation, the accretor's lines are very smeared out and difficult to detect with template-based methods. Spectral disentangling however clearly revealed its signature in multi-epoch spectroscopic data, allowing us to constrain both component's temperatures and rotation rates. Puzzlingly, while the accretor is spinning quickly in all targets, the rotation is consistently sub-critical (even considering inclination effects). Traditional models of angular momentum transfer suggest the MT should have spun it up to critical rotation (Packet, 1981). Given that rotation is sub-critical, the accretors must have either 1) slowed down after MT ended or 2) not reached critical rotation in the first place. Option 1) is unlikely, as mechanisms to slow down stellar rotation are either too inefficient to explain the current observations (tidal synchronisation (Zahn, 2008)), or do not apply to the temperature range the accretors occupy (magnetic braking (Kraft, 1967)). Thus, mechanisms by which angular momentum is transferred require re-assessment, potentially favouring models that limit the angular momentum gained by the accretor, such as via interactions with an accretion disk (Popham and Narayan, 1991).

Chapter 4 treated the analysis of over 80,000 APOGEE spectra whose targets have a *Gaia* non-single star solution. We used isochrones to place physical constraints on the spectral parameters and flux ratios of pairs of templates to be used with the TODCOR algorithm (Zucker and Mazeh, 1994). TODCOR performed 2-dimensional cross correlation with each photometrically feasible pair of templates to determine 1) the best-fit pair, its associated flux ratio and each component's $T_{\rm eff}$ and $\log g$, 2) each component's shift for the spectrum in question, 3) the classification of the binary as single- or double-lined, or in need of further analysis. We found that a single epoch can frequently identify an SB2 system as such, highlighting the value of even few-epoch studies for binary identification. Additionally, spectral parameters recovered for the primary with TODCOR were found to be in general agreement with parameters derived for a single-star model from Zhang and Green (2024). Going forward, multiple visits of the same target may be combined to derive a spectroscopic orbital solution or refine an existing *Gaia* spectroscopic or astrometric orbit. Further, flux ratios (for SB2) and flux ratio upper limits (for SB1) may be used in conjunction with *Gaia* astrometric solutions to fully solve the astrometric orbit of each visible component.

5.2. Future Prospects

5.2.1. *Gaia* DR4

Gaia performed its last observation on the 10th of January 2025, and was decommissioned on the 27th of March of the same year. However, much of the data gathered by the satellite over the past decade has not yet been released, including the majority of RVS spectra. DR4 is expected to arrive in 2026, and will, among many other data, contain about 100 million RVS spectra at a resolution of $R \sim 11,500$. This dataset will allow for statistical analysis of various types of systems at both unparalleled volume and detail. Importantly, within the frame of this work, the multi-epoch observations of binary targets will allow spectral disentangling to be performed on an industrial scale, revealing millions of systems as SB2s or SB1s in a data-driven way. This will allow us to do a number of things:

- Independently analyse the constituents of the SB2 systems, ascertaining each component's effective temperature, surface gravity, and rotational velocity. This will provide

a large catalogue of well-characterised binary systems, deepening our understanding of their period and mass ratio distributions.

- Identify exotic systems containing stripped stars in different mass regimes. Currently, the list of known stripped stars is short, but they form a crucial component of binary stellar evolution. Expanding the catalogue of known systems and determining their properties (temperature, hydrogen fraction, rotational velocity) will allow for huge advances in the field of stripped star research, and, by extension, binary evolution research.

- Analyse binary interaction products. By placing constraints on current mass ratios, periods, and stellar rotation rates, the histories of the systems can be explored. This will allow us to constrain important parameters such as MT conservativeness, stellar spin-up effectiveness and the various spin-down mechanisms at work (magnetic braking, tidal synchronisation, ...)

- Identify potential SB1 systems with unseen but massive companions. Where disentangling suggests the system contains only one luminous component, but the spectroscopic orbital or a supplementary astrometric orbital solution suggests a massive companion, a compact secondary may be present. High-resolution spectroscopic data can place tight constraints on the velocity of the primary and be combined with spectroscopic or dynamical mass (-ratio) estimates to infer the mass of the secondary. This will allow us to potentially find many more dormant BH and NS candidates, filling the current gap in our understanding of the evolution from stellar binaries to gravitational wave mergers.

- The number of COs found will also allow us to revise and refine our current binary population models. Over the last few years, predictions for the number of dormant BHs found with *Gaia* have gotten more conservative, but still optimistic compared to the actual number found (see figure 5.1). Even if we find no further COs, we can assess the correctness of our current models predicting the formation of these systems, given the sheer size of the *Gaia* DR4 sample and the likelihood of a null detection given predicted CO frequency and orbital configuration. Ultimately, this will shed light onto critical but poorly understood in CO formation, such as massive star wind loss and SN birth kicks.

5.2.2. Other surveys & Data

Gaia is not the only large survey set to release a treasure trove of data in the coming years. WEAVE (Dalton et al., 2012), 4MOST (de Jong et al., 2019), SDSS (Kollmeier et al., 2017) and DESI (DESI Collaboration et al., 2016) are all set to provide or have already released large spectroscopic datasets of (among others) Milky Way targets, an appreciable fraction of which will be binary stars. For SDSS-V, we expect multi-epoch spectra for around 380,000 OBA stars (Kollmeier et al., 2017), drawn from (Zari et al., 2021), fantastic candidates for potential massive star, binary and CO studies.

Much of what has been said about *Gaia* DR4 also applies to these surveys in terms of possible science goals achievable with these data. Of course, there are notable differences between all these datasets, particularly with regards to volume surveyed, number of epochs

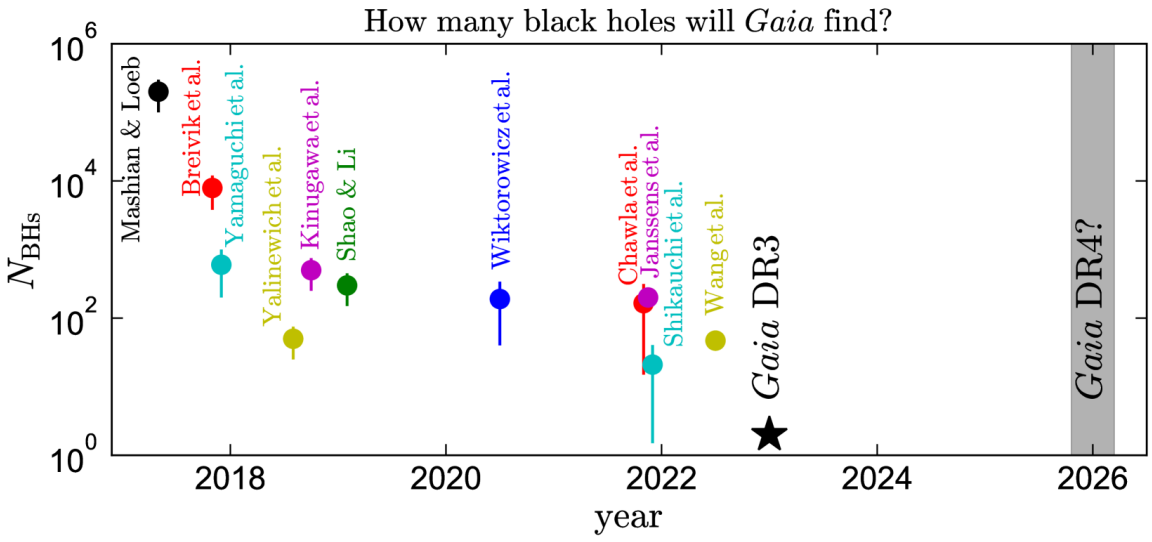

Figure 5.1: Predicted number of dormant BHs found by *Gaia* from various population models by publication time. Also shown is the actual number of systems found in *Gaia* DR3, as well as an approximate timeframe for the release of *Gaia* DR4. Figure from El-Badry (2024)

per object gathered, expected S/N, spectral resolution and wavelength coverage. Regardless, the binary spectroscopist will not be wanting for data in the coming years and decades.

Further, there are many currently ongoing efforts among individual researchers and groups to obtain high-quality spectra for likely CO targets (see section 1.4 for a summary of some of them), as well as post MT binaries (*UVES observations of (post-) mass transfer binaries*, 0115.D-0130(A); PI: R. Seeburger & *FEROS observations of low mass (post-) mass transfer binaries*, 0114.D-6017(A); PI: R. Seeburger, to name just two). These high-resolution data will allow us to constrain crucial parameters such as stellar rotation as well as detect potential ongoing MT to further elucidate binary interaction processes.

5.2.3. Stellar clusters

This thesis and much of the projected future work has focused on stars in the Milky Way field, where stellar density is comparatively low and star-star interactions (outside of bound systems) are rare. However, many stars live in dense associations, such as globular clusters, where interactions are frequent and impact both the evolution of the stars and the dynamics of the cluster. Binaries are able to impart their orbital energy into the potential of the cluster, shaping its evolution over astronomical timespans. Additionally, due to the cluster's short relaxation timescale, interactions are common, and as binaries have a large cross-section compared to single stars, they are particularly likely to experience these encounters. This can result in the binary being disrupted, but may also increase the binding energy of the system, providing a potential explanation for the large number of rapidly rotating Be stars found in young clusters (Wang et al., 2020). Dynamical exchange of objects in bound systems within a cluster can create exotic binaries not reproducible by standard binary evolution, such as very massive BHs in tight orbits with MS stars. Star clusters are also the birth places of a majority of massive stars, which are both much more likely to live in multiple systems than their lower-mass siblings, and are potential progenitors for COs. Their importance for both binary studies and research into BHs and NSs thus cannot be overstated.

By applying the methods detailed in this thesis to the fascinating environment of globular clusters, we can shed light on some of the unanswered questions both on the effect of the cluster environment on binaries within and the effect of these binaries on cluster dynamics and evolution.

A

Appendices for Chapter 2: 'Autonomous Disentangling for Spectroscopic Surveys'

A.1. Method - Further Detail

A.1.1. Normalisation

Spectra are generally normalised before analysis is performed. Here, we seek to perform continuum normalisation, where each datapoint is divided by the continuum value at its position. Since the distance from a star is comparatively hard to determine accurately, it is advantageous to remove it as a fitting parameter from the problem. Continuum normalisation aids in doing that, by removing information about the specific flux at each pixel, while still retaining the important information contained in the line depth relative to the continuum.

Generally, for continuum normalisation, a polynomial or spline is fit to the spectrum, representing the low-frequency variations, and then subtracted. In this work, each datapoint is divided by the median value of Q pixels around it, where the value of Q governs what this normalisation looks like. Q values close to N_{px} will lead to a normalised spectrum that mostly keeps its shape, but now has an average flux near 1. Q values close to 1 will lead to a flattening out of the entire spectrum, and a loss of features; it is thus important to choose the size of Q correctly. More specifically, the window needs to be wide enough to fully cover the wider lines in the spectrum as not to create "humps" or "wings" on either side when normalising, but narrow enough to efficiently remove the shape of the continuum. Further, when normalising in this manner, we wish to ignore pixels with associated NaN flux values.

Finally, we subtract 1 from the normalised spectrum. This leads to an average flux near 0, with emission lines extending above, and absorption lines below 0. We do this to effectively remove low-frequency variations from the disentangling process completely, and allow the lines to dominate the process.

A.1.2. Interpolation

As in the disentangling prescription used in this work, the shifts $\Delta\Lambda$ are not necessarily of integer pixel value, we need a way to evaluate the component spectra at intermediate pixel values; for one component, this can be achieved by linear interpolation as follows:

$$x(\Lambda) = r_j \cdot x(\Lambda_{n+1}) + (1 - r_j) \cdot x(\Lambda_n), \tag{A.1}$$

where Λ is some intermediate wavelength between Λ_n and Λ_{n+1}, and r_j a shift-dependent (and thus epoch-dependent) interpolation factor given by

$$r_j = \frac{\Lambda - \Lambda_n}{\Lambda_{n+1} - \Lambda_n}. \tag{A.2}$$

Here, the numerator represents the distance of the wavelength at which we want to evaluate, Λ, from the nearest lower integer pixel wavelength Λ_n, and the bottom represents the distance between two integer pixel wavelengths. r_j thus gives the fractional distance between Λ and Λ_n. The relative contribution of the spectrum at Λ_n to the linearly interpolated spectrum at Λ is then $1 - r_j$, the complement of r_j to unity. Thus, the fractional contribution of the spectrum at Λ_{n+1} to the linear interpolation at Λ is r_j.

This makes intuitive sense: if the interpolated point is close to Λ_n, r_j is close to 0, and most of the contribution to $x(\Lambda)$ comes from $x(\Lambda_n)$, thus its associated coefficient $(1 - r_j)$ is close to 1, while $x(\Lambda_{n+1})$'s coefficient (r_j) is close to 0. Conversely, if the interpolated point is close to Λ_{n+1}, r_j is close to 1, and most of the contribution to $x(\Lambda)$ comes from $x(\Lambda_{n+1})$, thus its associated coefficient (r_j) is close to 1, while $x(\Lambda_n)$'s coefficient $(1 - r_j)$ is close to 0.

At this point, it should be noted that this also needs to work if the shift is larger than 1 pixel. For shifts between -1 and 1 pixels, Λ_n and Λ_{n+1} are simply the original pixel, and the one to the left/right of it. For larger shifts, the pixels need to be chosen accordingly, such that they "bracket" the intermediate pixel.

This linear interpolation can be generalised to higher orders, using a lagrange polynomial:

$$x(\Lambda) = \sum_{o=0}^{O} w_o(\Lambda) \cdot x\left(\Lambda_{o'}\right), \tag{A.3}$$

where O is the order of the polynomial,

$$o' = o - f_j^K - \mathrm{int}\left(\frac{\mathrm{O}}{2}\right). \tag{A.4}$$

Here, f_j^K is the result of the floor operation on the wavelength shift in pixels of component k at epoch j. Then, w can be computed from:

$$w_o(\Lambda) = \prod_{\substack{0 \le m \le O \\ m \neq o}} \frac{\Lambda - \Lambda_{m'}}{\Lambda_{o'} - \Lambda_{m'}}, \tag{A.5}$$

with

$$m' = m - f_j^K - \mathrm{int}\left(\frac{\mathrm{O}}{2}\right). \tag{A.6}$$

In the case of $O = 1$, this reduces to the linear case discussed above.

Using the interpolation, Eq. 2.5 can then be written as:

$$\vec{c}_{j,pred} = \Big(\{r_j^A \cdot x^A(\Lambda^A_{j,n+1}) + (1 - r_j^A) \cdot x^A(\Lambda^A_{j,n})\Big) + \Big(r_j^B \cdot x^B(\Lambda^B_{j,n+1}) + (1 - r_j^B) \cdot x^B(\Lambda^B_{j,n})\}\Big). \quad \text{(A.7)}$$

A.1.3. Matrix Structure: Details

The index of the first non-zero element in the first row of each block of **M** depends on the size of the shift.

Let s_j^K be the shift of the spectrum of component k at epoch j in units of the resolution element δ:

$$s_j^K = \frac{\Delta\Lambda_j^K}{\delta}. \quad \text{(A.8)}$$

We then make use of the $floor(m)$ operation, which returns the next lowest integer for any number m; for example, $floor(3.2)$ returns 3, $floor(-1.5)$ returns -2, $floor(0.7)$ returns 0, etc. For component k at epoch j, then:

$$f_j^K \equiv floor(s_j^K) \quad \text{(A.9)}$$

$$r_j^K \equiv s_j^K - f_j^K. \quad \text{(A.10)}$$

Here, r_j^K gives distance in the positive Λ direction from f_j^K for each s_j^K - specifically, this r_j^K is equal to the r_j^A or r_j^B in Equation A.7. f_j^K, then, is the nearest lower integer pixel for each shift s_j^K, meaning $\Lambda_{i+f_j^K}$ is equivalent to $\Lambda^A_{j,n}$ or $\Lambda^B_{j,n}$ in Equation A.7. It gives the index of the first non-zero element of the first row of each block of **M**, or, equivalently, the shift of the (off-)diagonal. The values of this (off)diagonal are $1 - r_j^K$. Consequently, $\Lambda_{i+f_j^K+1}$ ($\equiv \Lambda^A_{j,n+1}$ or $\Lambda^B_{j,n+1}$ in Equation A.7) gives the index of the second non-zero element of the first row of each block of the matrix, or the shift of its associated (off-)diagonal, with values r_j^K.

For a shift in the negative Λ direction that is smaller than 1 integer pixel, the block for component k and epoch j would look as follows:

$$\begin{pmatrix} 1-r_j^K & r_j^K & 0 & 0 & 0 & ... \\ 0 & 1-r_j^K & r_j^K & 0 & 0 & ... \\ 0 & 0 & 1-r_j^K & r_j^K & 0 & ... \\ 0 & 0 & 0 & 1-r_j^K & r_j^K & ... \\ ... & ... & ... & ... & ... & ... \end{pmatrix}$$

For a shift in the negative Λ direction that is between 1 and 2 integer pixels, the block for component k and epoch j would look as follows:

$$\begin{pmatrix} 0 & 1-r_j^K & r_j^K & 0 & 0 & ... \\ 0 & 0 & 1-r_j^K & r_j^K & 0 & ... \\ 0 & 0 & 0 & 1-r_j^K & r_j^K & ... \\ 0 & 0 & 0 & 0 & 1-r_j^K & ... \\ ... & ... & ... & ... & ... & ... \end{pmatrix}$$

For a shift in the positive Λ direction that is smaller than 1 integer pixel, the block for component k and epoch j would look as follows:

$$\begin{pmatrix} r_j^K & 0 & 0 & 0 & 0 & ... \\ 1-r_j^K & r_j^K & 0 & 0 & 0 & ... \\ 0 & 1-r_j^K & r_j^K & 0 & 0 & ... \\ 0 & 0 & 1-r_j^K & r_j^K & 0 & ... \\ ... & ... & ... & ... & ... & ... \end{pmatrix}$$

The task of disentangling the composite spectra from all epochs into two rest-frame spectra can then be expressed as a minimisation of the sum over epochs:

$$\vec{x}_{best} = \underset{\vec{x}^A,\vec{x}^B}{\arg\min} \sum_j^{N_{ep}} ||\vec{x}_j^A + \vec{x}_j^B - \vec{c}_j||_2. \tag{A.11}$$

This can be written, more explicitly, as the sum over epochs and pixels:

$$\vec{x}_{best} = \underset{\vec{x}^A,\vec{x}^B}{\arg\min} \sum_j^{N_{ep}} \sum_i^{N_{px}} ||x^A(\Lambda_{j,i}^A - \Delta\Lambda_j^A) + x^B(\Lambda_{j,i}^A - \Delta\Lambda_j^B) - c_j(\Lambda_i)||_2. \tag{A.12}$$

Then using the interpolation described, as well as the notation in Equation A.10, we get:

$$\begin{aligned} \underset{\vec{x}^A,\vec{x}^B}{\arg\min} \sum_j^{N_{ep}} \sum_i^{N_{px}} ||(r_j^A \cdot x^A(\Lambda_{i+f_j^A+1}) \\ + (1-r_j^A) \cdot x^A(\Lambda_{i+f_j^A}) \\ + r_j^B \cdot x^B(\Lambda_{i+f_j^B+1}) \\ + (1-r_j^B) \cdot x^B(\Lambda_{i+f_j^B}) - c_j(\Lambda_i)||_2. \end{aligned} \tag{A.13}$$

A.1.4. Selection and scaling of optimisation parameters

For most optimisers it is advantageous to have normalised parameters. In this case, we are performing some rescaling by taking the common logarithm of q, and dividing all epoch velocities ($\vec{v}^A$) by 100. This ensures that the optimiser can take similarly large steps in different directions with relative ease, as well as changing the mass ratio to a more sensible scale - a step from a $q = 1$ to $q = 2$ is relatively large, meaning a doubling of the secondary mass, while a step from $q = 50$ to $q = 51$ will cause very little difference in the overall solution. In log-space however, steps of similar size have a more consistent effect along the parameter range.

Even with these considerations finding these parameters is not trivial, considering the dimensionality of the parameter space is frequently high. (Simon and Sturm, 1994), Hadrava (1995), Sablowski and Weber (2017) and others have suggested optimising over the orbital parameters instead, which can reduce the dimensionality of the problem to 7, which, in the case of many epochs, can be significantly less than fitting each epoch velocity individually. Here, however, we wish to demonstrate that even for a smaller number of epochs, spectral disentangling is viable, and thus optimise on the velocities and mass ratio.

A.1.5. TIRAVEL

If we wish to forgo using templates to find initial guesses for the velocities of the primary, or do not have suitable templates available, we can employ the TIRAVEL algorithm (Zucker and Mazeh, 2006) in order to find the relative inter-epoch velocities. This algorithm is most suitable to SB1s, or SB2s with comparatively faint secondaries. TIRAVEL achieves this by computing the cross-correlations between all epochs and then determining the velocitiy vector, with an offset, that solves for all the inter-epoch velocities by maximising the value of the CCF at the inter-epoch velocity shifts. The offset arises from the fact that this method employs no templates, and thus no knowledge of what a rest-frame spectrum looks like is included. In this implementation, we set the observed RV of the first epoch to 0, and then calculate the other RVs relative to this. Once TIRAVEL has computed a candidate velocity vector, we create an estimation of the primary's spectrum by shifting all epoch spectra by their relative RVs and co-adding the spectra. This should, in theory, minimise the contribution from the secondary (in an SB2) and boost the signal of the primary - being more efficient the more epochs are available.

The gross offset of all velocities from their true values might seem problematic at first, but we remind ourselves that the systemic velocity is corrected for in a later step in our disentangling pipeline. This also accounts for any constant offset among all velocities that arises due to TIRAVEL, and thus this should cause no further issues.

A.2. Additional Results

A.2.1. High Resolution Simulations

We repeat the simulations from section 2.3 for the same systems, but now with a higher resolution of $R \approx 20,000$. Here, the disentangler's difficulty with (close to) equal mass binaries becomes even more apparent, demonstrating that this is not a resolution issue. We also note that there are now fewer problems arising for small velocities (such as for the K=50 km/s systems), as the resolving power is now high enough to accurately determine even the smaller velocity shifts. Further, we see that the higher mass (3 M_{odot}) primary still generally poses a bigger challenge than the lower mass (1.1 M_{odot}) primary, again, due to the wider lines and fewer features overall.

A.2.2. The "Giraffe"

We perform "blind" disentangling on the Giraffe system, both in the native resolution regime of $R \approx 60,000$, and on spectra artificially reduced to $R \approx 2,000$, as with the Unicorn in section 2.3.2.

In Figure A.3 we see the performance of the optimiser on the parameters of the Giraffe in the higher resolution regime, with the wavelength window the same as for the Unicorn. Compared to the Unicorn, we note a markedly higher difficulty in recovering the light ratio correctly. This is likely due to the fact that the primary and secondary spectra of the Giraffe look more similar to each other than those of the Unicorn. Due to the rapid rotation of the Unicorn's secondary, the lines of that component are significantly broadened, leading to a somewhat non-typical spectrum that is quite distinct in shape from the spectrum of the primary. Here, however, the secondary is rotating much more slowly, thus this effect is

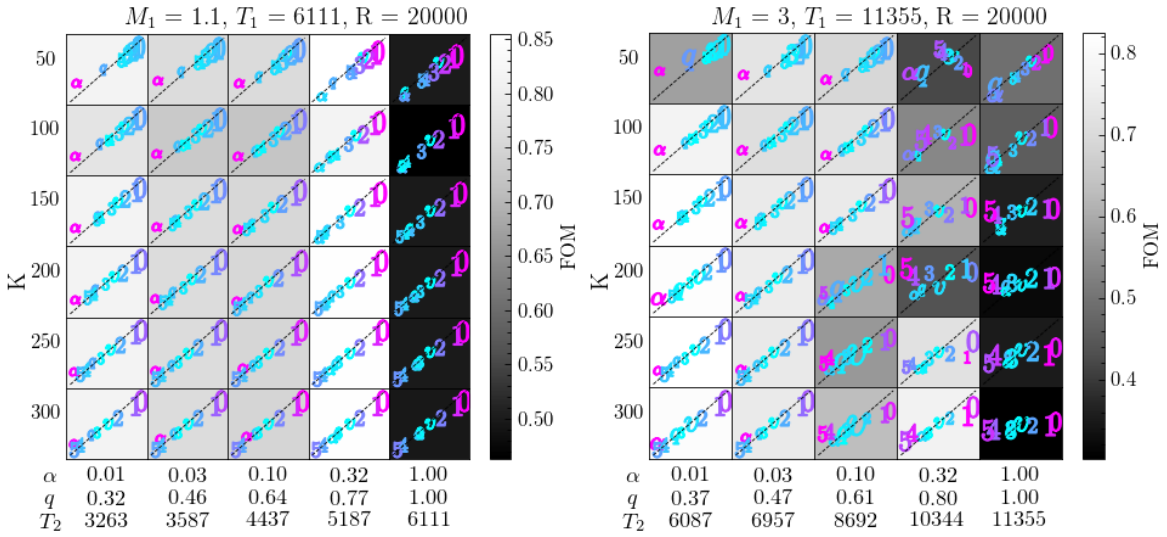

Figure A.1: As Figure 2.6, with a higher resolution of $R \approx 20,000$.

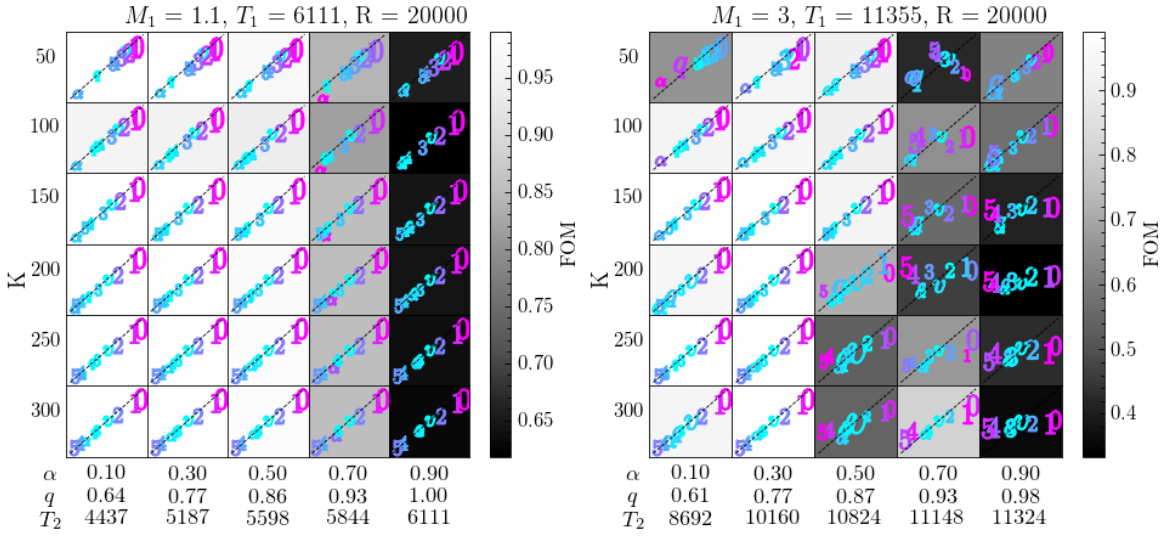

Figure A.2: As Figure 2.7, with a higher resolution of $R \approx 20,000$.

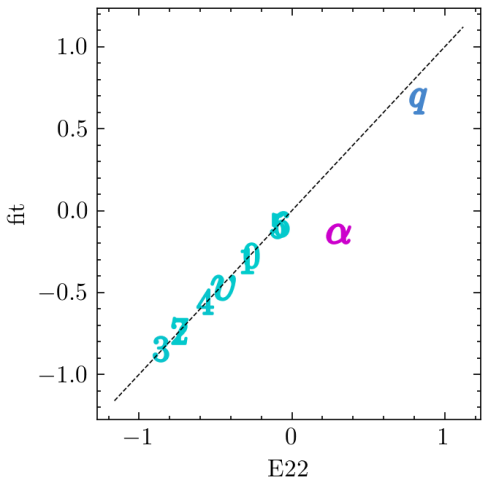

Figure A.3: The parameters of the giraffe as recovered by the optimiser (y-axis) compared to the ones found by E22 (x-axis). in the case of agreement, we expect the points for each parameter to lie on the grey, dashed, diagonal line.

minimal. Looking at Figure A.5 lends credence to this idea, as we can see the two spectra are fairly similar in shape. We also see the effect of the underestimation of the light ratio: relative to the E22 models, the lines of the primary spectrum appear deeper (meaning a larger fraction of total light is attributed to the primary, and thus the light ratio is lower).

Figure A.4 shows the performance of the optimiser on the data at the artificially reduced resolution, again on a larger wavelength window analogous to the Unicorn. We note the same difficulty with accurately assessing the light ratio, as well as some small issues with the velocities, and, resulting from this, the mass ratio, owing to the lower resolving power. The effects of the incorrect light ratio in particular become very apparent in Figure A.6. Many lines of the primary appear deeper in the E22 models than in the spectrum found here, due to the too-low light ratio found by the optimiser.

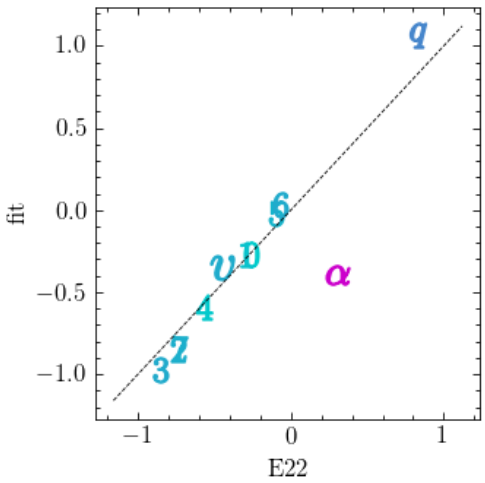

Figure A.4: Analogous to Figure A.3, with an artificially reduced resolution of $R \approx 2,000$.

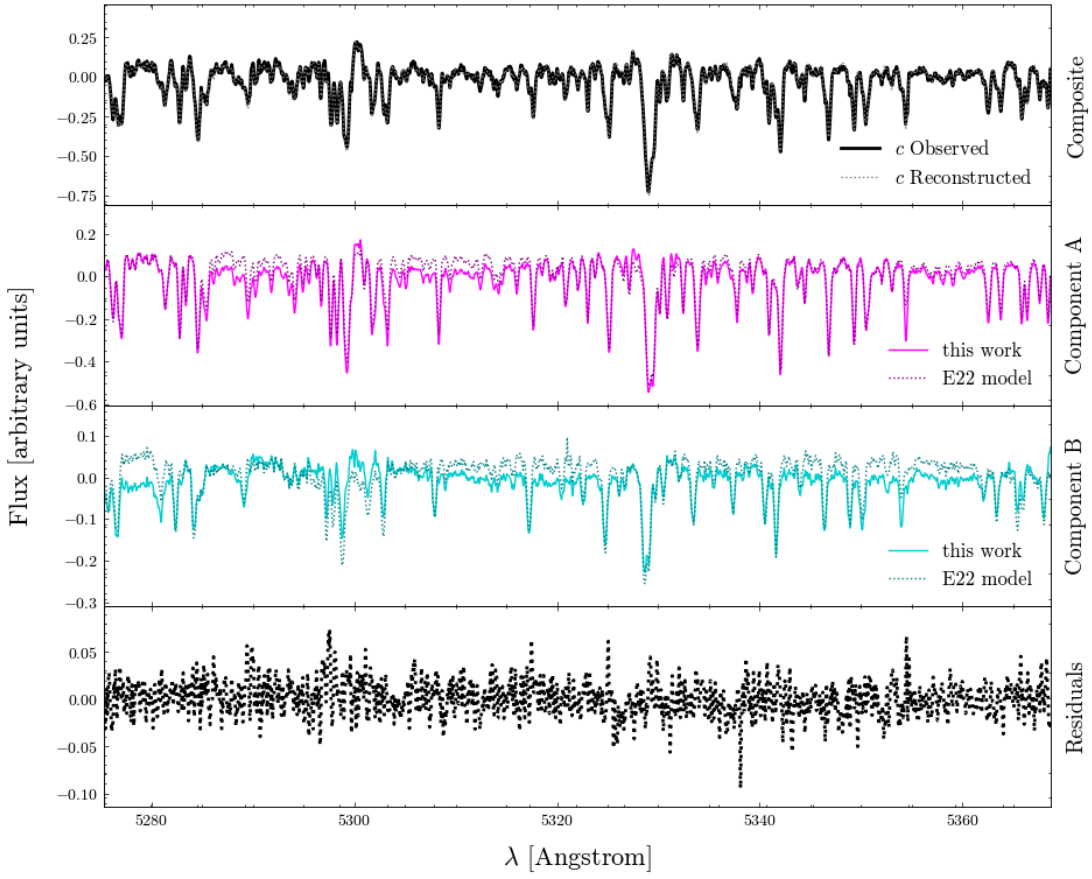

Figure A.5: The results of the autonomous disentangling applied to the Giraffe for one epoch. The top panel shows the observed spectrum (black, solid line) as well as the reconstruction from the velocity shifted disentangled component spectra (grey, dashed line). The other two panels display the disentangled rest-frame solutions for the primary and secondary, respectively, in magenta and cyan. The dashed, darker lines in these two panels indicate the model spectrum found by E22 to most closely fit the disentangled solutions found there. The bottom panel shows the residual between the reconstructed and observed composite spectra. We see generally good agreement between the solutions from this work and E22 models.

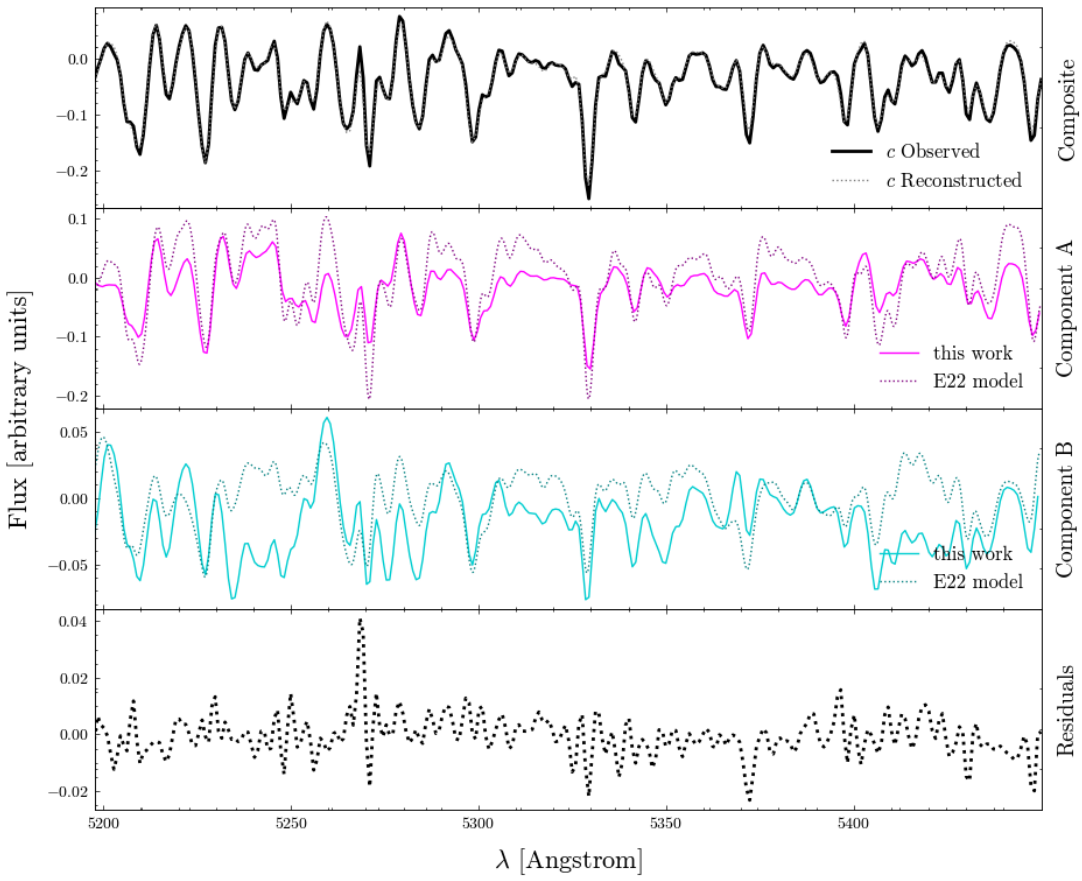

Figure A.6: Analogous to Figure A.5, with an artificially reduced resolution of $R \approx 2,000$.

B

Appendices for Chapter 3: 'The Physical Properties of Post Mass Transfer Binaries'

B.1. Supplemental material

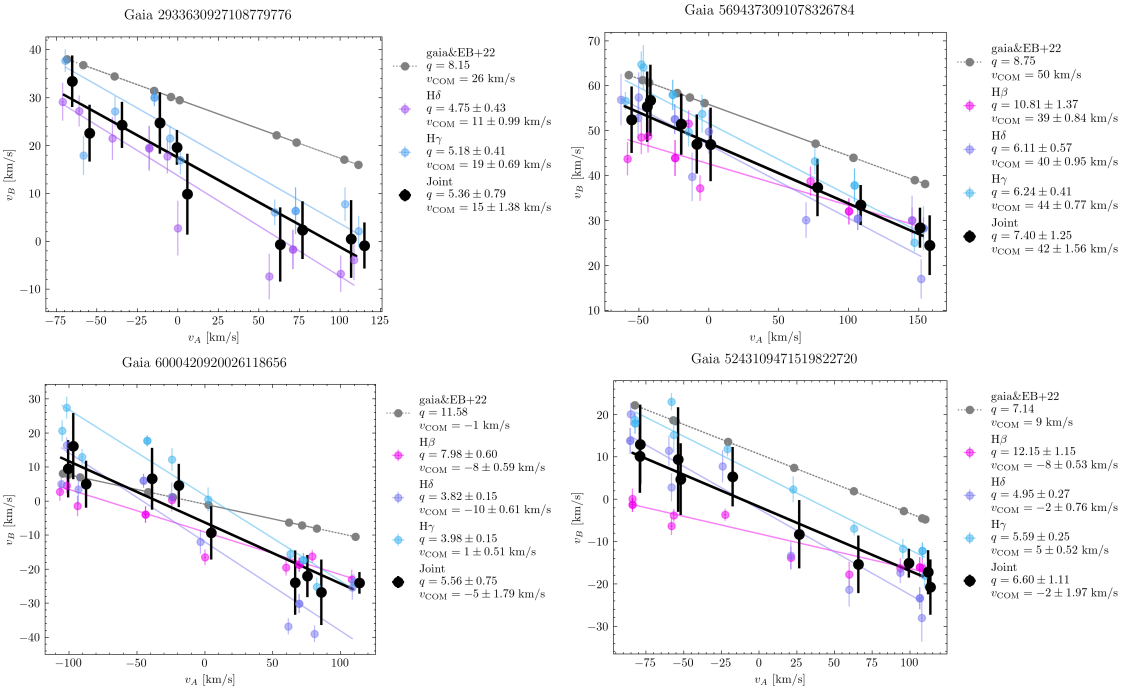

Figure B.1: Plots showing the results of the TODCOR (Zucker and Mazeh, 1994) algorithm applied to a number of targets, analogous to Figures 3.4 and 3.5

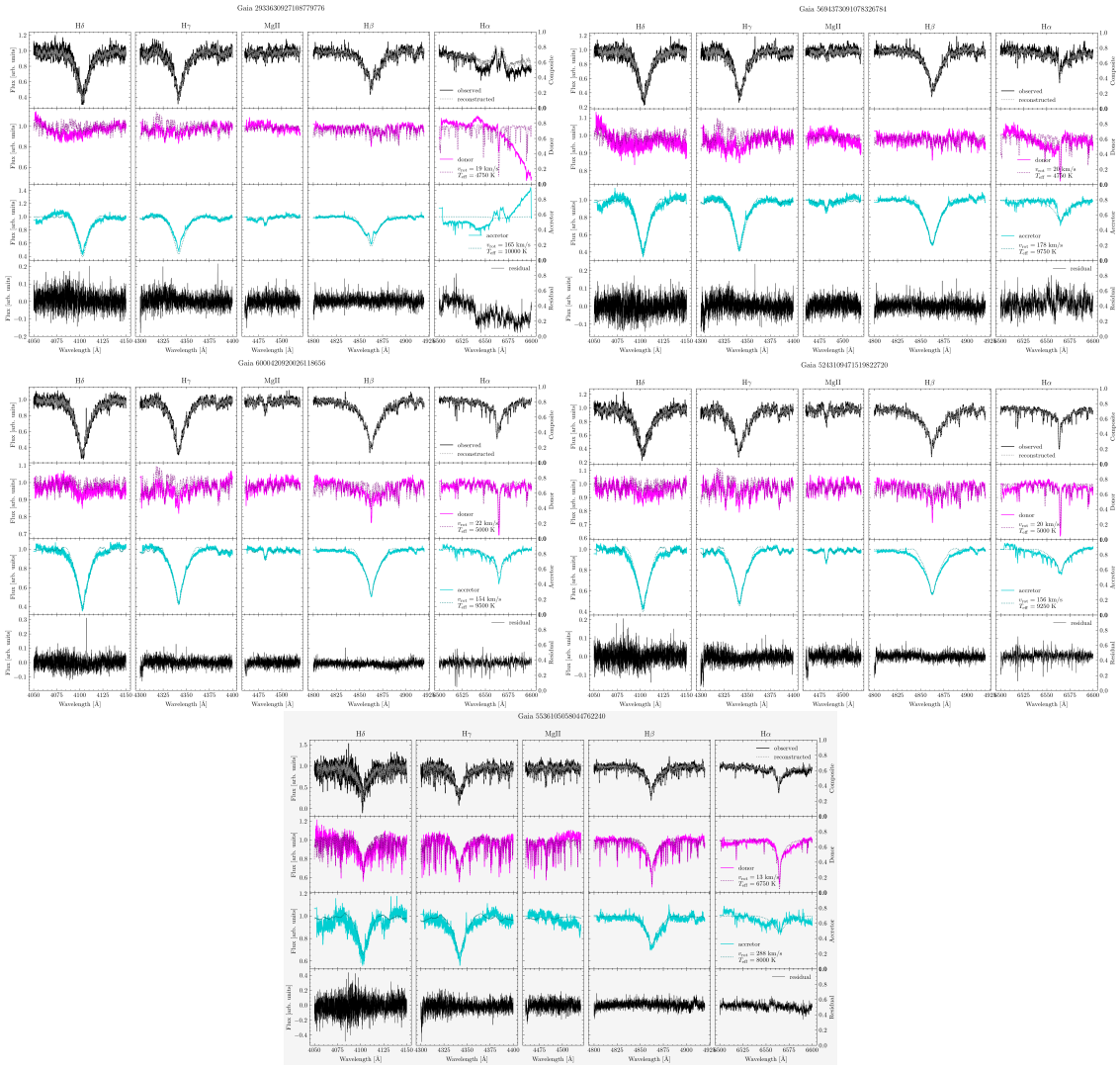

Figure B.2: Plots showing disentangled spectra in different wavelength regions for a number of targets, analogous to Figure 3.2.

Gaia Source ID	*G*mag *Gaia*	ω [mas] *Gaia*	ω [mas] EB+22	ω [mas] S+25	$P_{\rm orb}$ [days] EB+22	$P_{\rm orb}$ [days] S+25	$R_{\rm don}$ [R⊙] EB+22	$R_{\rm don}$ [R⊙] S+25	$R_{\rm acc}$ [$R_\odot$] EB+22	$R_{\rm acc}$ [$R_\odot$] S+25
Gaia 2933630927108779776	11.1	0.92	0.95	0.92	14.71	14.70	7.2 ± 0.2	6.2 ± 0.2	2.3 ± 0.2	2.3 ± 0.2
Gaia 5694373091078326784	11.9	0.59	0.63	0.60	12.88	12.85	5.5 ± 0.2	4.9 ± 0.2	1.9 ± 0.2	2.4 ± 0.2
Gaia 6000420920026118656	10.7	1.08	1.11	1.08	15.31	15.27	6.2 ± 0.2	5.2 ± 0.2	2.5 ± 0.2	2.5 ± 0.2
Gaia 5243109471519822720	10.5	1.37	1.39	1.37	14.91	14.93	6.6 ± 0.2	5.1 ± 0.2	1.9 ± 0.2	2.0 ± 0.2
Gaia 2966694650501747328	11.2	0.86	0.90	0.86	10.40	10.43	4.7 ± 0.1	3.9 ± 0.2	2.1 ± 0.1	2.1 ± 0.2
Gaia 5536105058044762240	12.2	0.57	0.59	0.58	12.18	12.20	5.0 ± 0.2	4.2 ± 0.2	2.5 ± 0.2	3.1 ± 0.2

Table B.1: Table summarising *Gaia* parameters and additional results of the spectral analysis for the donor (don) and accretor (acc) for each system from EB+22 and this work (S+25)

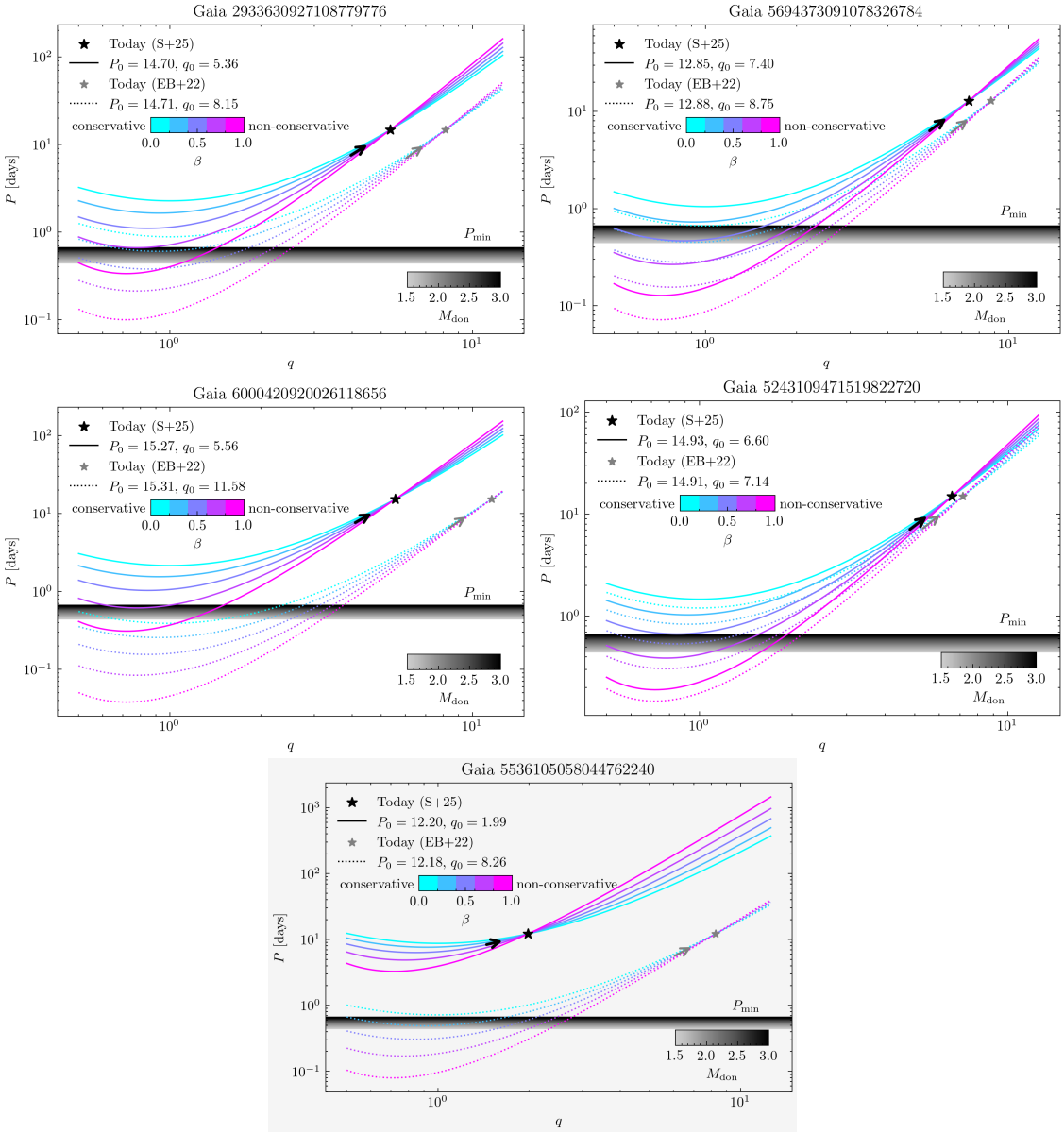

Figure B.3: Plots showing the evolution of $P(q)$ subject to the conservatives of MT for a number of objects, analogous to Figure 3.7.

C

Appendices for Chapter 4: 'Exploring *Gaia* binaries with APOGEE'

C.1. Supplemental material

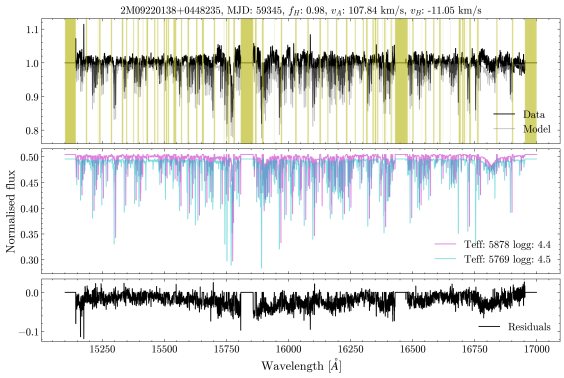

(a) An SB2 with a flux ratio near 1. We note that the effective temperatures and surface gravities of the templates are very similar but their RVs differ by over 100 km/s, identifying this system as a likely twin SB2.

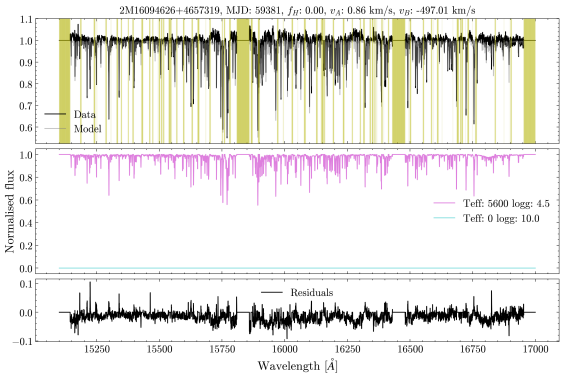

(b) An SB1. We note the flux ratio of 0 and the featureless companion spectrum, indicating no detectable flux from the secondary.

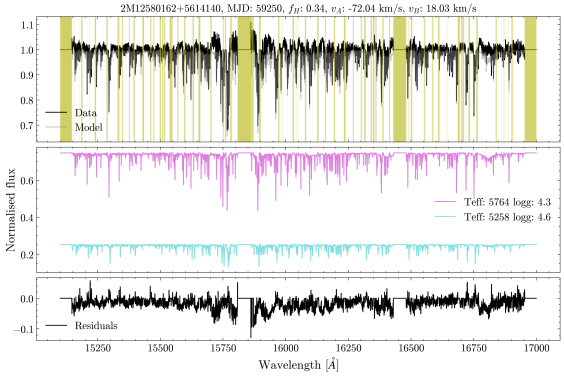

(c) An SB2 with a flux ratio around 0.35. Temperatures and surface gravities imply both components lie on the MS.

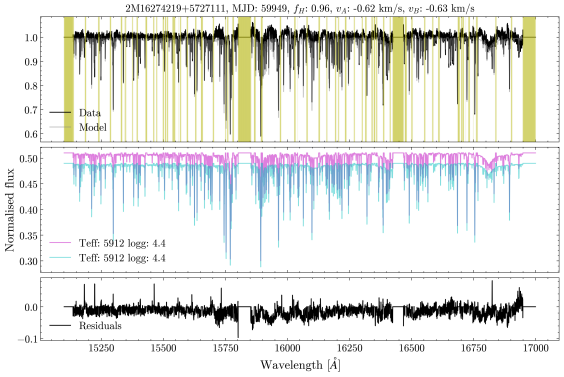

(d) An SB1 with two identical templates shifted to the same velocity.

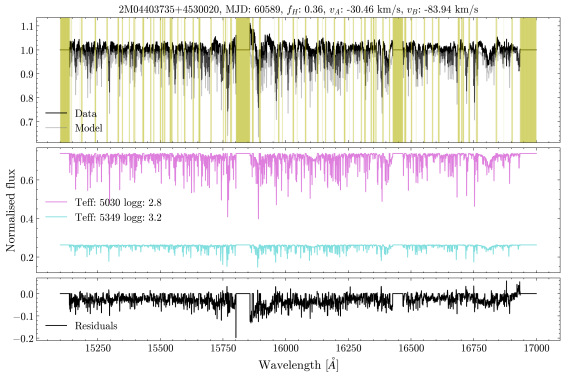

(e) An SB2 with a flux ratio around 0.35. Note the low surface gravity of the cooler star, indicating it likely has ascended the red giant branch.

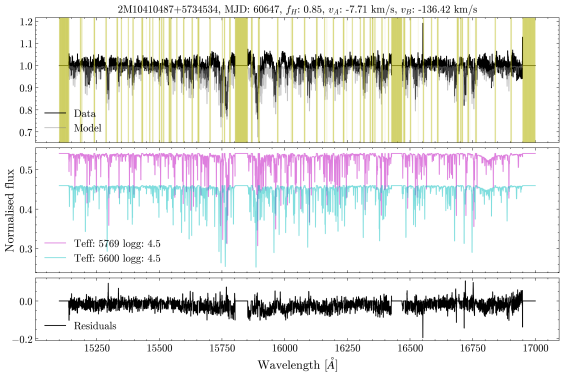

(f) A potential triple. While by eye, the residual does not seem to contain a strong spectral signature, it is revealed in the CCF in panel 4.4f.

Figure C.1: The spectra for each of the 6 selected targets, showing the whole wavelength range. Top panels show the normalised, observed spectrum in black, with the reconstructed spectrum in grey. This reconstruction is computed by shifting and co-adding the best-fit component spectra. Yellow areas are masked out. Middle panels show the two best-fit component spectra, scaled by their respective flux ratio. In the bottom panel, we see the residual, the difference between the observed and reconstructed spectrum.

List of publications

Papers used in this thesis:

[1] **Seeburger, R.**, Rix, H.-W., El-Badry, K., Xiang, M., & Fouesneau, M. (2024), **Monthly Notices of the Royal Astronomical Society, 530, 1935**; *Autonomous disentangling for spectroscopic surveys*

[2] **Seeburger, R.**, Rix, H.-W., El-Badry, K., Müller-Horn, J., Dimoff, A., Henneco, J., Villaseñor, J. (submitted to Astronomy & Astrophysics); *The Physical Properties of Post Mass Transfer Binaries*

[3] **Seeburger, R.**, Saydjari, A., Rix, H.-W., El-Badry, K., Müller-Horn, J., Villaseñor, J., Li, J., Pennell, B. (in prep); *Exploring Gaia Binaries with APOGEE*

Papers not used in this thesis:

[1] Müller-Horn, J., El-Badry, K., Rix, H.-W., Shenar, T., **Seeburger, R.**, Villasenor, J., Bodensteiner, J., Latham, W. D., Bieryla, A., Buchhave, A. L., Isaacson, H., & Howard, W. A. (2025), **arXiv e-prints, arXiv:2504.06973**; *HIP 15429: a newborn Be star on an eccentric binary orbit*

[2] Li, J., Ting, Y.-S., Rix, H.-W., Green, G. M., Hogg, D. W., Ren, J.-J., Müller-Horn, J., & **Seeburger, R.** (2025), **arXiv e-prints, arXiv:2501.14494**; *Identification of 30,000 White Dwarf-Main Sequence binaries candidates from Gaia DR3 BP/RP(XP) low-resolution spectra*

[3] Fouesneau, M., Momcheva, I. G., Chadayammuri, U., Demianenko, M., Dumont, A., Hviding, R. E., Kahle, K. A., Pulatova, N., Rajpoot, B., Scheuck, M. B., **Seeburger, R.**, Semenov, D., & Villaseñor, J. I. (2024), **arXiv e-prints, arXiv:2409.20252**; *What is the Role of Large Language Models in the Evolution of Astronomy Research?*

[4] Pulatova, N. G., Rix, H.-W., Tugay, A. V., Zadorozhna, L. V., **Seeburger, R.**, & Demianenko, M. (2024), **Astronomy & Astrophysics, 686, A223**; *What excites the optical emission in X-ray-selected galaxies?*

[5] Fürnkranz, V., Rix, H.-W., Coronado, J., & **Seeburger, R.**(2024), **Astrophysical Journal, 961, 113**; *The Age Distribution of Stellar Orbit Space Clumps*

[6] El-Badry, K., Rix, H.-W., Cendes, Y., Rodriguez, A. C., Conroy, C., Quataert, E., Hawkins, K., Zari, E., Hobson, M., Breivik, K., Rau, A., Berger, E., Shahaf, S., **Seeburger, R.**, Burdge, K. B., Latham, D. W., Buchhave, L. A., Bieryla, A., Bashi, D., Mazeh, T., & Faigler, S. (2023), **Monthly Notices of the Royal Astronomical Society, 521, 4323**; *A red giant orbiting a black hole*

[7] **Seeburger, R.**, Higgins, P. M., Whiteford, N. P., & Cockell, C. S. (2023), **Astrobiology, 23, 415**; *Linking Methanogenesis in Low-Temperature Hydrothermal Vent Systems to Planetary Spectra: Methane Biosignatures on an Archean-Earth-like Exoplanet*

[8] El-Badry, K., Rix, H.-W., Quataert, E., Howard, A. W., Isaacson, H., Fuller, J., Hawkins, K., Breivik, K., Wong, K. W. K., Rodriguez, A. C., Conroy, C., Shahaf, S., Mazeh, T., Arenou, F., Burdge, K. B., Bashi, D., Faigler, S., Weisz, D. R., **Seeburger, R.**, Almada Monter, S., & Wojno, J. (2023), **Monthly Notices of the Royal Astronomical Society, 518, 1057**; *A Sun-like star orbiting a black hole*

[9] Pulatova, N., Tugay, A., Zadorozhna, L., **Seeburger, R.**, Lukina, O., Gugnin, O., & Malyi, O. (2022), **Journal of Physical Studies, 26, 4901**; *X-ray galaxies selected from HyperLEDA database*

[10] El-Badry, K., **Seeburger, R.**, Jayasinghe, T., Rix, H.-W., Almada, S., Conroy, C., Price-Whelan, A. M., & Burdge, K. (2022), **Monthly Notices of the Royal Astronomical Society, 512, 5620**; *Unicorns and giraffes in the binary zoo: stripped giants with subgiant companions*

Bibliography

Abbott, B. P., Abbott, R., Abbott, T. D., Abernathy, M. R., Acernese, F., Ackley, K., Adams, C., Adams, T., Addesso, P., Adhikari, R. X., et al., "Observation of Gravitational Waves from a Binary Black Hole Merger," *Physical Review Letters*, vol. 116, p. 061102, 2016, doi:10.1103/PhysRevLett.116.061102, publisher: APS ADS Bibcode: 2016PhRvL.116f1102A.

Abbott, R., Abbott, T., Acernese, F., Ackley, K., Adams, C., Adhikari, N., Adhikari, R., Adya, V., Affeldt, C., Agarwal, D., et al., "GWTC-3: Compact Binary Coalescences Observed by LIGO and Virgo during the Second Part of the Third Observing Run," *Physical Review X*, vol. 13, no. 4, p. 041039, 2023, doi:10.1103/PhysRevX.13.041039.

Abbott, R., Abbott, T. D., Abraham, S., Acernese, F., Ackley, K., Adams, A., Adams, C., Adhikari, R. X., Adya, V. B., Affeldt, C., et al., "Population properties of compact objects from the second LIGO-virgo gravitational-wave transient catalog," vol. 913, no. 1, p. L7, 2021, doi:10.3847/2041-8213/abe949, arXiv: 2010.14533 [astro-ph.HE] Number: L7 tex.adsnote: Provided by the SAO/NASA Astrophysics Data System.

Antonini, F. and Rasio, F. A., "Merging black hole binaries in galactic nuclei: Implications for advanced-LIGO detections," vol. 831, no. 2, p. 187, 2016, doi:10.3847/0004-637X/831/2/187, arXiv: 1606.04889 [astro-ph.HE] Number: 187 tex.adsnote: Provided by the SAO/NASA Astrophysics Data System.

Bagnuolo, W. G., Jr. and Gies, D. R., "Tomographic Separation of Composite Spectra: The Components of the O-Star Spectroscopic Binary AO Cassiopeiae," *The Astrophysical Journal*, vol. 376, p. 266, 1991, doi:10.1086/170276, publisher: IOP ADS Bibcode: 1991ApJ...376..266B.

Benacquista, M. J. and Downing, J. M. B., "Relativistic binaries in globular clusters," *Living Reviews in Relativity*, vol. 16, no. 1, p. 4, 2013, doi:10.12942/lrr-2013-4, arXiv: 1110.4423 [astro-ph.SR] Number: 4 tex.adsnote: Provided by the SAO/NASA Astrophysics Data System.

Blaauw, A., "On the origin of the O- and B-type stars with high velocities (the "run-away" stars), and some related problems," *Bulletin of the Astronomical Institutes of the Netherlands*, vol. 15, p. 265, 1961, aDS Bibcode: 1961BAN....15..265B.

Bodensteiner, J., Shenar, T., Mahy, L., Fabry, M., Marchant, P., Abdul-Masih, M., Banyard, G., Bowman, D. M., Dsilva, K., Frost, A. J., et al., "Is HR 6819 a triple system containing a black hole?: An alternative explanation," *Astronomy & Astrophysics*, vol. 641, p. A43, 2020, doi:10.1051/0004-6361/202038682.

Bondi, H. and Hoyle, F., "On the mechanism of accretion by stars," vol. 104, p. 273, 1944, doi:10.1093/mnras/104.5.273, tex.adsnote: Provided by the SAO/NASA Astrophysics Data System.

Brahm, R., Jordán, A., and Espinoza, N., "CERES: A Set of Automated Routines for Echelle Spectra," *Publications of the Astronomical Society of the Pacific*, vol. 129, p. 034002, 2017, doi:10.1088/1538-3873/aa5455, publisher: IOP ADS Bibcode: 2017PASP..129c4002B.

Breivik, K., Chatterjee, S., and Larson, S. L., "Revealing Black Holes with Gaia," *The Astrophysical Journal*, vol. 850, p. L13, 2017, doi:10.3847/2041-8213/aa97d5, publisher: IOP ADS Bibcode: 2017ApJ...850L..13B.

Bresolin, F., Crowther, P. A., and Puls, J., "Massive Stars as Cosmic Engines," *Massive Stars as Cosmic Engines*, vol. 250, 2008, aDS Bibcode: 2008IAUS..250.....B.

Bressan, A., Marigo, P., Girardi, L., Salasnich, B., Dal Cero, C., Rubele, S., and Nanni, A., "PARSEC: stellar tracks and isochrones with the PAdova and TRieste Stellar Evolution Code," *Monthly Notices of the Royal Astronomical Society*, vol. 427, no. 1, pp. 127–145, 2012, doi:10.1111/j.1365-2966.2012.21948.x.

Buchner, J., "UltraNest - a robust, general purpose Bayesian inference engine," *The Journal of Open Source Software*, vol. 6, p. 3001, 2021, doi:10.21105/joss.03001, aDS Bibcode: 2021JOSS....6.3001B.

Burkart, J., Quataert, E., and Arras, P., "Dynamical resonance locking in tidally interacting binary systems," *Monthly Notices of the Royal Astronomical Society*, vol. 443, pp. 2957–2973, 2014, doi:10.1093/mnras/stu1366, publisher: OUP ADS Bibcode: 2014MNRAS.443.2957B.

Carnall, A. C., "SpectRes: A Fast Spectral Resampling Tool in Python," , 2017, doi:10.48550/ARXIV.1705.05165, version Number: 1.

Carvalho, A. and Johns-Krull, C. M., "A Simple Code for Rotational Broadening of Broad Wavelength Range High-Dispersion Spectra," *Research Notes of the American Astronomical Society*, vol. 7, p. 91, 2023, doi:10.3847/2515-5172/acd37e, publisher: IOP ADS Bibcode: 2023RNAAS...7...91C.

Chugai, N. N., "Pulsar Space Velocities and Neutrino Chirality," *Soviet Astronomy Letters*, vol. 10, p. 87, 1984, aDS Bibcode: 1984SvAL...10...87C.

Coelho, P. R. T., "A new library of theoretical stellar spectra with scaled-solar and -enhanced mixtures," *Monthly Notices of the Royal Astronomical Society*, vol. 440, pp. 1027–1043, 2014, doi:10.1093/mnras/stu365, publisher: OUP ADS Bibcode: 2014MNRAS.440.1027C.

Conti, P. S., "On the relationship between Of and WR stars." *Memoires of the Societe Royale des Sciences de Liege*, vol. 9, pp. 193–212, 1975, aDS Bibcode: 1975MSRSL...9..193C.

Cropper, M., Katz, D., Sartoretti, P., Prusti, T., de Bruijne, J. H. J., Chassat, F., Charvet, P., Boyadjian, J., Perryman, M., Sarri, G., et al., "Gaia Data Release 2. Gaia Radial Velocity Spectrometer," *Astronomy and Astrophysics*, vol. 616, p. A5, 2018, doi:10.1051/0004-6361/201832763, aDS Bibcode: 2018A&A...616A...5C.

Cui, X.-Q., Zhao, Y.-H., Chu, Y.-Q., Li, G.-P., Li, Q., Zhang, L.-P., Su, H.-J., Yao, Z.-Q., Wang, Y.-N., Xing, X.-Z., et al., "The Large Sky Area Multi-Object Fiber Spectroscopic Telescope (LAMOST)," *Research in Astronomy and Astrophysics*, vol. 12, no. 9, pp. 1197–1242, 2012, doi:10.1088/1674-4527/12/9/003.

Dalton, G., Trager, S. C., Abrams, D. C., Carter, D., Bonifacio, P., Aguerri, J. A. L., MacIntosh, M., Evans, C., Lewis, I., Navarro, R., et al., "WEAVE: the next generation wide-field spectroscopy facility for the William Herschel Telescope," vol. 8446, p. 84460P, 2012, doi:10.1117/12.925950, conference Name: Ground-based and Airborne Instrumentation for Astronomy IV ADS Bibcode: 2012SPIE.8446E..0PD.

Dekker, H., D'Odorico, S., Kaufer, A., Delabre, B., and Kotzlowski, H., "Design, construction, and performance of UVES, the echelle spectrograph for the UT2 Kueyen Telescope at the ESO Paranal Observatory," vol. 4008, pp. 534–545, 2000, doi:10.1117/12.395512, conference Name: Optical and IR Telescope Instrumentation and Detectors ADS Bibcode: 2000SPIE.4008..534D.

Dervişoğlu, A., Tout, C. A., and Ibanoğlu, C., "Spin angular momentum evolution of the long-period Algols," *Monthly Notices of the Royal Astronomical Society*, vol. 406, pp. 1071–1083, 2010, doi:10.1111/j.1365-2966.2010.16732.x, publisher: OUP ADS Bibcode: 2010MNRAS.406.1071D.

DESI Collaboration, Aghamousa, A., Aguilar, J., Ahlen, S., Alam, S., Allen, L. E., Allende Prieto, C., Annis, J., Bailey, S., Balland, C., et al., "The DESI Experiment Part I: Science,Targeting, and Survey Design," , 2016, doi:10.48550/arXiv.1611.00036, publication Title: arXiv e-prints ADS Bibcode: 2016arXiv161100036D.

Di Carlo, U. N., Mapelli, M., Giacobbo, N., Spera, M., Bouffanais, Y., Rastello, S., Santoliquido, F., Pasquato, M., Ballone, A., Trani, A. A., et al., "Binary black holes in young star clusters: the impact of metallicity," *Monthly Notices of the Royal Astronomical Society*, vol. 498, pp. 495–506, 2020, doi:10.1093/mnras/staa2286, publisher: OUP ADS Bibcode: 2020MNRAS.498..495D.

Drout, M. R., Massey, P., and Meynet, G., "The Yellow and Red Supergiants of M33," *The Astrophysical Journal*, vol. 750, p. 97, 2012, doi:10.1088/0004-637X/750/2/97, publisher: IOP ADS Bibcode: 2012ApJ...750...97D.

Edenhofer, G., Zucker, C., Frank, P., Saydjari, A. K., Speagle, J. S., Finkbeiner, D., and Enßlin, T. A., "A parsec-scale Galactic 3D dust map out to 1.25 kpc from the Sun," *Astronomy and Astrophysics*, vol. 685, p. A82, 2024, doi:10.1051/0004-6361/202347628, aDS Bibcode: 2024A&A...685A..82E.

Eggleton, P. P., "Aproximations to the radii of Roche lobes." *The Astrophysical Journal*, vol. 268, pp. 368–369, 1983, doi:10.1086/160960, publisher: IOP ADS Bibcode: 1983ApJ...268..368E.

El-Badry, K., "Gaia's binary star renaissance," *New Astronomy Reviews*, vol. 98, p. 101694, 2024, doi:10.1016/j.newar.2024.101694, publisher: Elsevier ADS Bibcode: 2024NewAR..9801694E.

El-Badry, K. and Burdge, K. B., "NGC 1850 BH1 is another stripped-star binary masquerading as a black hole," *Monthly Notices of the Royal Astronomical Society*, vol. 511, pp. 24–29, 2022, doi:10.1093/mnrasl/slab135, publisher: OUP ADS Bibcode: 2022MNRAS.511L..24E.

El-Badry, K., Burdge, K. B., and Mróz, P., "NGC 2004 #115: a black hole imposter containing three luminous stars," *Monthly Notices of the Royal Astronomical Society*, vol. 511, pp. 3089–3100, 2022a, doi:10.1093/mnras/stac274, publisher: OUP ADS Bibcode: 2022MNRAS.511.3089E.

El-Badry, K. and Quataert, E., "A stripped-companion origin for Be stars: clues from the putative black holes HR 6819 and LB-1," *Monthly Notices of the Royal Astronomical Society*, vol. 502, pp. 3436–3455, 2021, doi:10.1093/mnras/stab285, publisher: OUP ADS Bibcode: 2021MNRAS.502.3436E.

El-Badry, K. and Rix, H.-W., "What are the spectroscopic binaries with high-mass functions near the Gaia DR3 main sequence?" *Monthly Notices of the Royal Astronomical Society*, vol. 515, pp. 1266–1275, 2022, doi:10.1093/mnras/stac1797, publisher: OUP ADS Bibcode: 2022MNRAS.515.1266E.

El-Badry, K., Rix, H.-W., Cendes, Y., Rodriguez, A. C., Conroy, C., Quataert, E., Hawkins, K., Zari, E., Hobson, M., Breivik, K., et al., "A red giant orbiting a black hole," *Monthly Notices of the Royal Astronomical Society*, vol. 521, pp. 4323–4348, 2023a, doi:10.1093/mnras/stad799, publisher: OUP ADS Bibcode: 2023MNRAS.521.4323E.

El-Badry, K., Rix, H.-W., Quataert, E., Howard, A. W., Isaacson, H., Fuller, J., Hawkins, K., Breivik, K., Wong, K. W. K., Rodriguez, A. C., et al., "A Sun-like star orbiting a black hole," *Monthly Notices of the Royal Astronomical Society*, vol. 518, pp. 1057–1085, 2023b, doi:10.1093/mnras/stac3140, publisher: OUP ADS Bibcode: 2023MNRAS.518.1057E.

El-Badry, K., Seeburger, R., Jayasinghe, T., Rix, H.-W., Almada, S., Conroy, C., Price-Whelan, A. M., and Burdge, K., "Unicorns and giraffes in the binary zoo: stripped giants with subgiant companions," *Monthly Notices of the Royal Astronomical Society*, vol. 512, pp. 5620–5641, 2022b, doi:10.1093/mnras/stac815, publisher: OUP ADS Bibcode: 2022MNRAS.512.5620E.

Ferluga, S., Floreano, L., Bravar, U., and Bédalo, C., "Separating the spectra of binary stars: I. A simple method: Secondary reconstruction," *Astronomy and Astrophysics Supplement Series*, vol. 121, no. 1, pp. 201–209, 1997, doi:10.1051/aas:1997315.

Fong, D. C.-L. and Saunders, M., "LSMR: An Iterative Algorithm for Sparse Least-Squares Problems," *SIAM Journal on Scientific Computing*, vol. 33, no. 5, pp. 2950–2971, 2011, doi:10.1137/10079687X.

Foreman-Mackey, D., Hogg, D. W., Lang, D., and Goodman, J., "emcee: The MCMC Hammer," *Publications of the Astronomical Society of the Pacific*, vol. 125, p. 306, 2013, doi:10.1086/670067, publisher: IOP ADS Bibcode: 2013PASP..125..306F.

Forsythe, G. E., Malcolm, M. A., and Moler, C. B., *Computer methods for mathematical computations*, Prentice-Hall series in automatic computation, Prentice-Hall, Englewood Cliffs, N.J, 1977, ISBN 978-0-13-165332-0.

Fouesneau, M., "pyphot," *Zenodo*, 2024, doi:10.5281/zenodo.7016774, publisher: Zenodo ADS Bibcode: 2022zndo...7016774F.

Fraley, G. S., "Supernovae Explosions Induced by Pair-Production Instability," *Astrophysics and Space Science*, vol. 2, pp. 96–114, 1968, doi:10.1007/BF00651498, publisher: Springer ADS Bibcode: 1968Ap&SS...2...96F.

Freedman, R. A., Geller, R. M., and Kaufmann, W. J., *Universe*, W.H. Freeman and Company, a Macmillan Higher Education Company, New York, tenth edition ed., 2014, ISBN 978-1-4641-2492-1.

Frost, A. J., Bodensteiner, J., Rivinius, T., Baade, D., Merand, A., Selman, F., Abdul-Masih, M., Banyard, G., Bordier, E., Dsilva, K., et al., "HR 6819 is a binary system with no black hole: Revisiting the source with infrared interferometry and optical integral field spectroscopy," *Astronomy & Astrophysics*, vol. 659, p. L3, 2022, doi:10.1051/0004-6361/202143004.

Gaia Collaboration, Arenou, F., Babusiaux, C., Barstow, M. A., Faigler, S., Jorissen, A., Kervella, P., Mazeh, T., Mowlavi, N., Panuzzo, P., et al., "Gaia Data Release 3. Stellar multiplicity, a teaser for the hidden treasure," *Astronomy and Astrophysics*, vol. 674, p. A34, 2023, doi:10.1051/0004-6361/202243782, aDS Bibcode: 2023A&A...674A..34G.

Gaia Collaboration, Brown, A. G. A., Vallenari, A., Prusti, T., De Bruijne, J. H. J., Babusiaux, C., Biermann, M., Creevey, O. L., Evans, D. W., Eyer, L., et al., "*Gaia* Early Data Release 3: Summary of the contents and survey properties," *Astronomy & Astrophysics*, vol. 649, p. A1, 2021, doi:10.1051/0004-6361/202039657.

Gaia Collaboration, Panuzzo, P., Mazeh, T., Arenou, F., Holl, B., Caffau, E., Jorissen, A., Babusiaux, C., Gavras, P., Sahlmann, J., et al., "Discovery of a dormant 33 solar-mass black hole in pre-release Gaia astrometry," *Astronomy and Astrophysics*, vol. 686, p. L2, 2024, doi:10.1051/0004-6361/202449763, aDS Bibcode: 2024A&A...686L...2G.

Gaia Collaboration, Prusti, T., de Bruijne, J. H. J., Brown, A. G. A., Vallenari, A., Babusiaux, C., Bailer-Jones, C. A. L., Bastian, U., Biermann, M., Evans, D. W., et al., "The Gaia mission," *Astronomy and Astrophysics*, vol. 595, p. A1, 2016, doi:10.1051/0004-6361/201629272, publisher: EDP ADS Bibcode: 2016A&A...595A...1G.

Giacconi, R., Gursky, H., Paolini, F. R., and Rossi, B. B., "Evidence for x rays from sources outside the solar system," vol. 9, no. 11, pp. 439–443, 1962, doi:10.1103/PhysRevLett.9.439, tex.adsnote: Provided by the SAO/NASA Astrophysics Data System.

Giesers, B., Dreizler, S., Husser, T.-O., Kamann, S., Anglada Escudé, G., Brinchmann, J., Carollo, C. M., Roth, M. M., Weilbacher, P. M., and Wisotzki, L., "A detached stellar-mass black hole candidate in the globular cluster NGC 3201," *Monthly Notices of the Royal Astronomical Society*, vol. 475, pp. L15–L19, 2018, doi:10.1093/mnrasl/slx203, publisher: OUP ADS Bibcode: 2018MNRAS.475L..15G.

González, J. F. and Levato, H., "Separation of composite spectra: the spectroscopic detection of aneclipsing binary star," *Astronomy & Astrophysics*, vol. 448, no. 1, pp. 283–292, 2006, doi:10.1051/0004-6361:20053177.

Green, G. M., "dustmaps: A Python interface for maps of interstellar dust," *The Journal of Open Source Software*, vol. 3, p. 695, 2018, doi:10.21105/joss.00695, aDS Bibcode: 2018JOSS....3..695G.

Götberg, Y., Drout, M. R., Ji, A. P., Groh, J. H., Ludwig, B. A., Crowther, P. A., Smith, N., de Koter, A., and de Mink, S. E., "Stellar Properties of Observed Stars Stripped in Binaries in the Magellanic Clouds," *The Astrophysical Journal*, vol. 959, p. 125, 2023, doi:10.3847/1538-4357/ace5a3, publisher: IOP ADS Bibcode: 2023ApJ...959..125G.

Götberg, Y., de Mink, S. E., and Groh, J. H., "Ionizing spectra of stars that lose their envelope through interaction with a binary companion: role of metallicity," *Astronomy and Astrophysics*, vol. 608, p. A11, 2017, doi:10.1051/0004-6361/201730472, aDS Bibcode: 2017A&A...608A..11G.

Götberg, Y., de Mink, S. E., Groh, J. H., Kupfer, T., Crowther, P. A., Zapartas, E., and Renzo, M., "Spectral models for binary products: Unifying subdwarfs and Wolf-Rayet stars as a sequence of stripped-envelope stars," *Astronomy and Astrophysics*, vol. 615, p. A78, 2018, doi:10.1051/0004-6361/201732274, publisher: EDP ADS Bibcode: 2018A&A...615A..78G.

Hadrava, P., "Orbital elements of multiple spectroscopic stars." *Astronomy and Astrophysics Supplement Series*, vol. 114, p. 393, 1995, aDS Bibcode: 1995A&AS..114..393H.

Hadrava, P., "KOREL - User's guide," *Publications of the Astronomical Institute of the Czechoslovak Academy of Sciences*, vol. 92, pp. 15–35, 2004, aDS Bibcode: 2004PAICz..92...15H.

Hadrava, P., "Disentangling of spectra - theory and practice," , 2009, doi:10.48550/arXiv.0909.0172, arXiv:0909.0172 [astro-ph].

Harris, C. R., Millman, K. J., Van Der Walt, S. J., Gommers, R., Virtanen, P., Cournapeau, D., Wieser, E., Taylor, J., Berg, S., Smith, N. J., et al., "Array programming with NumPy," *Nature*, vol. 585, no. 7825, pp. 357–362, 2020, doi:10.1038/s41586-020-2649-2.

Heber, U., "Hot Subdwarf Stars," *Annual Review of Astronomy and Astrophysics*, vol. 47, pp. 211–251, 2009, doi:10.1146/annurev-astro-082708-101836, aDS Bibcode: 2009ARA&A..47..211H.

Heger, A., Fryer, C. L., Woosley, S. E., Langer, N., and Hartmann, D. H., "How massive single stars end their life," vol. 591, no. 1, pp. 288–300, 2003, doi:10.1086/375341, arXiv: astro-ph/0212469 [astro-ph] tex.adsnote: Provided by the SAO/NASA Astrophysics Data System.

Heger, A., Müller, B., and Mandel, I., "Black holes as the end state of stellar evolution: Theory and simulations," , 2023, doi:10.48550/arXiv.2304.09350, aDS Bibcode: 2023arXiv230409350H.

Heggie, D. C., "Binary evolution in stellar dynamics." vol. 173, pp. 729–787, 1975, doi:10.1093/mnras/173.3.729, tex.adsnote: Provided by the SAO/NASA Astrophysics Data System.

Henneco, J., Schneider, F. R. N., and Laplace, E., "Contact tracing of binary stars: Pathways to stellar mergers," *Astronomy and Astrophysics*, vol. 682, p. A169, 2024, doi:10.1051/0004-6361/202347893, aDS Bibcode: 2024A&A...682A.169H.

Herschel, W., "Catalogue of 500 New Nebulae, Nebulous Stars, Planetary Nebulae, and Clusters of Stars; With Remarks on the Construction of the Heavens," *Philosophical Transactions of the Royal Society of London Series I*, vol. 92, pp. 477–528, 1802, aDS Bibcode: 1802RSPT...92..477H.

Herschel, W., "Account of the Changes That Have Happened, during the Last Twenty-Five Years, in the Relative Situation of Double-Stars; With an Investigation of the Cause to Which They Are Owing," *Philosophical Transactions of the Royal Society of London Series I*, vol. 93, pp. 339–382, 1803, aDS Bibcode: 1803RSPT...93..339H.

Hills, J. G. and Fullerton, L. W., "Computer simulations of close encounters between single stars and hard binaries," *The Astronomical Journal*, vol. 85, pp. 1281–1291, 1980, doi:10.1086/112798, publisher: IOP ADS Bibcode: 1980AJ.....85.1281H.

Hook, I. M., Jørgensen, I., Allington-Smith, J. R., Davies, R. L., Metcalfe, N., Murowinski, R. G., and Crampton, D., "The Gemini-North Multi-Object Spectrograph: Performance in Imaging, Long-Slit, and Multi-Object Spectroscopic Modes," *Publications of the Astronomical Society of the Pacific*, vol. 116, pp. 425–440, 2004, doi:10.1086/383624, publisher: IOP ADS Bibcode: 2004PASP..116..425H.

Hunter, J. D., "Matplotlib: A 2D Graphics Environment," *Computing in Science & Engineering*, vol. 9, no. 3, pp. 90–95, 2007, doi:10.1109/MCSE.2007.55.

Ilijic, S., "Thoughts about disentangling in wavelength and in Fourier-space," vol. 318, pp. 107–110, 2004, conference Name: Spectroscopically and Spatially Resolving the Components of the Close Binary Stars ADS Bibcode: 2004ASPC..318..107I.

Ilijic, S., Hensberge, H., Pavlovski, K., and Freyhammer, L. M., "Obtaining normalised component spectra with FDBinary," vol. 318, pp. 111–113, 2004, conference Name: Spectroscopically and Spatially Resolving the Components of the Close Binary Stars ADS Bibcode: 2004ASPC..318..111I.

Ilijić, S., "fd3: Spectral disentangling of double-lined spectroscopic binary stars," *Astrophysics Source Code Library*, p. ascl:1705.012, 2017, aDS Bibcode: 2017ascl.soft05012I.

Janka, H.-T., "Neutron star kicks by the gravitational tug-boat mechanism in asymmetric supernova explosions: Progenitor and explosion dependence," vol. 837, no. 1, p. 84, 2017, doi:10.3847/1538-4357/aa618e, arXiv: 1611.07562 [astro-ph.HE] Number: 84 tex.adsnote: Provided by the SAO/NASA Astrophysics Data System.

Janssens, S., Shenar, T., Sana, H., and Marchant, P., "Detection of single-degenerate massive binaries with Gaia: The impact of blue supergiants, triples, mass precision, and high-precision parallax requirements," *Astronomy and Astrophysics*, vol. 670, p. A79, 2023, doi:10.1051/0004-6361/202244818, aDS Bibcode: 2023A&A...670A..79J.

Jayasinghe, T., Stanek, K. Z., Thompson, T. A., Kochanek, C. S., Rowan, D. M., Vallely, P. J., Strassmeier, K. G., Weber, M., Hinkle, J. T., Hambsch, F.-J., et al., "A unicorn in monoceros: the 3 M dark companion to the bright, nearby red giant V723 Mon is a non-interacting, mass-gap black hole candidate," *Monthly Notices of the Royal Astronomical Society*, vol. 504, no. 2, pp. 2577–2602, 2021, doi:10.1093/mnras/stab907.

Jayasinghe, T., Thompson, T. A., Kochanek, C. S., Stanek, K. Z., Rowan, D. M., Martin, D. V., El-Badry, K., Vallely, P. J., Hinkle, J. T., Huber, D., et al., "The 'Giraffe': discovery of a stripped red giant in an interacting binary with an 2 M lower giant," *Monthly Notices of the Royal Astronomical Society*, vol. 516, no. 4, pp. 5945–5963, 2022, doi:10.1093/mnras/stac2187.

Jermyn, A. S., Bauer, E. B., Schwab, J., Farmer, R., Ball, W. H., Bellinger, E. P., Dotter, A., Joyce, M., Marchant, P., Mombarg, J. S. G., et al., "Modules for Experiments in Stellar Astrophysics (MESA): Time-dependent Convection, Energy Conservation, Automatic Differentiation, and Infrastructure," *The Astrophysical Journal Supplement Series*, vol. 265, p. 15, 2023, doi:10.3847/1538-4365/acae8d, publisher: IOP ADS Bibcode: 2023ApJS..265...15J.

de Jong, R. S., Agertz, O., Berbel, A. A., Aird, J., Alexander, D. A., Amarsi, A., Anders, F., Andrae, R., Ansarinejad, B., Ansorge, W., et al., "4MOST: Project overview and information for the First Call for Proposals," *The Messenger*, vol. 175, pp. 3–11, 2019, doi:10.18727/0722-6691/5117, aDS Bibcode: 2019Msngr.175....3D.

Kaufer, A., Stahl, O., Tubbesing, S., Nørregaard, P., Avila, G., Francois, P., Pasquini, L., and Pizzella, A., "Commissioning FEROS, the new high-resolution spectrograph at La-Silla." *The Messenger*, vol. 95, pp. 8–12, 1999, aDS Bibcode: 1999Msngr..95....8K.

Kippenhahn, R. and Weigert, A., "Entwicklung in engen Doppelsternsystemen I. Massenaustausch vor und nach Beendigung des zentralen Wasserstoff-Brennens," *Zeitschrift fur Astrophysik*, vol. 65, p. 251, 1967, aDS Bibcode: 1967ZA.....65..251K.

Kollmeier, J., Anderson, S. F., Blanc, G. A., Blanton, M. R., Covey, K. R., Crane, J., Drory, N., Frinchaboy, P. M., Froning, C. S., Johnson, J. A., et al., "SDSS-V Pioneering Panoptic Spectroscopy," vol. 51, p. 274, 2019, conference Name: Bulletin of the American Astronomical Society ADS Bibcode: 2019BAAS...51g.274K.

Kollmeier, J. A., Zasowski, G., Rix, H.-W., Johns, M., Anderson, S. F., Drory, N., Johnson, J. A., Pogge, R. W., Bird, J. C., Blanc, G. A., et al., "SDSS-V: Pioneering Panoptic Spectroscopy," , 2017, doi:10.48550/ARXIV.1711.03234, version Number: 1.

Kopal, Z., "The classification of close binary systems," *Annales d'Astrophysique*, vol. 18, p. 379, 1955, aDS Bibcode: 1955AnAp...18..379K.

Kraft, R. P., "Studies of Stellar Rotation. V. The Dependence of Rotation on Age among Solar-Type Stars," *The Astrophysical Journal*, vol. 150, p. 551, 1967, doi:10.1086/149359, publisher: IOP ADS Bibcode: 1967ApJ...150..551K.

Krynski, P., Siess, L., Jorissen, A., and Davis, P. J., "Formation of Ba stars : impact of wind Roche lobe overflow and circumbinary disk in shaping the orbital parameters," , 2025, doi:10.48550/arXiv.2504.10939, aDS Bibcode: 2025arXiv250410939K.

Kurucz, R. L., "Model atmospheres for G, F, A, B, and O stars." *The Astrophysical Journal Supplement Series*, vol. 40, pp. 1–340, 1979, doi:10.1086/190589, publisher: IOP ADS Bibcode: 1979ApJS...40....1K.

Lam, C. Y., Lu, J. R., Udalski, A., Bond, I., Bennett, D. P., Skowron, J., Mróz, P., Poleski, R., Sumi, T., Szymański, M. K., et al., "An Isolated Mass-gap Black Hole or Neutron Star Detected with Astrometric Microlensing," *The Astrophysical Journal*, vol. 933, p. L23, 2022, doi:10.3847/2041-8213/ac7442, publisher: IOP ADS Bibcode: 2022ApJ...933L..23L.

Lam, M. C., "SpectRes in C," , 2023, doi:10.5281/ZENODO.7879105.

Lam, M. C., "SpectRes in C," , 2024, doi:10.5281/zenodo.12584681.

Langer, N., Schürmann, C., Stoll, K., Marchant, P., Lennon, D. J., Mahy, L., de Mink, S. E., Quast, M., Riedel, W., Sana, H., et al., "Properties of OB star-black hole systems derived from detailed binary evolution models," *Astronomy and Astrophysics*, vol. 638, p. A39, 2020, doi:10.1051/0004-6361/201937375, aDS Bibcode: 2020A&A...638A..39L.

Laplace, E., Justham, S., Renzo, M., Götberg, Y., Farmer, R., Vartanyan, D., and de Mink, S. E., "Different to the core: The pre-supernova structures of massive single and binary-stripped stars," *Astronomy and Astrophysics*, vol. 656, p. A58, 2021, doi:10.1051/0004-6361/202140506, aDS Bibcode: 2021A&A...656A..58L.

Laplace, E., Schneider, F. R. N., and Podsiadlowski, P., "It's written in the massive stars: The role of stellar physics in the formation of black holes," *Astronomy and Astrophysics*, vol. 695, p. A71, 2025, doi:10.1051/0004-6361/202451077, publisher: EDP ADS Bibcode: 2025A&A...695A..71L.

Leiner, E., Mathieu, R. D., Gosnell, N. M., and Sills, A., "Observations of Spin-down in Post-mass-transfer Stars and the Possibility for Blue Straggler Gyrochronology," *The Astrophysical Journal*, vol. 869, p. L29, 2018, doi:10.3847/2041-8213/aaf4ed, publisher: IOP ADS Bibcode: 2018ApJ...869L..29L.

Lennon, D. J., Dufton, P. L., Villaseñor, J. I., Evans, C. J., Langer, N., Saxton, R., Monageng, I. M., and Toonen, S., "The VLT-FLAMES survey of massive stars. NGC 2004#115: A triple system hosting a possible short period B+BH binary," *Astronomy and Astrophysics*, vol. 665, p. A180, 2022, doi:10.1051/0004-6361/202142413, aDS Bibcode: 2022A&A...665A.180L.

Lieb, E. H. and Yau, H.-T., "A Rigorous Examination of the Chandrasekhar Theory of Stellar Collapse," *The Astrophysical Journal*, vol. 323, p. 140, 1987, doi:10.1086/165813, publisher: IOP ADS Bibcode: 1987ApJ...323..140L.

Liu, J., Zhang, H., Howard, A. W., Bai, Z., Lu, Y., Soria, R., Justham, S., Li, X., Zheng, Z., Wang, T., et al., "A wide star-black-hole binary system from radial-velocity measurements," *Nature*, vol. 575, pp. 618–621, 2019, doi:10.1038/s41586-019-1766-2, aDS Bibcode: 2019Natur.575..618L.

Loeb, A. and Rasio, F. A., "Collapse of Primordial Gas Clouds and the Formation of Quasar Black Holes," *The Astrophysical Journal*, vol. 432, p. 52, 1994, doi:10.1086/174548, publisher: IOP ADS Bibcode: 1994ApJ...432...52L.

Lurie, J. C., Vyhmeister, K., Hawley, S. L., Adilia, J., Chen, A., Davenport, J. R. A., Jurić, M., Puig-Holzman, M., and Weisenburger, K. L., "Tidal Synchronization and Differential Rotation of Kepler Eclipsing Binaries," *The Astronomical Journal*, vol. 154, p. 250, 2017, doi:10.3847/1538-3881/aa974d, publisher: IOP ADS Bibcode: 2017AJ....154..250L.

Mahy, L., Sana, H., Shenar, T., Sen, K., Langer, N., Marchant, P., Abdul-Masih, M., Banyard, G., Bodensteiner, J., Bowman, D. M., et al., "Identifying quiescent compact objects in massive Galactic single-lined spectroscopic binaries," *Astronomy & Astrophysics*, vol. 664, p. A159, 2022, doi:10.1051/0004-6361/202243147.

Majewski, S. R., Schiavon, R. P., Frinchaboy, P. M., Allende Prieto, C., Barkhouser, R., Bizyaev, D., Blank, B., Brunner, S., Burton, A., Carrera, R., et al., "The Apache Point Observatory Galactic Evolution Experiment (APOGEE)," *The Astronomical Journal*, vol. 154, p. 94, 2017, doi:10.3847/1538-3881/aa784d, publisher: IOP ADS Bibcode: 2017AJ....154...94M.

Mandel, I. and de Mink, S. E., "Merging binary black holes formed through chemically homogeneous evolution in short-period stellar binaries," *Monthly Notices of the Royal Astronomical Society*, vol. 458, pp. 2634–2647, 2016, doi:10.1093/mnras/stw379, publisher: OUP ADS Bibcode: 2016MNRAS.458.2634M.

Mapelli, M., "Binary black hole mergers: formation and populations," *Frontiers in Astronomy and Space Sciences*, vol. 7, p. 38, 2020, doi:10.3389/fspas.2020.00038, aDS Bibcode: 2020FrASS...7...38M.

Mapelli, M., "Formation Channels of Single and Binary Stellar-Mass Black Holes," in "Handbook of Gravitational Wave Astronomy," p. 16, 2021, doi:10.1007/978-981-15-4702-7_16-1, aDS Bibcode: 2021hgwa.bookE..16M.

Marchant, P., Langer, N., Podsiadlowski, P., Tauris, T. M., and Moriya, T. J., "A new route towards merging massive black holes," *Astronomy and Astrophysics*, vol. 588, p. A50, 2016, doi:10.1051/0004-6361/201628133, aDS Bibcode: 2016A&A...588A..50M.

Marshall, J. L., Burles, S., Thompson, I. B., Shectman, S. A., Bigelow, B. C., Burley, G., Birk, C., Estrada, J., Jones, P., Smith, M., et al., "The MagE spectrograph," vol. 7014, p. 701454, 2008, doi:10.1117/12.789972, conference Name: Ground-based and Airborne Instrumentation for Astronomy II Place: eprint: arXiv:0807.3774 ADS Bibcode: 2008SPIE.7014E..54M.

Metzger, B. D., "Luminous Fast Blue Optical Transients and Type Ibn/Icn SNe from Wolf-Rayet/Black Hole Mergers," *The Astrophysical Journal*, vol. 932, p. 84, 2022, doi:10.3847/1538-4357/ac6d59, publisher: IOP ADS Bibcode: 2022ApJ...932...84M.

de Mink, S. E., Langer, N., Izzard, R. G., Sana, H., and de Koter, A., "The Rotation Rates of Massive Stars: The Role of Binary Interaction through Tides, Mass Transfer, and Mergers," *The Astrophysical Journal*, vol. 764, p. 166, 2013, doi:10.1088/0004-637X/764/2/166, publisher: IOP ADS Bibcode: 2013ApJ...764..166D.

Moe, M. and Di Stefano, R., "Mind Your Ps and Qs: The Interrelation between Period (P) and Mass-ratio (Q) Distributions of Binary Stars," *The Astrophysical Journal Supplement Series*, vol. 230, p. 15, 2017, doi:10.3847/1538-4365/aa6fb6, publisher: IOP ADS Bibcode: 2017ApJS..230...15M.

Murphy, J. W., Khan, R., Williams, B., Dolphin, A. E., Dalcanton, J., and Díaz-Rodríguez, M., "The Progenitor Age and Mass of the Black Hole Formation Candidate N6946-BH1," *The Astrophysical Journal*, vol. 860, p. 117, 2018, doi:10.3847/1538-4357/aac2be, publisher: IOP ADS Bibcode: 2018ApJ...860..117M.

Müller-Horn, J., Göttgens, F., Dreizler, S., Kamann, S., Martens, S., Saracino, S., and Ye, C. S., "Binary properties of the globular cluster 47 Tuc (NGC 104). A dearth of short-period binaries," , 2024, doi:10.48550/arXiv.2412.13189, publication Title: arXiv e-prints ADS Bibcode: 2024arXiv241213189M.

Nagarajan, P., El-Badry, K., Chawla, C., Niccolò Di Carlo, U., Breivik, K., Rodriguez, C. L., Agrawal, P., Delfavero, V., and Chatterjee, S., "Realistic predictions for Gaia black hole discoveries: comparison of isolated binary and dynamical formation models," , 2025, doi:10.48550/arXiv.2502.03527, aDS Bibcode: 2025arXiv250203527N.

Nelder, J. A. and Mead, R., "A Simplex Method for Function Minimization," *The Computer Journal*, vol. 7, no. 4, pp. 308–313, 1965, doi:10.1093/comjnl/7.4.308.

Offner, S. S. R., Moe, M., Kratter, K. M., Sadavoy, S. I., Jensen, E. L. N., and Tobin, J. J., "The Origin and Evolution of Multiple Star Systems," vol. 534, p. 275, 2023, doi:10.48550/arXiv.2203.10066, conference Name: Protostars and Planets VII Place: eprint: arXiv:2203.10066 ADS Bibcode: 2023ASPC..534..275O.

Packet, W., "On the spin-up of the mass accreting component in a close binary system," *Astronomy and Astrophysics*, vol. 102, pp. 17–19, 1981, aDS Bibcode: 1981A&A...102...17P.

Paczynski, B., "A Polytropic Model of an Accretion Disk, a Boundary Layer, and a Star," *The Astrophysical Journal*, vol. 370, p. 597, 1991, doi:10.1086/169846, publisher: IOP ADS Bibcode: 1991ApJ...370..597P.

Paxton, B., Bildsten, L., Dotter, A., Herwig, F., Lesaffre, P., and Timmes, F., "Modules for Experiments in Stellar Astrophysics (MESA)," *The Astrophysical Journal Supplement Series*, vol. 192, p. 3, 2011, doi:10.1088/0067-0049/192/1/3, publisher: IOP ADS Bibcode: 2011ApJS..192....3P.

Paxton, B., Cantiello, M., Arras, P., Bildsten, L., Brown, E. F., Dotter, A., Mankovich, C., Montgomery, M. H., Stello, D., Timmes, F. X., et al., "Modules for Experiments in Stellar Astrophysics (MESA): Planets, Oscillations, Rotation, and Massive Stars," *The Astrophysical Journal Supplement Series*, vol. 208, p. 4, 2013, doi:10.1088/0067-0049/208/1/4, publisher: IOP ADS Bibcode: 2013ApJS..208....4P.

Paxton, B., Marchant, P., Schwab, J., Bauer, E. B., Bildsten, L., Cantiello, M., Dessart, L., Farmer, R., Hu, H., Langer, N., et al., "Modules for Experiments in Stellar Astrophysics (MESA): Binaries, Pulsations, and Explosions," *The Astrophysical Journal Supplement Series*, vol. 220, p. 15, 2015, doi:10.1088/0067-0049/220/1/15, publisher: IOP ADS Bibcode: 2015ApJS..220...15P.

Paxton, B., Schwab, J., Bauer, E. B., Bildsten, L., Blinnikov, S., Duffell, P., Farmer, R., Goldberg, J. A., Marchant, P., Sorokina, E., et al., "Modules for Experiments in Stellar Astrophysics (MESA): Convective Boundaries, Element Diffusion, and Massive Star Explosions," *The Astrophysical Journal Supplement Series*, vol. 234, p. 34, 2018, doi:10.3847/1538-4365/aaa5a8, publisher: IOP ADS Bibcode: 2018ApJS..234...34P.

Paxton, B., Smolec, R., Schwab, J., Gautschy, A., Bildsten, L., Cantiello, M., Dotter, A., Farmer, R., Goldberg, J. A., Jermyn, A. S., et al., "Modules for Experiments in Stellar Astrophysics (MESA): Pulsating Variable Stars, Rotation, Convective Boundaries, and Energy Conservation," *The Astrophysical Journal Supplement Series*, vol. 243, p. 10, 2019, doi:10.3847/1538-4365/ab2241, publisher: IOP ADS Bibcode: 2019ApJS..243...10P.

Perez, F. and Granger, B. E., "IPython: A System for Interactive Scientific Computing," *Computing in Science & Engineering*, vol. 9, no. 3, pp. 21–29, 2007, doi:10.1109/MCSE.2007.53.

Phillips, D. L., "A Technique for the Numerical Solution of Certain Integral Equations of the First Kind," *Journal of the ACM*, vol. 9, no. 1, pp. 84–97, 1962, doi:10.1145/321105.321114.

Picco, A., Marchant, P., Sana, H., and Nelemans, G., "Forming merging double compact objects with stable mass transfer," *Astronomy and Astrophysics*, vol. 681, p. A31, 2024, doi:10.1051/0004-6361/202347090, aDS Bibcode: 2024A&A...681A..31P.

Pols, O. R., "Mass and Angular Momentum Loss in Massive Binary Evolution," vol. 367, p. 387, 2007, aDS Bibcode: 2007ASPC..367..387P.

Popham, R. and Narayan, R., "Does Accretion Cease When a Star Approaches Breakup?" *The Astrophysical Journal*, vol. 370, p. 604, 1991, doi:10.1086/169847, publisher: IOP ADS Bibcode: 1991ApJ...370..604P.

Portegies Zwart, S. F., "Collisions in Compact Star Clusters." , 2000, doi:10.48550/arXiv.astro-ph/9912434, conference Name: Massive Stellar Clusters Volume: 211 ADS Bibcode: 2000ASPC..211..181P.

Rezzolla, L., Most, E. R., and Weih, L. R., "Using Gravitational-wave Observations and Quasi-universal Relations to Constrain the Maximum Mass of Neutron Stars," *The Astrophysical Journal*, vol. 852, p. L25, 2018, doi:10.3847/2041-8213/aaa401, publisher: IOP ADS Bibcode: 2018ApJ...852L..25R.

Riccioli, G. B., *Almagestvm novvm astronomiam veterem novamqve complectens observationibvs aliorvm*, 1651, doi:10.3931/e-rara-520, publication Title: Bononiae ADS Bibcode: 1651anav.book.....R.

Rivinius, T., Baade, D., Hadrava, P., Heida, M., and Klement, R., "A naked-eye triple system with a nonaccreting black hole in the inner binary," *Astronomy and Astrophysics*, vol. 637, p. L3, 2020, doi:10.1051/0004-6361/202038020, publisher: EDP ADS Bibcode: 2020A&A...637L...3R.

Rodriguez, C. L. and Loeb, A., "Redshift Evolution of the Black Hole Merger Rate from Globular Clusters," *The Astrophysical Journal*, vol. 866, p. L5, 2018, doi:10.3847/2041-8213/aae377, publisher: IOP ADS Bibcode: 2018ApJ...866L...5R.

Rodriguez, C. L., Zevin, M., Pankow, C., Kalogera, V., and Rasio, F. A., "Illuminating Black Hole Binary Formation Channels with Spins in Advanced LIGO," *The Astrophysical Journal*, vol. 832, p. L2, 2016, doi:10.3847/2041-8205/832/1/L2, publisher: IOP ADS Bibcode: 2016ApJ...832L...2R.

Röpke, F. K. and De Marco, O., "Simulations of common-envelope evolution in binary stellar systems: physical models and numerical techniques," *Living Reviews in Computational Astrophysics*, vol. 9, p. 2, 2023, doi:10.1007/s41115-023-00017-x, aDS Bibcode: 2023LRCA....9....2R.

Sablowski, D. P. and Weber, M., "Spectral disentangling with Spectangular," *Astronomy & Astrophysics*, vol. 597, p. A125, 2017, doi:10.1051/0004-6361/201628716.

Sana, H., de Mink, S. E., de Koter, A., Langer, N., Evans, C. J., Gieles, M., Gosset, E., Izzard, R. G., Le Bouquin, J. B., and Schneider, F. R. N., "Binary Interaction Dominates the Evolution of Massive Stars," *Science*, vol. 337, p. 444, 2012, doi:10.1126/science.1223344, aDS Bibcode: 2012Sci...337..444S.

Saracino, S., Kamann, S., Guarcello, M. G., Usher, C., Bastian, N., Cabrera-Ziri, I., Gieles, M., Dreizler, S., Da Costa, G. S., Husser, T. O., et al., "A black hole detected in the young massive LMC cluster NGC 1850," *Monthly Notices of the Royal Astronomical Society*, vol. 511, pp. 2914–2924, 2022, doi:10.1093/mnras/stab3159, publisher: OUP ADS Bibcode: 2022MNRAS.511.2914S.

Saracino, S., Shenar, T., Kamann, S., Bastian, N., Gieles, M., Usher, C., Bodensteiner, J., Kochoska, A., Orosz, J. A., and Sana, H., "Updated radial velocities and new constraints on the nature of the unseen source in NGC1850 BH1," *Monthly Notices of the Royal Astronomical Society*, vol. 521, pp. 3162–3171, 2023, doi:10.1093/mnras/stad764, publisher: OUP ADS Bibcode: 2023MNRAS.521.3162S.

Schneider, F. R. N., Izzard, R. G., Langer, N., and de Mink, S. E., "Evolution of Mass Functions of Coeval Stars through Wind Mass Loss and Binary Interactions," *The Astrophysical Journal*, vol. 805, p. 20, 2015, doi:10.1088/0004-637X/805/1/20, publisher: IOP ADS Bibcode: 2015ApJ...805...20S.

Seeburger, R., Rix, H.-W., El-Badry, K., Xiang, M., and Fouesneau, M., "Autonomous disentangling for spectroscopic surveys," *Monthly Notices of the Royal Astronomical Society*, vol. 530, pp. 1935–1955, 2024, doi:10.1093/mnras/stae982, publisher: OUP ADS Bibcode: 2024MNRAS.530.1935S.

Sepinsky, J. F., Willems, B., Kalogera, V., and Rasio, F. A., "Interacting Binaries with Eccentric Orbits. II. Secular Orbital Evolution due to Non-conservative Mass Transfer," *The Astrophysical Journal*, vol. 702, pp. 1387–1392, 2009, doi:10.1088/0004-637X/702/2/1387, publisher: IOP ADS Bibcode: 2009ApJ...702.1387S.

Shahaf, S., Mazeh, T., Faigler, S., and Holl, B., "Triage of astrometric binaries - how to find triple systems and dormant black hole secondaries in the Gaia orbits," vol. 487, no. 4, pp. 5610–5617, 2019, doi:10.1093/mnras/stz1636, arXiv: 1905.08542 [astro-ph.SR] tex.adsnote: Provided by the SAO/NASA Astrophysics Data System.

Shakura, N. I., Postnov, K. A., Kochetkova, A. Y., Hjalmarsdotter, L., Sidoli, L., and Paizis, A., "Wind accretion: Theory and observations," *Astronomy Reports*, vol. 59, no. 7, pp. 645–655, 2015, doi:10.1134/S1063772915070112, arXiv: 1407.3163 [astro-ph.HE] tex.adsnote: Provided by the SAO/NASA Astrophysics Data System.

Sheinis, A. I., Bolte, M., Epps, H. W., Kibrick, R. I., Miller, J. S., Radovan, M. V., Bigelow, B. C., and Sutin, B. M., "ESI, a New Keck Observatory Echellette Spectrograph and Imager," *Publications of the Astronomical Society of the Pacific*, vol. 114, pp. 851–865, 2002, doi:10.1086/341706, publisher: IOP ADS Bibcode: 2002PASP..114..851S.

Shenar, T., Bodensteiner, J., Abdul-Masih, M., Fabry, M., Mahy, L., Marchant, P., Banyard, G., Bowman, D. M., Dsilva, K., Hawcroft, C., et al., "The "hidden" companion in LB-1 unveiled by spectral disentangling," *Astronomy & Astrophysics*, vol. 639, p. L6, 2020, doi:10.1051/0004-6361/202038275.

Shenar, T., Sana, H., Mahy, L., El-Badry, K., Marchant, P., Langer, N., Hawcroft, C., Fabry, M., Sen, K., Almeida, L. A., et al., "An X-ray-quiet black hole born with a negligible kick in a massive binary within the Large Magellanic Cloud," *Nature Astronomy*, vol. 6, no. 9, pp. 1085–1092, 2022a, doi:10.1038/s41550-022-01730-y.

Shenar, T., Sana, H., Mahy, L., Maíz Apellániz, J., Crowther, P. A., Gromadzki, M., Herrero, A., Langer, N., Marchant, P., Schneider, F. R. N., et al., "The Tarantula Massive Binary Monitoring: VI. Characterisation of hidden companions in 51 single-lined O-type binaries: A flat mass-ratio distribution and black-hole binary candidates," *Astronomy & Astrophysics*, vol. 665, p. A148, 2022b, doi:10.1051/0004-6361/202244245.

Sigurdsson, S. and Phinney, E. S., "Binary–Single Star Interactions in Globular Clusters," *The Astrophysical Journal*, vol. 415, p. 631, 1993, doi:10.1086/173190, publisher: IOP ADS Bibcode: 1993ApJ...415..631S.

Simon, K. P. and Sturm, E., "Disentangling of composite spectra." *Astronomy and Astrophysics*, vol. 281, pp. 286–291, 1994, aDS Bibcode: 1994A&A...281..286S.

Skrutskie, M. F., Cutri, R. M., Stiening, R., Weinberg, M. D., Schneider, S., Carpenter, J. M., Beichman, C., Capps, R., Chester, T., Elias, J., et al., "The Two Micron All Sky Survey (2MASS)," *The Astronomical Journal*, vol. 131, pp. 1163–1183, 2006, doi:10.1086/498708, publisher: IOP ADS Bibcode: 2006AJ....131.1163S.

Soberman, G. E., Phinney, E. S., and van den Heuvel, E. P. J., "Stability criteria for mass transfer in binary stellar evolution." *Astronomy and Astrophysics*, vol. 327, pp. 620–635, 1997, doi:10.48550/arXiv.astro-ph/9703016, aDS Bibcode: 1997A&A...327..620S.

Strassmeier, K. G., Weber, M., Granzer, T., and Järvinen, S., "Rotation, activity, and lithium abundance in cool binary stars," *Astronomische Nachrichten*, vol. 333, p. 663, 2012, doi:10.1002/asna.201211719, aDS Bibcode: 2012AN....333..663S.

Subramaniam, A., Pandey, S., Jadhav, V. V., and Sahu, S., "UVIT/AstroSat studies of blue straggler stars and post-mass transfer systems in star clusters: detection of one more blue lurker in M67," *Journal of Astrophysics and Astronomy*, vol. 41, p. 45, 2020, doi:10.1007/s12036-020-09668-1, publisher: Springer ADS Bibcode: 2020JApA...41...45S.

Sukhbold, T., Ertl, T., Woosley, S. E., Brown, J. M., and Janka, H. T., "Core-collapse Supernovae from 9 to 120 Solar Masses Based on Neutrino-powered Explosions," *The Astrophysical Journal*, vol. 821, p. 38, 2016, doi:10.3847/0004-637X/821/1/38, publisher: IOP ADS Bibcode: 2016ApJ...821...38S.

Sukhbold, T., Woosley, S. E., and Heger, A., "A high-resolution study of presupernova core structure," vol. 860, no. 2, p. 93, 2018, doi:10.3847/1538-4357/aac2da, arXiv: 1710.03243 [astro-ph.HE] Number: 93 tex.adsnote: Provided by the SAO/NASA Astrophysics Data System.

Tauris, T. M., Kramer, M., Freire, P. C. C., Wex, N., Janka, H. T., Langer, N., Podsiadlowski, P., Bozzo, E., Chaty, S., Kruckow, M. U., et al., "Formation of Double Neutron Star Systems," *The Astrophysical Journal*, vol. 846, p. 170, 2017, doi:10.3847/1538-4357/aa7e89, publisher: IOP ADS Bibcode: 2017ApJ...846..170T.

The Astropy Collaboration, Price-Whelan, A. M., Lim, P. L., Earl, N., Starkman, N., Bradley, L., Shupe, D. L., Patil, A. A., Corrales, L., Brasseur, C. E., et al., "The Astropy Project: Sustaining and Growing a Community-oriented Open-source Project and the Latest Major Release (v5.0) of the Core Package*," *The Astrophysical Journal*, vol. 935, no. 2, p. 167, 2022, doi:10.3847/1538-4357/ac7c74.

The Astropy Collaboration, Price-Whelan, A. M., Sipőcz, B. M., Günther, H. M., Lim, P. L., Crawford, S. M., Conseil, S., Shupe, D. L., Craig, M. W., Dencheva, N., et al., "The Astropy Project: Building an Open-science Project and Status of the v2.0 Core Package*," *The Astronomical Journal*, vol. 156, no. 3, p. 123, 2018, doi:10.3847/1538-3881/aabc4f.

The Astropy Collaboration, Robitaille, T. P., Tollerud, E. J., Greenfield, P., Droettboom, M., Bray, E., Aldcroft, T., Davis, M., Ginsburg, A., Price-Whelan, A. M., et al., "Astropy: A community Python package for astronomy," *Astronomy & Astrophysics*, vol. 558, p. A33, 2013, doi:10.1051/0004-6361/201322068.

Tikhonov, A. N., "Solution of incorrectly formulated problems and the regularization method." *Sov Dok*, vol. 4, pp. 1035–1038, 1963.

Tokovinin, A. and Moe, M., "Formation of close binaries by disc fragmentation and migration, and its statistical modelling," *Monthly Notices of the Royal Astronomical Society*, vol. 491, pp. 5158–5171, 2020, doi:10.1093/mnras/stz3299, publisher: OUP ADS Bibcode: 2020MNRAS.491.5158T.

Townsend, R. H. D., Owocki, S. P., and Howarth, I. D., "Be-star rotation: how close to critical?" *Monthly Notices of the Royal Astronomical Society*, vol. 350, no. 1, pp. 189–195, 2004, doi:10.1111/j.1365-2966.2004.07627.x.

Traven, G., Feltzing, S., Merle, T., Van Der Swaelmen, M., Čotar, K., Church, R., Zwitter, T., Ting, Y.-S., Sahlholdt, C., Asplund, M., et al., "The GALAH survey: multiple stars and our Galaxy: I. A comprehensive method for deriving properties of FGK binary stars," *Astronomy & Astrophysics*, vol. 638, p. A145, 2020, doi:10.1051/0004-6361/202037484.

Vanbeveren, D., Mennekens, N., Shara, M. M., and Moffat, A. F. J., "Spin rates and spin evolution of O components in WR+O binaries," *Astronomy and Astrophysics*, vol. 615, p. A65, 2018, doi:10.1051/0004-6361/201732212, aDS Bibcode: 2018A&A...615A..65V.

Vink, J. S., de Koter, A., and Lamers, H. J. G. L. M., "Mass-loss predictions for O and B stars as a function of metallicity," vol. 369, pp. 574–588, 2001, doi:10.1051/0004-6361:20010127, arXiv: astro-ph/0101509 [astro-ph] tex.adsnote: Provided by the SAO/NASA Astrophysics Data System.

Virtanen, P., Gommers, R., Oliphant, T. E., Haberland, M., Reddy, T., Cournapeau, D., Burovski, E., Peterson, P., Weckesser, W., Bright, J., et al., "SciPy 1.0: fundamental algorithms for scientific computing in Python," *Nature Methods*, vol. 17, no. 3, pp. 261–272, 2020, doi:10.1038/s41592-019-0686-2.

Vogt, S. S., Allen, S. L., Bigelow, B. C., Bresee, L., Brown, B., Cantrall, T., Conrad, A., Couture, M., Delaney, C., Epps, H. W., et al., "HIRES: the high-resolution echelle spectrometer on the Keck 10-m Telescope," vol. 2198, p. 362, 1994, doi:10.1117/12.176725, conference Name: Instrumentation in Astronomy VIII ADS Bibcode: 1994SPIE.2198..362V.

Walker, R., *Spectral Atlas for Amateur Astronomers: A Guide to the Spectra of Astronomical Objects and Terrestrial Light Sources*, Cambridge University Press, 1 ed., 2017, ISBN 978-1-316-69420-6 978-1-107-16590-8, doi:10.1017/9781316694206.

Wang, C., Langer, N., Schootemeijer, A., Castro, N., Adscheid, S., Marchant, P., and Hastings, B., "Effects of Close Binary Evolution on the Main-sequence Morphology of Young Star Clusters," *The Astrophysical Journal*, vol. 888, p. L12, 2020, doi:10.3847/2041-8213/ab6171, publisher: IOP ADS Bibcode: 2020ApJ...888L..12W.

Wang, S., Zhao, X., Feng, F., Ge, H., Shao, Y., Cui, Y., Gao, S., Zhang, L., Wang, P., Li, X., et al., "A potential mass-gap black hole in a wide binary with a circular orbit," *Nature Astronomy*, vol. 8, pp. 1583–1591, 2024, doi:10.1038/s41550-024-02359-9, aDS Bibcode: 2024NatAs...8.1583W.

Wheeler, A. J., Abruzzo, M. W., Casey, A. R., and Ness, M. K., "KORG: A Modern 1D LTE Spectral Synthesis Package," *The Astronomical Journal*, vol. 165, p. 68, 2023, doi:10.3847/1538-3881/acaaad, publisher: IOP ADS Bibcode: 2023AJ....165...68W.

Wheeler, A. J., Casey, A. R., and Abruzzo, M. W., "Korg: Fitting, Model Atmosphere Interpolation, and Brackett Lines," *The Astronomical Journal*, vol. 167, p. 83, 2024, doi:10.3847/1538-3881/ad19cc, publisher: IOP ADS Bibcode: 2024AJ....167...83W.

Willcox, R., MacLeod, M., Mandel, I., and Hirai, R., "The Impact of Angular Momentum Loss on the Outcomes of Binary Mass Transfer," *The Astrophysical Journal*, vol. 958, p. 138, 2023, doi:10.3847/1538-4357/acffb1, publisher: IOP ADS Bibcode: 2023ApJ...958..138W.

Xiang, M., Rix, H.-W., Ting, Y.-S., Kudritzki, R.-P., Conroy, C., Zari, E., Shi, J.-R., Przybilla, N., Ramirez-Tannus, M., Tkachenko, A., et al., "Stellar labels for hot stars from low-resolution spectra. I. The HotPayne method and results for 330 000 stars from LAMOST DR6," *Astronomy and Astrophysics*, vol. 662, p. A66, 2022, doi:10.1051/0004-6361/202141570, publisher: EDP ADS Bibcode: 2022A&A...662A..66X.

Yamaguchi, M. S., Kawanaka, N., Bulik, T., and Piran, T., "Detecting Black Hole Binaries by Gaia," *The Astrophysical Journal*, vol. 861, p. 21, 2018, doi:10.3847/1538-4357/aac5ec, publisher: IOP ADS Bibcode: 2018ApJ...861...21Y.

York, D. G., Adelman, J., Anderson, J. E., Jr., Anderson, S. F., Annis, J., Bahcall, N. A., Bakken, J. A., Barkhouser, R., Bastian, S., Berman, E., et al., "The Sloan Digital Sky Survey: Technical Summary," *The Astronomical Journal*, vol. 120, no. 3, pp. 1579–1587, 2000, doi:10.1086/301513.

Zahn, J. P., "The dynamical tide in close binaries." *Astronomy and Astrophysics*, vol. 41, pp. 329–344, 1975, aDS Bibcode: 1975A&A....41..329Z.

Zahn, J. P., "Tidal friction in close binary systems." vol. 57, pp. 383–394, 1977, tex.adsnote: Provided by the SAO/NASA Astrophysics Data System.

Zahn, J. P., "Tidal dissipation in binary systems," vol. 29, pp. 67–90, 2008, doi:10.1051/eas:0829002, conference Name: EAS Publications Series Place: eprint: arXiv:0807.4870 ADS Bibcode: 2008EAS....29...67Z.

Zari, E., Rix, H. W., Frankel, N., Xiang, M., Poggio, E., Drimmel, R., and Tkachenko, A., "Mapping luminous hot stars in the Galaxy," *Astronomy and Astrophysics*, vol. 650, p. A112, 2021, doi:10.1051/0004-6361/202039726, aDS Bibcode: 2021A&A...650A.112Z.

von Zeipel, H., "The radiative equilibrium of a rotating system of gaseous masses," *Monthly Notices of the Royal Astronomical Society*, vol. 84, pp. 665–683, 1924, doi:10.1093/mnras/84.9.665, publisher: OUP ADS Bibcode: 1924MNRAS..84..665V.

Zhang, X. and Green, G., "Unveiling the Milky Way dust extinction curve in 3D," , 2024, doi:10.5281/ZENODO.11394477.

Ziosi, B. M., Mapelli, M., Branchesi, M., and Tormen, G., "Dynamics of stellar black holes in young star clusters with different metallicities - II. Black hole-black hole binaries," *Monthly Notices of the Royal Astronomical Society*, vol. 441, pp. 3703–3717, 2014, doi:10.1093/mnras/stu824, publisher: OUP ADS Bibcode: 2014MNRAS.441.3703Z.

Zucker, S. and Mazeh, T., "Study of Spectroscopic Binaries with TODCOR. I. A New Two-dimensional Correlation Algorithm to Derive the Radial Velocities of the Two Components," *The Astrophysical Journal*, vol. 420, p. 806, 1994, doi:10.1086/173605, publisher: IOP ADS Bibcode: 1994ApJ...420..806Z.

Zucker, S. and Mazeh, T., "tiravel Template-Independent RAdial VELocity measurement," *Monthly Notices of the Royal Astronomical Society*, vol. 371, no. 3, pp. 1513–1518, 2006, doi:10.1111/j.1365-2966.2006.10789.x.

Özel, F., Psaltis, D., Narayan, R., and McClintock, J. E., "The Black Hole Mass Distribution in the Galaxy," *The Astrophysical Journal*, vol. 725, pp. 1918–1927, 2010, doi:10.1088/0004-637X/725/2/1918, publisher: IOP ADS Bibcode: 2010ApJ...725.1918O.

List of Figures

List of Tables

Acknowledgements

I have been fantasising about writing this Acknowledgements section basically since I started my PhD almost four years ago. Especially in the last few weeks of finishing up this thesis, thoughts of who to list, how to thank them, in what order, how to group people, etc, has filled a lot of my thoughts. That being said, I have come to the conclusion that there is no best or most coherent way to list everyone. So if you are just here to see if I named you (don't worry, I have done the same for friends and colleagues), just ctrl+F your name.

I would like to start by expressing my gratitude to my supervisors, Hans-Walter Rix and Kareem El-Badry. Coming to this project from a completely different background (in cosmology!), there were many initial hurdles to overcome. Your advice, your criticism and praise has bolstered me for the past four years, helping me develop from a student into an independent junior researcher. Kareem, your direct and to-the-point style of communication has been invaluable, as has been your sense of humour. Hans-Walter, your ability to entertain any idea and your honest engagement with what I brought to the table has strengthened my resolve and faith in myself, as well as sharpened my scientific arguing skills.

To my Thesis Committee: Gregory Green, Fabian Schneider and Fritz Röpke. Thank you for your thoughts, your excitement about my work, and your perspective. It is easy to get bogged down in my small little corner of research, and it was been invaluable getting some outside viewpoint, at least once a year.

Of course, my scientific career did not start in 2021. Catherine, thank you for being my cheerleader all throughout undergrad, and even after. Your love and passion for astronomy has been infectious, as has your zest for life. I hope I have made you proud. To all my undergraduate lecturers, supervisors and tutors: I might have loathed that coursework and been annoyed at the 9 a.m. lectures, but they have brought me here today. Thank you for your time, your work, your words.

Studying physics at university was a decision I made with little second-guessing. Franz, your jokes and no-nonsense attitude fanned my spark for physics into a flame that by now has become a bonfire. I hope I can keep giving back.

MPIA is, perhaps, the best place in the world to do a PhD. Scenic bike routes lead up to a grey concrete block full of some of the brightest and most genuine people alive. I have interacted with and learned from too many colleagues to name over the years, but I want to highlight at least some.

To the Milky Way/Binary PhDs and PostDocs past and present. Neige and Johanna, thank you for taking the time prior to joining to let me find out if this was the right fit for me. Verena, Emily, Jiadong, Maosheng, Jaime, Matthew, Eleonora, Leigh, Xiangyu, Taavet, Johanna, and Ben, thank you for your scientific input, and your patience with my more grumpy moments. And my procrastination.

If I have seen further it is by standing on the shoulders of giants: my PhD Elders. Eric, you were one of the first people I met in Heidelberg, and you have filled my time with lots of laughter. Evert, your sense for art has been an inspiration, as has your quick wit. Verena, I would have been way more lonely without someone close to home (even though Purkersdorf is not in Vienna). Nico, your grit and tenacity in all things in life is inspirational. I am excited to see what all of you get up to in the future.

Of course, I did not have to suffer through the last four years on my own. Molly, your talent is wasted in astronomy - I hope one day you see the light and absolutely destroy everyone on GBBO. Marten, we are starting and finishing this together - you made this bonanza a fun one. Alex and Callie, thank you for bread and bike rides, and your kind and compassionate perspective - as astronomers, we often get lost in space beyond our own planet; thank you for reminding all of us it is worth protecting. Roel, thanks for the beer and whatever the heck that punch thing you make is. Taavet, I don't think anyone in this city has seen my mug as much as you have - thank you for endless hours in the gym, on the bike, in front of the TV, sharing chocolate, carbonara and tea (and Villu pics!). Lynn, I don't think I need to go into detail here; let's keep up the bit. (But also, thank you for late-night chats, hospital visits and wonderful trips to London).

To the Outreachies. Selina, Jan, Lukas, Dane, Sophia, Johanna, Dominik, Cade - let's keep sharing the joy of astronomy with the public (whether they like it or not).

Astronomers are notoriously bad at programming, and I am grateful that the MPIA Data Science Department exists. Morgan, your expertise and dry humour have made me a better programmer, and given me the courage to be wrong (and get my spaghetti code absolutely eviscerated). Iva, your knowledge is only matched by your heart - thank you for always having an open ear, not just to my data science questions. Raphael, thank you for spreading the good news of Balatro.

To the MPIA technical and canteen staff, for making sure I was fed with a never-ending supply of hard-boiled eggs, and for making sure I could actually get into the building.

Over the years, I have had the joy to interact with many fantastic people both within and outside my field, from all across the world. Thank you all for broadening my horizons.

To my fellow junior binary star and black hole researchers. Bethany, thank you for including me in your home (and your work!), I hope we can keep propping each other up. Jan, your dedication to what is right is admirable; thank you for your courage and your open heart. Soetkin, I cannot fathom how you can have a successful scientific and swimming career while most of us are struggling to do just one of these. Let's actually finish The Mind at some point.

Naturally, once we stop being junior researchers, we suddenly know everything there is to know about our field. Or at least that is what I reckon, based on the great (not so junior) researchers who have inspired and motivated me. Tomer, Julia, Eva, Andrew, and countless others - thank you for letting me learn from and with you, and sharing your insights with me and the community.

To my co-authors. If you did indeed ctrl+F your name, you probably saw it pop up already in the main body of this thesis. Thank you for your time, your thoughts, your some-

times last-minute comments and helpful discussions. In particular I want to say thank you to Johanna, Jaime and Alex, who helped me iron out some of the kinks in the introduction of this thesis (and I haven't ironed a shirt in about 4 years).

As an academic, it can be hard to remember that there is a whole world outside of your institute. When times seemed dark and work endless, I could count on my fellow rainbow (party) people to show me the light (frequently quite literally in the form of a disco ball). Dimitris, David, Cedar, Rodri, Efraim, Laura, Fran - thank you for reminding me that life is more than work, and that we can find community if we just look for it. In the wise words of Mother Gaga: Ra, ra, ah-ah-ah, roma, roma-ma, gaga, ooh, la, la.

Tuesday evenings have been marked in my calendar since time immemorial. Phil and Kailen, thank you for opening your home to me and being there at times of crisis (like when I haven't eaten for at least four hours). Fabi, Maha, Chase - thank you for making Tuesdays one of my favourite days of the week! And, of course, Huxley: thank you for bringing joy to my life every time I see you. Go Pokepals!

To my fellow Strixhaven Students. Lion, thank you for whisking us all away into a world that is much kinder (and more exciting) than the one we live in. Brady, Phil, Sam, thank you for going on monster hunts and acts of domestic terrorism (in DnD!) with me. And thank you for feeding me the nectar of my people.

Though Mannheim and Frankfurt are all far away, it was always worth for a Hangout. Aly, Svenja, Belle, Marlon, Milena, Moritz, and many others. Thank you for your lack of judgement, for creating spaces where people can be themselves and come into their own. Thank you for never being selfish with your knowledge, your resources or your time.

Gemma, Irene, Mateus - thank you for making time and space to be creative and explore together. Eric (a different one) - Giggy will forever live in our hearts.

Emily and Till, my favourite and most/least unhinged Saarländer. Thank you for providing a safe haven (Till) in the storm (Emily). For Lads' nights (Till) and Girls' out on the town (Emily). And thank you for vaping instead of smoking when I'm around.

To my fellow travellers with PLUS. Brienne, I struggle to express myself at times; thank you for being on my wavelength. Ralph, your kindness and down-to-earth calm can weather any storm. Cornelia, it takes courage to be true to yourself (I would know). Jona, thank you for showing me that you can be gentle in all things. Frau Herrmann: Thank you for being there, week after week, to create space for us.

While this thesis has taken up the better part of four years, I did not mysteriously pop into existence in 2021 as a fully formed MPhys degree holder, ready to take on the beast that is a PhD.

Some may say your early 20s are like a second puberty. For me they were certainly formative years. Callum, Sam, Dan, Annaliina; I hope you are all proud of what you have achieved since we graduated, I know I am. Seonagh, words cannot describe how grateful I am to call you my friend. Thank you for holding up a mirror when I needed it, and catching me when I stumbled. Lawful Neutral LLC would be in shambles without you (and me too).

To the Tworgs. Alex, you bring paneer and joy to everyone around you; I hope the smaller distance between us going forwards means I will get to partake more often. Arthur, you are the man of my dreams (on par with Hardin Scott). To many more years of horrible movies and good drinks.

Without Greenwichstuck, I would be a much better adjusted individual. Thank god for Vlad, Toby, Liggins, Jack, Jem, and the Bristol kids. We have all grown up but half of you

are still Weebs. Thank you for showing me the value of finding unabashed joy in the things you love, however silly they may be.

Bel, only a handful of people live a life as cool as yours. Maybe one day we can all manage to meet up more regularly again (and even make another video!) Until then, keep creating!

To Jolly. Thank you for endless, unfettered merriment through the nerdiest of pastimes, for making art and trying new things together. Thank you for millions of custom little Star Trek trinkets and more tapas than should be able to fit inside a person.

To my friends from Home. Heli, Steffi, Janis, Claudi, you have known me for longer than almost anyone else on this list, and somehow have stuck around. Thank you for joining me through all the ups and downs over the last almost 20 years. Chiara, for bringing some life to the horror of Stuttgart HBF (and also all the deep chats).

To my family (German incoming!) Mama, Papa, danke für eure bedingungslose Unterstützung, Liebe und Zuneigung die letzten 27 Jahre. Ihr habt mir eine Freude an der Wissenschaft und Wertschätzung für Bildung mitgegeben, die ich immer in mir tragen werde. Hanni, ohne eine Schwester wäre ich noch schräger geworden - Danke dass du mich immer verteidigt hast. Mimi, Lilli - Katzen sind, historisch gesehen, eine wichtige Komponente jedes Physikers. Alle Omas, Opas, Onkel, Tanten, Cousins und Cousinen: danke für Kuchen, Bücher, Osterjausen, Theaterbesuche und Mittelalterfeste.

Thank you all for your support, your ideas, your passion and your love over the years. I am taking a piece of all of you with me to the next chapter. Ad Astra per Aspera!